NATIONAL AERONAUTICS AND SPACE ADMINISTRATION

Technical Report 32-1526
Volume XIV
The Deep Space Network

Progress Report
For January and February 1973

JET PROPULSION LABORATORY
CALIFORNIA INSTITUTE OF TECHNOLOGY
PASADENA, CALIFORNIA

April 15, 1973

Prepared Under Contract No. NAS 7-100
National Aeronautics and Space Administration

Preface

This report presents DSN progress in flight project support, TDA research and technology, network engineering, hardware and software implementation, and operations. Each issue presents material in some, but not all, of the following categories in the order indicated:

Description of the DSN

Mission Support
  Interplanetary Flight Projects
  Planetary Flight Projects
  Manned Space Flight Projects
  Advanced Flight Projects

Radio Science

Supporting Research and Technology
  Tracking and Ground-Based Navigation
  Communications, Spacecraft/Ground
  Station Control and Operations Technology
  Network Control and Data Processing

Network Engineering and Implementation
  Network Control System
  Ground Communications
  Deep Space Stations

Operations and Facilities
  Network Operations
  Network Control System Operations
  Ground Communications
  Deep Space Stations
  Facility Engineering

In each issue, the part entitled "Description of the DSN" describes the functions and facilities of the DSN and may report the current configuration of one of the five DSN systems (Tracking, Telemetry, Command, Monitor and Control, and Test and Training).

The work described in this report series is either performed or managed by the Tracking and Data Acquisition organization of JPL for NASA.

Contents

DESCRIPTION OF THE DSN

MISSION SUPPORT

Planetary Flight Projects

Manned Space Flight Projects

SUPPORTING RESEARCH AND TECHNOLOGY

Tracking and Ground-Based Navigation

Communications, Spacecraft /Ground

Contents (contd)

Station Control and Operations Technology

Contents (contd)

Network Control and Data Processing

NETWORK ENGINEERING AND IMPLEMENTATION

Network Control System

Deep Space Stations

Contents (contd)

OPERATIONS AND FACILITIES

Deep Space Stations

Facility Engineering

DSN Functions and Facilities

N. A. Renzetti
Mission Support Office

The objectives, functions, and organization of the Deep Space Network are summarized. The Deep Space Instrumentation Facility, the Ground Communications Facility, and the Network Control System are described.

The Deep Space Network (DSN), established by the National Aeronautics and Space Administration (NASA) Office of Tracking and Data Acquisition under the system management and technical direction of the Jet Propulsion Laboratory (JPL), is designed for two-way communications with unmanned spacecraft traveling approximately 16,000 km (10,000 mi) from Earth to planetary distances. It supports or has supported, the following NASA deep space exploration projects: Ranger, Surveyor, Mariner Venus 1962, Mariner Mars 1964, Mariner Venus 67, Mariner Mars 1969, Mariner Mars 1971, Mariner Venus–Mercury 1973 (JPL); Lunar Orbiter and Viking (Langley Research Center); Pioneer (Ames Research Center); Helios (West Germany); and Apollo (Manned Spacecraft Center), to supplement the Spaceflight Tracking and Data Network (STDN).

The Deep Space Network is one of two NASA networks. The other, STDN, is under the system management and technical direction of the Goddard Space Flight Center. Its function is to support manned and unmanned Earth-orbiting and lunar scientific and communications satellites. Although the DSN was concerned with unmanned lunar spacecraft in its early years, its primary objective now and into the future is to continue its support of planetary and interplanetary flight projects.

A development objective has been to keep the network capability at the state of the art of telecommunications and data handling and to support as many flight projects as possible with a minimum of mission-dependent hardware and software. The DSN provides direct support of each flight project through that project's tracking and data system. This management element is responsible for the design and operation of the hardware and software in the DSN which are required for the conduct of flight operations.

Beginning in FY 1973 a modified DSN interface has been established with the flight projects. In lieu of the SFOF, a multimission Mission Control and Computing Center (MCCC) has been activated as a separate functional and management element within JPL. This function, as negotiated with each flight project, will provide all computing and mission operations support for missions controlled from JPL. DSN computing support will be provided separately by the DSN. Radio metric, telemetry, and command data interfaces with the DSN are a joint DSN, MCCC, and flight project responsibility. The organization and procedures necessary to carry out these new activities will be reported in this document in the near future.

The DSN function, in supporting a flight project by tracking the spacecraft, is characterized by five network systems:

(1) DSN Tracking System. Generates radio metric data; i.e., angles, one- and two-way doppler and range, and transmits raw data to mission control.

(2) DSN Telemetry System. Receives, decodes, records, and retransmits engineering and scientific data generated in the spacecraft to Mission Control.

(3) DSN Command System. Accepts coded signals from mission control via the GCF and transmits them to the spacecraft in order to initiate spacecraft functions in flight.

(4) DSN Monitor and Control System. Instruments, transmits, records, and displays those parameters of the DSN necessary to verify configuration and validate the network. Provides operational direction and configuration control of the network and primary interface with flight project Mission Control personnel.

(5) DSN Test and Training System. Generates and controls simulated data to support development, test, training and fault isolation within the DSN. Participates in mission simulation with flight projects.

The facilities needed to carry out these functions have evolved in three technical areas: (1) the Deep Space Stations (DSSs) and the telecommunications interface through the RF link with the spacecraft is known as the Deep Space Instrumentation Facility (DSIF); (2) the Earth-based point-to-point voice and data communications from the stations to Mission Control is known as the Ground Communications Facility (GCF); (3) the network monitor and control function is known as the Network Control System (NCS).

I. Deep Space Instrumentation Facility

A. Tracking and Data Acquisition Facilities

A world-wide set of Deep Space Stations with large antennas, low-noise phase-lock receiving systems, and high-power transmitters provide radio communications with spacecraft. The DSSs and the deep space communications complexes (DSCCs) they comprise are given in Table 1.

Radio contact with a spacecraft usually begins when the spacecraft is on the launch vehicle at Cape Kennedy, and it is maintained throughout the mission. The early part of the trajectory is covered by selected network stations of the Air Force Eastern Test Range (AFETR) and the STDN of the Goddard Space Flight Center.[1] Normally, two-way communications are established between the spacecraft and the DSN within 30 min after the spacecraft has been injected into lunar, planetary, or interplanetary flight. A compatibility test station at Cape Kennedy (discussed later) tests and monitors the spacecraft continuously during the launch checkout phase. The deep space phase begins with acquisition by 26-m DSSs. These and the remaining DSSs listed in Table 1 provide radio communications until the end of the mission.

To enable continuous radio contact with spacecraft, the DSSs are located approximately 120 deg apart in longitude; thus a spacecraft in deep space flight is always within the field-of-view of at least one DSS, and for several hours each day may be seen by two DSSs. Furthermore, since most spacecraft on deep space missions travel within 30 deg of the equatorial plane, the DSSs are located within latitudes of 45 deg north and south of the equator. All DSSs operate at S-band frequencies: 2110-2120 MHz for Earth-to-spacecraft transmission and 2290-2300 MHz for spacecraft-to-Earth transmission. An X-band capability is being readied for future missions beginning in 1973.

---

[1] The 9-m (30-ft) diam antenna station established by the DSN on Ascension Island during 1965 to act in conjunction with the STDN orbital support 9-m (30-ft) diam antenna station was transferred to the STDN in July 1968.

To provide sufficient tracking capability to enable returns of useful data from around the planets and from the edge of the solar system, a 64-m (210-ft) diam antenna subnet will be required. Two additional 64-m (210-ft) diam antenna DSSs are under construction at Madrid and Canberra and will operate in conjunction with DSS 14 to provide this capability. These stations are scheduled to be operational by the middle of 1973.

B. Compatibility Test Facilities

In 1959, a mobile L-band compatibility test station was established at Cape Kennedy to verify flight-spacecraft/DSN compatibility prior to the launch of the Ranger and Mariner Venus 1962 spacecraft. Experience revealed the need for a permanent facility at Cape Kennedy for this function. An S-band compatibility test station with a 1.2-m (4-ft) diameter antenna became operational in 1965. In addition to supporting the preflight compatibility tests, this station monitors the spacecraft continuously during the launch phase until it passes over the local horizon.

Spacecraft telecommunications compatibility in the design and prototype development phases was formerly verified by tests at the Goldstone DSCC. To provide a more economical means for conducting such work and because of the increasing use of multiple-mission telemetry and command equipment by the DSN, a Compatibility Test Area (CTA) was established at JPL in 1968. In all essential characteristics, the configuration of this facility is identical to that of the 26-m (85-ft) and 64-m (210-ft) diameter antenna stations.

The JPL CTA is used during spacecraft system tests to establish the compatibility with the DSN of the proof test model and development models of spacecraft, and the Cape Kennedy compatibility test station is used for final flight spacecraft compatibility validation testing prior to launch.

II. Ground Communications Facility

The GCF provides voice, high-speed data, wideband data, and teletype communications between the Mission Operations Center and the DSSs. In providing these capabilities, the GCF uses the facilities of the worldwide NASA Communications Network (NASCOM)[2] for all long distance circuits, except those between the Mission Operations Center and the Goldstone DSCC. Communications between the Goldstone DSCC and the Mission Operations Center are provided by a microwave link directly leased by the DSN from a common carrier.

Early missions were supported by voice and teletype circuits only, but increased data rates necessitated the use of high-speed and wideband circuits for DSSs. Data are transmitted to flight projects via the GCF using standard GCF/NASCOM formats. The DSN also supports remote mission operations centers using the GCF/NASCOM interface.

III. Network Control System

The DSN Network Control System is comprised of hardware, software, and operations personnel to provide centralized, real-time control of the DSN and to monitor and validate the network performance. These functions are provided during all phases of DSN support to flight projects. The Network Operations Control Area is located in JPL Building 230, adjacent to the local Mission Operations Center. The NCS, in accomplishing the monitor and control function does not alter, delay, or serially process any inbound or outbound data between the flight project and tracking stations. Hence NCS outages do not have a direct impact on flight project support. Voice communications are maintained for operations control and coordination between the DSN and flight projects, and for minimization of the response time in locating and correcting system failures.

The NCS function will ultimately be performed in data processing equipment separate from flight project data processing and specifically dedicated to the NCS function. During FY 1973, however, DSN operations control and monitor data will be processed in the JPL 360/75 and in the 1108. In FY 1974 the NCS data processing function will be partly phased over to an interim NCS processor, and finally, in FY 1975, the dedicated NCS data processing capability will be operational. The final Network Data Processing Area will be located remote from the Network Operations Control Area so as to provide a contingency operating location to minimize single point of failure effects on the network control function. A preliminary description of the NCS appears elsewhere in this document.

---

[2] Managed and directed by the Goddard Space Flight Center.

Table 1. Tracking and data acquisition stations of the DSN

DSCC	Location	DSS	DSS serial designation	Antenna		Year of initial operation
				Diameter, m (ft)	Type of mounting	
Goldstone	California	Pioneer	11	26(85)	Polar	1958
		Echo	12	26(85)	Polar	1962
		(Venus)[a]	13	26(85)	Az-El	1962
		Mars	14	64(210)	Az-El	1966
Tidbinbilla	Australia	Weemala (formerly Tidbinbilla)	42	26(85)	Polar	1965
		Ballima (formerly Booroomba)	43	64(210)	Az-El	Under construction
–	Australia	Honeysuckle Creek[b]	44	26(85)	X-Y	1973
–	South Africa	Hartebeesthoek	51	26(85)	Polar	1961
Madrid	Spain	Robledo	61	26(85)	Polar	1965
		Cebreros	62	26(85)	Polar	1967
		Robledo	63	64(210)	Az-El	Under construction

[a] A research-and-development facility used to demonstrate the feasibility of new equipment and methods to be integrated into the operational network. Besides the 26-m (85-ft) diam Az-El mounted antenna, DSS 13 has a 9-m (30-ft) diam Az-El mounted antenna that is used for interstation time correlation using lunar reflection techniques, for testing the design of new equipment, and for support of ground-based radio science.

[b] To be shared with STDN until January 1974.

Mariner Venus/Mercury 1973 Mission Support

E. K. Davis
DSN Systems Engineering

During January and February 1973, DSN preparations for Mariner Venus/Mercury 1973 mission support included continuing implementation of new capabilities, initiation of training, test and operations planning, and revision of plans to match new budget guidelines. The DSN Progress Review was held on February 2, 1973 to evaluate the progress of these ongoing activities. Much of the information in this article stems from Progress Review material.

I. Planning Activities

A. NASA Support Plan

NASA Headquarters approval of the NASA Support Plan (NSP) was expected prior to January 1, 1973. However, this approval has been delayed until the effects of recent budget reductions on NSP commitments are clear. We have requested that review and approval be completed prior to the next Mariner Venus/Mercury 1973 (MVM 73) Quarterly Review on March 29 and 30, 1973.

B. DSN Preparation Plan

The DSN Preparation Plan for MVM 73 (JPL internal document 615-105, Jan. 15, 1973) was approved, published, and distributed during this reporting period. The implementation plans contained in this document served as a basis for evaluating the status presented during the DSN Progress Review.

C. DSN Operations Plan

Preparation of the Network Operations Plan for MVM 73 is on schedule. A draft of the document, including ground communications and Deep Space Station (DSS) portions, was completed during this reporting period. The approved version is scheduled for completion in March 1973 as a prerequisite to start of DSN testing for MVM 73 in April 1973.

D. DSN Support Team

The DSN Support Team for MVM 73 has continued to meet twice each month to resolve open items in the areas of DSN/Mission Control and Computing Center (MCCC)/Project interface requirements and design. All significant action items have been completed with results published in appropriate documentation. Therefore, it is anticipated that the DSN Support Team will be discontinued at the end of February 1973 in favor of a DSN Test/Operations Support Team headed by the Network Operations Planning Engineer.

E. Mission Sequence Planning Support

The Network Operations Organization has been involved in supporting the Mission Sequence Working Group in design of the MVM 73 mission. Sequences have been reviewed for consistency with Network operational capabilities. The Network Operations Manager has served on the Mission Sequence Design Review Board. Network operations people attend the working group meetings and have made presentations on Deep Space Station prepass and hand-over procedures. Work has been initiated to define DSS track time allocations in support of the sequence and to resolve MVM 73/Pioneer 10 encounter schedule conflicts.

II. Program Control

A. Interface Control Document

The MVM 73 Spacecraft/Mission Operations System/Tracking and Data System/Mission Control and Computing Center System Interface Control Document (ICD) is in work. However, all DSN portions of this document have been completed and approved by the appropriate cognizant engineers for tracking, telemetry, command, simulation, monitor, and radio frequency systems. The ICD forms the baseline for interface configuration and change control. Any changes that would alter the approved interface require joint approval of the interfacing agencies prior to implementation. Maintenance of interface integrity for the DSN side of these interfaces is the responsibility of the DSN Change Control Board.

B. DSN Progress Review

Validation and evaluation of DSN plans and progress for MVM 73 is accomplished through a series of reviews as set forth in the DSN Support Requirements Document for MVM 73. The DSN Progress Review is one in the series that leads to operational readiness; see Table 1.

The DSN Progress Review was conducted on February 2, 1973. The purpose was to: (1) review status of DSN development and implementation tasks, (2) review detailed DSN test and training plans, (3) review the status of DSN/Spacecraft compatibility test plans and test results, (4) verify that DSN preparations are following the plans, and (5) identify open areas and assign actions for resolution.

The Review Committee was cochaired by the DSN Implementation Manager and the DSN Operations Manager. Other Committee members included the TDS Manager, DSN Manager, and Project people representing the areas of data processing, flight operations, and spacecraft telecommunications. The Review was conducted in accordance with the agenda shown in Table 2. The named presenters are the cognizant development engineers for DSN implementation and the cognizant operations engineers for test and training activities. Summaries of information presented are included in the appropriate paragraphs of Sections III and IV of this article.

Following the presentations, the Review Committee met to consolidate comments, define problem areas, and assign action items. A complete package of the review material was prepared and distributed to all participants and attendees. Results of assigned action items will be addressed in future articles.

III. Implementation Activities

A. GCF Status

The presentation was made by the cognizant development engineer using GCF level-6 implementation schedules and configuration diagrams as a basis for discussion. Basically, GCF implementation is on schedule. Circuits between JPL and Boeing, Kent, are operational. GCF engineers are fully cognizant of and are accommodating recent changes in requirements and plans. Completion of the 28.5 kbps and 230 kbps wideband data line implementation is expected to continue on schedule. Inability of the NASA Communications Network (NASCOM) to provide training for NASCOM-furnished wide-band data line (WBDL) equipment in February/March 1973 may cause difficulty, but work-arounds will be designed. The high level of activity associated with coded multiplexer delivery and installation is a critically tight schedule to be closely monitored.

B. DSS Status

DSS implementation status was given by cognizant hardware/software development engineers using task summaries and schedules as a basis for discussion. Most implementation is targeted toward an April 1, 1973 completion for start of DSS/DSN test activities. Notable planned exceptions are: DSSs 43 and 63, planetary ranging, and DSS 14 S-band/X-band (S/X) implementation. Many problems discussed have to do with implementation that appears to be from one to two months later than required for test activities and readiness commitments. Consequently, many action items assigned require additional detailed schedule review between the Network Operations Project Engineer (NOPE)/Cognizant Operations Engineers (COEs) and Cognizant Design Engineers (CDEs).

1. Telemetry and Command Data Subsystem software and hardware. Telemetry and Command Data Subsystem (TCD) software development is on schedule. Integration of all modules shall be completed in early February 1973 through loading of all program elements. Included are TCD executive, command, TCP telemetry, and Data Decoder Assembly (DDA) telemetry elements. Standalone verification tests for all modules are completed. In regard to hardware, the dual high density recorder assemblies are on schedule. However, the Symbol Synchronizer Assembly (SSA)-DDA coupler modification appears to be one month late to support start of tests. Also, DSS time must be scheduled for the modification installation.

2. Digital Instrumentation Subsystem. Digital Instrumentation Subsystem (DIS) hardware and software development for monitor purposes is on schedule. There appear to be no problems to completing implementation on the required 1 April date. DIS implementation to provide high-speed tracking capabilities extends well beyond April 1, 1973 for some DSSs. This was not unexpected. For some time we have recognized that replacement of teletypewriter (TTY) by high-speed data line (HSDL) for transmission of radio metric data might occur late in our planned test period at certain DSSs. However, implementation at some DSSs must be completed by April/May to permit early verification of the tracking system design and performance.

3. Simulation Conversion Assembly hardware and software. Installation of Simulation Conversion Assembly (SCA) modifications at some DSSs extends into May 1973. Stations that start testing in April 1973 require an operational SCA. Also, DSS time must be scheduled for modification installations.

4. Planetary ranging hardware and software. Planetary ranging is committed to be operational on October 1, 1973 at DSS 14 and on January 1, 1974 at DSSs 43 and 63. Also, it is desirable that this capability be available at CTA 21 in July 1973 or at DSS 71 in September/October 1973 for RF compatibility testing. The hardware schedule presented shows that subsystem testing will be completed on or later than the committed dates. Completion of system tests and operational status would push this well beyond the needed dates. Software schedules appear to be consistent with need dates.

5. S/X-band experiment. Modification of the feed cone assemblies was completed and reinstallation on the DSS 14 antenna and testing were accomplished between January 22 and 30, 1973 as scheduled. Included are the ellipsoidal reflector over the S-band feed and a dichroic mirror over the X-band feed with each feed mounted in separate cone structures. The dichroic mirror passes the X-band signal and reflects the S-band signal. Preliminary test results show that the electrical performance is excellent: no S-band degradation and less than 0.2 dB degradation at X-band due to the dichroic plate. No warping problems were observed in the plate during thermal testing at a power of 300 kW. It was planned that DSS 14 S/X-band capabilities would be completed for operations in an R&D mode by October 1, 1973. S/X-band RF compatibility tests with an S/X-band transponder and DSS 14 Block IV receiver were planned for June/July 1973. Late installation of the coherent reference generator, Block IV receiver, and S/X ranging is not compatible with this plan.

6. DSSs 43 and 63. DSS 43 implementation is on schedule for a July 1, 1973 completion and start of testing for MVM 73 as planned. DSS 63 has encountered problems and is projecting a September 1, 1973 completion date rather than the planned July 1, 1973. The October 1, 1973 readiness date for MVM 73 appears to be in jeopardy unless system tests are permitted to begin earlier than September 1, 1973. The geodetic survey for DSS 63 is completed and DSS 43 is in work.

IV. Test and Training Activities

The DSN/Spacecraft Compatibility Test Plan (JPL internal document 615-115, Feb. 12, 1973) has been approved and published. During the coordination of this plan, it became clear that spacecraft, DSN, and mission operations tests required during the spacecraft thermal-vacuum period could not be accommodated in a serial manner during the time available. A working group has been established to design a test program that meets requirements through combining compatible test objectives into integrated tests.

Flight spacecraft No. 2 subsystems/DSN compatibility tests were completed in January 1973 as scheduled. All planned tests were completed and no anomalies were observed. All tests passed established acceptance criteria. Included were radio frequency, command, and functional telemetry tests.

Training of the DSN Operations Control Team (OCT) for MVM 73 was initiated during this reporting period. Classroom training, consisting of presentations by mission operations and DSN operations planning people, is about 50% completed. Pertinent lectures have been videotaped. These tapes will be used for continued training of DSN operations people including one-site training at the Deep Space Stations.

Recent reorganizations within the DSN have consolidated planning, engineering, and operations functions. This has resulted in significant changes in the way the DSN accomplishes implementation, testing, and operational readiness. Revised test phases, responsibilities, and milestones are illustrated in Fig. 1. DSN testing for MVM 73 will be conducted in accordance with the provisions set forth in this new plan as illustrated in Fig. 2.

Table 1. DSN reviews for MVM 73

Review	Date
DSN Functional Design	December 1971
Telemetry/Command Data Software Functional Design	June 1972
DSN Detailed Design	July 1972
Telemetry/Command Data Software Detailed Design	October 1972
DSN Progress	February 1973
Telemetry/Command Data Software Verification Test	March 1973
DSN Operational Readiness	August 1973
Project Launch Readiness	October 1973

Table 2. DSN Progress Review for MVM 73–introduction and agenda

Topic	Speaker
Introduction	E. K. Davis
Purpose	
Agenda	
Review committee	
DSN development/implementation status	
GCF status	R. H. Evans
Wideband data line (28.5 KBPS)	
Wideband data line (230 KBPS)	
RIC circuits	
DSS status	
TCD software/hardware	J. H. Wilcher/ R. Mancini
DIS monitor	R. N. Flanders
DIS high-speed tracking	R. N. Flanders/ J. R. Smith
SCA–hardware and software	R. N. Flanders
Planetary ranging	J. R. Smith
S/X-band	R. L. Weber
DSS 43 and 63	R. C. Rydgig
DSN test/training status	
Test sequence	C. W. Harris
Test matrix	
Test definition	
Test plan	C. W. Harris
Schedule overview	
Scoe activities/status	
Detailed test schedule	I. L. Emig
Training activities	T. M. Taylor
Requirements	
Plan	
Schedule	
Problem areas	C. W. Harris
DSN-spacecraft compatibility test status	
Test plan	E. K. Davis
Current status	
Key features	
Open areas	
Quick-look test report summary	W. L. Brown
Flight No. 1 subsystem tests	
Flight No. 2 subsystem tests	
Problem areas	
Committee discussion	
Review comments	
Identify and assign action items	

NEW CAPABILITY TE
(MULTIMISSION TES

TEST → FUNCTION ↓	FIRST MODEL DEMONSTRATION (HW ASSY OR SW MODULES)	FIRST STATION SUBSYSTEM ON-SITE ACCEPTANCE TEST	UNIT BY UNIT ACCEPTANCE TES (HW ONLY)
COORDINATING AUTHORITY	430 SUBSYSTEM ENGINEER	430 SUBSYSTEM ENGINEER 33 PROJECT ENGINEER	430 SUBSYSTEM ENGINEER
TEST REQUIREMENTS/ ACCEPTANCE CRITERIA	430 SUBSYSTEM ENGINEERS	430 SUBSYSTEM ENGINEERS	422 SUBSYSTEM C
PROCEDURES	33 CDE	33 CDE	33 CDE
TEST CONDUCT	33 CDE	33 CDE	33 CDE
TEST REPORT	33 CDE	33 CDE	33 CDE
PERFORMANCE EVALUATION	430 SUBSYSTEM ENGINEERS	430 SUBSYSTEM ENGINEERS 430 SSE 421 SW COE	422 SUBSYSTEM C
SUBSEQUENT EVENT	AGREEMENT BY 430 SSE ON PROCEEDING TO FIRST STATION S/S/ASSY DEMO	AGREEMENT ON PROCEEDING TO NETWORK INSTALLATION	33 CDE TRANSFER FACILITY OPERAT (422) SUBSYSTEM
MILESTONE NAME	SUBSYSTEM/ASSEMBLY FIRST UNIT DEMONSTRATION SW ASSY DIV 33 CDE TO 421 SW COE TRANSFER SUBSYSTEM/HW ASSY DIV 33 CDE TO 422 SUBSYSTEM COE TRAN		
MILESTONE SYMBOL	FIRST UNIT DEMO △ SOFTWARE TRANSFER ○		

LEGEND

XXXX ◸	TEST RESPONSIBILITY FOR HARDWARE
◢ XXXX	TEST RESPONSIBILITY FOR SOFTWARE
XXX	TEST RESPONSIBILITY INDEPENDENT OF HARDWARE VERSUS SOFTWARE

*	OR GCF AND/OR NCS EG
SSE	SUBSYSTEM ENGINEER
CDE	COGNIZANT DESIGN EN
COE	COGNIZANT OPERATION
SCOE	SYSTEM COGNIZANT OP

TING S)			MISSION PREPARATION TESTING (SINGLE MISSION TESTS)			
	SUBSYSTEM ON-SITE ACCEPTANCE TEST	SYSTEM PERFORMANCE DEMONSTRATION	MISSION CONFIGURATION TEST (SYSTEM LEVEL)	OPERATIONAL VERIFICATION TEST	PERFORMANCE DEMONSTRATION TEST	CONFIGURATION VERIFICATION TEST
	430 SUBSYSTEM ENGINEER 33 PROJECT ENGINEER	430 SYSTEM ENGINEER	430 DSN MANAGER FOR PROJECT X	421 NOPE		
E	422 SUBSYSTEM COE 421 SW COE	430 SYSTEM ENGINEERS	430 DSN MANAGER FOR PROJECT X	421 NOPE	421 NOPE	421 NOPE
	422 SUBSYSTEM COE 421 SW COE	421 SCOE	421 NOPE	421 NOPE	421 NOPE	421 NOPE
	422 SUBSYSTEM COE 421 SW COE	421 SCOE	421 NOPE	421 NOPE	421 NOPE	421 NOPE
	422 SUBSYSTEM COE 421 SW COE	421 SCOE	421 NOPE	421 NOPE	421 NOPE	421 NOPE
OE	422 FACILITY OPERATIONS MANAGER	430 SYSTEM ENGINEERS, AND 421 NETWORK OPERATIONS MANAGER	430 DSN MANAGER FOR PROJECT X	421 SUPERVISOR OCT	421 NETWORK OPERATIONS MANAGER, AND 430 DSN MANAGER FOR PROJECT X	420 DSN OPERATIONS MANAGER
TO ONS COE	422 S/S COE TRANSFER TO STATION DIRECTOR * 421 SW COE TRANSFER TO STATION DIRECTOR *	FACILITIES PLACED UNDER CONFIGURATION CONTROL FOR APPROPRIATE MISSIONS AND RETURNED TO OPERATIONAL STATUS	TECHNICAL PERFORMANCE DEMONSTRATION	FACILITY PROFICIENCY DEMONSTRATION	NOPE TRANSFER MD CONFIGURATIONS TO OCT; MOS TESTS	CONFIGURATION FREEZE
	NSFER	SUBSYSTEM IMPLEMENTATION COMPLETE	NETWORK SYSTEM PERFORMANCE DEMONSTRATION	MISSION CONFIGURATION COMPLETE		DSN OPERATIONAL READINESS
	○	◇	□	▽		⌂

UIVALENT

GINEER

IS ENGINEER

ERATIONS ENGINEER

NOPE	NETWORK OPERATIONS PROJECT ENGINEER
OCT	OPERATIONS CONTROL TEAM
MOS	MISSION OPERATIONS SYSTEM
33, 430, 422, ETC =	DIVISION OR SECTION/ORGANIZATION No.

Fig. 1. Relation of tests, responsibilities, and milestones

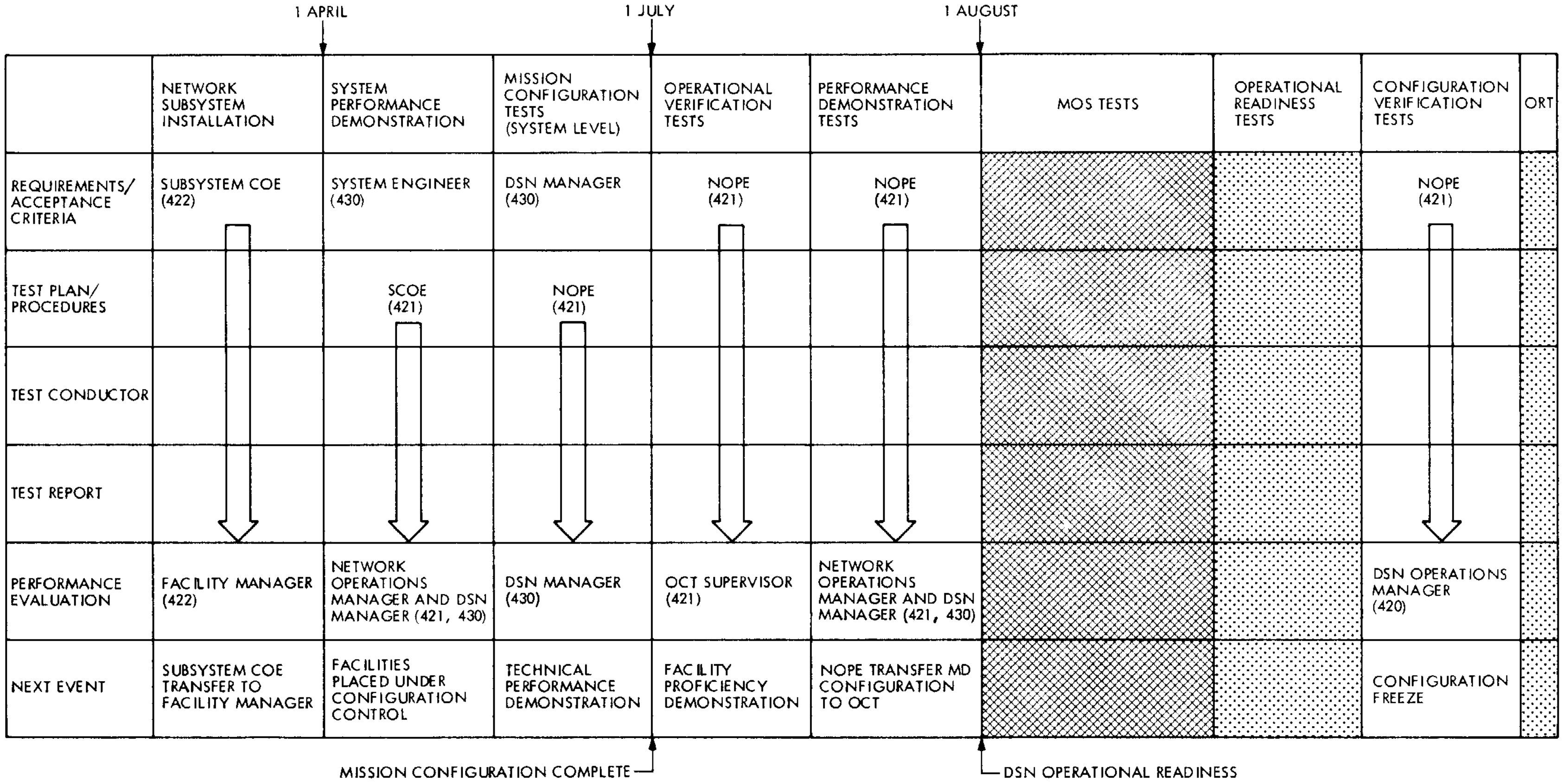

	NETWORK SUBSYSTEM INSTALLATION	SYSTEM PERFORMANCE DEMONSTRATION	MISSION CONFIGURATION TESTS (SYSTEM LEVEL)	OPERATIONAL VERIFICATION TESTS	PERFORMANCE DEMONSTRATION TESTS	MOS TESTS	OPERATIONAL READINESS TESTS	CONFIGURATION VERIFICATION TESTS	ORT
REQUIREMENTS/ ACCEPTANCE CRITERIA	SUBSYSTEM COE (422)	SYSTEM ENGINEER (430)	DSN MANAGER (430)	NOPE (421)	NOPE (421)			NOPE (421)	
TEST PLAN/ PROCEDURES		SCOE (421)	NOPE (421)						
TEST CONDUCTOR									
TEST REPORT									
PERFORMANCE EVALUATION	FACILITY MANAGER (422)	NETWORK OPERATIONS MANAGER AND DSN MANAGER (421, 430)	DSN MANAGER (430)	OCT SUPERVISOR (421)	NETWORK OPERATIONS MANAGER AND DSN MANAGER (421, 430)			DSN OPERATIONS MANAGER (420)	
NEXT EVENT	SUBSYSTEM COE TRANSFER TO FACILITY MANAGER	FACILITIES PLACED UNDER CONFIGURATION CONTROL	TECHNICAL PERFORMANCE DEMONSTRATION	FACILITY PROFICIENCY DEMONSTRATION	NOPE TRANSFER MD CONFIGURATION TO OCT			CONFIGURATION FREEZE	

OCT = OPERATIONS CONTROL TEAM
COE = COGNIZANT OPERATIONS ENGINEER
SCOE = SYSTEM COGNIZANT OPERATIONS ENGINEER
NOPE = NETWORK OPERATIONS PROJECT ENGINEER

Fig. 2. Mission preparation text matrix (420 responsibility)

Viking Mission Support

D. J. Mudgway
DSN Systems Engineering

DSN support for Viking has been reexamined in the light of new budget constraints. Some impact on existing plans and schedules is expected to result. An earlier decision to use the single-station configuration for providing dual-carrier capability was abandoned in favor of the more predictable dual-station approach. The first Viking/DSN Progress Review has been postponed to permit the impact of the changes necessitated by the budget constraints to be evaluated.

I. Introduction

The period covered in this report has been notable mainly because of the impact of unexpected budget cuts on the previous plans and schedules for Viking support. A considerable amount of effort was devoted to renegotiating these changes with the Viking Project and with JPL implementing divisions. The nature and outcome of this work is discussed in succeeding paragraphs.

As a consequence of this activity, it was decided to defer the first Viking/DSN Progress Review, previously scheduled for February 1, 1973, to March 22, 1973 to permit a more realistic presentation of Viking configurations and capabilities to be made.

II. Network Configurations

Immediate previous issues of the DSN Progress Report have covered each of the DSN systems configurations with the exception of the Command System. In November 1972, the Command System was redesigned to improve the operational capability of the System in the Viking Mission Control and Computing Center (VMCCC) to improve the DSS/VMCCC interface and to effectively improve the command storage capability at the DSSs.

The new configuration resulting from the redesign will be presented at the DSN Progress Review on March 22, 1973, and subsequently reported in the DSN Progress Report.

III. Interfaces

The telecommunications interfaces between the DSN and the Orbiter and Lander have now been formally approved by Project Management and are identified in Refs. 1 and 2.

The data interfaces between the DSN and the Viking Mission Control and Computing System have been defined in Ref. 3, which still remains in the final review cycle.

IV. Schedules

The previous issue of the DSN Progress Report presented the final version of a DSN implementation schedule and the agreed upon Viking readiness dates.

The extent to which the January budget revisions have impacted these agreements is not known at this time. However, any changes that result will be consistent with the constraint to have "all Viking hardware and software in place prior to launch." Therefore, with one or two exceptions, it is expected that the impact will be minor.

The revised schedules will be presented at the March Progress Review and reported in the next issue of the DSN Progress Report.

V. Problem Areas

In December, an in depth review of the progress made at DSS 13 in investigating the uplink and downlink interference effects inherent in a high power dual carrier environment was held. It was shown that meticulous attention to waveguide component cleanliness, welding of all joints in the cone, hyperbola, and quadripod, and conductive taping of all antenna panel joints reduced the interference of concern to an insignificant level. On these grounds it was decided to:

(1) Assume the dual-carrier signal antenna configuration for Viking support at all 64-m-diameter antenna DSSs.

(2) Investigate possible ways to reduce the Viking requirement from four carrier frequencies to three.

(3) Immediately apply the above techniques to the DSS 14 antenna.

(4) Review the progress on the DSS 14 64-m-diameter antenna in April 1973.

These recommendations were accepted by the Project and further DSN planning commenced on this basis.

However, during the course of the January budget review, the decision to commit the single-station approach to Viking support was rescinded on the basis that it represented an undemonstrated capability and an indeterminate cost.

The dual-station approach was recommended for formal commitment at this time, while the application of the DSS 13 techniques to the 64-m-diameter antennas was to be continued at a reduced level under the DSN development program with the intent of making this capability available to the Project to enhance the mission, if the development program is successful.

This change in plans will complicate network operations somewhat, since all orbital operations will now require two stations (one 64-m DSS and one 26-m DSS) for each view period. Further evaluation of the operational consequences of this configuration is in progress.

A detailed technical review by D. A. Bathker and D. W. Brown of the dual-carrier investigations at DSS 13 is contained elsewhere in this issue.

References

1. *Viking 75 Project Orbiter System, Lander System, and Viking Mission Control and Computing Center System to TDS Interface Requirements Document, Volume II, Viking Orbiter System to Deep Space Network*, Project Document ID-3703111. NASA Langley Research Center, Hampton, Va., Dec. 19, 1972.

2. *Viking 75 Project Orbiter System, Lander System, and Viking Mission Control and Computing Center System to TDS Interface Requirements Document, Volume III, Viking Lander System to Deep Space Network*, Project Document ID-3703111. NASA Langley Research Center, Hampton, Va., Nov. 29, 1972.

3. *Viking 75 Project Orbiter System, Lander System, and Viking Mission Control and Computing Center System to TDS Interface Requirements Document, Volume IV, Viking Mission Control and Computing Center System to Deep Space Network*, Project Document ID-3703111. NASA Langley Research Center, Hampton, Va., in preparation.

Apollo Mission Support

R. B. Hartley
TDA Planning Office

The support provided by the DSN to the Spaceflight Tracking and Data Network during the Apollo 17 mission is described. Support was provided by three 26-m-diameter antenna deep space stations, the 64-m-diameter antenna Mars Deep Space Station (DSS 14), the Ground Communications Facility, and the Mission Control and Computing Center. Premission and mission activities of the DSN are discussed, and the mission is described.

I. Introduction

The DSN support provided to the Spaceflight Tracking and Data Network (STDN) has been described in Refs. 1 through 4 and earlier issues of the JPL Space Programs Summary, Vol. II series. This article describes the support provided for the Apollo 17 (AS 512) mission, the sixth manned lunar landing and the third of the "J" type missions devoted primarily to scientific objectives.

II. Mission Description

Apollo 17, the tenth manned Apollo spacecraft flown above the three-stage Saturn V launch vehicle carried astronauts Eugene A. Cernan, Commander (CDR), Ronald E. Evans, Command Module Pilot (CMP), and Harrison H. Schmitt, a geologist by profession, Lunar Module Pilot (LMP). The mission goal was exploration of the area around the Taurus Mountains and Littrow Crater with the aim of filling in gaps in current knowledge of the moon and its history.

Launch from Cape Kennedy Pad 39A occurred at 5:33:00.83 GMT on December 7, 1972 at a launch azimuth of 92.0 deg. A countdown hold of 2 h 40 min was required when the launch auto-sequencer failed to pressurize a third stage LOX tank, and then failed to recognize that the launch controllers had manually pressurized the tank after observing the discrepancy. The sequencer was reprogrammed to overlook the one countdown step, and the countdown proceeded normally. This was the first Apollo program launch hold for technical reasons (Apollo 14 was held for weather). The launch was the first Apollo launch to occur at night. The geometry of the Sun and moon constrain a launch to one or two days in any month to allow acceptable Sun lighting angles at the landing site during touchdown. During December, the geometry was such that a daylight launch would have required the spacecraft to spend many hours in the shadow of the Earth, causing an unacceptable amount of spacecraft cooling. The trajectory of the night launch avoided this long duration in the shadow.

Due to the unusual launch time, translunar injection (TLI) occurred over the Atlantic Ocean in the beginning of the third revolution in Earth parking orbit (the customary TLI occurs over the Pacific Ocean in the second orbit). A 5-min 46-s burn of the S-IVB engine placed the spacecraft on a translunar trajectory. Following TLI, the Command Service Module (CSM) separated from the booster and docked with the unattended Lunar Module (LM). During docking, three of the docking latches did not lock. The crew manually recocked and fired two of the problem latches and they seized properly, completing an adequate docking. The CSM extracted the LM from the S-IVB, and the S-IVB was directed by ground command to crash on the moon in a seismic experiment involving the seismometers left there by the Apollo 12, 14, 15, and 16 missions. The S-IVB impacted the moon at 20:32:43 GMT on December 10 at lunar coordinates 4° 12′ S, 12° 18′ W, approximately 160 km northwest of the planned site.

Midcourse correction 1 was deleted due to the accuracy of the TLI maneuvers. Midcourse correction 2 was a short 1.7 s burn of the Service Propulsion System (SPS) for a velocity change of 3.0 m/s (9.9 ft/s) and a trim of 0.2 m/s (0.7 ft/s) with the Reaction Control System (RCS). Midcourse corrections 3 and 4 were not required.

At 22:33 GMT on December 9, the ground elapsed time (GET) clocks were advanced from 65:00 GET to 67:40 GET to compensate for the 2-h 40-min delay in the launch. This time clock change, together with a faster translunar trajectory, timed to speed up moon arrival by 2 h 40 min, put the mission back onto the original GMT/GET schedule. After this change, all mission events occurred within minutes of the premission plan. Table 1 reflects both the GET times and the actual elapsed times (AET) of each event.

Several minor problems occurred during translunar cruise. Several erroneous master alarms were observed in the spacecraft. The master alarm system warns the astronauts when some measurement in the spacecraft is found to be reaching an unusual value, but the master alarm was sounding without reason. The alarm was bypassed during sleep periods to avoid unnecessarily waking the astronauts. On December 9, mission control found it impossible to wake the astronauts, and they overslept more than an hour. As usual, only one astronaut (the CMP) was sleeping with his headset on, and the headset inadvertently fell off, leaving the crew out of contact with mission control. In such a circumstance, Houston normally sends a master alarm command to the spacecraft, setting off the warning signals. Since the master alarm was disabled, the crew could not be reached, causing some concern at mission control; without a master alarm, the crew might have slept through a spacecraft emergency. Other problems included a pressure oscillation in a hydrogen tank and several losses of communication; a 3-min dropout at 60:55 GET caused by a ground problem at the Ascension STDN site; a 9-min dropout at 86:08 GET caused by a maser failure at the Madrid STDN site, and a 4-min delay in acquisition due to an antenna pointing problem at the Goldstone STDN site during the first lunar revolution, resulting in a rapid handover to DSS 11.

Shortly before entering lunar orbit, the astronauts jettisoned a door covering the Scientific Instruments Module (SIM) of the Service Module. The SIM bay carries scientific instruments for observation of the moon from lunar orbit.

A successful lunar orbit insertion (LOI) burn of 6 min 33 s, for a velocity change of 911.32 m/s (2989.9 ft/s), put the spacecraft into a 315.4 × 97.2 km (170.3 × 52.5 nmi) orbit. Two orbits later, a descent orbit insertion (DOI) burn of 22 s for a velocity change of 60.41 m/s (198.2 ft/s) lowered the orbit to 109.5 × 27.6 km (59.1 × 14.9 nmi).

During lunar orbit 12, the CSM and LM separated, with astronauts Cernan and Schmitt in the LM preparing for descent to the lunar surface on orbit 13. A LM-only descent orbit burn (DOI-2) at 18:55:42 on December 11 placed the LM into a 110.4 × 11.5 km (59.6 × 6.2 nmi) orbit. Landing occurred at 19:54:59 GMT on December 11 at lunar coordinates 20° 9′ 50.5″ N and 30° 46′ 19.3″ E, approximately 369 m east of the planned landing site. After a short eating period, the astronauts began extravehicular activity 1 (EVA1), during which they deployed the lunar rover, set up the Apollo Lunar Surface Experiments Package (ALSEP) and activated the ALSEP transmitters. The ALSEP signals were received at Goldstone at 2:53:32 GMT on December 12, at a signal level of −133 dBm on a 26-m-diameter antenna. Several 9-m (30-ft) stations later reported signal fluctuations of ±1 dB with a period of approximately 45 s and an average level of −137 dBm. Shortly after deployment of the rover, the CDR inadvertently knocked the right rear fender extension off. A temporary fix was attempted using tape, but the extension fell off again during the one short traverse of the first extravehicular activity (EVA1), resulting in the astronauts and rover being covered with considerable dust. The EVA ended after 7 h 12 min.

After a sleep period, the crew began the second EVA. Prior to starting the traverse, the crew replaced the rover fender extension with a set of four plastic maps taped together and held in position with a clamp from a portable utility lamp in the LM. The fix worked perfectly and alleviated the dust problem. The crew visited four sites, obtaining photographs and samples and deploying three explosive charges to be detonated by timers after liftoff as part of seismic studies. During this traverse, the LMP noticed an orange-colored material that may provide evidence of recent volcanic activity on the moon and could be the youngest lunar material ever brought back to Earth. EVA2 lasted 7 h 38 min, the longest EVA of the Apollo program.

Following another sleep period, EVA3 was begun. Five sites were visited and one explosive charge was deployed. The LMP attempted unsuccessfully to repair the Lunar Surface Gravimeter (part of ALSEP), which had not been working since deployment. The third EVA was 7 h 16 min long. At the end of this EVA, the crew had explored the surface for a total of 22 h 6 min and had driven the rover 32.0 km (19.9 mi) at speeds up to 17.8 kph (11.1 mph), all three figures setting records for the Apollo program. Other records broken were the amount of rocks and soil collected: 117 kg (258 lb) and the time spent on the moon: 74 h 59 min. Approximately 2120 photographs were taken during the EVAs.

Following EVA 3 and an 8-h sleep period, the LM blasted off the lunar surface to rejoin the orbiting CSM. The liftoff was observed on Earth via the television camera on the rover. This camera continued to provide television views of the moon until its temperature control unit failed at 08:13 GMT on December 16. It had been expected to last until battery depletion on approximately December 25. Rendezvous and docking were also televised, the first use of the CSM television camera on Apollo 17. The crew transferred the samples and exposed film to the CSM, then jettisoned the LM for its deorbit and subsequent crash on the moon. The crash occurred at 6:50:19 on December 15 at 19° 54′ N and 30° 30′ E. The event was observed by the seismometers from Apollos 12, 14, 15 and 16, and by the four geophones of the Apollo 17 ALSEP.

The CSM remained in lunar orbit for another 40 h conducting orbital science. On this flight, however, there was no Particle and Fields Subsatellite, as its space was given over to a lunar sounder experiment. Also there was not enough time in the mission plan for a Bistatic Radar Experiment. Trans-Earth injection (TEI) was initiated at 23:35:09 GMT on December 16 with an SPS burn of 144.9 s for a velocity change of 928.51 m/s (3046.3 ft/s). The TEI maneuver was very accurate, and midcourse corrections 5 and 6 were not needed. The CMP conducted an EVA on December 17 to retrieve exposed film and other scientific materials from the SIM bay. Apollo 17 landed at 19:24:59 GMT December 19 at 17° 52′ S and 166° 8′ W, approximately 630 km (340 nmi) southeast of Pago Pago.

III. Requirements for DSN Support

A. DSN 26-m-Diameter Antenna Stations

As was done with previous Apollo missions, DSSs 11, 42, and 61 were committed to support Apollo 17 under direct STDN/Manned Spacecraft Center (MSC) control. Their responsibilities included two-way tracking of the CSM, LM, S-IVB, and the rover's lunar communications relay unit (LCRU), which transmits on a frequency of 2265.5 MHz and receives on the LM uplink frequency. Scheduling authority for these stations was retained by the DSN for the entire mission, since the DSN has complete maintenance and operations responsibilities.

B. DSN 64-m-Diameter Antenna Stations

The Mars station, DSS 14, was required to receive voice, telemetry, biomedical, and television data and to relay the data to the Goldstone prime STDN station (GDS). No uplink was required. DSS 14 was also required to receive 15-min television transmissions from the LCRU approximately once each day from LM liftoff through December 25. Contrary to previous missions, there were no requirements for Bistatic Radar reception or for precision doppler recording at DSS 14.

Several months before launch, NASA questioned the DSN as to whether DSS 43, the 64-m-diameter antenna station under construction in Australia, could be committed for Apollo use to avoid the need for the Parkes, Australia, 64-m-diameter radio-astronomy antenna. Since the operational date of DSS 43 was not until mid-1973, committed support was impossible. Nevertheless, the station did track on an uncommitted basis as backup to Parkes, and the acquired data were used.

IV. DSN Premission Preparations and Testing

A. DSN 26-m-Diameter Antenna Stations

A light level of testing was conducted continuously from Apollo 16 to Apollo 17. As the testing pace increased in late November 1972, a few problems surfaced. DSS 11 experienced a transmitter tripoff due to a primary ac overcurrent sensing. Because of several similar problems in the past at DSS 11, considerable attention was focused upon the problem, which turned out to be nothing more than a chafed high-voltage cable. DSS 11 was found to have a doppler problem on December 6 during an STDN test. The problem was traced to a modified doppler detector that had been installed at STDN request. With the original detector returned to service, the problem disappeared. DSS 11 also experienced a pump failure on heat exchanger No. 2, and the pump was replaced. DSSs 11, 42, and 61 were placed on mission status by the STDN on December 1.

B. DSS 14

DSS 14 conducted the normal premission tests as shown in Table 2. In addition, since DSS 14 experienced overloading during Apollo 16 when trying to receive a weak LM signal in the presence of a strong CSM television signal, a 20-dB attenuator was added after the Mod III maser. This configuration was then tested, even though the Mod III maser was only to be used as backup to the (polarization diversity S-band) (PDS) maser.

V. DSN Operations During Mission

A. 26-m-Diameter Antenna Stations

DSSs 11, 42, and 61 successfully supported all phases of the Apollo 17 mission. The problems experienced are noted in Table 3.

B. DSS 14

Nine Apollo passes were tracked, as shown in Table 3. The station had originally been scheduled for short LCRU tracks through December 25, but, as mentioned earlier, the LCRU ceased to operate on December 16.

DSS 14 experienced a pointing problem on the first pass. The antenna was pointed manually from 18:40 to 19:09 GMT because the station was unable to process the 29-point acquisition message. The problem was apparently caused by a bad punch point at the start of the acquisition message tape. Normal tracking was again interrupted at 20:57 due to a bad sample on the drive tape. A new drive tape was prepared from the same acquisition message, and normal tracking operations resumed at 21:26 GMT.

Beginning at 17:00 on December 8, problems were experienced with the Mod III maser. The maser was out of service three times until it was reliably back in service at 16:30 on December 10. Since the Mod III maser is only used for backup on Apollo, its problems did not affect Apollo support.

C. Ground Communications Facility Participation

The Ground Communications Facility (GCF) provided voice, teletype, and high-speed data circuits to support the DSN Apollo operations. In addition, JPL acts as the West Coast switching center for the NASA Communications Network and handles many non-DSN circuits, including video channels, in support of Apollo. There were no known GCF anomalies.

D. Mission Control and Computing Center Participation

The Mission Control and Computing Center (MCCC) areas and equipment used for the Apollo 17 mission included the Operations Area, the Network Analysis Area, the Mariner computer terminal area, and the Univac 1108 and 360/75 computers. The MCCC support was limited to backup predict generation for DSS 14 (and DSS 43), and some off-line monitoring in the operations areas.

References

1. Hartley, R. B., "Apollo Mission Support," in *The Deep Space Network*, Space Programs Summary 37-64, Vol. II, pp. 7–11. Jet Propulsion Laboratory, Pasadena, Calif., Aug. 31, 1970.
2. Hartley, R. B., "Apollo Mission Support," in *The Deep Space Network Progress Report*, Technical Report 32-1526, Vol. II, pp. 33–41. Jet Propulsion Laboratory, Pasadena, Calif., Apr. 15, 1971.
3. Hartley, R. B., "Apollo Mission Support," in *The Deep Space Network Progress Report*, Technical Report 32-1526, Vol. V, pp. 29–38. Jet Propulsion Laboratory, Pasadena, Calif., Oct. 15, 1971.
4. Hartley, R. B., "Apollo Mission Support," in *The Deep Space Network Progress Report*, Technical Report 32-1526, Vol. X, pp. 41–48. Jet Propulsion Laboratory, Pasadena, Calif., Aug. 15, 1972.

Table 1. Apollo 17 sequence of major events

Event	GET, h:min:s	AET, h:min:s	Date/GMT, h:min:s
Launch	0:00:00	0:00:00	12– 7/05:33:01
Insertion	0:11:47	0:11:47	12– 7/05:44:48
TLI ignition	3:12:35	3:12:35	12– 7/08:45:36
TLI cutoff	3:18:21	3:18:21	12– 7/08:51:22
Transposition/ docking	3:43:00	3:43:00	12– 7/09:16:01
CSM/LM eject	4:45:00	4:45:00	12– 7/10:18:01
S4B evasive maneuver[a]	5:30:00	5:30:00	12– 7/11:03:01
S4B first midcourse[a]	6:36:00	6:36:00	12– 7/12:09:01
First midcourse (deleted)			
Second midcourse	35:29:59	35:29:59	12– 8/17:03:00
LM communication test begin	41:16:00	41:16:00	12– 8/22:49:01
LM communication test end	41:59:00	41:59:00	12– 8/23:32:01
LM communication test begin	60:12:00	60:12:00	12– 9/17:45:01
LM communication test end	60:26:00	60:26:00	12– 9/17:59:01
Third midcourse (deleted)			
Fourth midcourse (deleted)			
SIM door jettison	84:12:00	81:32:00	12–10/15:05:01
CSM first occultation	88:43:22	86:03:22	12–10/19:36:23
LOI	88:54:21	86:14:21	12–10/19:47:22
S4B impact	89:39:42	86:59:42	12–10/20:32:43
DOI	93:11:00	90:31:00	12–11/00:04:01
Separation	110:27:55	107:47:55	12–11/17:20:56
CSM circularization	111:57:28	109:17:28	12–11/18:50:29
DOI-2	112:02:41	109:22:41	12–11/18:55:42
PDI	112:49:53	110:09:53	12–11/19:42:54
Touchdown	113:01:58	110:21:58	12–11/19:54:59
EVA 1 begin	117:01:36	114:21:36	12–11/23:54:37
ALSEP activated	120:00:31	117:20:31	12–12/02:53:32
EVA 1 end	124:13:47	121:33:47	12–12/07:06:48
EVA 2 begin	140:34:49	137:54:49	12–12/23:27:50
EVA 2 end	148:12:10	145:32:10	12–13/07:05:11
EVA 3 begin	163:32:35	160:52:35	12–13/22:25:36
EVA 3 end	170:48:06	168:08:06	12–14/05:41:07
Lunar orbit plane change	182:33:53	179:53:53	12–14/17:26:54
LM ascent	188:01:36	185:21:36	12–14/22:54:37
CSM/LM docking	190:17:03	187:37:03	12–15/01:10:04
LM jettison	193:58:35	191:18:35	12–15/04:51:36
LM deorbit	195:38:13	192:58:13	12–15/06:31:14
LM crash	195:57:18	193:17:18	12–15/06:50:19
TEI	236:42:08	234:02:08	12–16/23:35:09
Fifth midcourse (deleted)			
CSM EVA begin	257:34:24	254:54:24	12–17/20:27:25
CSM EVA end	258:41:42	256:01:42	12–17/21:34:43
Sixth midcourse (deleted)			
Seventh midcourse[a]	301:18:00	298:38:00	12–19/16:11:01
CM/SM separation	304:03:48	301:23:48	12–19/18:56:49
Entry interface	304:18:41	301:38:41	12–19/19:11:42
Splashdown	304:31:58	301:51:58	12–19/19:24:59

[a] Time approximate.

Table 2. DSS 14 tests

Date	Test
Nov. 8, 1972	Support constraint testing
Nov. 15, 1972	Configuration verification test
Dec. 1, 1972	Apollo 17 OVT
Dec. 2, 1972	24-h interface test with GDS

Table 3. Apollo 16 tracking

Date/GMT, h:min	Problems
DSS 11	
Dec 7/18:31 – 03:47	100-channel event recorder inoperative 23:52 – 01:57
Dec 8/18:40 – 04:20	None
Dec 9/18:45 – 04:42	None
Dec 10/18:42 – 05:11	Declination angle DATEX jumping intermittently 00:42 – 01:20. No data loss
Dec 11/19:26 – 06:12	None
Dec 12/19:43 – 06:10	None
Dec 13/20:33 – 07:52	None
Dec 14/20:49 – 08:48	None
Dec 15/21:15 – 09:19	None
Dec 16/22:04 – 10:03	None
Dec 17/22:26 – 10:13	None
Dec 18/22:36 – 10:23	Antenna drives off in both axes (06:31 – 06:40) due to bad interpolation on predict
DSS 14	
Dec 7/19:04 – 03:25	Problem with 29-point acquisition message 18:40 – 19:09 and 20:57 – 21:26. Cut new tape from same message. Antenna stowed 22:35 – 23:35 due to high winds
Dec 9/18:53 – 03:00	Backup Mod III maser red 9/1500 – 10/0200
Dec 10/18:52 – 03:27	Lost 20 min of 1-s doppler data due to punch being on 60-s rate
Dec 11/19:29 – 05:37	None
Dec 12/19:43 – 06:36	None
Dec 13/20:11 – 07:43	None
Dec 14/20:41 – 08:49	None
Dec 15/21:17 – 03:28	None
Dec 16/22:39 – 04:30	None
DSS 42	
Dec 7/23:09 – 11:53	None
Dec 8/23:39 – 12:03	None
Dec 9/23:53 – 12:05	None
Dec 11/00:27 – 12:21	None
Dec 12/01:22 – 12:50	None
Dec 13/01:57 – 13:22	None
Dec 14/03:05 – 13:56	None
Dec 15/04:26 – 14:26	None
Dec 16/06:10 – 15:09	None
Dec 17/06:18 – 15:17	None
Dec 18/06:34 – 15:02	None
Dec 19/07:22 – 13:54	None
DSS 61	
Dec 7/10:43 – 19:06	None
Dec 8/11:24 – 20:18	None
Dec 9/11:28 – 20:35	None
Dec 10/11:26 – 20:33	None
Dec 11/11:52 – 21:37	None
Dec 12/11:54 – 22:22	None
Dec 13/12:56 – 23:52	None
Dec 14/12:48 – 00:59	None
Dec 15/13:22 – 01:30	None
Dec 16/14:06 – 03:09	None
Dec 17/14:13 – 03:16	None
Dec 18/13:59 – 03:31	None
Dec 19/16:38 – 19:23	None

S-Band Planetary Radar Receiver Development

C. F. Foster
R.F. Systems Development Section

G. F. Lutes
Communications Systems Research Section

This article describes the design of a wideband 2295/2388-MHz converter, which is a part of the DSS 14 bistatic radar receiver. This receiver is an open-loop superhetrodyne receiver used for development of communication techniques. This converter design eliminates the need for separate converters at each frequency. The 2295/2388-MHz converter has been installed at DSS 14 and is now being used in the Venus radar mapping experiments.

I. Introduction

During this period the design and installation of a 2295/2388-MHz converter has been completed. This converter is a major subsystem of the S-Band Planetary Radar Receiver (Ref. 1), used to support wideband, high-resolution radar experiments. The design was initiated because of the need for a greater dynamic RF input range, and to reduce changeover time required when a new operating frequency was desired.

II. Implementation

The 2295/2388-MHz converter is contained in an aluminum box mounted in the DSS 14 antenna (Fig. 1). It consists of a local oscillator (LO) chain with drive level monitor, a balanced mixer, and an IF amplifier (Fig. 2). Because of design requirements, all components are wideband. The first multiplier in the LO chain is ×2 (Fig. 3) and has been designed around commercial wideband hybrid amplifiers and a wideband doubler module with the following specifications: bandwidth is greater than 10 MHz, distortion is less than 5%, and input and output impedance is 50 ohms. The ×32 multiplier is a commercial unit with a typical bandwidth as shown in Fig. 4. Its harmonics and spurious response are 60 dB down, and phase noise is equal to -92 dB rad^2/Hz at 10 Hz.

The balanced mixer is also a commercial module, and has a bandwidth of dc to 4 GHz.

The IF amplifier has a maximum noise figure of 1.5 dB, a bandwidth of 5 to 60 MHz, an input/output voltage standing wave ratio (VSWR) of 1.3 to 1 over the rated bandwidth, and a 1-dB output power compression point of +31 dBm. The overall tuning range of the converter is limited by the bandwidth of the ×32 frequency multiplier which allows tuning from 2202 to 2414 MHz.

The noise figure of this converter over the design operating range is plotted (Fig. 5) and the converter limiting curve is shown in Fig. 6. The total harmonic distortion is 5%.

III. Conclusion

The 2295/2388-MHz converter has been installed at DSS 14 and is being used to support the Venus radar mapping experiments. Its improved performance has been demonstrated not only in improved technical parameters but also it has eliminated down time due to operator confusion associated with the past system of switches and cable changes when changing operating frequencies.

Reference

1. Foster, C. F., "S-Band Planetary Radar Receiver Development," in *The Deep Space Network*, Space Programs Summary 37-41, Vol. III, pp. 107–110. Jet Propulsion Laboratory, Pasadena, Calif., Sept. 30, 1966.

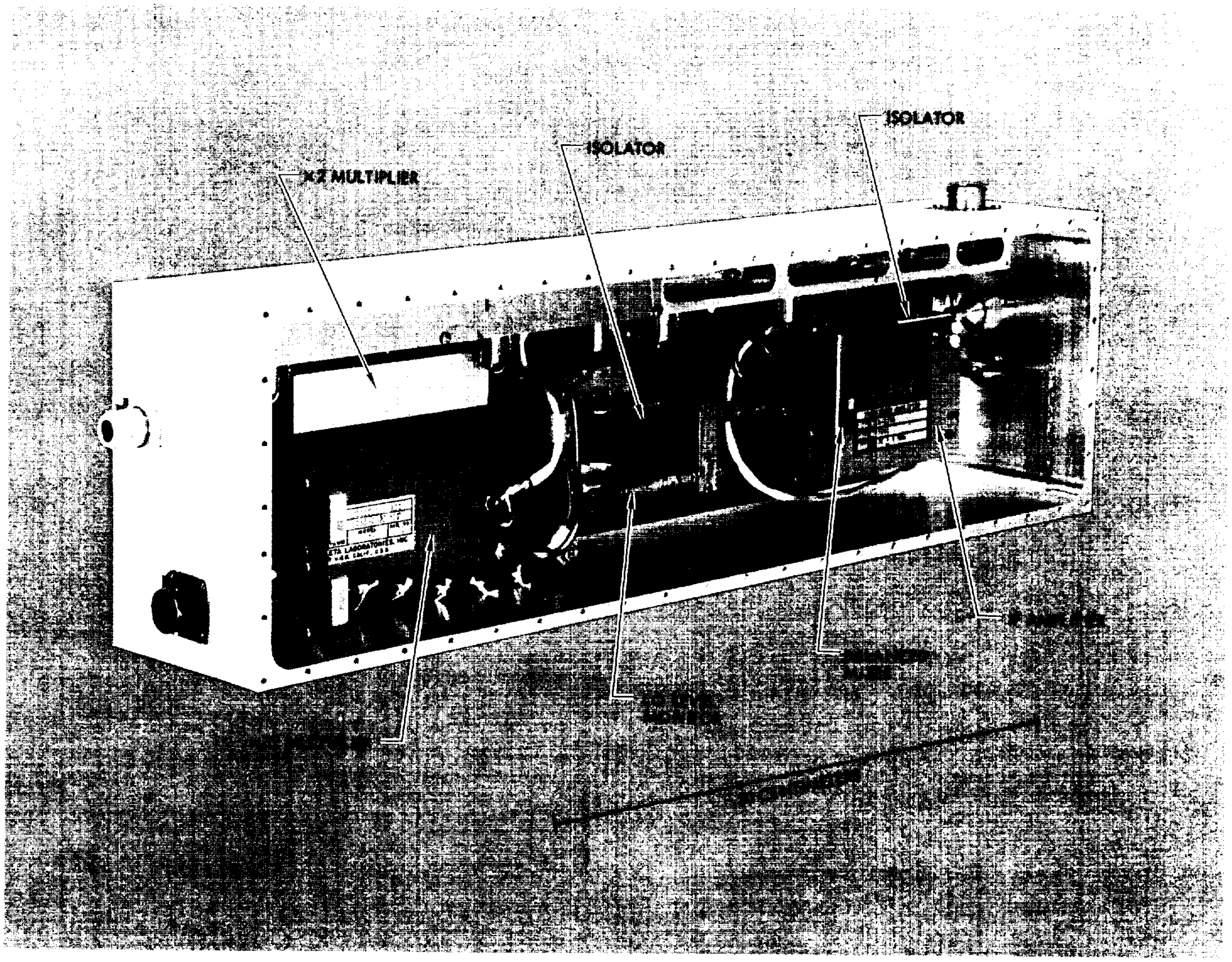

Fig. 1. 2295/2388-MHz converter

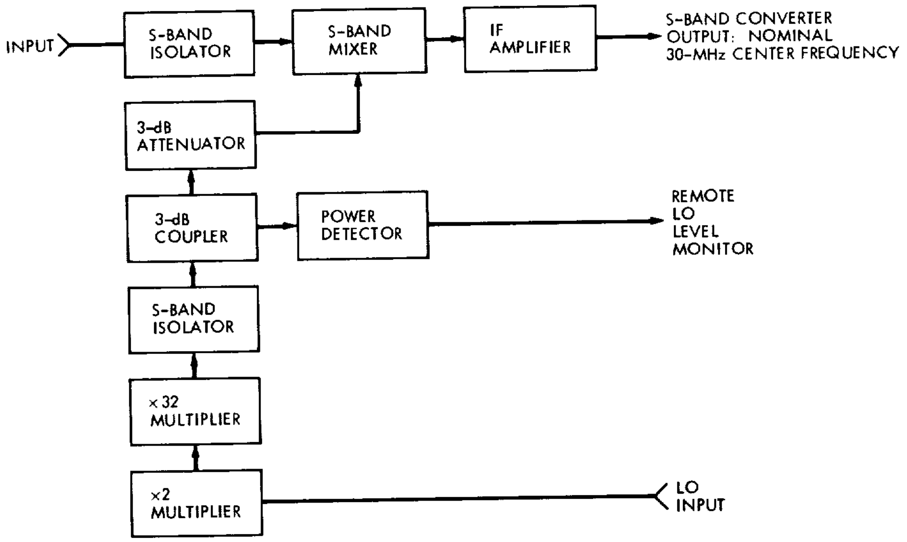

Fig. 2. Block diagram of 2295/2388-MHz converter

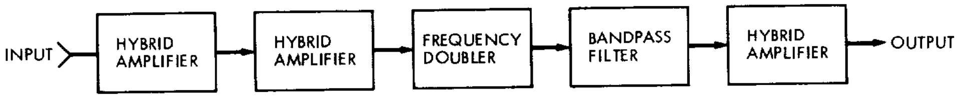

Fig. 3. Block diagram of ×2 frequency multiplier

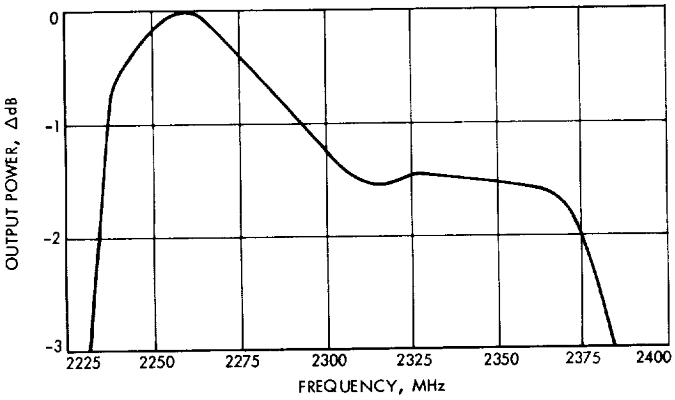

Fig. 4. ×32 multiplier bandpass

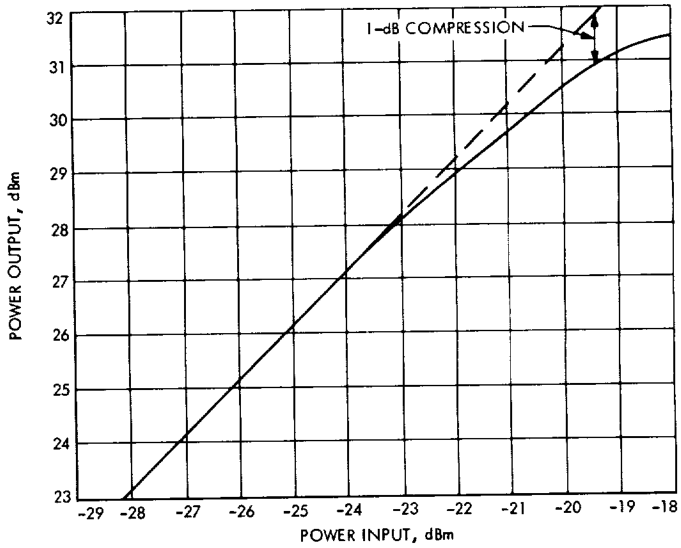

Fig. 6. 2295/2388-MHz converter limiting curve

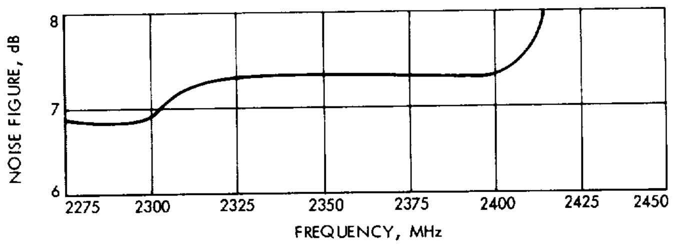

Fig. 5. 2295/2388-MHz converter noise figure vs received frequency

Computer Control of High-Power Transmitters

R. L. Leu
R. F. Systems Development Section

The objectives of this task are to develop techniques and equipment for complete control, monitor, and fault isolation for minimum recovery time from a fault and to reduce the skill level required for operation and maintenance. This report covers the computer program for control, monitor, and major fault isolation of the Venus Deep Space Station high-power transmitters.

I. Introduction

The objective of this task is to develop techniques and equipment for complete control, monitoring, and fault isolation for minimum recovery time from a failure. Initially a very simple control program and the associated interface hardware were developed to gain experience in computer control of high-power transmitters. From this experience a new control, monitor, and major fault isolation program was written. A computer-transmitter interface was designed and built to utilize full capability of the software program.

A PDP-11/20 computer with peripherals is the principal device used for controlling the high-power transmitters. Since the transmitters have been built for several years, no attempt was made to modify existing equipment to provide a more desirable interface. All new equipment shall be designed for direct access to the computer.

II. Program

The software was written to control, monitor, and isolate major faults of the R&D 450 kW transmitter at DSS 13. The main program (Fig. 1) is broken into three major groups: mission parameters, system turn-on, and mission monitor. During the last two parts of the main program, several subroutines are used or are available if required. These are too numerous to list and some will be referred to later. However, a very important subroutine is called "TTYCON" which means teletype control of the program. A simplified flow diagram of the main program is shown in Fig. 2 and the TTYCON subroutine in Fig. 3. All data input from the teletype (TTY) could easily be input from a master computer; therefore the TTY simulates a master computer.

III. Description

To provide the operator of the TTY with all the input and output options, a brief instruction procedure can be printed out at the start of the program.

The mission parameters must be input by the operator. These parameters are klystron serial number, power level, and frequency. The program is written to store data from only one klystron. If a different klystron is used, its parameters must be loaded into memory. If the input serial number from the TTY does not match the number in storage, the operator is told to load the data. The klystron data includes maximum or minimum parameters, power out versus beam voltage at several frequencies, and initial klystron perveance data.

The serial number, the required RF power, and operating frequency are input at the TTY. The computer then extracts from the stored klystron data a nominal beam voltage level and the program is ready for part two: transmitter turn-on.

During the initial phase of the turn-on, the computer activates the control power and coolant assembly and verifies the appropriate responses. Then the computer draws on an X-Y plotter, a representative of the initial perveance of the klystron.

Next the arc detector is tested for interlock (I/L) faults. If there are interlocks, one reset cycle is tried; if not successful, the computer goes to TTYCON mode. If arc detector faults are clear or cleared, the drive is raised to the maximum limit. The drive power level is then compared to the minimum limit required to operate the klystron. Insufficient drive causes an error message to be printed and the program goes to TTYCON mode. Otherwise the drive is lowered, and the filament voltage and current and the magnet current are tested. If not at the correct level, the necessary adjustments are made. Next the filament time delay (TD) is tested for completion, and when the TD has cleared, the "beam ready" indication is verified. If beam ready, the program goes to TTYCON mode. Otherwise it tests for I/L open indication. If I/L is open, one reset cycle is attempted and error messages are printed if they still are present after the reset. When the beam ready and I/L open indications are not present, the program prints "safe-run key off."

With the beam ready and the program in the TTYCON mode, the program is continued by striking the CR key on the TTY. On the initial turn-on, the beam voltage is set to 20 kV dc. At this point the crowbar (CB) test circuit is activated. If the CB fired, the I/Ls are reset and the beam voltage is turned on again. Should the CB not fire, the CB logic indicator is tested to determine if it activated and the appropriate messages are printed. The program goes to TTYCON mode to await further commands.

After the CB has test fired and the beam voltage is on, the voltage is run up to maximum, and a continuous plot of beam voltage versus beam current is recorded (the drive is tested to verify it is at its lower limit). The beam voltage is then set to the value for the required mission, and the drive is raised until the klystron is saturated.

At this point all analog voltages and currents are printed for reference. The program now goes into its monitor routine and should a fault occur or an adjustment be required, an appropriate message is printed. Should the mission requirements need changing or the system shut off, pushing any key on the TTY interrupts the program. At this interrupt the program jumps to the TTYCON mode to allow changes or commands.

IV. Computer-Transmitter Interface

The computer/transmitter interface at present consists of 216 discrete command circuits, 216 discrete monitor circuits, and 16 analog monitor circuits. The PDP 11/20 has an interface card (DR 11) that has 16 bits of output and 16 bits of input each on a separate connector. These inputs and outputs are transistor-transistor logic (TTL) compatible. However, the transmitter, due to its high noise environment, has a digital control and monitor system that operates on +28 Vdc.

The transmitter/computer interface was designed to take the TTL logic level commands from the computer and convert them to +28 Vdc. The TTL inputs to the computer are obtained in the interface by shifting the +28 Vdc indication to TTL logic level.

The analog voltages used in the transmitter have previously been conditioned to ±5 Vdc full scale, directly compatible with the PDP 11/20 analog-to-digital converter (AD01).

V. Preliminary Testing

The program was initially tested using a simulator for the transmitter digital controls and monitors and dc power supplies to simulate the analogs. At this time the computer and interface are being integrated into the transmitter at DSS 13. Due to the high noise environment of the transmitter, considerable care is being taken to isolate the computer from this noise environment.

The present plans are to complete the initial phase of computer operation; that is, the control, monitoring, and major fault isolation. The transmitter will then be operated for several weeks to establish a high confidence in this type operation. The computer is only an automatic operator; at any time the system can be run manually. The next step will be to start software development of detailed fault isolation of the various major assemblies in the transmitter.

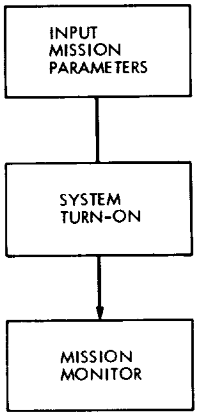

Fig. 1. Transmitter control block diagram

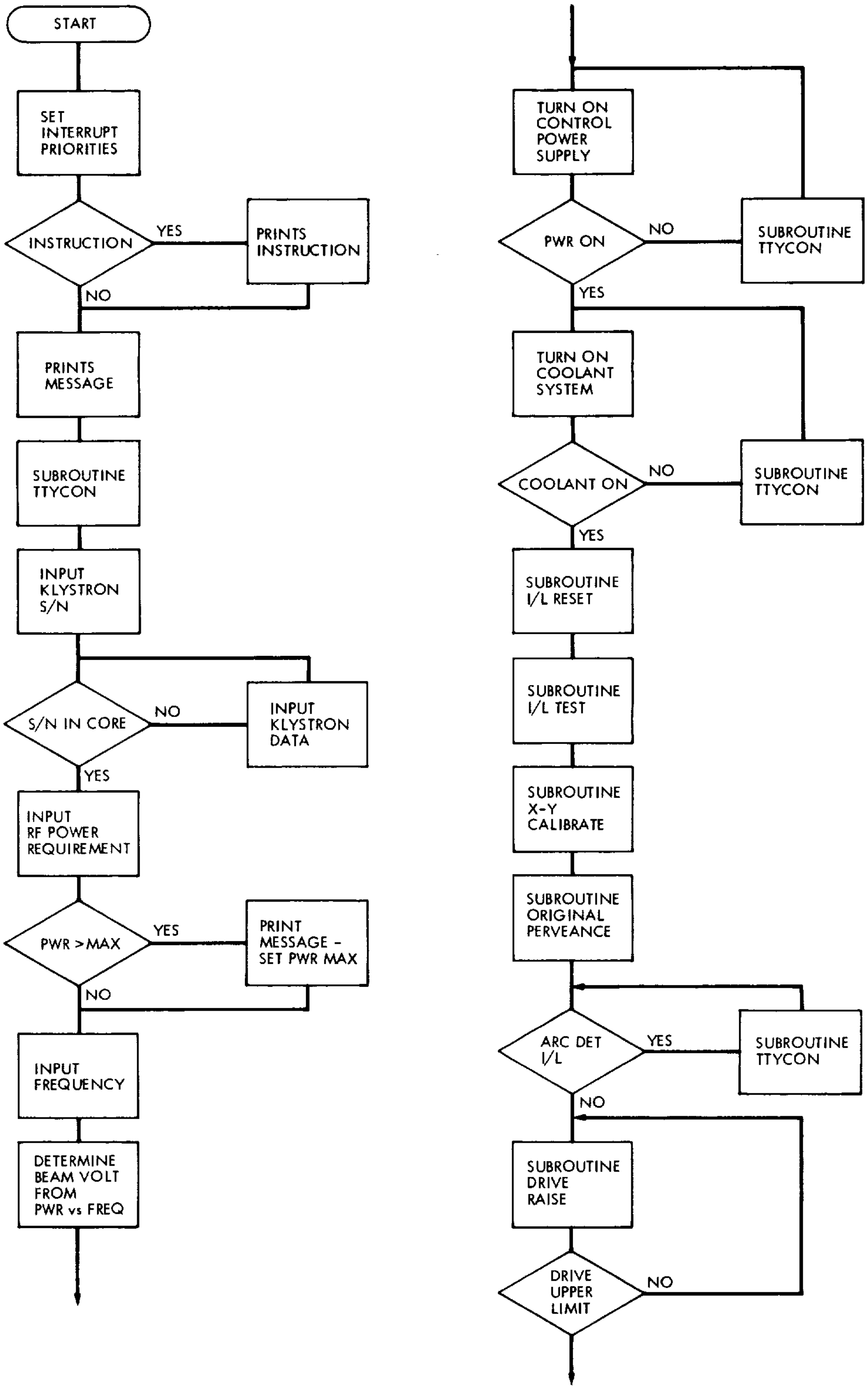

Fig. 2. Transmitter control flow diagram

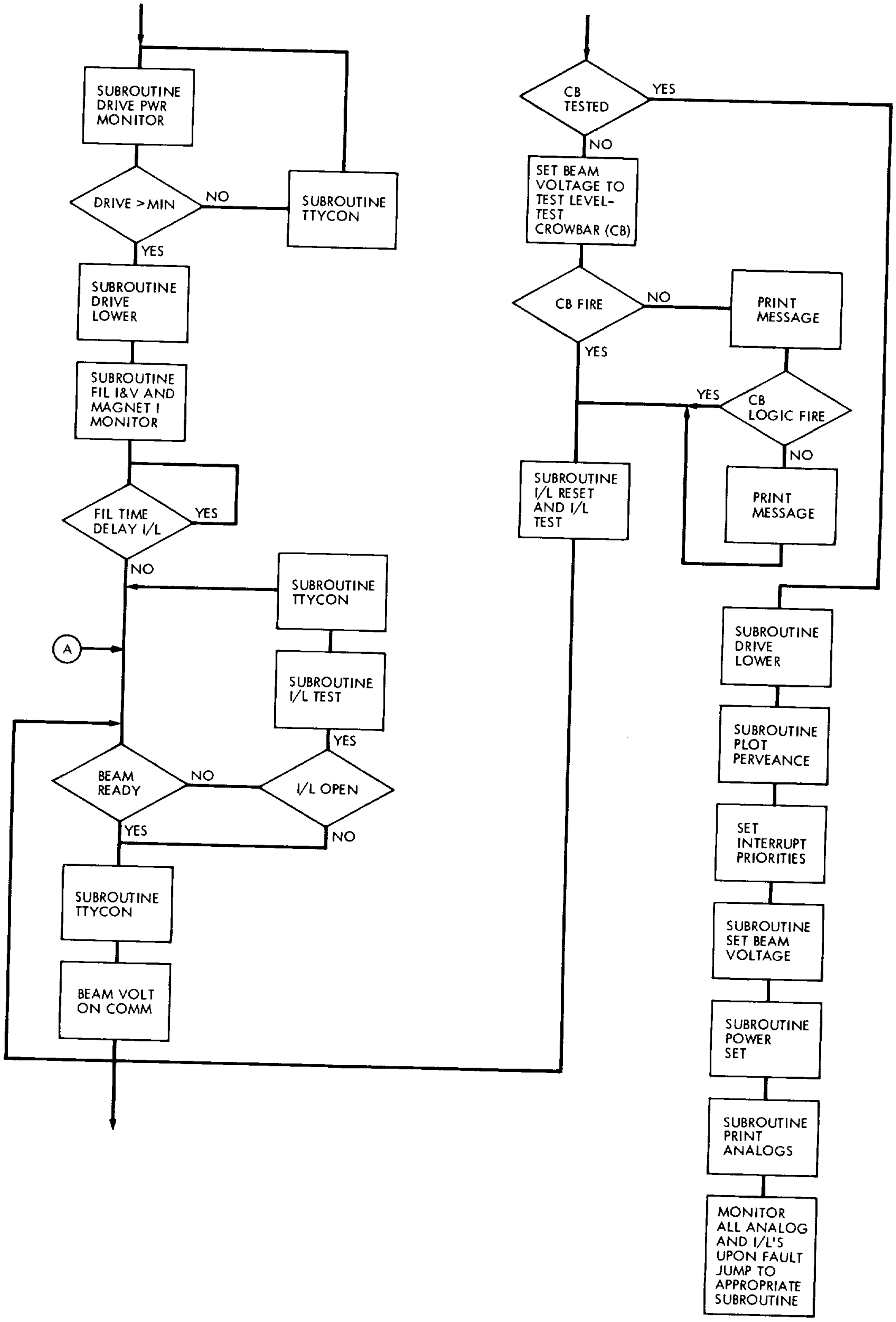
SUBROUTINE DRIVE PWR MONITOR
DRIVE >MIN
NO
SUBROUTINE TTYCON
YES
SUBROUTINE DRIVE LOWER
SUBROUTINE FIL I&V AND MAGNET I MONITOR
FIL TIME DELAY I/L
YES
NO
SUBROUTINE TTYCON
A
SUBROUTINE I/L TEST
YES
BEAM READY
NO
I/L OPEN
YES
NO
SUBROUTINE TTYCON
BEAM VOLT ON COMM
CB TESTED
YES
NO
SET BEAM VOLTAGE TO TEST LEVEL-TEST CROWBAR (CB)
CB FIRE
NO
PRINT MESSAGE
YES
YES
CB LOGIC FIRE
NO
SUBROUTINE I/L RESET AND I/L TEST
PRINT MESSAGE
SUBROUTINE DRIVE LOWER
SUBROUTINE PLOT PERVEANCE
SET INTERRUPT PRIORITIES
SUBROUTINE SET BEAM VOLTAGE
SUBROUTINE POWER SET
SUBROUTINE PRINT ANALOGS
MONITOR ALL ANALOG AND I/L'S UPON FAULT JUMP TO APPROPRIATE SUBROUTINE

Fig. 2. (contd)

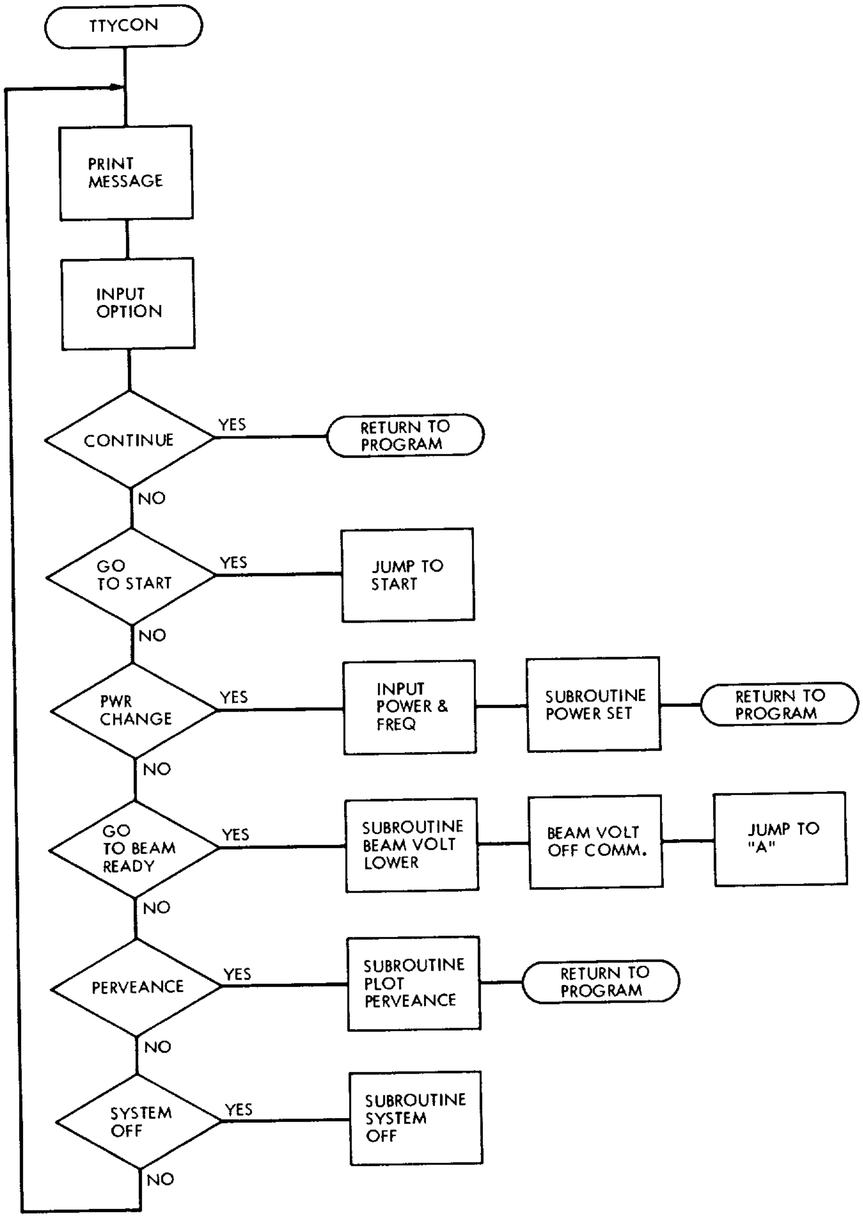

Fig. 3. TTYCON subroutine flow diagram

A New Method to Predict Wet Zenith Range Correction From Surface Measurements

C. C. Chao
Tracking and Orbit Determination Section

A study of the radiosonde balloon data measured in 1967 through 1968 indicates that during local noon the wet zenith range correction of the troposphere refraction is strongly correlated with surface vapor pressure. A simple analytical expression connecting the wet zenith range correction with surface temperature and vapor pressure was found based on an adiabatic atmosphere model:

$$\Delta\rho_{\text{wet}}\,(\text{in cm}) = 1.63 \times 10^{2}\,\frac{e_0^{1.23}}{T_0^{2}} + 2.05 \times 10^{2}\,\alpha\,\frac{e_0^{1.46}}{T_0^{3}}$$

where e_0 *is surface vapor pressure in* N/m^2, T_0 *is surface temperature in K and* α *is the temperature lapse rate with respect to altitude in K/km. The (1*σ*) agreement between the surface prediction and balloon data is good to 2 cm.*

I. Introduction

The search for a simple method to estimate the total water content of the atmosphere has been made by many researchers since the turn of this century. However, conclusions about the correlation between total water content and surface measurements vary from excellent to poor depending on the place and the time of day (or year) the observations were made (Ref. 1).

In Ref. 2 it was shown that the wet zenith range correction of the troposphere can be predicted from the surface extrapolated temperature, surface relative humidity and the linear temperature lapse rate from radiosonde balloon measurement. The prediction was based on the assumption of constant relative humidity in the troposphere which was found, from balloon measurement, generally not to be true. Thus an error of 5 cm in zenith range prediction from balloon data usually occurs. A more accurate model to predict the wet zenith range correction from surface measurements alone is needed for the calibration of more accurate radio tracking techniques. It not only can avoid the cost of data processing of daily radiosonde balloon measurements but also provides real time calibration since surface measurements and spacecraft radio metric data can easily be recorded simultaneously at each tracking station.

The purpose of this study can be summarized as follows:

(1) To find a better method to predict the wet zenith range correction from surface measurements similar to the surface prediction for the dry part.

(2) To compare the new method with the method by Berman (Ref. 2).

(3) To find the explanation for the wide-range variation of correlation between surface measurement and total water content made by earlier researchers (Ref. 1).

II. Analysis

The refractivity due to water vapor is computed by the following equation (Ref. 3):

$$N_w = 3.73 \times 10^3 \frac{e}{T^2} \tag{1}$$

Here e is the partial water vapor pressure in N/m^2 and T is the absolute temperature in K. The zenith range correction due to water vapor is the integration of Eq. (1) as expressed below.

$$\Delta R_{wz} = 10^{-6} \int_0^\infty N_w dz \tag{2}$$

or

$$\Delta R_{wz} = 0.373 \times 10^{-2} \int_0^\infty \frac{e}{T^2}\, dz \tag{3}$$

To integrate the above equation analytically, we have to find the functions $e(z)$ and $T(z)$. In Ref. 4, the temperature measurements indicate that the temperature linearly decreases with altitude in the first 12 km where most of the water vapor is contained. In the first attempt, the relations between vapor pressure and altitude were derived from the following equations, similarly as for the dry atmosphere [Ref. 4]:

$$\frac{de}{dz} = -\rho_w g \quad \text{hydrostatic equation} \tag{4}$$

$$e = \rho_w R_w T \quad \text{perfect gas law} \tag{5}$$

$$T = T_0 - \alpha(z - z_0) \text{ linear lapse function} \tag{6}$$

with

ρ_w = density of water vapor

R_w = gas constant for water vapor

α = temperature lapse rate, K/km

T_0 = surface temperature, K

A simple relation between ΔR_{wz} and e_0, T_0 was derived from Eqs. (3), (4), (5), (6). Unfortunately, the value of ΔR_{wz} obtained with this first model was an order of magnitude larger than the radiosonde balloon data. In support of the result, an adiabatic approximation is probably more adequate than the ideal gas model [Ref. 5].

To test this possibility, Eq. (5) should be replaced by the adiabatic law given by:

$$e = k^\gamma \rho_w^\gamma \tag{7}$$

From Eq. (4) and Eq. (7) we can obtain the following relation:

$$e = \left[e_0^{(\gamma-1)/\gamma} - \frac{\gamma - 1}{\gamma}\left(\frac{g}{k}\right) z \right]^{\gamma/(\gamma-1)} \tag{8}$$

With $\gamma = 1.3$ for water vapor (Ref. 5), we found the above relation agrees quite well with balloon measurement (see Fig. 1). Thus by substituting Eq. (8) and Eq. (6) into Eq. (3), we obtain the integral for the zenith range correction.

$$\Delta R_{wz} = 0.373 \times 10^{-2} \int_0^{h_w} \frac{\left[e_0^{(\gamma-1)/\gamma} - \frac{\gamma-1}{\gamma}(g/k)\, z \right]^{\gamma/(\gamma-1)}}{(T_0 - \alpha z)^2} dz \tag{9}$$

The upper limit of the above integral should be the altitude h_w, at which water vapor vanishes. According to the balloon measurements, h_w is around 12 km and α is about 7 K/km, thus the denominator $(T_0 - \alpha z)^2$ will not vanish during integration. Since the above integral cannot be integrated directly, we first expand the integrand as follows:

$$\frac{\left[e_0^{(\gamma-1)/\gamma} - \frac{\gamma-1}{\gamma}(g/k)\, z \right]^{\gamma/(\gamma-1)}}{[T_0 - \alpha z]^2} = \frac{\left[e_0^{(\gamma-1)/\gamma} - \frac{\gamma-1}{\gamma}(g/k)\, z \right]^{\gamma/(\gamma-1)}}{T_0^2} \times \left[1 + \frac{2\alpha z}{T_0} + \frac{6}{2!}\left(\frac{\alpha z}{T_0}\right)^2 + \cdots \right] \tag{10}$$

Because

$$\frac{\alpha z}{T_0} \approx 0.1$$

it is therefore adequate to keep the first order term and carry out the integration.

$$\Delta R_{wz} = \frac{0.373 \times 10^{-2}}{T_0^2 (g/k)} \times \left\{ \frac{\gamma}{2\gamma - 1} e_0^{(2\gamma-1)/\gamma} + \frac{2\alpha\gamma^2}{(2\gamma - 1)(3\gamma - 2)(g/k)} \frac{e_0^{(3\gamma-2)/\gamma}}{T_0} \right\} \tag{11}$$

After we substitute the value of the constants for water vapor a simplified relation is reached.

$$\Delta R_{wz} = 1.63 \times 10^2 \frac{e_0^{1.23}}{T_0^2} + 2.05 \times 10^2 \alpha \frac{e_0^{1.46}}{T_0^3} \tag{12}$$

The unit of ΔR_{wz} from the above equation is in cm. It is clear that ΔR_{wz} can be computed from surface temperature, surface vapor pressure and the temperature lapse rate. The temperature lapse rate, which cannot be predicted from surface measurement alone, appears only in the second term of Eq. (12). Since this second term is smaller by an order of magnitude, a mean value of α can be used in this model with adequate accuracy.

III. Comparison with Balloon Measurement

Before applying the surface prediction method of Eqs. (11) or (12), we should be careful about the assumptions we made in deriving that equation. The surface temperature T_0 in the equation should be the surface temperature of a linearly decreasing temperature profile as illustrated in Fig. 2. Radiosonde balloon data show that this condition comes closest to being met around local noon. Thus, for good prediction, the measurement of T_0 and e_0 should be made around local noon. The value of e_0 is computed from the following relation (Ref. 3):

$$e_0 = 6.1 (RH)_0 \times 10^2 \exp_{10} \left\{ \frac{7.4475\, T_c}{234.7 + T_c} \right\} \tag{13}$$

where

$e_0 =$ surface vapor pressure, N/m^2

$(RH)_0 =$ surface relative humidity (fraction of 1)

$T_c =$ surface temperature, °C

$\exp_{10} y = 10^y$

A few hundred data points were selected around local noon from two years of radiosonde balloon measurements (1967 through 1968). The data shown in the plots in Fig. 3 indicate that the zenith wet range correction is well predicted by Eq. (12). This data sample, shows an rms direction from theory equal to 2 cm (1 σ). The deviations of the data from theory could be caused by two factors: (1) the inadequacy of the theory, (2) the uncertainties in the balloon measurement. If the second factor is dominant uncertainty, the surface prediction may be more accurate than the current data indicates. Unfortunately sufficiently accurate data are not available to test this possibility.

IV. Comparison with Berman's Method

Berman's equation, which was derived under the assumption of constant relative humidity (Ref. 2), can be given as

$$\Delta R_{wz} = 56.6 \frac{(RH)_0}{\alpha} \left(1 - \frac{38.45}{T_e} \right)^2 \times \exp \left(\frac{17.15\, T_e - 4684.13}{T_e - 38.45} \right) \tag{14}$$

where

$\Delta R_{wz} =$ wet zenith range correction in cm

$T_e =$ linearly extrapolated surface temperature, K

$(RH)_0 =$ surface relative humidity $(0 \leq (RH)_0 \leq 1)$

Both the temperature lapse rate, α, and the linearly extrapolated surface temperature, T_e in Eq. (14) can not be measured at the surface. As suggested in Ref. 2, α and T_e can be estimated from less frequent (perhaps every several days or the monthly mean) radiosonde measurement. Comparing to Eq. (12), Eq. (14) is more sensitive to the errors in α and T_e. Table 1 shows the values of the partial derivatives of ΔR_{wz} with respect to α and T_0 or T_e for the two methods. It clearly indicates that the new method, Eq. (12), is about one order of magnitude less sensitive to the errors in α and T_0.

Thirty-eight balloon measurements made in 20 days in August 1967 at Yucca Flats near Las Vegas, Nevada, were chosen as reference to compare the two methods. Half of the balloon data were made near local noon and the other half were made near midnight. Figure 4 shows the values of ΔR_{wz} computed from different methods. It clearly reveals the following clues:

1. Near local noon, the new method Eq. (12) has consistently better agreement with radiosonde balloon data than Berman's method.
2. The new method has a larger deviation from balloon data during midnight.

(3) Berman's model has even greater deviations during midnight. This is possibly due to the violation of the constant *RH* assumption at night.

(4) Berman's model should be used near local noon with better accuracy and T_e being directly measured at surface.

V. Explanation of the Correlation Made by Earlier Researchers

In Ref. 1, the monthly correlation coefficients between the total water content in the atmosphere and surface absolute humidity vary from -0.29 to $+0.83$ depending upon the time and place the measurements were made. This may be explained by the fact that their measurements were not all made near local noon when the temperature profile is close to a straight line. Figure 4 gives a clear indication that correlation between total water content and surface measurement depends on the time of the day when the measurement is made.

A method to give good surface prediction of water content or wet zenith range correction during local night needs further study.

VI. Acknowledgments

The author would like to thank Dr. O. H. von Roos and Dr. K. M. Ong for the discussions and the help for verifying the derivations of the equations.

Table 1. Values of partial derivatives with respect to α and T_0[a]

Partial derivative	New method, Eq. (12)	Berman's method, Eq. (14)
$\left\lvert \frac{\partial R_{wz}}{\partial T_0} \right\rvert$	0.11 cm/K	0.8 cm/K
$\left\lvert \frac{\partial R_{wz}}{\partial \alpha} \right\rvert$	0.3 cm/(K/km)	2.0 cm/(K/km)

[a] $T_0 = 304.8$ K, $e_0 = 14.5$ mb, $RH = 31\%$, $\Delta R_{wz} = 15$ cm.

References

1. Reber, E. E., and Swope, J. R., "On the Correlation of the Total Precipitable Water and Absolute Humidity at the Surface," *J. of Appl. Meteorol.*, Vol. II, 1972.

2. Berman, A. L., "A New Tropospheric Range Refraction Model," in *Supporting Research and Advanced Development,* Space Programs Summary 37-65, Vol. II, pp. 140–153. Jet Propulsion Laboratory, Pasadena, Calif., Sept. 30, 1970.

3. Bean, B. R., and Dutton, E. J., *Radio Meteorology,* Monograph 92, p. 7, National Bureau of Standards, Wash., D.C., Mar. 1966.

4. Chao, C. C., "New Tropospheric Range Corrections With Seasonal Adjustment," in *The Deep Space Network Progress Report,* Technical Report 32-1526, Vol. VI. Jet Propulsion Laboratory, Pasadena, Calif., Dec. 15, 1971.

5. Jeans, J. H., *The Dynamical Theory of Gases,* Dover Publications, Inc., Fourth Edition (Chapter 15).

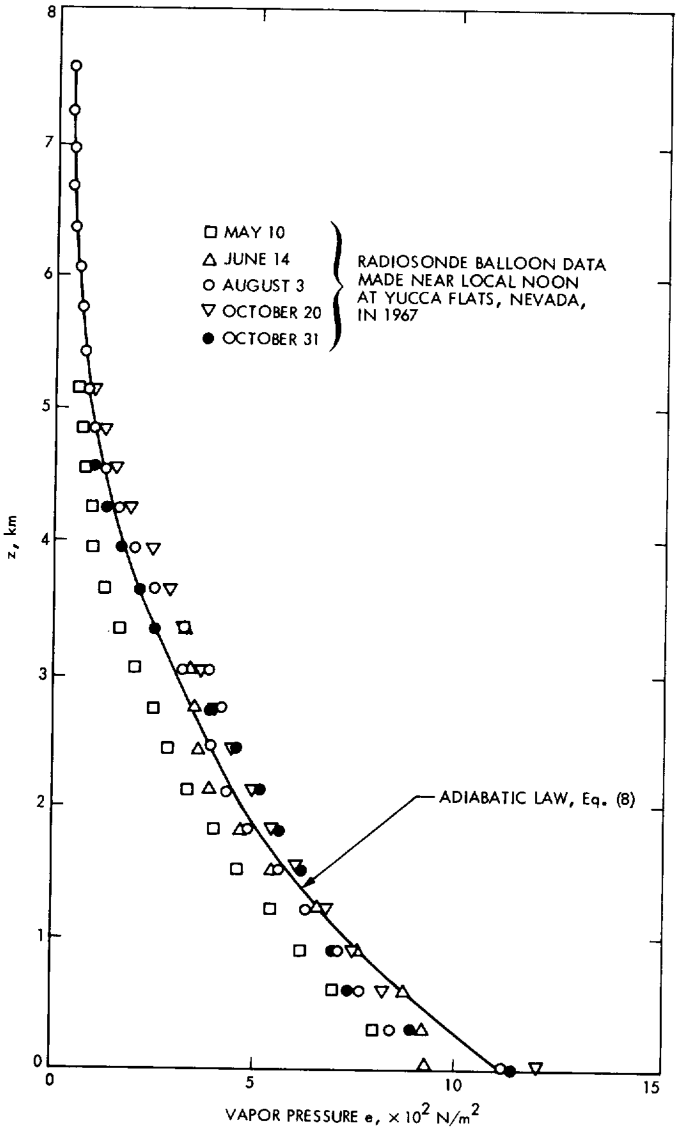

Fig. 1. Vapor pressure vs altitude

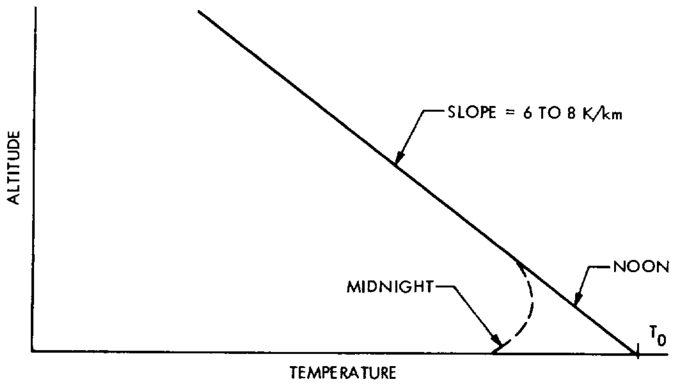

Fig. 2. Schematic drawing of temperature profile near Earth's surface

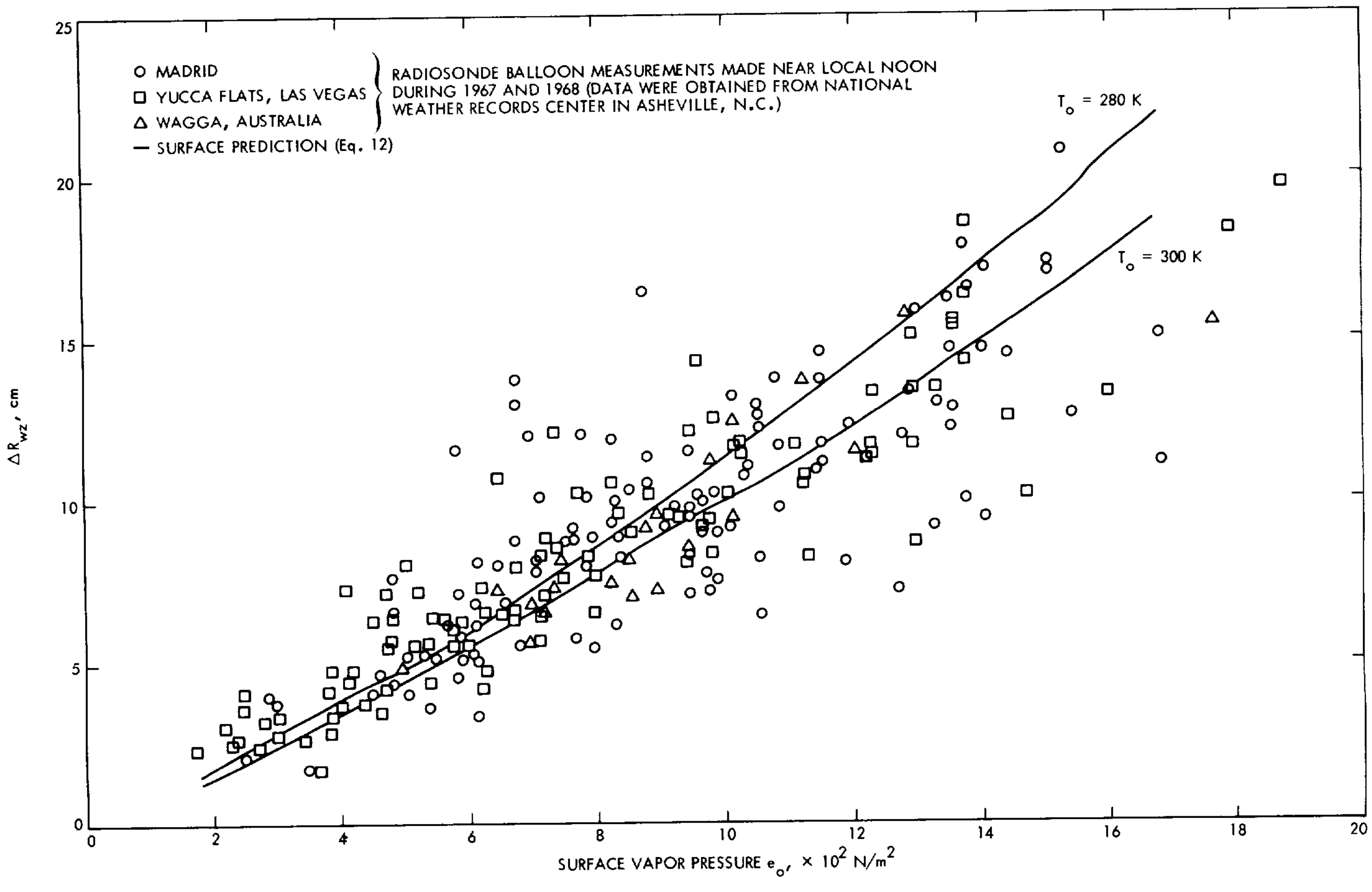

Fig. 3. Wet zenith range corrections from radiosonde balloon and surface measurement vs surface vapor pressure

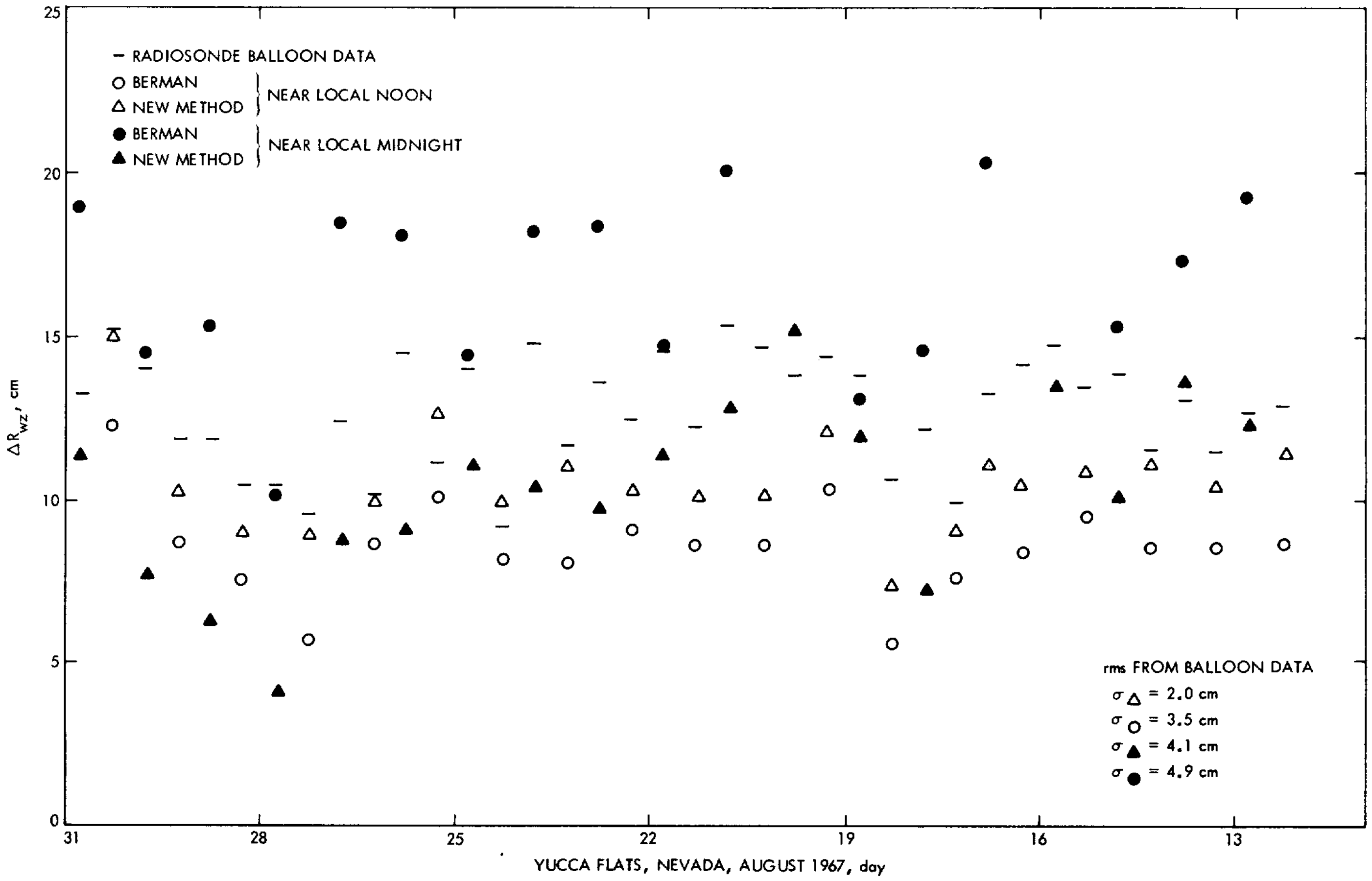

Fig. 4. Wet zenith range corrections computed from radiosonde data and surface measurements

An Analysis of Noise Bursts on the 64-m-Diameter Antenna at Goldstone

M. S. Reid and C. T. Stelzreid
Communications Elements Research Section

To provide more information for the noise-burst study, a comparison of noise bursts with the polarization diversity S-band (PDS) and S-band megawatt transmit (SMT) cones was made. For a period of approximately one month, DSS 14 conducted its regular tracking missions alternately with the PDS and SMT cones. The S-band total power system temperature strip chart recordings were analyzed for noise bursts. The conclusion is that with respect to noise-burst performance, the PDS and SMT cones are similar.

To provide more information for the noise-burst study, a comparison of noise bursts with the polarization diversity S-band (PDS) and S-band megawatt transmit (SMT) cones was made. S-band system temperature (T_{op}) strip chart recordings were used for this comparison. The data recorded on these strip charts were total power at S-band during regular station tracking missions. The results are presented in tabular and graphical form. The method of analysis is described below. The conclusion is that with respect to noise-burst performance, the PDS and SMT cones are similar.

To compare the PDS and SMT noise bursts, a comparison period was set up. This was October 1, 1972 through November 3, 1972. In this period DSS 14 tracked alternate days through the PDS and SMT cones. An agreed schedule of PDS and SMT tracking was set up, and the S-band T_{op} strip chart recordings were analyzed for noise bursts.

At the end of this comparison period, it was found that several charts were not usable or missing. Most of these were SMT recordings. To gain a firmer PDS analysis, several charts made prior to October 1, 1972 were analyzed. These were all PDS charts. In all, 41 tracks were analyzed for the PDS cone and 9 for the SMT cone.

The normal strip chart speed was 5.1 cm (2 in.)/h, which is equivalent to 3 min per 0.25 cm (0.1 in.) of chart. In each 0.25 cm (0.1 in.) (or 3 min of tracking time) a data point was found such that the peak T_{op} of the noise burst in Kelvins was recorded. This data point was called T_{NB}. Thus for each 3 min of tracking time one data point, T_{NB} was recorded, where T_{NB} was given by

T_{NB} = peak recorded T_{op} minus normal system temperature for the given antenna elevation angle averaged over 3 min.

Only tracking time with the transmitter on was analyzed. The following information was recorded for each day's track:

(1) Transmitter power.

(2) Number of data points in the track equals tracking time with the transmitter on, in min/3.

(3) Number of unreadable spikes (i.e., noise-burst spike ambiguous because it was confused with the automatic gain control (AGC) recording).

(4) Number of spikes whose maximum value is unknown (i.e., number of spikes that hit the chart maximum limit, i.e., 10 in. of chart or (usually) 500 K T_{op}).

(5) The value of the maximum spike in the track (in Kelvins).

(6) The value of the minimum spike in the track (usually zero Kelvins if there was a 3-min period of tracking when no noise bursts were recorded, which was not always the case).

For each day's tracking an average noise burst, $\overline{T}$, was computed thus:

$$\overline{T} = \frac{\sum T_{NB}}{\text{No. of 3-min periods in the track}}$$

For each cone and for each transmitter power (TX) an average noise burst $\overline{\overline{T}}$ for all the data analyzed was found thus:

$$\overline{\overline{T}} = \frac{\sum \overline{T}}{\text{No. of days}}$$

The results are presented in Table 1.

From the above table it may be seen that the PDS and SMT cones are remarkably similar, when compared by their average noise burst, $\overline{\overline{T}}$. This might be an indication that the major noise burst sources are outside the cones. It may also be seen from the table that the average noise burst, $\overline{\overline{T}}$, increases with increasing transmitter power. This may be seen in Fig. 1, which is a graph of average noise burst $\overline{\overline{T}}$ (K) against transmitter power (kW). The data lie approximately on a straight line on the log-log scales used in the figure. The following equation describes this line:

$$\overline{\overline{T}} = 1.6\,(TX)^{0.6}$$

where $\overline{\overline{T}}$ is the average noise burst in Kelvins and TX is the transmitter power in kW.

It must be noted that although the averaged data approximate to a straight line that implies repeatability, the character of the noise-burst phenomenon is random. This may be seen from the standard deviations of each set of $\overline{\overline{T}}$ as shown in Table 1. These standard deviations are large, which indicates that many hours of data need to be averaged before any repeatability becomes apparent.

Table 1. Summary of noise-burst analysis

Cone	*TX* power, kW	No. of days averaged	$\bar{T}_{MIN}$, K	$\bar{T}_{MAX}$, K	$\bar{\bar{T}}$, K	Standard deviation of $\bar{\bar{T}}$, K
PDS	10	4	0.63	120.4	7.02	4.5
PDS	20	15	0	134.2	10.4	12.2
SMT	20	4	1.5	88.9	10.7	8.4
PDS	200	4	3.1	176.0	44.2	30.5
SMT	200	1	3.0	418.0	46.7	–
PDS	400	18	2.1	330.6	68.2	52.4
SMT	400	4	2.8	397.0	68.8	41.3

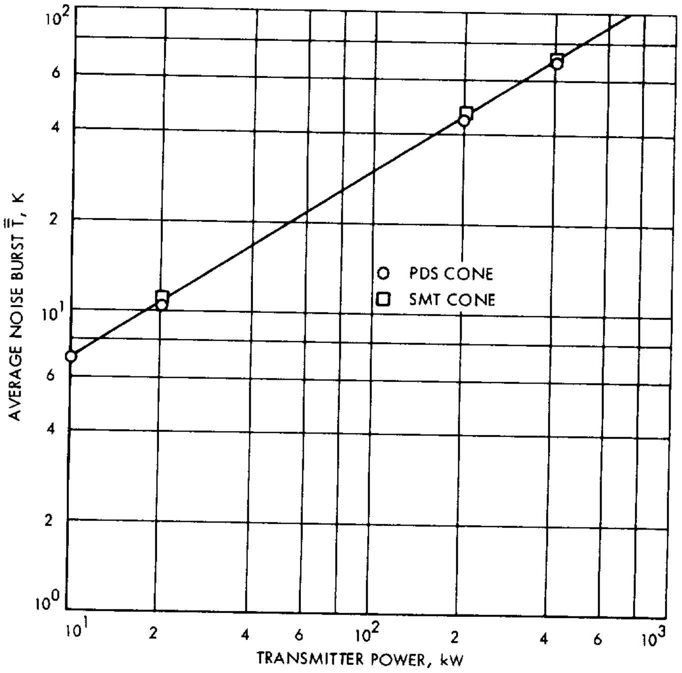

Fig. 1. PDS and SMT noise-burst analysis from T_{op} strip chart recordings, Aug.–Nov. 1972, DSS 14

Low-Noise Receivers: Solid-State Pump Source for S-Band Traveling-Wave Masers

R. Quinn
Communications Elements Research Section

Low-noise traveling-wave masers have been used by the Jet Propulsion Laboratory Deep Space Network for ten years. The requirements for the maser pump source are presently met by reflex klystron oscillators, although other microwave energy sources have been tested and evaluated on the basis of cost, reliability, output power, tunability, frequency stability, and power stability. Gunn-effect diode oscillators have recently reached a stage of development that makes them superior to the reflex klystron oscillator. This article describes a Gunn-effect oscillator that has been tested, packaged, and evaluated in the laboratory and is now ready for installation in the Deep Space Network.

I. Introduction

The traveling-wave masers presently used in the Deep Space Network use reflex klystrons as pump sources. The limited electronic tunability and lifetime, as well as the high-voltage requirements of the reflex klystron have made desirable the development of a solid-state pump source that would serve as a suitable replacement. This article describes a new maser pump package using a Gunn-effect oscillator.

II. The Gunn-Effect Oscillator

Recent improvements in Gunn-effect diode performance have made possible a solid-state device with sufficient power and stability to meet the pump requirements of a traveling-wave maser (TWM). TWM pump frequency, stability, and power requirements have been previously reported (Ref. 1). The varactor-tuned, Gunn-effect oscillator used is a Varian model VSU-9012Y, which is electronically tunable from 12.6 to 12.9 GHz. Varactor (diode) tuning permits very fast tuning rates and is accomplished by varying the voltage applied to the tuning bias terminal of the oscillator. By amplitude modulating the tuning bias voltage at a 100-kHz rate, the Gunn oscillator can be frequency modulated across its entire tuning range. Frequency modulation of the TWM pump source reduces the frequency stability requirements and permits the TWM to be tuned across its full range with no further pump frequency adjustment.

III. Control Circuitry

The control unit for the Gunn oscillator is mounted in the maser control rack and operating voltages are connected to the pump package by antenna cables (Fig. 1).

Unlike the reflex klystron, the Gunn-effect oscillator operates from a low-voltage power source. The control unit uses three, relatively low-cost, commercial voltage-regulated power supplies. The Gunn oscillator bias voltage (7.0 V at 1A) has no front panel adjustment, as the proper operating voltage adjustment is made at the time of installation and is regulated at that point. The tuning varactor bias voltage is adjustable through one of two 10-turn counting dials (duodial) on the control panel. Figure 2 shows a correspondence of the package output frequency and power to the varactor tuning duodial and voltage. The second duodial adjusts the frequency modulation control voltage.

IV. Pump Package Description

The Gunn-effect oscillator is mounted on a temperature-controlled heat sink in the pump package together with a combined protective and audio oscillator circuit (Fig. 3). The protective circuit prevents the application of a negative or excessive voltage to the Gunn bias or tuning varactor terminals and the 100-kHz audio oscillator modulates the voltage at the tuning varactor terminal of the Gunn oscillator. Amplitude modulation of the tuning varactor bias voltage results in frequency modulation of the Gunn-effect oscillator.

A commercial temperature controller is mounted on the inside wall of the pump package and is set to maintain the heat sink temperature at 45°C ± 0.5°C over an ambient temperature range of 15°C to 35°C. A 28-V power supply for the temperature controller is mounted in the rear of the maser control rack and does not require adjustment. The Gunn-effect oscillator assembly is readily interchangeable with the reflex klystron and has been installed in an existing pump package. The only modification required was the drilling of four holes necessary to mount the temperature controller. No new or special antenna cabling is needed and only minor changes in the maser control rack and junction box wiring are necessary.

V. Performance

The Gunn-effect oscillator has been used in the lab to pump a new S-band TWM, which has a superconducting magnet. This combination of magnetic field and pump source versatility has shown performance superior in several ways to that of other S-band TWMs. The maser gain, during single-frequency operation, is comparable to that obtained when using a reflex klystron, but frequency modulation of the oscillator produces broadband energy sufficient to increase the maser gain 2 dB above that obtained when pumped by a frequency-modulated klystron. Stagger tuning of the maser/magnet combination separates the maser into two halves and permits an increase in maser bandwidth (Ref. 2). Figure 4 demonstrates that through wide separation of the maser halves, simultaneous maser operation at two frequencies separated by 100 MHz is possible. This kind of two-frequency operation requires wideband pump energy previously unavailable from a single pump source.

References

1. Clauss, R. C., and Quinn, R. B., "Low Noise Receivers: Microwave Maser Development," in *The Deep Space Network Progress Report*, Technical Report 32-1526, Vol. IX, pp. 128–136, Jet Propulsion Laboratory, Pasadena, Calif., June 15, 1972.
2. Clauss, R., Wiebe, E., and Quinn, R., "Low Noise Receivers: Microwave Maser Development," in *The Deep Space Network Progress Report*, Technical Report 32-1526, Vol. XI, pp. 71–80, Jet Propulsion Laboratory, Pasadena, Calif., Oct. 15, 1972.

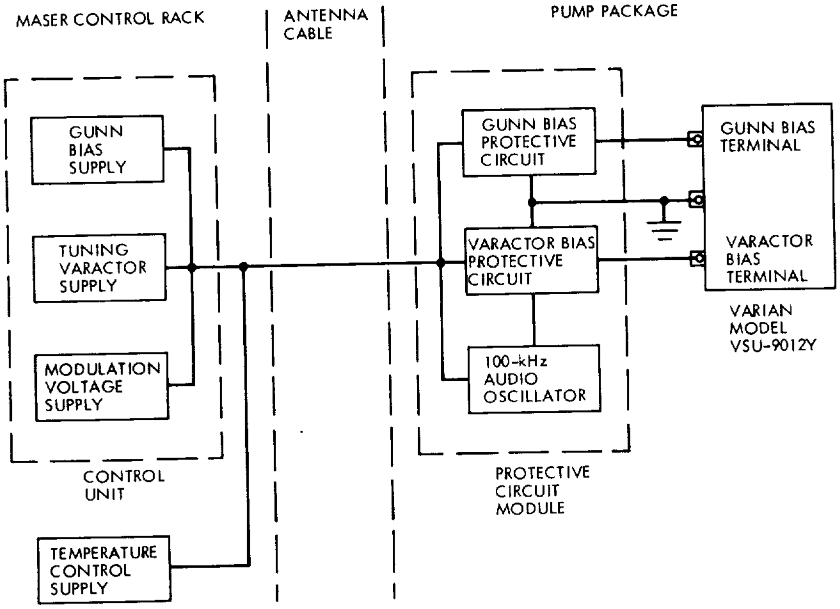

Fig. 1. Block diagram of Gunn-effect oscillator and related control circuitry

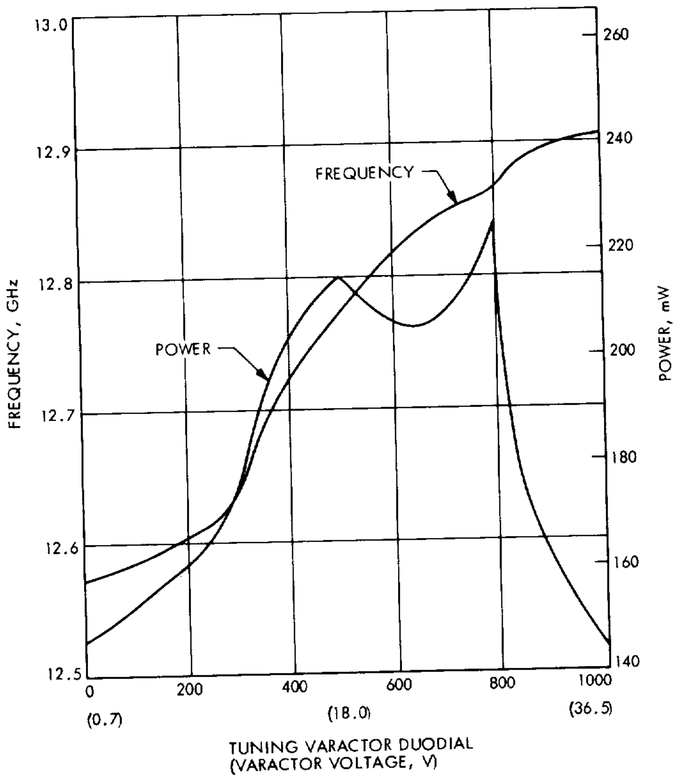

Fig. 2. Varactor bias voltage vs frequency and power

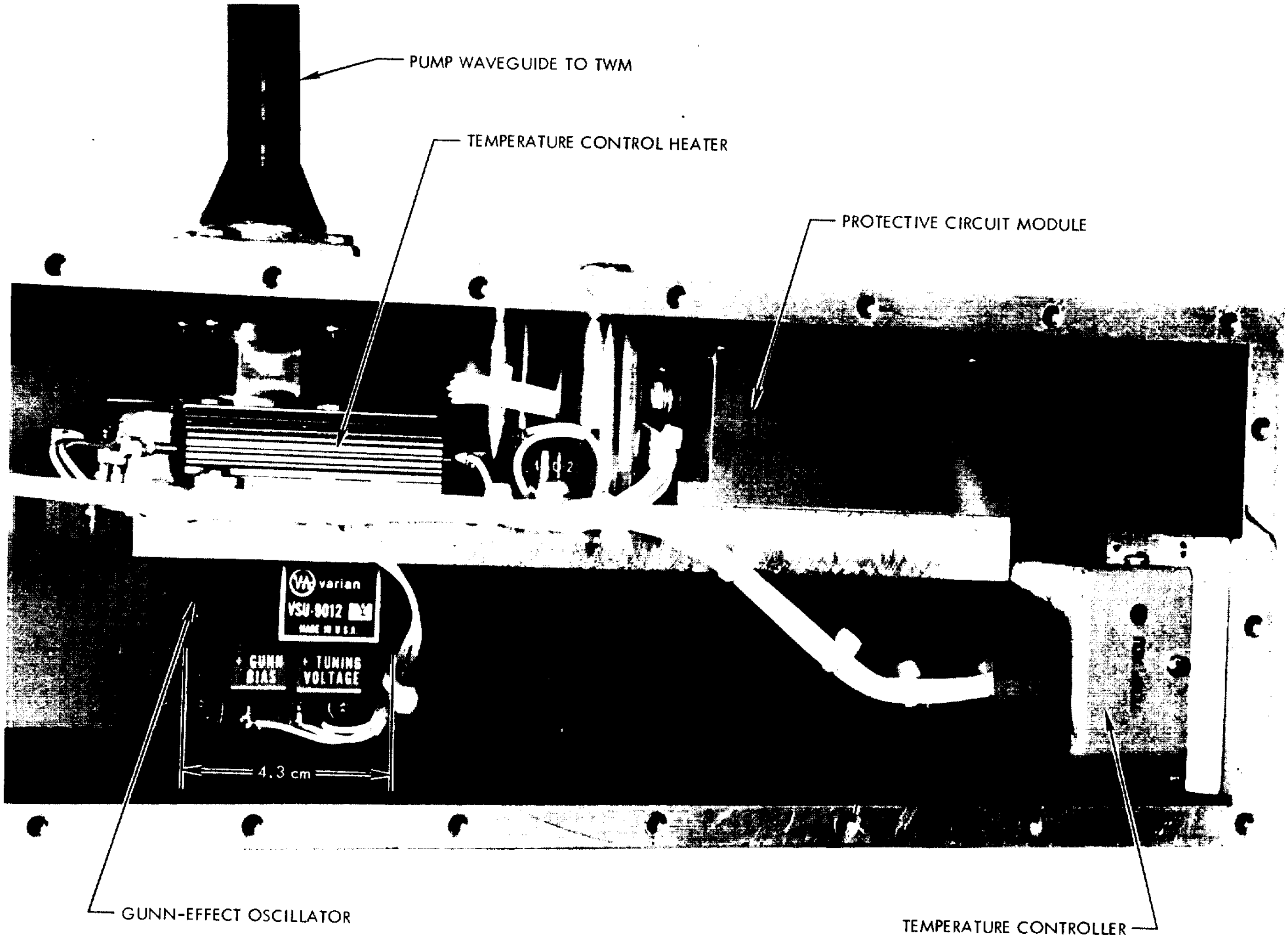

Fig. 3. TWM pump package with Gunn-effect oscillator

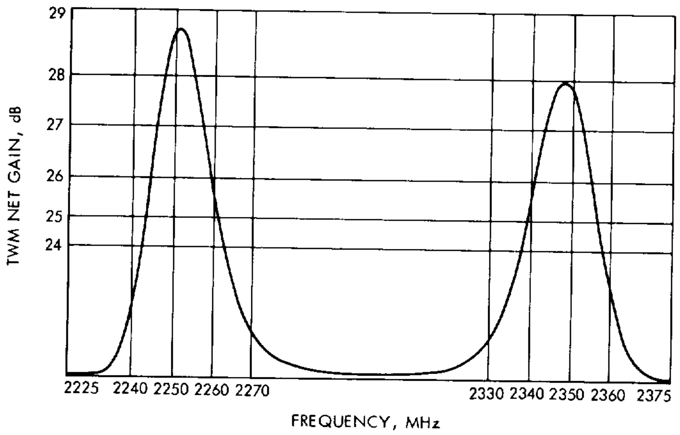

Fig. 4. Simultaneous two-frequency operation

Structural Stiffness Matrix Wavefront Resequencing Program (WAVEFRONT)

R. Levy
DSIF Engineering Section

The computer program WAVEFRONT is a preprocessor that resequences the stiffness matrix for wavefront reduction prior to processing by structural analysis computer programs. The program operation, deck, input data requirements and suggested usage are described here. Summary data extracted from example applications show that this program is an effective preprocessor for the NASTRAN structural analysis program and is generally preferable to alternative bandwidth reduction preprocessors.

I. Introduction

Computational efficiency and reduction of core storage requirements for finite-element structural analysis computer programs depends upon the ordering of the structural stiffness matrix. Effective ordering makes it possible to arrange for storage and to perform computations only within a compact region that is densely populated with nonzero coefficients and to omit computations and storage provisions for an empty region with zero coefficients. Depending upon the coding and storage method used during decomposition of the stiffness matrix for problem solution, compactness typically depends either on the matrix bandwidth (i.e., the ELAS program), or on the matrix wavefront (i.e., the SAMIS program). It is also possible to employ a mixed coding method[1] (i.e., the NASTRAN program) that can operate on a combination of bandwidth and wavefront.

In preparing the analytical model for processing by one of the finite-element analysis computer programs it is possible to order the node labels by inspection to produce a relatively compact stiffness matrix. Nevertheless, for complex models with many nodes, development of an effective ordering sequence could be laborious and also require a skilled analyst. Consequently, it is often practical to label the nodes in some convenient manner that will facilitate and simplify preparation of all the input data without regard to sequencing effectiveness, and then to produce an improved sequencing by an automated procedure that reorders the nodes.

WAVEFRONT is a preprocessor computer program that reorders the nodes of the structural stiffness matrix prior to entering a structural analysis computer program. It was originally developed to reduce the matrix wavefront for follow-on processing by the SAMIS computer

---

[1] Bandwidth is the distance of an extreme matrix element from the diagonal. Wavefront at a particular row of the decomposition is the number of columns that affect the arithmetic in lower rows. With the mixed coding method, the term "active columns" is the wavefront minus the number of columns within the bandwidth.

program. However, the wavefront reduction capability has subsequently been found to be effective for NASTRAN program processing and the input and output data are now NASTRAN-oriented.

II. Program Approach

The resequencing objective is to minimize or reduce the number of degrees of freedom (DOF) that are contained in the stiffness matrix wavefront. This has the effect of diminishing both computational time and storage requirements. A specific measure of the objective would depend upon the particular coding of the stiffness matrix decomposition, and measures for computation time efficiency are not necessarily the same as measures for minimum storage. A possible measure for computational time is either the root mean square or the sums of squares of the wavefront for all rows of the stiffness matrix. The measure for storage could be either the maximum wavefront at any row if fixed-wavefront storage is used, or the average wavefront of all the rows if variable wavefront storage is used. For bandwidth-oriented decomposition algorithms, there are equivalent candidate measures defined in terms of bandwidth, rather than wavefront. As a simplification, the measure adopted here is the maximum wavefront at any of the rows. It is proposed on the basis of both intuition and experiment that a superior reordering in terms of the adopted measure tends also to be superior in terms of the other foregoing alternative measures. Furthermore, it is assumed that all nodes of the analytical model tend to have about the same numbers of associated degrees of freedom. Therefore, as a simplification, the approach is designed to minimize or reduce the maximum wavefront of the nodal connectivity matrix, instead of to reduce the wavefront as expressed in degrees of freedom of the stiffness matrix.

The resequencing algorithm is a 'minimum growth' method. That is, assuming that at a particular execution phase the procedure has progressed to identify the first i nodes of the resequenced nodal connectivity matrix, then the new $(i + 1)$-th node is selected as the node that will cause the smallest increase of the wavefront existing for the i-th node. To start the procedure, the first node selected can be either defined by the user or, by default, can be determined by the program as a node with the minimum number of connections. Further details of the algorithm in addition to a hand-executed example are given in Ref. 1.

It is evident that the effectiveness of the final sequencing obtained by this algorithm depends upon the starting point. Consequently, provisions are made within the program to perform user-specified numbers of complete resequencing cycles with starting points after the first cycle chosen at random by the program. During this cyclic repetition, the program will abort any cycle currently in progress as soon as it determines that the maximum wavefront is as large as the terminal maximum wavefront of a previously completed cycle. Consequently, unsuccessful cycles that terminate early require less computation time than cycles that go to completion and achieve an improvement. Each time a resequencing cycle produces a reduction of the previous maximum wavefront, a set of NASTRAN-type sequence cards are punched by the program for insertion in the NASTRAN data deck. When there are several such sequence card sets produced, the last set is the best.

III. Data Input

The input data deck consists of a title card, an option card, a set of cards that supplies the node labels and initial sequencing, and a set of cards that supplies the finite element connections. Specific requirements are as follows:

(1) *Title card:* Format (80A1).
Contains any alphameric title desired by the user for problem identification and echo.

(2) *Option card:* Format (6I10).

Fields 1 and 2: blank.

Field 3: ROWA = integer to supply the original sequence number for the node that is to be first in the first new resequence cycle. If blank or zero and for sequence cycles greater than 1, the program will pick the first row.

Field 4: KCYCLE = the number of cycles of resequencing to be performed. If blank or zero, one cycle will be performed.

Field 5: JPRINT, if not zero, then the initial connectivity matrix terms will be printed.

Field 6: NEWCNT, if not zero, then at the end of a cycle that achieves an improved wavefront, a table of the wavefront at each row of the new connectivity matrix will be printed plus a summary of the maximum, average, and rms wavefront for this sequencing.

(3) *Node label card set.*

(a) First card: a dummy card with any text signifies the beginning of this set. The card will be echoed.

(b) Node cards: Format (A6, 2X, A8).

First field: not blank.

Second field: node label in the form of a string of characters with no intervening blanks. The label can be placed anywhere within the field. NASTRAN "GRID" cards may be used for this set.

Note: initial nodal sequencing is established by the program from the order in which these cards are submitted. The sequence and node list is echoed.

(c) Last card: Format (A16).

Blank to signify termination of this card set.

(4) *Connection card set.*

(a) First card: a dummy card as in item 3 above.

(b) Element connection cards: Format (A3, SX, NA8), where S and N depend upon the type of connection as tabulated below:

Connection type	First field	S	N
2-node	CBA CTU	21	2
2-node	CON	13	2
3-node	CTR	21	3
4-node	CQD CQU CSH CTW	21	4

The last N fields for all of these cards contain associated node labels in the same form as for item 3b. Except for the CROD connection card, most of the customary NASTRAN connection cards can be used.

(c) Last card: Format (A3).
Blank to signify termination of this set. This is also the last input data card.

IV. Program Deck Description

The program is coded in Fortran V for the Univac 1108 Exec-8 computer. One subroutine, TIMER, is installation-dependent. TIMER returns the current central processing unit (CPU) time and is not essential to program execution. It can be replaced by any dummy subroutine of the same name. The program is currently dimensioned to resequence problems containing up to 600 nodes and 1800 distinct edges (one edge per bar, three edges per triangular plate, six edges per quadrilateral plate). Duplicate edges formed by adjacent plates are detected and need not be provided for in the dimensions. Core size for the sum of the instruction and data banks is about 36,000 words. The dimensioning parameters are contained in a Fortran procedure definition processor element PARAM, included under the name PSPEC. The problem size dimensions can be changed here by updating the parameters PE to be equal to the number of edges and PN to be equal to the number of nodes. Comment cards contained in this element list the routines that are to be recompiled when PSPEC is updated. A problem dimensioned for 1000 nodes and 4000 edges was found to require about 58,000 total words of storage. No overlay segmentation is included, although this would be a consideration for problems of larger size.

The program consists of a main program, WAVEFRONT, which calls the subroutine WAVSEQ each time a new sequencing cycle is to be performed. During each cycle, WAVSEQ makes one call to a subroutine FILLUP, which supplies the nodal connectivity matrix, and repeated calls to the subroutine NEXTRO, which selects the next row to be placed in the nodal connectivity matrix, and to ROSTRK, which reorganizes the connectivity matrix to account for rows and columns that are or are not in the current wavefront. The aforementioned main program and four subroutines are the primary operational modules. These and all remaining auxiliary subprograms, which consist of about 600 card images, are listed in Table 1.

V. Suggested Usage

Before using WAVEFRONT or any alternative resequencing program as a finite element program preprocessor, two questions should be considered:

(1) Is it worthwhile to resequence?

(2) If the decision has been made to resequence, what type of sequencing should be used?

The answers to both questions are problem-dependent and no simple rules can be given. Nevertheless, we will make some suggestions that reflect our present practice and experience, particularly as related to NASTRAN processing.

If the problem is small and the stiffness matrix decomposition will be performed within NASTRAN only a limited number of times, the effort of assembling the data for resequencing and the associated computation time will not be justified by associated savings during the NASTRAN program run. To be a little more specific with respect to the implications of "small," this might represent from 75 to 400 or more degrees of freedom, depending upon how effective is the initial sequence that has been established. On the other hand, it might be preferable to label nodes according to a recognizable pattern that lends itself most readily to interpretation and checking and never to expend effort to obtain effective computational sequencing except by an automatic resequencing program.

With respect to NASTRAN processing, the second question resolves itself into a choice between a wavefront or a bandwidth sequencing procedure. Here, the following facts are pertinent:

(1) Wavefronts for structural models do not exceed and are often considerably less than bandwidths.

(2) Although resequencing by a wavefront approach will usually result in a more compact stiffness matrix than when resequenced by a bandwidth approach, NASTRAN presumably does not process an active column (derived from the wavefront) as rapidly as a column within the band. We estimate the expected time penalty to be between 20% and 50%.

(3) The preprocessor computation time for wavefront resequencing is likely to exceed the preprocessor time for bandwidth resequencing.

Although the first two of the above items tend to offset each other, our experience, based on many NASTRAN tests, has been that the decomposition time for a wavefront-sequenced model varies from slightly less than to considerably less than for the same model with bandwidth sequencing.

The third item above indicates that savings in the decomposition time for wavefront sequencing can be partly, or possibly fully, overcome by the additional computation time for wavefront sequencing. One reason that the wavefront sequencing program uses more computation time is that the user has the freedom to specify large numbers of resequencing cycles. Our experience has been that the first few cycles tend to produce the most significant reductions in the wavefront and many additional cycles often produce only minor further reductions. Consequently, a reasonable way to proceed with WAVEFRONT is to perform only a limited number of resequencing cycles in an initial run. Then, if it appears that useful further reductions are possible, perform another run that begins with the row that gave the best result in the initial run. This will tend to allow unfruitful resequencing cycles in the second run to be identified quickly, which will reduce the associated computation time.

Also, in considering possible disadvantages of the longer computation time to perform wavefront rather than bandwidth sequencing, the number of times that the NASTRAN program will be required to perform the decomposition for the same problem should be considered. Usually it takes several NASTRAN runs for a new structural model to eliminate anomalies in topology or constraints. Constraint changes do not invalidate an existing set of sequence definitions and moderate changes in topology will not have a pronounced effect on the usefulness of an available wavefront sequence. The effectiveness of bandwidth sequencing is more vulnerable to topology changes and such changes might call for either repetition of the sequencing run or a user modification of the sequence to enforce an active column. Furthermore, depending upon the charging algorithm at the particular installation, extra CPU seconds during resequencing could be less costly than the same number of CPU seconds in NASTRAN.

VI. Example Results and Comparisons

Reference 1 contains several examples of NASTRAN decomposition time comparisons that show advantages for sequencing by WAVEFRONT with respect to bandwidth sequencing by Rosen's (Ref. 2) program. Here, Table 2 contains some additional comparisons for bandwidth sequencing by the more recently developed BANDIT (Refs. 3 and 4) program. Some of the actual decomposition times with bandwidth sequencing are missing in the table because in these cases NASTRAN was permitted to proceed with the decomposition for only the type of sequencing that was estimated to result in the fastest decomposition.

Nevertheless, in these absences, examination of the NASTRAN estimated decomposition times or the resulting resequenced wavefronts and bandwidths indicates moderate to strong advantages for wavefront sequencing. It might also be noted that the sequencing that produces the faster decomposition times would also produce some additional time savings during forward and backward substitution phases of the load/deflection solution.

The last problem listed in the table shows the importance of sequencing for a moderate-to-small size structure. A bandwidth sequencing was not processed by NASTRAN, but since BANDIT provided a resequenced band equal to only twice the resequenced wavefront, this also would have provided a significant reduction of the decomposition time in comparison with the time for the unsequenced problem.

In summary, the experimental data shown previously in Ref. 1 and here in Table 2 indicate that resequencing of the connectivity matrix prior to NASTRAN processing can produce significant computation time reductions during the NASTRAN run. Furthermore, notwithstanding the possibilities of longer preprocessor computation times to perform wavefront sequencing than to perform bandwidth sequencing, as a general procedure wavefront sequencing appears to be preferential to bandwidth sequencing.

References

1. Levy, R., "Resequencing of the Structural Stiffness Matrix to Improve Computational Efficiency," in *Quarterly Technical Review*, Vol. I, No. 2, pp. 61–70, Jet Propulsion Laboratory, Pasadena, Calif., July 1971.
2. Rosen, R., "Matrix Bandwidth Minimization," in *Proceedings of the 23rd National Conference of the ACM*, p. 585. Brandon/Systems Press, Inc. New Jersey, 1968.
3. Cuthill, E., and McKee, S., "Reducing the Bandwidth of Sparse Symetric Matrices," *Applied Mathematics Laboratory Technical Note*, AML-40-69. Naval Ship Research and Development Center, Washington, D.C., June 1969.
4. Everstine, G. C., "The BANDIT Computer Program for the Reduction of Matrix Bandwidth for NASTRAN," *Computation and Mathematics Department Research and Development Report 3827*, Naval Ship Research and Development Center, Bethesda, Md., March 1972.

Table 1. List of WAVEFRONT routines

Name	Type	Called by	Function
PSPEC	Procedure		Sets dimension parameters
WAVEFRONT	Main program		
WAVSEQ	Subroutine	WAVEFRONT	Controls resequencing cycles
CONNIN	Subroutine	WAVEFRONT	Reads connection card input (bars, rods, plates)
CONV	Subroutine	WAVEFRONT, CONNIN	Converts input free-field node labels to integer
COUNT	Subroutine	WAVEFRONT	Determines maximum, average, rms, wavefront for initial and improved sequencing
UNIFRM	Function	WAVEFRONT	Supplies random number to pick first row
FILLUP	Subroutine	WAVSEQ	Supplies nodal connectivity matrix
NEXTRO	Subroutine	WAVSEQ	Picks the next row in the sequence
ROSTRK	Subroutine	WAVSEQ	Reorganizes connectivity to distinguish currently sequenced and unsequenced rows
CROSS	Subroutine	ROSTRK	Interchanges node labels
SORT	Subroutine	FILLUP	Arranges node labels of connectivity in ascending order
TIMER[a]	Subroutine	WAVEFRONT, FILLUP	Supplies CPU time

[a] Installation: dependent

Table 2. Sequencing and NASTRAN run comparisons

Problem description	Resequencing program	Nodes		Sequencing program		Predominant DOF per node	NASTRAN run			
							B[c]	C[d]	Decomposition time, CPU, s	
		Original	Resequenced	Cycles	CPU, s				Estimated	Actual
Tank, 575 nodes	WAVEFRONT	62[a]	34[a]	1	83	5	15	156	1430	1111
	BANDIT	210[b]	55[b]	3	55		257	0	2500	–
Quadripod, 172 nodes	WAVEFRONT	15[a]	9[a]	95	50	3	22	9	9	6
	BANDIT	37[b]	27[b]	3	41		48	9	22	12
Antenna, 64-m-diameter, 946 nodes	WAVEFRONT	51[a]	44[a]	3	266	3	7	121	783	700
	BANDIT	346[b]	121[b]	3	163		–[e]	–	–	–
Subreflector, 129 nodes	WAVEFRONT	45[a]	6[a]	60	33	6	16	18	14	12
	BANDIT	114[b]	40[b]	3	112		106[f]	96	421	–
Adapter cage, 78 nodes	WAVEFRONT	24[a]	8[a]	25	9	6	12	30	15	12
	None	24[b]	–	–	–		150	0	73	54

[a] In wavefront.

[b] In bandwidth.

$\left.\begin{array}{l}\text{[c]Bandwidth}\\ \text{[d]Active columns}\end{array}\right\}$ DOF allocated by NASTRAN.

[e] No NASTRAN run attempted, severe spilling anticipated.

[f] Approximately 70 decomposition columns spilled.

Tracking and Ground-Based Navigation: Hydrogen Maser Frequency Standard Automatic Cavity Tuning Servo

C. Finnie
Communications Elements Research Section

This is the first of a series of reports describing the automatic cavity tuning servo to be incorporated in the DSN prototype hydrogen maser frequency standard. It is a first-order sample data control system, featuring stability monitoring circuits for the detection of malfunction in the maser and its receiver-frequency synthesizing system. The control system ignores error measurements exceeding an adjustable limit. The system's counter calibrates the Zeeman oscillator used to correct the maser output frequency for ambient magnetic field.

I. Introduction

The hydrogen maser output frequency is derived from an oscillation in a microwave cavity. The oscillation is sustained by energy from an atomic spin energy inversion. The microwave cavity must be tuned to the center frequency of the atomic resonance or an output frequency error will result. This error is caused by the pulling of the atomic gain profile (apparent line shape) by the cavity frequency response; therefore, the tuning error is a function of the atomic linewidth and the cavity bandwidth. The cavity tuning servo modulates the atomic linewidth and detects the resultant change in the maser output frequency to determine the cavity tuning direction for reduced pulling effect.

II. Description

Further details of the general cavity tuning technique were reported earlier (Ref. 1) and will not be included here. The block diagram, Fig. 1, illustrates the elements of the tuning control system and its relation to the maser-receiver systems. The primary function of the tuner system is to center the maser oscillator cavity frequency to within 1 part in 10^{10} of the atomic hydrogen spin resonance frequency. Other housekeeping functions included in the design are:

(1) A tracking mode in which a maser can be accurately controlled to a constant operator-set frequency offset of the tuning reference

(2) A frequency monitoring mode which outputs individual frequency error measurements (binary-coded decimal and sign)

(3) The system can be used to update the maser output frequency on a slow noninterfering basis. The minimum adjustable increment is 1 part in 10^{16} every 200 s.

(4) The tuner sequence counter can be switched to measure the output frequency of the Zeeman test oscillator.

The tuner sequence counter for the tune mode is shown in Fig. 2. An up-down counter 1 measures the difference in alternate periods of the 0.01-Hz beat between the hydrogen maser and its tuning reference oscillator at 100 MHz. These are intervals τ_1, τ_3, τ_5, τ_7 (Fig. 2). The differences are indicated in Fig. 3 by $\Delta\tau_1$, which is the difference between τ_1 and τ_3; and $\Delta\tau_2$, which is the difference between τ_5 and τ_7. Incremental frequency error is given by:

$$\frac{\Delta f}{f_0} = \frac{\Delta\tau}{\tau_0^2} \cdot \frac{1}{f_0}$$

where

$\Delta\tau << \tau_0$

$\Delta\tau$ = counter measured error increment

$\tau_0 = 100$ s

$f_0 = 100$ MHz

This results in a sensitivity of 1 part in 10^{12} for each second of measured error interval. For a counter time base of 0.001 s the minimum frequency resolution is, therefore, 1 part in 10^{-15}.

In the count sequence shown in Fig. 2, two traces during the down counts τ_3 and τ_7 represent the cases where the first count, τ_1 or τ_5, exceed the second, τ_3 or τ_7, (solid line) and the opposite error sense (dashed line). The time scales of these lines differ to simplify the drawing. This implementation allows the use of a simple comparator to sense the magnitude of the error, and makes the error available for digital display. The magnitude and sign of the last measurement error is displayed on the tuner module.

Dead times τ_2 and τ_6 are used to allow the physical system to reach equilibrium after a change in hydrogen flux level. During period "a" (Fig. 2), the error is compared to an operator-set limit. This limit reflects the stability of the reference oscillator or an error level present during initial cavity tuning. Errors below this level are entered into the summing counter 2 in the correct direction to decode the flux modulation sequence. Counter 2 is connected to a 16-bit digital-to-analog (D-A) converter which, in turn, drives the cavity tuning varactor. Errors greater than the set point provide an alarm signal and are not entered into the No. 2 counter.

The requirement for the error limiting design results from operation with long integrating times (several days) at the Goldstone DSCC. Occasional (one in five days) disturbances would cause large tuning offsets. The error comparator prevents the loss of integration time by ignoring abnormally large errors. Typical interference causes were power outages or operator changes in equipment auxiliary to the maser tuning system.

The tracking mode count sequence is shown in Fig. 3. This mode recycles the section of the tune mode sequence through the τ_2, τ_3 time intervals of Fig. 2. At the end of each error down count the counter is reset to a constant equal to the desired offset between the two frequency standards plus 100 s. The error is therefore zero when the offset between the two oscillators is 100 s minus the set point. The individual measurement errors are summed in counter 2 and control the cavity frequency as in the tuning mode. The error comparison and control is identical to the tuning mode.

The tuning mode with an adjustable initial count provides the slewing mode. The stability monitoring mode is the same as the tuning mode but without hydrogen beam modulation. No error is transferred to the tuning varactor.

Reference

1. Finnie, C., "Design of Hydrogen Maser Cavity Tuning Servo," in *The Deep Space Network Progress Report,* Technical Report 32-1526, Vol. II, pp. 86–88. Jet Propulsion Laboratory, Pasadena, Calif., April 15, 1971.

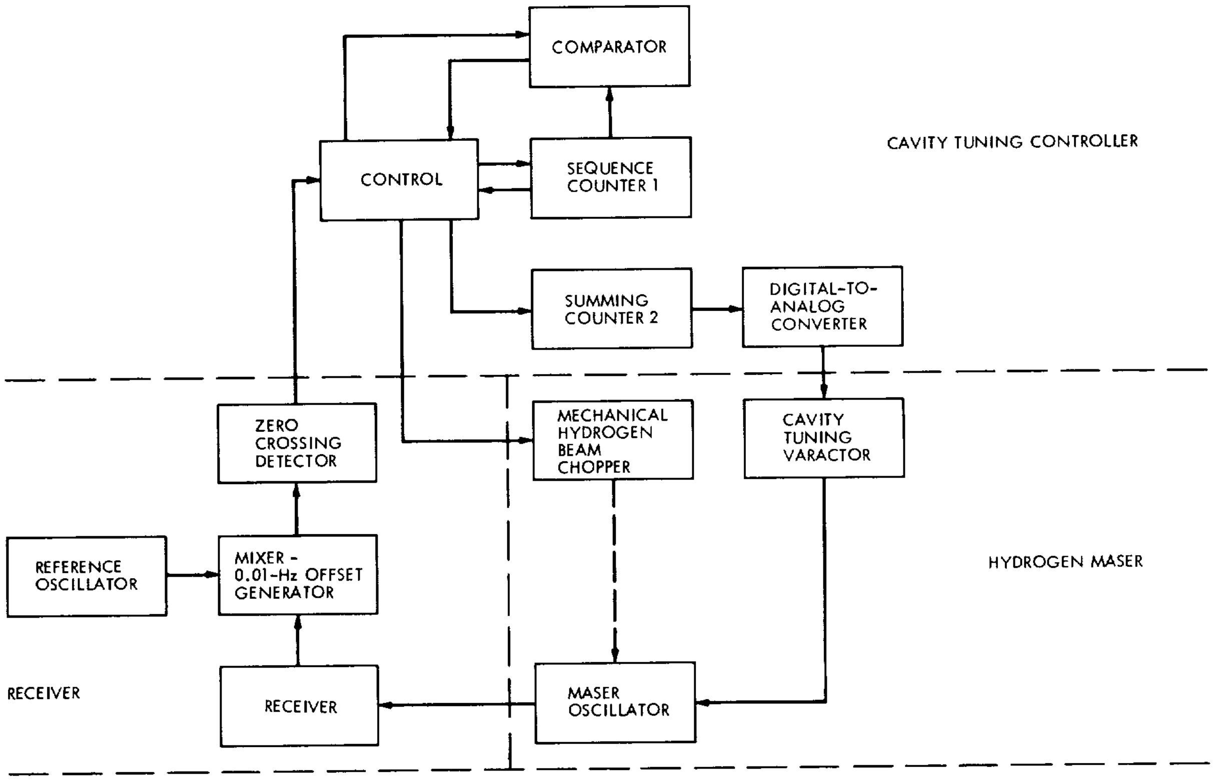

Fig. 1. Cavity tuning servo system block diagram

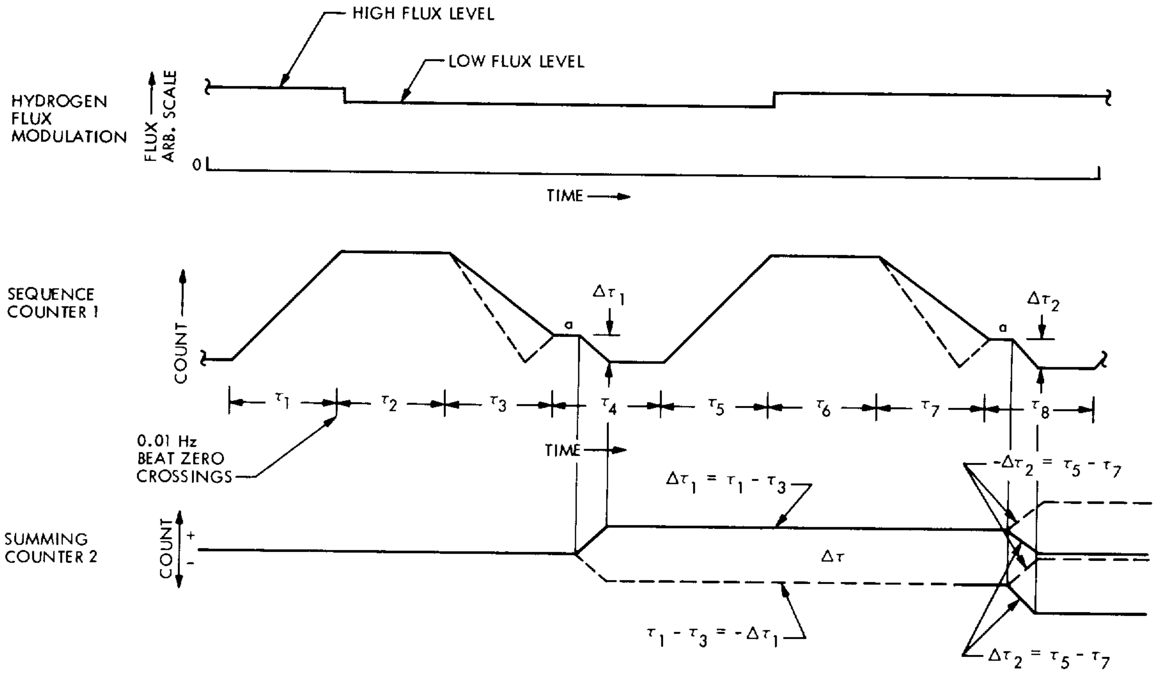

Fig. 2. Tuning mode count sequence diagram

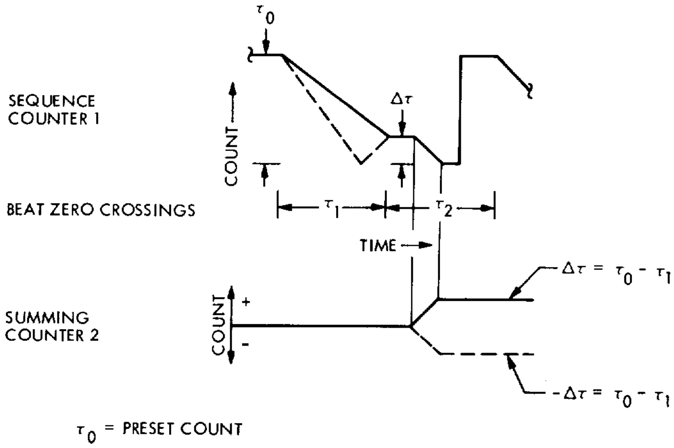

Fig. 3. Tracking mode count sequence diagram

Tracking and Ground-Based Navigation: Precision System Temperature Measurements at Goldstone

M. S. Reid, R. A. Gardner, and A. J. Freiley
Communications Elements Research Section

The system operating noise temperature performance of the low-noise research cones at the Goldstone Deep Space Communications Complex is reported for the period October 1, 1972 through January 31, 1973. System temperatures are reported for the S-band radar operational cone at DSS 13, the S-band megawatt transmit cone, and the polarization diversity S-band cone at DSS 14. In addition to these measurements, system temperature calibrations and antenna elevation profiles are reported for the 26-m-diam antenna at DSS 13 with and without the quadripod, and for the 64-m-diam antenna at DSS 14 at S- and X-bands with and without the reflex feed system.

The system operating noise temperature performance of the low-noise research cones at the Goldstone Deep Space Communications Complex is reported for the period October 1, 1972 through January 31, 1973. Most of the operating noise temperature calibrations were performed with the ambient termination technique[1] (Ref. 1). System temperature measurements were made on the following cones:

(1) S-band radar operational (SRO) cone, with maser serial number 96S5 (superconducting magnet) located in the cone, before intensive noise burst investigations began, at DSS 13.

(2) S-band megawatt transmit (SMT) cone, with maser serial number 96S4 located in the cone, before the tricone was reconfigured into a reflex feed system, at DSS 14.

The averaged operating noise temperature calibrations for the SRO and SMT cones are summarized in Table 1. All data for the SMT cone were taken at 2295 MHz with the subreflector correctly aligned. All of the above calibration data were reduced with JPL computer program

---

[1] Most of these measurements were taken by DSS 13 (Venus) and DSS 14 (Mars) personnel.

5841000, CTS20B. Measurement errors of each data point average are recorded under the appropriate number in the tables. The indicated errors are the standard deviation of the individual measurements and of the means, respectively. They do not include instrumentation systematic errors. The averages were computed using only data with:

(1) Antenna at zenith.

(2) Clear weather.

(3) No RF spur in the receiver passband.

(4) Standard deviation of computed operating noise temperature due to measurement dispersion less than 0.15 K.

Figure 1 is a plot of system operating noise temperature of the SRO cone at 2278.5 MHz as a function of time in day numbers for this reporting period. In this figure data that satisfy the four conditions stated above are plotted as solid circles, while data that fail one or more conditions are plotted as open circles. Figure 2 is a similar plot which collects into one graph all of the available averaged system temperature calibrations for the SRO cone at 2278.5 MHz for the whole of calendar year 1972. It may be seen from Fig. 2 that during September the system temperature decreased on the average by more than 1 K. Table 1 shows that the average system temperature for the SRO cone at 2278.5 MHz for this reporting period, which started on October 1, 1972, was 14.9 K. This must be compared with the previous reporting periods for 1972 when the averages were: 16.4 K for June through September (Ref. 2), and 16.1 K for February through May (Ref. 3). Two changes were made to the system in September, both of which were expected to decrease the system temperature. The antenna surface was retaped, and the input section to the maser was rebuilt to counteract instabilities. The antenna retaping was expected to improve the system temperature by probably less than 0.5 K. Since the total system temperature improvement was approximately 1 K (see Fig. 2), this implies that the improvement due to the rebuilt maser input section was approximately 0.5 K.

Figure 3 is a plot of all available data for the SMT cone, both low-noise path with maser 96S4 located in the cone, and diplexed with maser 80S1 in the Mod-3 section. System temperature is plotted against time in day numbers and date for CY 1972. Figure 4 is a similar plot of all the polarization diversity S-band (PDS) cone data, both low-noise path and diplexed, for CY 1972. All data in Figs. 3 and 4 were taken at 2295 MHz. In these two figures the averaged precision measurements reduced by computer program CTS20B have been augmented by single Y-factor numbers. These data, however, were all taken with the ambient termination Y-factor method with the antenna at zenith, the subreflector correctly positioned in each case, but with no regard for weather conditions.

The subreflector and quadripod were removed from the 26-m-diam antenna at DSS 13 during November 1972. System temperature calibrations were made while the antenna, without quadripod, was pointed at zenith. These measurements were made by the Y-factor technique of switching to the ambient termination as well as using a microwave absorber over the horn. Additional data were supplied by using the Noise-Adding Radiometer (Ref. 4). All data were taken with maser 96S5 located in the SRO cone during clear weather conditions. Table 2 is a summary of the averaged system temperatures at the three operating frequencies.

Figure 5 shows antenna elevation profiles measured during October and November 1972, prior to and after the removal of the quadripod. System temperature is plotted as a function of antenna elevation angle. These data were measured with the Noise-Adding Radiometer. The solid curve was obtained prior to the quadripod removal at 2295 MHz and data points are shown for 2278.5, 2295, and 2388 MHz with no quadripod. All data in Fig. 5 were taken at 90-deg azimuth.

Figure 6 shows two antenna elevation profiles made with no quadripod on the antenna, both at 2296 MHz and 90-deg azimuth. The one curve shows data repeated from Fig. 5 for reference, and the second curve shows the profile obtained when a large reflector plate was mounted over the horn in order to direct the antenna beam over the edge of the parabola approximately at right angles to the antenna boresight axis.

The tricone system on the 64-m antenna at DSS 14 was rebuilt during January 1973. The new tricone consists of a reflex feed system to allow simultaneous S-band and X-band operation as required for the Mariner Mars 1973 S/X experiment (Refs. 5 and 6). This reflex feed system is sufficiently versatile that the reflector and dichroic plate can be retracted for normal station operation in the prereflex mode. System temperature measurements were made in January 1973 at S- and X-bands, both with the reflex feed system and with the reflex feed system retracted. These system temperature calibrations were made using the Noise-Adding Radiometer in clear weather conditions.

The lower half of Fig. 7 shows antenna elevation angle profiles at 2295 MHz with and without the reflex feed system. The cone in use was the SMT, and data are plotted as system temperatures in K versus antenna elevation angle in degrees, with the elliptical reflector extended and retracted. It must be noted that at low elevation angles the system temperature is lower in the reflex condition than it is in the original configuration. This may be seen in the upper half of Fig. 7, where the differential system temperature has been plotted as a function of elevation angle. The differential temperature is 3 K below 10-deg elevation.

Antenna elevation profiles have been plotted in Fig. 8 for 8415 MHz. These measurements were made using the multi-frequency X- and K-band (MXK) cone with the dichroic plate extended and retracted. The system operating noise temperature at 8415 MHz with the antenna at zenith is 20 K for the original system and 21.5 K for the reflex feed system.

References

1. Stelzried, C. T., "Operating Noise-Temperature Calibrations of Low-Noise Receiving System," *Microwave J.*, Vol. 14, No. 6, pp. 41–48, June 1971.
2. Reid, M. S., "Improved RF Calibration Techniques: System Operating Noise Temperature Calibrations," in *The Deep Space Network Progress Report,* Technical Report 32-1526, Vol. XII, pp. 83–87. Jet Propulsion Laboratory, Pasadena, Calif., Dec. 15, 1972.
3. Reid, M. S., "Improved RF Calibration Techniques: System Operating Noise Temperature Calibrations," in *The Deep Space Network Progress Report,* Technical Report 32-1526, Vol. X, pp. 123–128. Jet Propulsion Laboratory, Pasadena, Calif., Aug. 15, 1972.
4. Batelaan, P. D., Goldstein, R. M., and Stelzried, C. T., "A Noise-Adding Radiometer for Use in the DSN," in *The Deep Space Network,* Space Programs Summary 37-65, Vol. II, pp. 66–69. Jet Propulsion Laboratory, Pasadena, Calif., Sept. 30, 1970.
5. Levy, G. S., "Microwave Dual Frequency Propagation Experiment Using the Mariner Venus Mercury Probe," *Proceedings of the Symposium on the Future Application of Satellite Beacon Measurements,* GRAZ, pp. 9–13, June 1972.
6. Potter, P. D., "S- and X-Band RF Feed System," in *The Deep Space Network Progress Report,* Technical Report 32-1526, Vol. VIII, pp. 53–60. Jet Propulsion Laboratory, Pasadena, Calif., Apr. 15, 1972.

Table 1. System operating noise temperature calibrations of the SRO and SMT cones

Cone and Station	SRO, DSS 13			SMT, DSS 14	
Maser serial number and configuration	96S5			80S1 Mod-3 section diplexed	96S4 Low-noise path
Frequency, MHz	2278.5	2295	2388	2295	2295
Maser gain (dB)	45.3 ±0.71/0.15 22 measurements	41.8 1 measurement	31.9 1 measurement	No measurements	47.8 ±0.85/0.60 2 measurements
Follow-up receiver contributions, K	0.29 ±0.03/0.01 18 measurements	0.45 1 measurement	0.59 1 measurement	0.10 1 measurement	0.10 1 measurement
System operating noise temperature, K	14.9 ±0.22/0.05 18 measurements	14.5 ±0.18 1 measurement	16.4 ±0.20 1 measurement	26.3 ±0.28 1 measurement	15.7 ±0.19 1 measurement

Table 2. Averaged system temperatures of SRO cone on 26-m antenna at DSS 13 with no quadripod, Nov. 1972

Frequency, MHz	Follow-up receiver contribution, K	System temperature, K
2278.5	0.3	11.6
2295	0.5	11.6
2388	0.7	13.4

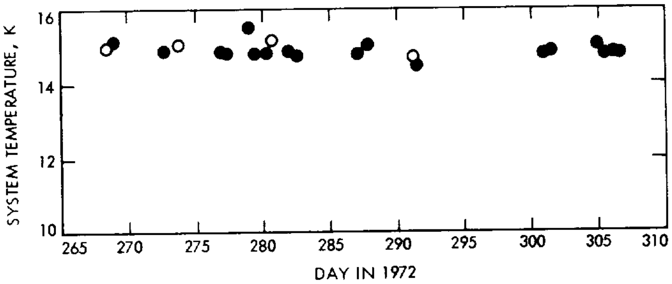

Fig. 1. System operating noise temperature calibrations of the SRO cone at 2278.5 MHz plotted as a function of time in day numbers

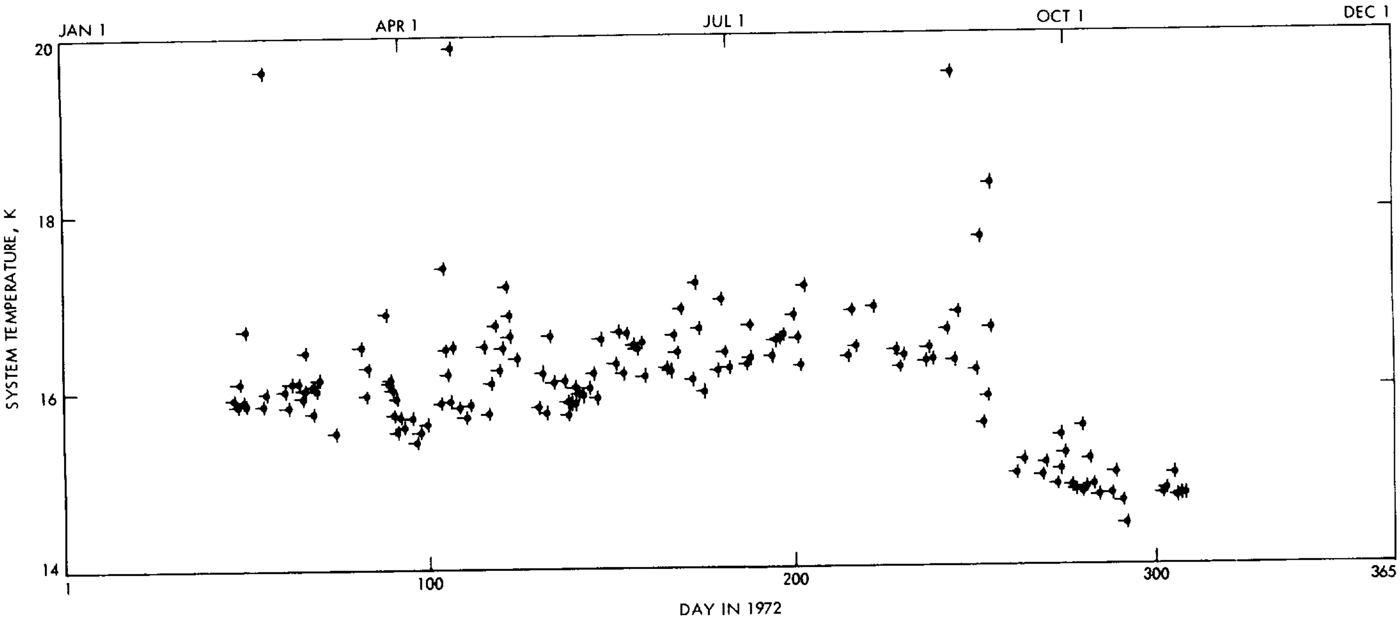

Fig. 2. System operating noise temperature calibrations of the SRO cone at 2278.5 MHz plotted as a function of time for CY 1972

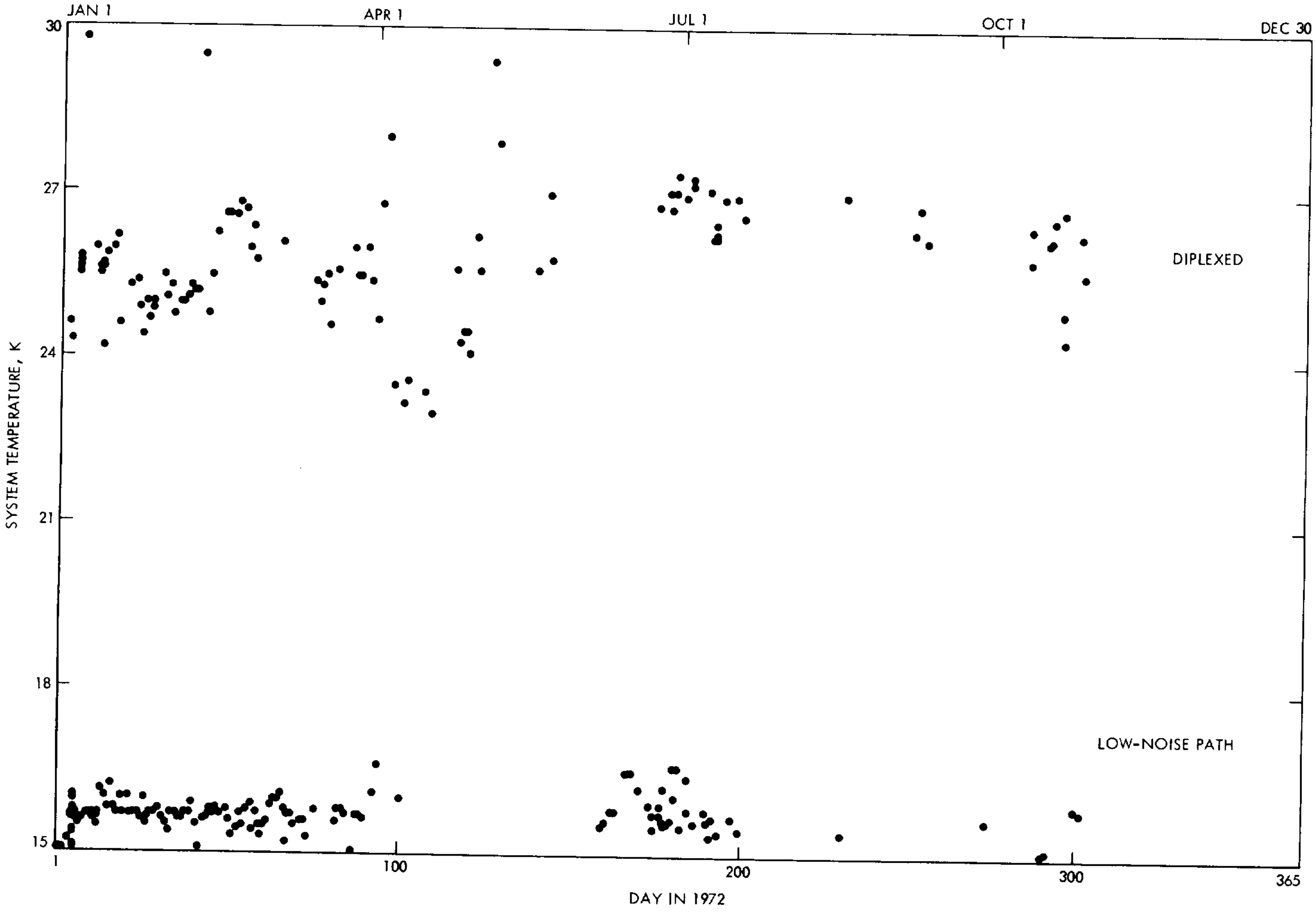

Fig. 3. System operating noise temperature calibrations of the SMT cone at 2295 MHz plotted as a function of time for CY 1972

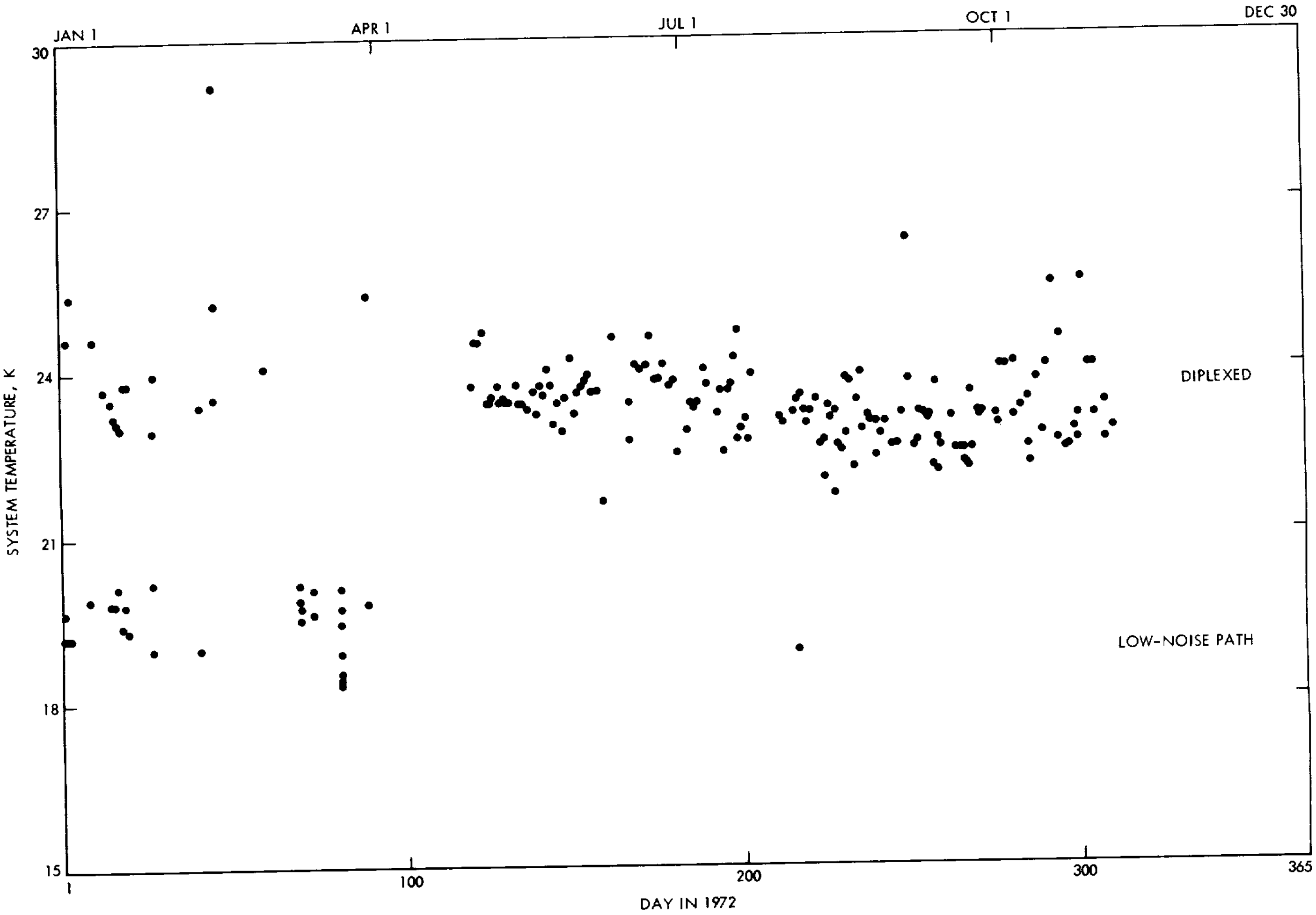

Fig. 4. System operating noise temperature calibrations of the PDS cone at 2295 MHz plotted as a function of time for CY 1972

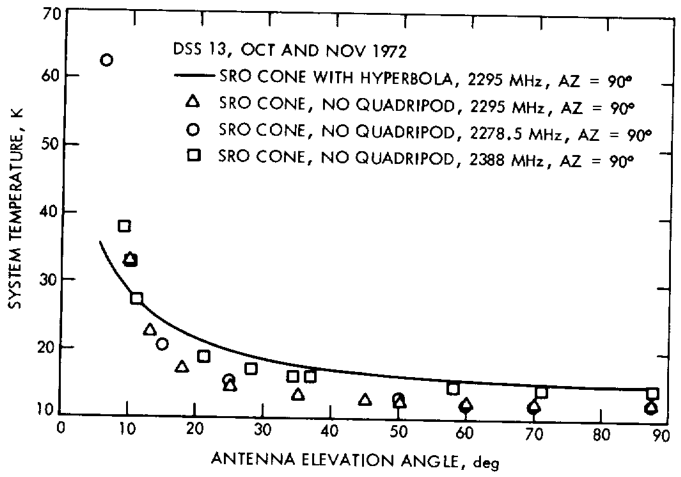

Fig. 5. Antenna elevation profiles of SRO cone with and without the quadripod

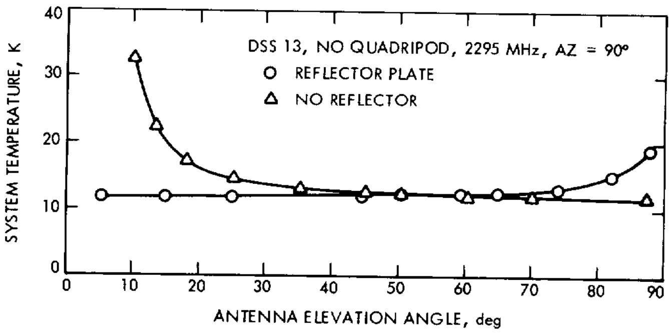

Fig. 6. Antenna elevation profiles of SRO cone with and without the reflector plate, with no quadripod

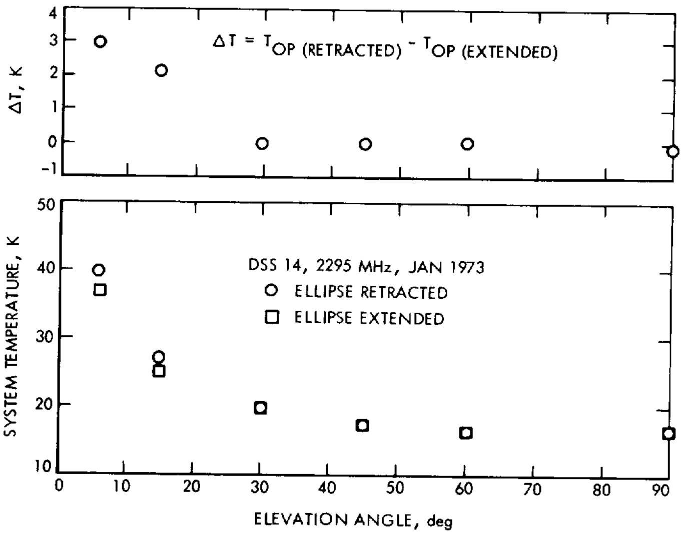

Fig. 7. Antenna elevation profiles of SMT cone with and without the reflex feed system, and the differential system temperatures

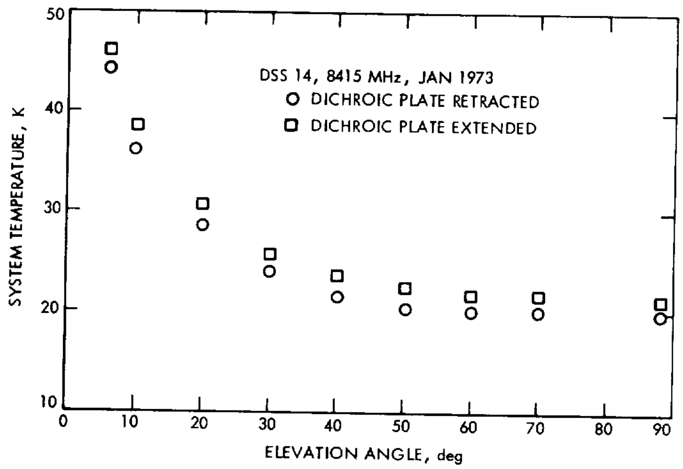

Fig. 8. Antenna elevation profiles of MXK cone with and without the dichroic plate

64-m-Diameter Antenna: Computation of RF Boresight Direction

M. S. Katow
DSIF Engineering Section

With the addition of the new "kickers" on the 64-m-diameter antenna, fore knowledge of any change in the RF boresight direction errors due to gravity loadings would be of operational value. Using ray tracing techniques, the before and after boresight errors are computed and the configurations documented by line sketches of the RF surfaces with a table of linear and angular deflections. This method of analysis indicates that the RF boresight direction with respect to the intermediate reference surface will have lower deviations after the modifications.

I. Introduction

To meet the RF boresight pointing specifications for gravity loading of the 64-m-diameter antenna, the manufacturer's (Rohr Corp.) engineer developed algorithms to compute the RF boresight direction with respect to the intermediate reference surface (IRS) mounted in the hub of the reflector structure (Ref. 1). Data on the deflected positions of the phase centers were combined with the position of the best-fitted paraboloid (Ref. 2) to the distorted surface of the main reflector by ray tracing to determine the boresight direction errors. Its computed prediction of small boresight error for the gravity loading case was attained for operational purpose.

An independent determination of the boresight errors was made at JPL, comparing answers from computed and field measured data (Ref. 2). Now, with the forthcoming structural modifications of new "kickers" to be added to the 64-m-diameter antenna, computed predictions of the boresight errors may be of operational value.

This reporting documents the computed RF boresight errors for gravity loading on the Tricone 64-m-diameter antenna before and after the modifications. Future reporting will be made to compare computed data to the field tested data when the field data become available.

II. Descriptions

Figure 1 illustrates the RF reflecting surfaces at the alignment position of 45 deg elevation angle. The hyperboloid system is shown on the symmetric axis of the paraboloid although in the actual Tricone configuration the axes are separated by 4° 31′ of arc.

Figures 2 and 3 illustrate the deflected positions at zenith look. The symbols used on these figures are defined in Table 1 and as follows:

A, B	quadripod base
A_2, B_2	deflected quadripod base
C	paraboloid vertex
C_2	deflected paraboloid vertex
C_3	vertex: best fit paraboloid
F	paraboloid focus point
F_2	deflected hyperboloid virtual focus point
F_3	deflected phase center virtual focus point
F_4	focus: best fit paraboloid
H	hyperboloid vertex align position
H_2	deflected hyperboloid vertex
P	primary phase center
P_2	hyperboloid primary focus point
P_3	deflected primary phase center

The ray tracing starts from the RF feed's phase center P_3, which results in the refracted position of the virtual focus at F_3. At present, a unity factor is used for this refraction calculation until better data become available. Then the ray from F_3 is reflected from the vertex of the best fit paraboloid and the boresight direction is shown by the angle δ in Fig. 4. A reflection factor of 0.83 obtained from the results of reflection calculations in the radiation program (Ref. 3) is used. The boresight error with respect to the IRS is then equal to ϕ minus δ.

Since the reporting of Ref. 2, the structural model has been improved by using 1/2 of the reflector instead of 1/4, with some bending members included.

III. Conclusions

The computed answers are deliniated in Table 1. The best sources of data were used for these cases.

From the computed cases, at least for gravity loadings, the RF boresight direction errors are predicted to be lower after adding new "kickers" to the 64-m-diameter antenna.

The horizon look values were not computed because the field measurement data with respect to the hyperboloid for some unexplained reason were not linear. However, on the linear basis, the pointing error should change in sign for direction and compute in value about 40% of the zenith value for the 45-deg alignment position.

References

1. Isber, A. M., "Obtaining Beam-Pointing Accuracy with Cassegrain Antennas," *Microwaves*, Aug. 1967.
2. Katow, M. S., and Schmele, L. W., "Antenna Structures: Evaluation Techniques of Reflector Distortions" in *Supporting Research and Advanced Development*, Space Programs Summary 37-40, Vol. IV, pp. 176–184. Jet Propulsion Laboratory, Pasadena, Calif., Aug. 31, 1966.
3. Katow, M. S., "210-Ft.-Antenna Quadripod Structural Analysis, II" in *The Deep Space Network*, Space Programs Summary 37-53, Vol. II, pp. 73–76. Jet Propulsion Laboratory, Pasadena, Calif., Sept. 30, 1968.
4. Bathker, D., "Radiation Pattern Programs" in *Computer Programs for Antenna Feed System Design and Analysis*, Vols. I and II, Technical Report 32-479. Edited by A. Ludwig. Jet Propulsion Laboratory, Pasadena, Calif., Apr. 15, 1967.

Table 1. Gravity deflection data: 64-m-diameter antenna

Part	Deflection symbol		Deflection description	Zenith look, aligned 45° elevation offsets					
				Standard structure			Modified kicker		
	Angular	Linear		Angle, rad	Linear, cm	Linear, (in.)	Angle, rad	Linear, cm	Linear, (in.)
Primary feed	–	UU	Hub translation[a]	–	0.80	0.316	–	0.75	0.294
	γ	SS	Primary phase center[b]	−0.001119	2.26	0.891	−0.000924	1.95	0.769
Hyperboloid system	–	RR	Primary hyperboloid focus[b]	–	5.09	2.004	–	4.82	1.898
	Ω	QQ	Hyperboloid vertex[b]	0.001286	12.93	1.549	0.001425	3.56	1.402
	–	OO	Virtual hyperboloid focus[b]	–	3.63	1.431	–	3.23	1.271
	–	TT	Primary feed offset[b]	–	2.83	1.113	–	2.87	1.129
	–	PP	Virtual hyperboloid focus offset[b]	–	0.58	0.2271	–	0.58	0.230
Paraboloid system	–	VV	Best fit paraboloid[a] (vertex offset)	–	−10.96	−4.316	–	−12.91	−5.082
	θ	MM	Best fit paraboloid[a] (focus point offset)	−0.002612	13.50	2.789	−0.002818	7.64	3.008
	α	NN	Incidence[a]	−0.002558	6.94	2.731	−0.002918	7.91	3.115
Elevation pointing error	β	–	Reflection angle[a]	0.002123	–	–	0.002422	–	–
	δ	–	Boresight angle[a]	−0.000489	–	–	−0.000396	–	–
	ϕ	–	IRS position[a]	−0.0006431	–	–	−0.000446	–	–
	$\phi - \delta$	–	Boresight error	−0.000154 (−0.009 deg)	–	–	−0.000050 (−0.003 deg)	–	–

[a] Primary data source: computed.

[b] Primary data source: field measurement (+ computed for modified kicker).

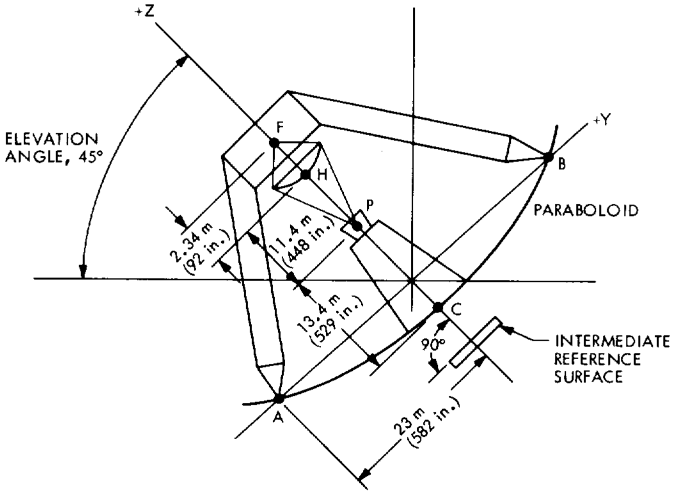

Fig. 1. RF geometry at allignment elevation

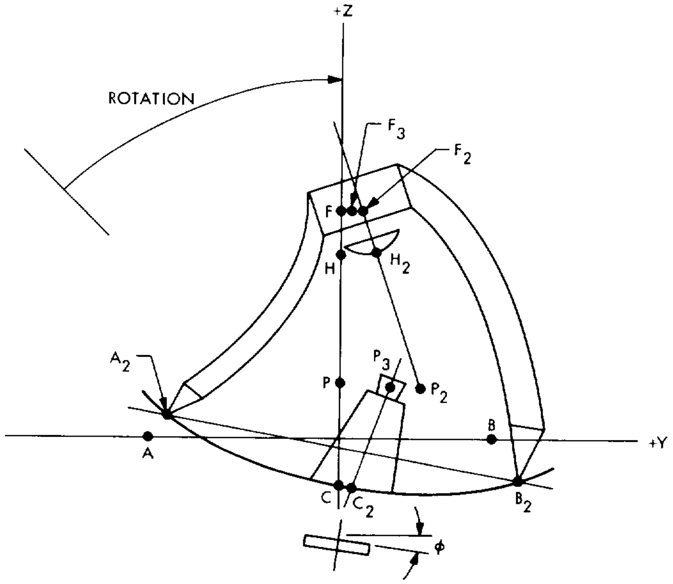

Fig. 2. Deflected RF geometry at zenith look

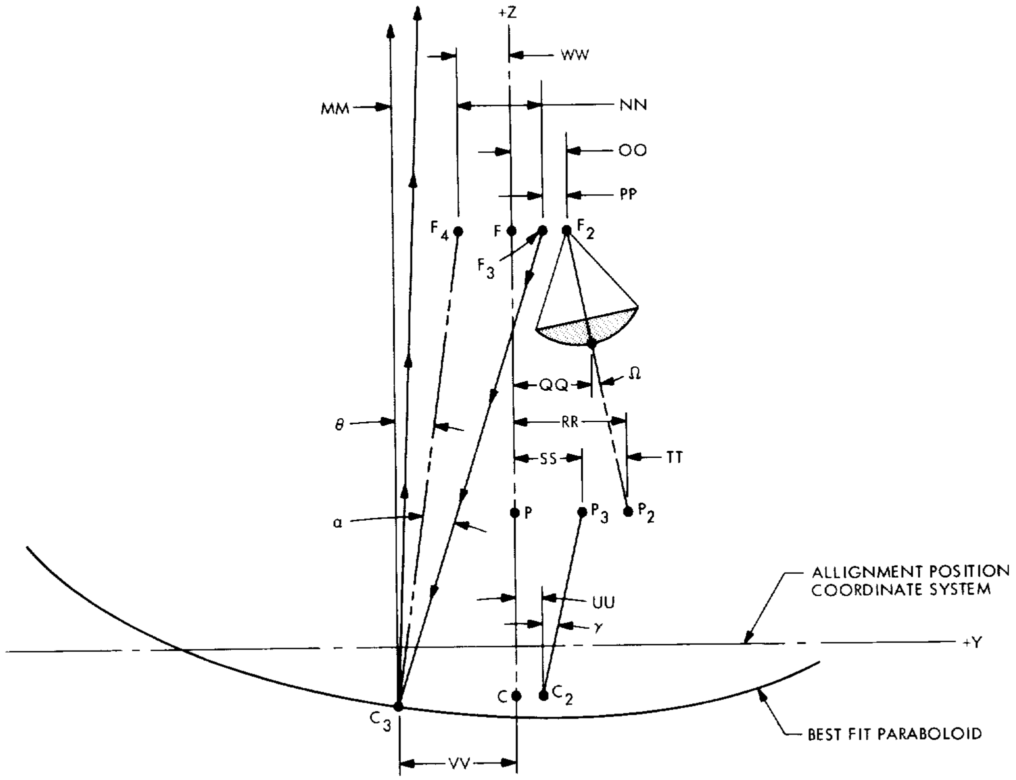

Fig. 3. RF geometry with the best fit paraboloid

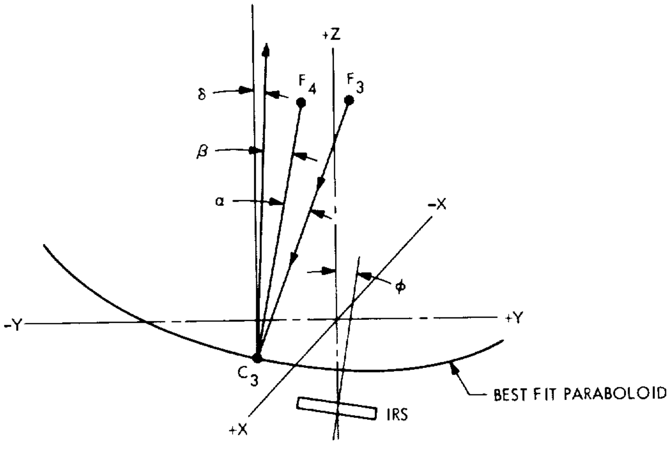

Fig. 4. RF boresight pointing error

S/X-Band Experiment: Zero Delay Device

T. Y. Otoshi and P. D. Batelaan
Communications Elements Research Section

A zero delay device currently being developed for the S/X band experiment is described. Preliminary group delay and transmission coefficient phase data are presented for some of the components in the zero delay device.

I. Introduction

The S/X band experiment to be performed with the Mariner Venus-Mercury 1973 spacecraft is a dual-frequency experiment to measure the electron content of the interplanetary media between Earth and the planets Venus and Mercury (Ref. 1). An uplink signal of approximately 2113 MHz will be transmitted to the spacecraft from the 64-m diam antenna at DSS 14. This uplink signal as received by the spacecraft radio system will be coherently multiplied by ratios of 240/221 and 880/221 to produce S- and X-band carrier frequencies of approximately 2295 and 8415 MHz. The coherent S- and X-band signals will then be transmitted back to the DSS 14 ground system. A measurement of the dispersiveness of the S- and X-band phase and range (or group delay) data as received back at the ground station provides scientific information required for determining total interplanetary electron content.

To calibrate group delay which is due only to the ground antenna system, a zero delay device (ZDD) is used. This device is physically installed on the ground antenna and permits group delay of the ground system to be calibrated as a function of antenna pointing direction and ambient temperatures. This article describes the ZDD which is currently being developed for the S/X experiment. Preliminary group delay and phase data on some ZDD components are also presented.

II. Description of the S/X ZDD

Figure 1 shows a simplified block diagram of the ZDD calibration system. The ZDD assembly will be installed in a low profile position on the side of the Mod-III section of the 64-m diam antenna at DSS 14. A reference 2113-MHz carrier with range-code modulation from the Mu-2 ranging machine and Block IV exciter assembly is fed into a 400-kW klystron amplifier. The amplified 2113-MHz signal is transmitted through the S-band megawatt transmit (SMT) cone microwave system and then radiated out of the SMT cone horn. A small fraction of the signal reflected from the subreflector is received by the ZDD

S-band horn. This received 2113-MHz signal is mixed with coherent 182 and 6302 MHz local oscillator frequencies provided by the Block IV exciter. As a result of mixing, down-link test signals of approximately 2295 and 8415 MHz are generated and radiated out of the ZDD S- and X-band horns back toward the subreflector. These down-link signals are received by the X-band (multiple-frequency X- and K-band (MXK) cone) and S-band (SMT cone) microwave systems. The microwave systems are followed by Block IV receivers and a Mu-2 ranging system which extract the desired S/X range information.

In essence, the function of the ZDD is to simulate a stationary spacecraft which is located on the ground antenna itself. For the S/X experiment, the ZDD will purposely be installed on the side of the Mod-III section. This location permits transmission line lengths between the ZDD and Block IV exciter to be kept physically short, and therefore, help minimize possible temperature effects on differential S/X phase and group delays.

Figure 2 is a preliminary detailed block diagram of the ZDD assembly. The ZDD assembly includes such components as S- and X-band horns, remotely controllable switches and step attenuators, mixers, and a band-pass filter. In order to have a reliable ZDD system, it is necessary that the individual components be electrically stable with regard to carrier phase and group delay. Some of the ZDD components were tested for group delay and phase stability as functions of ambient temperatures. The results are summarized in the following.

III. Test Results

A Hewlett-Packard Model 8542A automatic network analyzer was used to measure group delays and transmission coefficient phase. As described in Ref. 2, group delay can be determined from the slope of the transmission coefficient phase versus frequency characteristic curve. The advantages of using this network analyzer system are: (1) rapid and inexpensive data taking and (2) good accuracies achieved because calibration corrections are automatically applied by a computer. The tests were performed by the Western Automatic Test Service (WATS) of Palo Alto, California.

Figure 3 shows a remotely controllable step attenuator manufactured by Weinschel Engineering of Gaithersburg, Maryland. The attenuation of this device can be changed in 1-dB increments over a total dynamic range of 69 dB. Test data at pertinent S/X frequencies are summarized in Table 1. The group delay results shown are typical of data obtained over an S-band frequency range of 2000 to 2500 MHz and an X-band frequency range of 8000 to 9000 MHz. Significant test results of this device can be summarized as follows:

(1) The group delay is essentially the same at S- and X-band frequencies. In addition, the group delay is independent of attenuation setting.

(2) The transmission coefficient phase is somewhat dependent upon attenuation setting.

(3) Based on three sets of measurements in the attenuation range of 0 to 40 dB, the measured group delay values repeated to within 0.01 ns. Measured phase values repeated to within 0.1 and 0.3 deg at S- and X-band frequencies, respectively.

Figure 4 shows a remotely controllable broadband coaxial switch manufactured by Hewlett-Packard Company at Palo Alto. Test data at pertinent S/X frequencies are presented in Table 2. The group delay test results shown are typical of those obtained over the S-band frequency range of 2000 to 2500 MHz and those obtained over the X-band frequency range of 8000 to 9000 MHz. Based on the test results, it was found that for this device: (1) the group delay was essentially the same at both S- and X-band frequencies, (2) the group delay and phase values vary only slightly over the ambient temperature range of 4.4°C (40°F) to 37.8°C (100°F), and (3) based on three sets of measurements, the group delay nominal values of Table 2 repeated to within 0.01 ns and phase values typically to within 0.2 deg.

Figure 5 shows a 2113-MHz coaxial bandpass filter manufactured by Telonic Industries of Laguna Beach, California. This filter has a 3-dB bandwidth of 400 MHz. Its purpose is to filter out possible harmonic products that could be generated by the X-band mixer and reradiated out the ZDD S-band horn. Table 3 shows the test results over the filter passband. Properties of this filter can be summarized as follows: (1) the group delay varies about 1 ns in the 400-MHz passband and (2) group delay and phase data variations with temperature are small over the ambient temperature range of 4.4°C (40°F) to 37.8°C (100°F). It is also of interest to note that the group delay of 2 ns for the filter in the passband is about 7.5 times greater than the group delay of an air-dielectric coaxial line having the same physical length (8 cm) as the filter.

IV. Conclusions

Preliminary group and phase delay data have been presented for some components being installed in the ZDD assembly. It was found that for broadband coaxial devices such as the step attenuator and coaxial switches, the group delays were essentially the same at both S- and X-band frequencies. Variations of group delay and phase with ambient temperatures were negligibly small over the temperature ranges of 4.4°C (40°F) to 37.8°C (100°F).

References

1. Levy, G., Dickinson, R., and Stelzried, C., "RF Techniques Research: S/X Band Experiment," in *Supporting Research and Advanced Development*, Space Programs Summary 37-61, Vol. III, pp. 93–95, Jet Propulsion Laboratory, Pasadena, Calif., Feb. 20, 1970.
2. Adams, S. F., *Microwave Theory and Applications*, pp. 428–429, Prentice-Hall, Inc., Englewood Cliffs, N.J., 1969.

Table 1. Test data for Weinschel Model AE 97-69-3 step attenuator

Attenuator setting, dB	Group delay, ns			Estimated error limits, ns	Transmission coefficient phase, deg			Estimated error limits,[a] deg
	2110 MHz	2300 MHz	8420 MHz		2110 MHz	2300 MHz	8420 MHz	
0	0.93	0.95	0.93	±0.12	4.9	−59.7	30.0	±0.4
1	0.95	0.97	0.95		−2.6	−68.0	−0.4	
2	0.94	0.96	0.95		−0.7	−65.6	7.3	
3	0.94	0.96	0.96		−1.0	−66.1	5.7	
4	0.94	0.96	0.94		−0.7	−65.6	7.0	
5	0.93	0.96	0.96		−0.6	−65.6	7.6	
6	0.94	0.98	0.96		−0.2	−65.0	9.2	
7	0.94	0.96	0.95		0.4	−64.2	10.0	
8	0.93	0.97	0.96		1.5	−63.2	14.3	
9	0.94	0.97	0.95		0.2	−64.5	11.2	
10	0.96	0.98	0.96	±0.13	−14.3	−80.6	−46.4	±0.5
20	0.96	0.99	0.96	±0.14	−10.9	−77.1	−34.1	±0.5
30	0.98	1.00	0.99	±0.16	−18.6	−85.4	−68.5	±0.6
40	1.00	0.99	0.97	±0.22	−16.8	−83.7	−54.6	±0.8
50	1.06	1.03	1.07	±0.33	−35.5	−102.8	−129.9	±1.2
60	1.3	1.1	1.1	±0.67	−29.5	−98.6	−114.6	±2.4

[a] Manufacturer's specs on the HP 8542A automatic network analyzer.

Table 2. Test data for HP 8761A coaxial switch

Frequency, MHz	Group delay, ns			Transmission coefficient phase, deg		
	4.4°C (40°F)	21.1°C (70°F)	37.8°C (100°F)	4.4°C (40°F)	21.1°C (70°F)	37.8°C (100°F)
Port 1 to C						
2110	0.24	0.23	0.24	−164.4	−164.6	−164.5
2300	0.21	0.21	0.21	−178.9	−179.2	−179.1
8420	0.22	0.22	0.22	66.3	65.3	65.7
Port 2 to C						
2110	0.24	0.24	0.23	−164.4	−164.4	−164.5
2300	0.21	0.21	0.21	−178.9	−179.0	−179.1
8420	0.22	0.22	0.22	66.3	65.8	65.8

Table 3. Test results for Telonic TBP 2114-400-4EF1 bandpass filter

Frequency, MHz	21.1°C (70°F) Insertion loss, dB	Group delay, ns			Transmission coefficient phase, deg		
		4.4°C (40°F)	21.1°C (70°F)	37.8°C (100°F)	4.4°C (40°F)	21.1°C (70°F)	37.8°C (100°F)
1750	10.5	–	1.46	–	–	142.2	–
1800	5.5	–	2.19	–	–	110.6	–
1850	1.6	–	2.71	–	–	63.2	–
1910	0.42	2.32	2.37	2.39	2.2	4.1	5.0
2000	0.47	2.00	2.03	2.00	−65.7	−64.8	−64.2
2100	0.53	2.02	2.03	2.03	−137.8	−137.2	−136.9
2200	0.47	2.22	2.21	2.21	146.2	146.4	146.6
2290	0.80	3.22	3.24	3.23	62.9	62.7	62.9
2350	4.7	–	3.13	–	–	−15.5	–
2400	11.7	–	2.04	–	–	−62.4	–

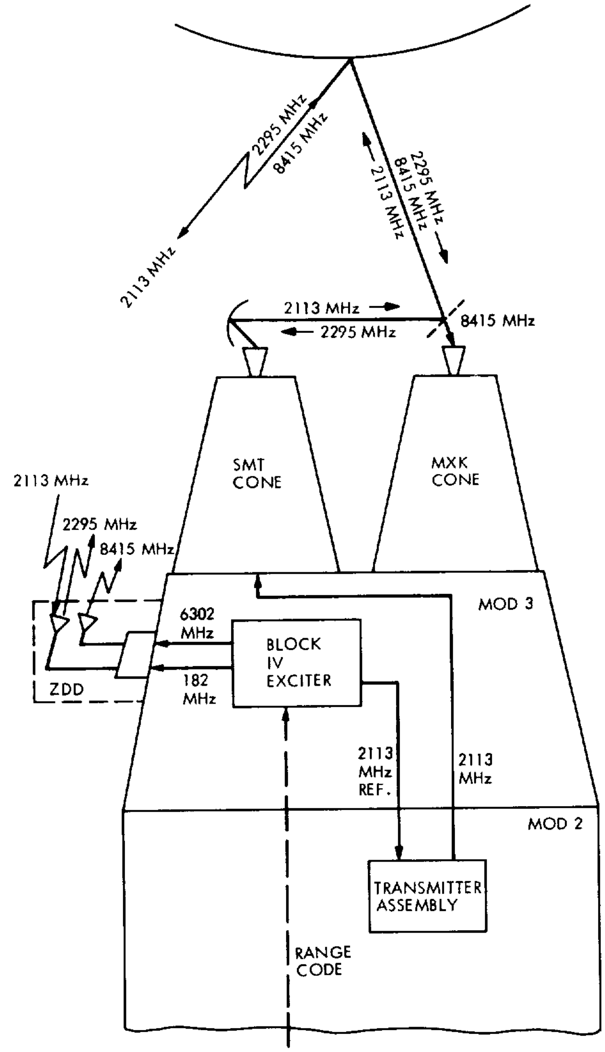

Fig. 1. Simplified block diagram of ZDD calibration system for S/X experiment

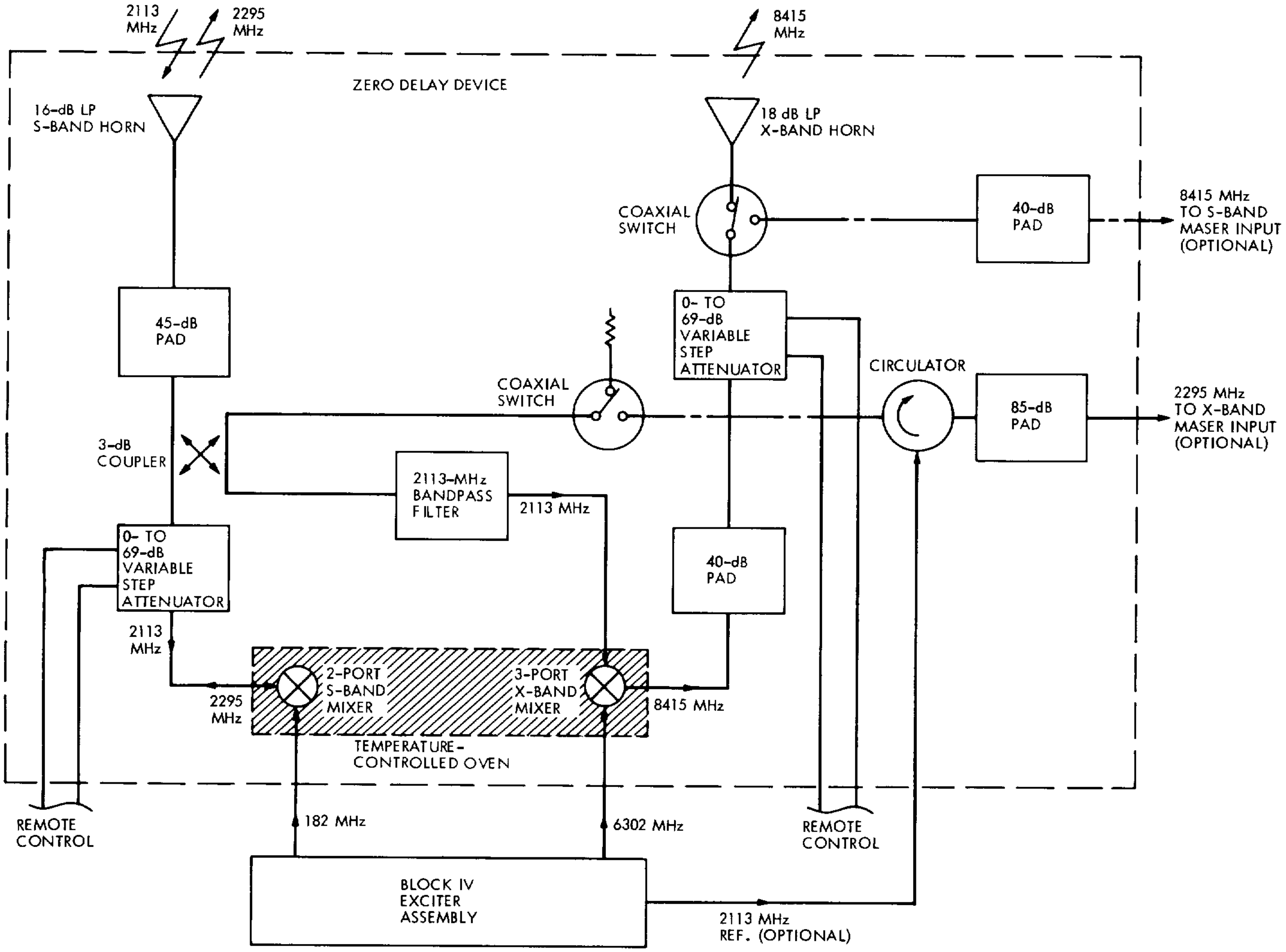

Fig. 2. Preliminary block diagram of ZDD assembly

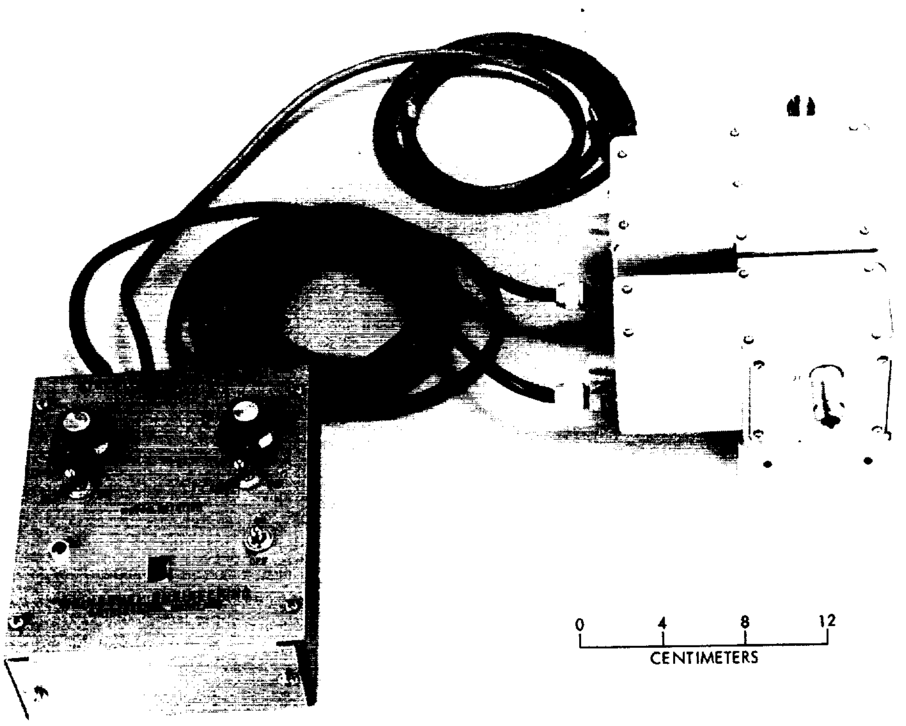

Fig. 3. Remotely controllable coaxial step attenuator, Weinschel Engineering Model AE 97-69-3

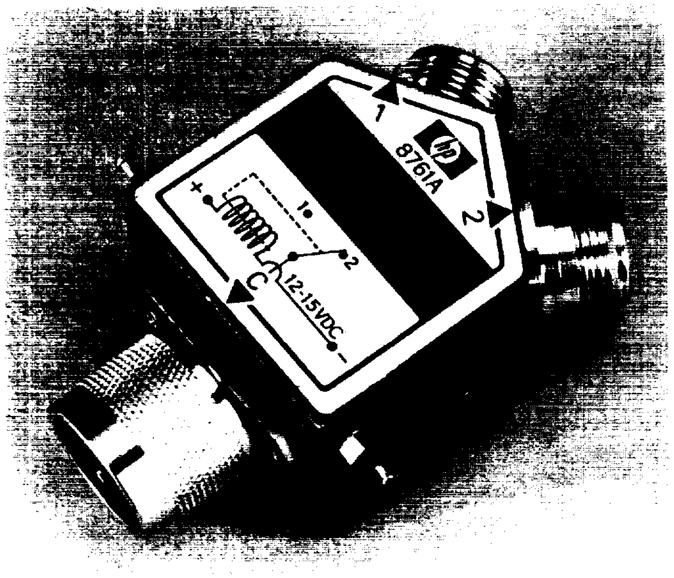

Fig. 4. Remotely controllable coaxial switch, Hewlett-Packard Model HP 8761A

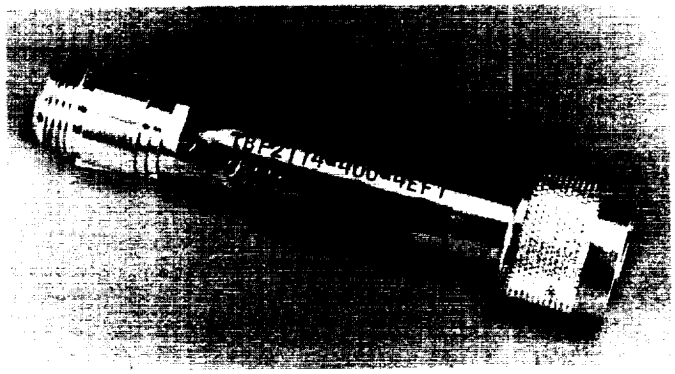

Fig. 5. Coaxial 2113-MHz bandpass filter, Telonic Industries Model TBP 2114-400-4EF1

A Comparison Between the Current and Proposed Inventory and Procurement Policies for the Deep Space Network

I. Eisenberger and F. R. Maiocco
Communication Systems Research Section
G. Lorden
California Institute of Technology

A comparison is made between the performance of a proposed policy and that of the current inventory and procurement procedures for the Network Supply Depot and the Complex Supply Facilities. Both procedures were simulated on a computer using identical input demand data. The comparison is based on four criteria: average inventory level, frequency of procurement orders, frequency of shortages and average inventory cost per year. The results of the study indicate that, with reference to maintenance and operating items, the inventory cost would be reduced by about 25% if the proposed policy were put into effect.

I. Introduction

The purpose of this article is to present the results of a computer simulation that compares the performance of a proposed policy (Ref. 1) to that of the current inventory and procurement procedure for the Network Supply Depot (NSD) and the Complex Supply Facilities (CSFs). Subsection II describes how the simulation program operates. Subsection III describes the operation of both the proposed policy (Method 1) and the current inventory and procurement policy (Method 2), and Subsection IV summarizes the simulation results.

It should be noted that in our preparation of a simulated global inventory system, no attempt was made to duplicate the overall software package of the Integrated Logistic System described in Ref. 2. Also no attempt was made to incorporate the numerous software tasks of the current Supply Inventory System as discussed in Ref. 3. The specific features simulated in this investigation were the determination of order sizes and reorder levels, and the procurement and shipping tasks of an inventory system.

The criteria for inventory performance used in the simulation are the same ones used in Ref. 1. These criteria are:

(1) Average inventory level (NSD and CSFs combined).

(2) Frequency of procurement orders.

(3) Frequency of shortages.

(4) Average inventory cost per year.

The average inventory cost per year is computed using cost parameters h and k. The parameter h is the *holding cost* per unit per year, i.e., the cost resulting from buying one unit a year in advance of the demand and maintaining it in inventory. Values of h between 5 cents and 2 dollars were used. The parameter k is the *order cost*, i.e. the fixed portion of the cost of placing an NSD procurement order. The value of k was taken to be 5 dollars in all the simulation runs performed. Varying k along with h is unnecessary since the actions of Methods 1 and 2 depend only on the ratio of h and k. As the description in Subsection III indicates, the actions of Method 2 are unaffected by h and k, being based entirely on estimated demand rates.

Penalty costs for shortages were not considered in the present investigation since it is not feasible to assign a dollar cost to the possible consequences of maintenance and operations (M & O) items shortages, such as loss of tracking station operational availability and loss of n kilobits of data. The criticality of shortages is expressed, instead, by a parameter q called the *cost-criticality quantile* (Ref. 1). It denotes the probability of incurring no shortage at a given CSF during one order cycle. The value of this parameter can be adjusted to achieve an acceptably low frequency of shortages. The higher the quantile q, the higher the CSF minimum stockage levels. Thus, as q is increased up to 1, the frequency of shortages is reduced to zero, but at the cost of higher inventory levels and costs.

II. How the Simulation Program Operates

The simulation program operates in a very straightforward way. True mean demand rates for the six CSFs are input and are used to generate purely random demands for a single inventory item at the CSFs on a day-to-day basis. Thus, in the simulation, as in the real world, random fluctuations cause higher than average demand experience at some times, lower than average at other times. But the true mean demand rates used to generate the demand data remain fixed throughout a simulation run. The same day-to-day demand experienced at the CSFs is fed simultaneously to Methods 1 and 2 and they respond by taking actions of two types: placing procurement orders (which arrive at NSD in 45 days) and making shipments from NSD inventory to CSFs (which arrive in 60 days). The computer keeps track of such things as inventory levels (and backorders) at NSD and at the CSFs, shipments enroute to CSFs, and procurement orders enroute to NSD. The computer also tallies shortages (units not available from a CSFs inventory when demanded), procurement orders made by NSD, and total inventory levels in the system. All of this bookkeeping is done separately for Method 1 and Method 2. At the end of a 100-year run, the key outputs are the average (total) inventory levels for Methods 1 and 2, the number of procurement orders each method placed, and the number of shortage units each method incurred at all CSFs combined. The first two of these outputs are combined using assumed cost parameters, h and k, to yield an overall *inventory* cost for each method.

What information is supplied to determine the actions of Methods 1 and 2? Rather than let the two procedures operate with full knowledge of the true CSF demand rates, which would be unrealistic, the simulation program only allows the two methods to keep track of the CSF demand histories for the most recent three years. (The idea is that demand data more than three years old are probably of doubtful reliability in practice.) As a consequence of this 3-year data base, both methods function with continuously updated *estimates* of CSF demand rates. These estimates of annual demand rates are made simply by dividing the observed 3-year demands by 3, with one important exception. One of the key features of the proposed inventory policy is the setting of CSF minimum levels by a Bayesian estimation approach. (A discussion of the advantages of this technique is given in Ref. (4).) This approach is used in Method 1 and is based upon the same information as the straightforward demand estimates; namely, the most recent 3 years' experience. In addition to the recent demand histories, both Methods 1 and 2 base their actions on the daily-updated information about NSD and CSF inventory levels, backorders (if any), and CSF shipments and NSD procurements enroute. Thus, the two methods operate in the simulation approximately as they would in practice.

Another feature of the simulation program is the allowance it makes for demands of different order sizes occurring at the CSFs. The idea is that a CSF may experience demands not just for a single unit, but perhaps more than one unit at a time. This possibility obviously places a greater strain on CSF inventories and makes the problem of minimizing shortages more difficult. Some of the simulation runs were performed with demands of size 1, 3, and 5 occurring, some with sizes 1 and 3; most were performed with only demands of size one allowed.

III. How Methods 1 and 2 Operate

The operation of Method 1 is discussed thoroughly in Ref. 1. We give here only a brief summary to emphasize the differences from Method 2. The procurement policy incorporates the conventional economic order quantity

(EOQ) considerations, but also takes into account the fact that coordination of inventory cycles between CSFs increases efficiency. Thus, NSD procurement orders are apportioned to the CSFs based on their current inventory levels in such a way that their minimum levels will be reached at nearly the same time. The NSD order quantity is not fixed, but rather is designed in each instance to take this apportionment process into account and to achieve an optimal average time between NSD procurements. This optimal time depends on the demand rates and on the ratio of the holding cost parameter, h, to the order cost parameter, k. Like the conventional EOQ, it represents the optimal trade-off between ordering infrequently to reduce ordering costs and ordering frequently to reduce average inventory levels.

An additional feature of Method 1 is the incorporation of the *reserve policy* for NSD (Refs. 1 and 4). Under this policy, a portion of each procurement order (perhaps 10 to 20%) is placed in NSD inventory before apportioning, and shipping the remainder to the CSFs. Shortly before the end of the order cycle, this reserve supply is used to even out the imbalances between CSF inventory levels caused by random fluctuations in demand. This is done by apportioning the reserve supply among those CSFs that have the lowest inventory levels (relative to their minimum levels). The effect is to forestall the necessity for NSD reprocurement as long as possible, thereby getting the "best possible mileage" out of each NSD order quantity. Except for these reserve supplies, Method 1 maintains no NSD inventory.

The Bayesian estimation technique mentioned earlier in this report is the means of setting CSF minimum stockage levels under Method 1. These levels are revised as demand data accumulate (subject to the 3-year limitation imposed for this simulation study). Just as the optimal average time between NSD procurements is critical for the determination of NSD order quantities, a parameter q, called the *cost-criticality quantile* (Ref. 1), is the key determinant of minimum stockage levels. In standard inventory models (Ref. 5) the value of this parameter is derived from the demand rate and the ratio of the holding cost, h, to a so-called *penalty cost*, the cost of shortages. Thus the cost-criticality quantile is determined by trading off the "cost" of shortages against the cost of maintaining higher inventories (particularly minimum levels). Since dollar costs of shortages are very difficult to assess, we have taken the approach that the cost-criticality quantile itself is a parameter to be chosen, like h and k. It should be chosen so that the resulting average number of shortages per year is acceptable. (Our studies of the effect of q on shortage levels were reported in (Ref. 1). As Tables 1 through 4 indicate, higher values of q always yield fewer shortages, while lower values result in lower average inventory levels and costs.

In contrast to Method 1, Method 2 makes no allowance for optimal trade-offs between holding costs and ordering costs to determine NSD order quantities, or between inventory costs and frequency of shortages to determine CSF minimum stockage levels.

The station Directors Conference Proceedings, Ref. 6, described (Method 2) the current NSD Station Stockage Policy that is pictorially represented in Fig. 1. The station stockage policy is a 180-day usage (6 months supply) plus a 30-day buffer stock. The station minimum level is 105 days of stock (60 days shipping time plus 45 days procurement time) or a 4.5-month supply including the 30-day buffer stock.

Discussions with NSD personnel indicate that NSD's procurement policy is to procure the sum of all CSFs' annual demands once NSD's inventory reaches its reorder point. However, the question of NSD's reorder point is subject to evaluation. Based on preliminary assessments of Method 2, NSD's reorder level was set equal to the sum of the two largest CSF demands. The reason being that during NSD's procurement time, NSD should have a sufficient amount of stock on hand to fill at least the two CSFs that have the largest demands should both require stock shipments during NSD's procurement time. Further, as the estimated demand varies over time, the simulation program permits Method 2 to vary its reorder level at the NSD.

IV. Simulation Results

Most of the simulation runs in the present study were repeated at four levels of q: 0.65, 0.75, 0.85, 0.95. The cases presented in Tables 1 through 4 are those where the average number of units short per year was approximately 0.5 or 0.6, or the closest figure available on the low side. In some instances the results for two different values of q (with the same h) are given to illustrate the trade-off between cost savings and low frequency of shortages. Each of the Tables 1 through 4 shows the results of the simulation for a different true annual demand rate. The ratios of demand rates for the six CSFs were fixed in all cases for Table 1 as 1:2:3:4:5:5; for Table 2 the ratios of demand were 4:5:6:7:8:9; for Tables 3 and 4 the ratios were 4:5:6:7:8:10. In each table, only a single column of outputs is shown for Method 2, these being the averages over the different runs made for different values of h (which do not affect the actions of Method 2). The average inventory cost for Method 2 depends on h, however, since one part of that cost is h times the average inventory. The percentage cost savings in Table 1 illustrate a typical pattern. If we make some allowance for differences in shortage frequencies, the per cent cost savings realized by Method 1 decrease to a minimum and then increase as h varies through its range. The smallest cost reduction in Table 1 is 16% in the case $h = 0.2$. This value is smaller than the others because the optimum order cycle length in this case is very close to one year, which is the length used by Method 2 in all cases. For smaller h than 0.2, Method 1 achieves additional savings by ordering less frequently than once per year, because the reduced ordering costs more than offset the cost of the increased average inventory level. As h increases past 0.2, Method 1 saves additional money by ordering more frequently, since the optimal trade-off calls for lower inventory levels as the holding cost per unit gets larger. Other patterns appear in Tables 1 through 4. For instance, the per cent cost savings will be seen to increase as the annual demand gets larger.

Table 4 gives some results for a more complicated pattern of random demands. It is assumed that demands for 3 or 5 units at a time can also occur and that these account for 20% and 10% of the demands, respectively. Method 1 is specifically designed to accommodate this type of demand pattern (Ref. 1), while Method 2 is not. Thus, Table 4 reveals much higher frequencies of shortage for Method 2 than previous levels. The choices of q in Table 4 were made to control the frequency of shortages, as in previous cases, which requires higher minimum stockage levels than the unit demand pattern. This accounts for the lower percentage savings in inventory cost.

Useful information about the numbers of maintenance and operating items at various holding cost values is not presently available. However, the results in Tables 1 through 4 indicate that an average reduction of 25% in inventory cost per year is a reasonable estimate if Method 1 is utilized.

References

1. Eisenberger, I., Maiocco, F. R., and Lorden, G., *Proposed Inventory and Procurement Policy for the Deep Space Network*, JPL Document 890-25, Jet Propulsion Laboratory, Pasadena, Calif., October 1, 1972 (JPL internal document). See also, "An Inventory and Procurement Policy for the Deep Space Network," in *The Deep Space Network Progress Report*, Technical Report 32-1526, Vol. XII, pp. 131–148, Jet Propulsion Laboratory, Pasadena, Calif., Dec. 15, 1972.
2. Atwood, R. E., *System Requirements Document, Integrated Logistic System, Supply Management Subsystems*, Report 337D-2B1-1, M & O Document, DSIF Operations Section, Jet Propulsion Laboratory, Pasadena, Calif., Jan. 5, 1971 (JPL internal document).
3. Atwood, R., *Supply Inventory System (SIS) User's Guide*, Revision 1, Jet Propulsion Laboratory, Pasadena, Calif., Feb. 23, 1971 (unpublished rough draft of a JPL internal document).
4. Eisenberger, I., Maiocco, F. R., and Lorden, G., "An Inventory Policy for the Deep Space Network," in *The Deep Space Network Progress Report*, Technical Report 32-1526, Vol. IX, pp. 84–87, Jet Propulsion Laboratory, Pasadena, Calif., June 15, 1972.
5. Wagner, H. M., *Principles of Operations Research*, Chapter 19, Prentice-Hall, Inc., Englewood Cliffs, N.J., 1969.
6. *1972 DSIF Station Directors' Conference Proceedings*, Report 337-5A1, Section IV, pp. 4-1 to 4-8, Jet Propulsion Laboratory, Pasadena, Calif., Apr. 1, 1972 (JPL internal document).

Table 1. Simulation results: annual demand, 40 units

Category	Method 2	Method 1					
		$h = 0.05$	$h = 0.2$	$h = 0.5$	$h = 1.0$		$h = 2.0$
		$q = 0.65$	$q = 0.65$	$q = 0.75$	$q = 0.75$	$q = 0.85$	$q = 0.85$
Shortages/year	0.44	0.23	0.41	0.48	0.65	0.38	0.38
Procurements/year	0.95	0.42	0.78	1.07	1.34	1.40	1.61
Average inventory	69.7	85.5	58.9	49.3	43.6	50.1	45.8
Average inventory cost/year	—	6.40/8.20[a]	15.70/18.70[a]	30.00/39.60[a]	50.30/74.50[a]	57.00/74.50[a]	99.70/144.20[a]
% cost savings		22	16	24	33	23	31

[a] Average inventory cost/year: Method 1/Method 2.

Table 2. Simulation results: annual demand, 78 units

Category	Method 2	Method 1						
		$h = 0.05$	$h = 0.2$		$h = 0.5$		$h = 1.0$	
		$q = 0.75$	$q = 0.75$	$q = 0.85$	$q = 0.85$	$q = 0.95$	$q = 0.85$	$q = 0.95$
Shortages/year	0.27	0.2	0.53	0.22	0.44	0.1	0.6	0.26
Procurement orders/ year	0.97	0.56	1.0	1.01	1.46	1.5	1.82	1.83
Average inventory	119.4	119.7	79.9	86.0	70.5	80.2	65.4	74.4
Average inventory cost/year	—	8.80/10.80[a]	21.00/28.80[a]	22.30/28.80[a]	42.60/64.60[a]	47.60/64.60[a]	74.50/124.30[a]	83.60/124.30[a]
% cost reduction		19	27	23	34	26	40	33

[a] Method 1/Method 2.

Table 3. Simulation results: annual demand, 200 units with unit order sizes

Category	Method 2	Method 1			
		$h = 0.05$	$h = 0.2$		$h = 0.5$
		$q = 0.85$	$q = 0.85$	$q = 0.95$	$q = 0.95$
Shortages/year	0.094	0.18	0.51	0.05	0.21
Procurement orders/year	0.99	0.88	1.58	1.47	2.14
Average inventory	286.6	198.8	139.1	175.5	130.8
Average cost/year	—	14.30/19.30[a]	35.70/62.20[a]	42.50/62.20[a]	76.10/148.10[a]
% cost reduction		26	43	32	49

[a] Method 1/Method 2.

Table 4. Simulation results: annual demand, 200 units with multiple order sizes

Category	Method 2	Method 1	
		$h = 0.05$	$h = 0.2$
		$q = 0.95$	$q = 0.95$
Shortages/year	2.75	0.16	0.8
Procurement orders/ year	0.98	0.95	1.68
Average inventory	290.7	251.7	197.4
Average cost/year	—	17.30/19.40[a]	47.90/58.10[a]
% cost reduction		11	24

[a] Method 1/Method 2.

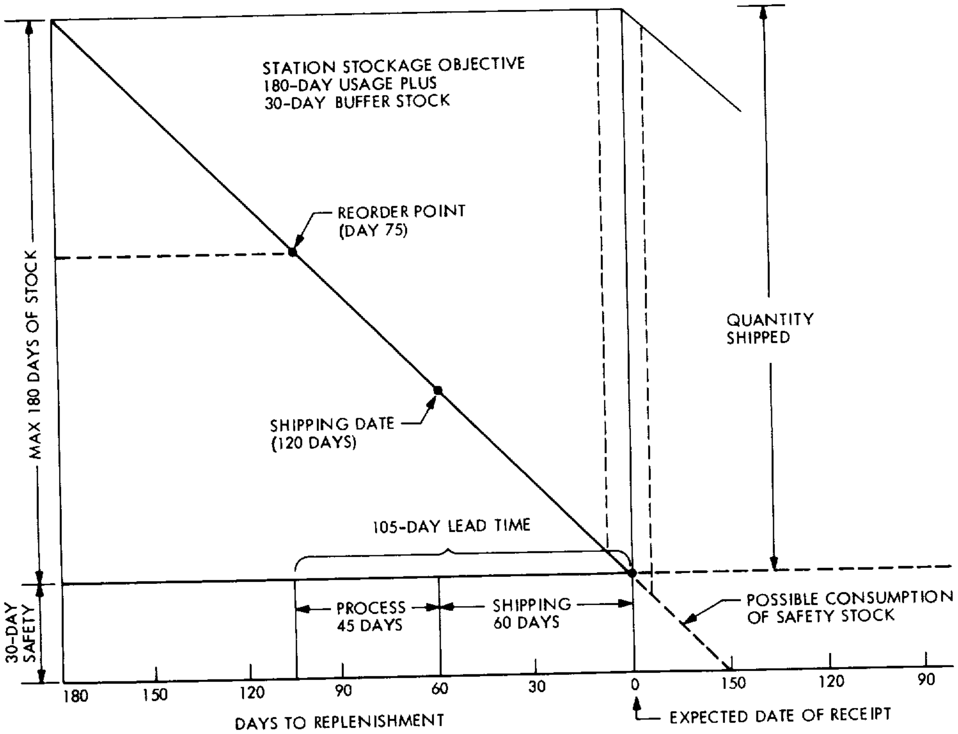

Fig. 1. Station stockage objective

CONSCAN Implementation at DSS 13

R. M. Gosline
R. F. Systems Development Section

The ability to do automatic boresighting of a large parabolic antenna without a monopulse feed or rotatable subreflector is desirable. A conical scan (CONSCAN) technique based on the movement of the main reflector under computer control has been developed. The functional features of the hardware and software as implemented at DSS 13 are described. Application to very precise antenna pointing is possible.

I. Introduction

Conical scan (CONSCAN) techniques (by scanning the main reflector) were demonstrated at DSS 13 in 1966 utilizing an SDS 910 computer, the 26-meter-diameter antenna, and a test transmitter located at the DSS 13 collimation tower. Successful boresight measurements were obtained on a static target although ground reflections and computer limitations prevented complete success. The tracking system was then interfaced with the SDS 930 computer and the program re-written in real-time Fortran II. Peripheral equipment on line included two magnetic tape units, a line printer, and a card reader/punch providing adequate development and de-bugging capability. A complete angle tracking program was developed with the conical scan technique being one of several options.

II. Algorithm

A mathematical analysis of the general technique is described in Refs. 1, 2, and 3.

The actual implementation preceded the detailed analysis on the recognition that a circular scanning antenna will cause a sinusoidal variation in the received signal whose amplitude and phase (with respect to the scanning function) contain information with which to improve the boresight.

The algorithm may be simply developed by fitting a sinusoid of the form

$$y = D + R\cos(\omega t - \phi) \tag{1}$$

to the sampled receiver power y_i by the method of least squares as detailed in Ref. 4. Expansion of Eq. (1) and substituting

$$A = R\cos\phi$$
$$B = R\sin\phi$$

yields

$$y = D + A\cos\omega t + B\sin\omega t$$

where A and B are the axial components of the boresight error. The least squares sum S is

$$S = \sum_{i=0}^{n-1} [y_i - (D + A \cos \omega t_i + B \sin \omega t_i)]^2$$

The scan frequency ω is known. S may be minimized by setting

$$\frac{\partial S}{\partial A} = \frac{\partial S}{\partial B} = \frac{\partial S}{\partial D} = 0$$

This yields

$$D = \frac{1}{n} \sum y_i \text{ (the dc component)}$$

$$A = \frac{2}{n} \sum y_i \cos \omega t_i$$

$$B = \frac{2}{n} \sum y_i \sin \omega t_i$$

The boresight error magnitude and direction may now be found from

$$R = \sqrt{A^2 + B^2}$$

and

$$\phi = \arctan B/A$$

but the A and B summations are applied directly as the azimuth and elevation corrections. Figure 1 is a functional diagram of the implementation. The circular scan is generated by adding sine and cosine functions to the azimuth and elevation ephemerides. The signal power samples (averaged over a one-second period) are multiplied by the appropriate sinusoidal function and summed over a complete scan cycle in each axis. A gain factor is applied to control stability before the corrections are added to the nominal ephemerides. The corrections are accumulative, i.e., the total corrections C, as a result of m complete cycles, is

$$C = G \sum_{i=1}^{m} A_i$$

In a stable condition the A_i terms become small.

III. Program Description

The program is best summarized with a brief description of the 15 control options that enable various combinations of modes. These options are selected by the SDS 930 typewriter.

(1) *Position offsets.* Provides for entering fixed-position offsets in azimuth, elevation, hour angle, or declination.

(2) *Sidereal rate mode.* Generates a sidereal rate from either right ascension or sidereal hour angle and declination coordinates.

(3) *Scan mode.* Enables conical scan mode and allows for input of scan radius, period, and a gain factor.

(4) *Stop mode.* Stops conical scan mode, on–off mode, and simulation mode, and removes all position and rate offsets.

(5) *3-Day fit mode.* Generates a second-order fit to three days of coordinates for tracking planets from almanac data.

(6) *Polynomial mode.* Generates an ephemeris from standard polynomial cards as supplied by the "PLACE" predicts program.

(7) *Zero az–el mode.* Generates an azimuth and elevation ephemeris of zero plus offsets.

(8) *Zero HA–dec mode.* Generates a local hour angle and declination ephemeris of zero plus offsets.

(9) *Time offset.* Allows for time offsets to any of the ephemeris modes.

(10) *Read offset table.* Reads punched paper tape containing offset data to be used as pointing corrections.

(11) *On–off source mode.* Provides the following antenna sequence for radio source calibration work:

   (a) Conical scan
   (b) Off source (in azimuth if elevation < 60 deg)
   (c) On source
   (d) Off source
   (e) Repeats (c) and (d) three times
   (f) Return to (a)

(12) *Track tolerance.* Provides for changing the nominal tracking tolerance of 0.010 deg. In the conical scan and on–off modes, the servo tracking error is checked against the tracking tolerance before the next angle increment is allowed to proceed.

(13) *Simulation mode.* Simulation of the receiver output and servo/readout system allows internal checking of the SDS 930 hardware and software.

(14) *Zero offset table.* Removes all table offsets from read offset table mode.

(15) *Rate offsets.* Provides for rate offsets in azimuth, elevation, hour angle, and declination.

Use is made of the priority interrupt system so that modes and parameters can be changed while the antenna is under computer control and tracking a target.

IV. Results

Typical offset data obtained by conical scanning are shown in Fig. 2. Even the fine structure of these plots is repeatable. An apparent periodicity of 13⅓ deg corresponds to one pole of the 27-pole resolver in the Datex readout system, and indicates a possible malfunction of that system.

Figure 3 is a typical plot obtained after using the offset data previously obtained and repeating the conical scan procedure. Very precise tracking is obtainable by this technique as demonstrated by Fig. 3.

The minimum useful scan period is about 60 seconds, depending on wind conditions and servo performance, which represents an order of magnitude improvement in measurement time over previous manual methods. Further data are needed to compare with the theoretical analysis in Refs. 1, 2, and 3.

With the completion of the development phase, it is now possible to implement the technique back into an SDS 910 or 920 computer for boresight measurements in the Deep Space Stations.

References

1. Ohlson, J. E., *Performance Analysis of Conical-Scan Tracking: Part I. Tracking of Radio Sources,* Document 3333-71-208, Oct. 20, 1971 (JPL internal document).
2. Ohlson, J. E., *Performance Analysis of Conical-Scan Tracking: Part II. Tracking of Spacecraft,* Document 3333-71-239, Dec. 2, 1971 (JPL internal document).
3. Ohlson, J. E., *Performance Analysis of Conical-Scan Tracking: Part III. Gain Fluctuation Effects,* Document 3333-72-076, Mar. 23, 1972 (JPL internal document).
4. Gosline, R. M., *Conical Scan Simulation,* M.S. thesis, West Coast University, Los Angeles, Calif., May 1, 1970.

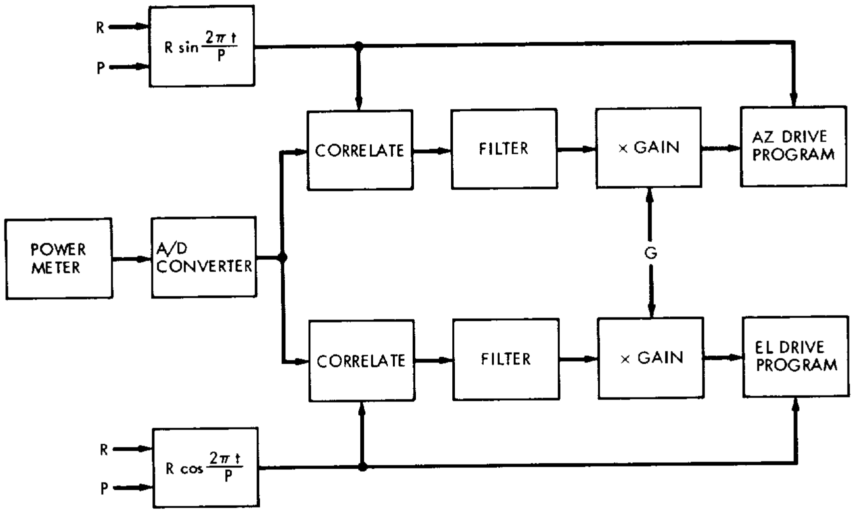

Fig. 1. Conical scan functional diagram

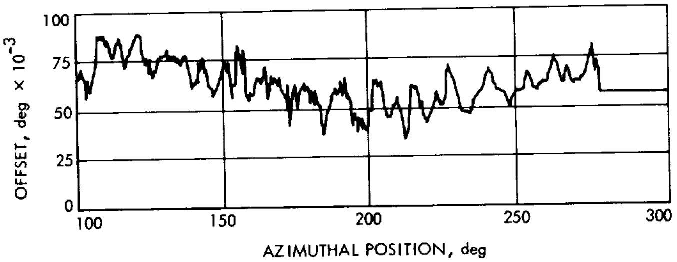

Fig. 2. Boresight errors before table corrections applied

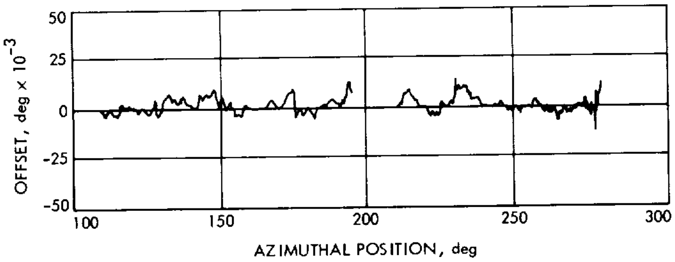

Fig. 3. Boresight errors after table corrections applied

DSN Research and Technology Support

E. B. Jackson
R.F. Systems Development Section

The activities of the Development Support Group in operating the Venus Deep Space Station (DSS 13) and the Microwave Test Facility (MTF) for the period December 16, 1972 through February 15, 1973 are presented, categorized by facility and section supported. Major activities include continuation of the intensive dual-carrier investigation, refurbishing of the S-band megawatt transmit (SMT) cassegrain feedcone, implementation of the dedicated antenna pointing computer for the 26-m antenna, and continuation of collection of Faraday rotation data. A description of the dual-carrier test program and results to date are given, together with details of other activities during the period.

During the two months ending February 15, 1973, the Development Support Group was primarily engaged in the following activities at DSS 13 and the Microwave Test Facility (MTF) at the Goldstone Deep Space Communications Complex.

I. DSS 13 Activities

A. In Support of Section 331

Planetary radar. Continuing support of the Mariner Venus/Mercury 1973 spacecraft mission, ranging measurements to the planet Venus were made. These measurements are made using the 64-m-diam antenna and 400-kW transmitter at DSS 14 for transmission and reception, with pseudonoise code generation, data processing, and control being performed at DSS 13. Ranging measurements with a resolution of five microseconds were made of Venus for a total of seven good signal runs during this period. The range to Venus has steadily increased and was 247×10^6 km on February 15, 1973.

B. In Support of Section 333

Faraday rotation data collection. Utilizing both a dual-channel phase-lock receiver and a non-phase-lock receiver with a rotating antenna, Faraday rotation data continue to be collected on a 24-hour per day basis, with the data being punched onto paper tape and printed on a teleprinter by the data system at DSS 13. These data, when mapped (in both frequency and direction) to the spacecraft look angle, are used to correct measured range and doppler data.

C. In Support of Section 335

1. 26-m antenna pointing computer. After adding core memory and refurbishing, a surplus SDS 910 computer (obtained from NASA) was interfaced with the prototype antenna pointing system rack and implemented to control the pointing of the 26-m antenna. Unlike the other computers at DSS 13, which are also used for tape generation, computation, etc., this computer has no assigned tasks other than moving and controlling the pointing of the 26-m antenna. With this dedicated computer and modification of the antenna drive computer program, the requirement for a skilled servo operator is lessened since the computer can assure that harmful acceleration rates are not applied to the antenna.

2. **Dual uplink carrier testing.** Evaluation has continued of the intermodulation products (IMP) present in the downlink as a result of dual uplink carriers being transmitted by a single transmitter klystron. After completing an intensive program of antenna "clean-up" (Ref. 1), intermodulation product levels had stabilized at the -165 to -170-dBm level, and further testing was scheduled to gain experience on effects of longer term operation. During the period December 16, 1972 through February 5, 1973, 336 hours of testing have been performed on this project. After approximately a month of fairly regular operation, the intermodulation product level gradually worsened toward the -150-dBm level. A review of the past days' operating logs revealed nothing significant, so disassembly of the waveguide system was commenced, with testing proceeding on smaller and smaller systems as pieces were removed. Upon removal of the diplexer, system noise decreased. Examination of the diplexer revealed that the plating around the tuning posts had cracked. The diplexer is electroformed of nickel over copper; the posts are of wrought copper and are "grown in" (plated into place) during the electroforming. It is felt that thermal cycling and differential expansion or improper bonding during manufacture caused the plating to crack, thus allowing arcing to take place in this area of high field strength. The diplexer has been carefully cleaned and these posts have been soft soldered into place. Testing will be resumed with all waveguide system parts recleaned and reassembled. The object of further testing is to gather data on long-term intermodulation performance under routine maintenance of the system.

The maser originally used for these tests was a standard DSN Block II which had performed perfectly since initial successful cooldown. However, during the week ending December 24, 1972, this maser refrigerator warmed up three times, apparently due to contamination being introduced into the system. The refrigerator and maser were replaced with a pseudo-Block III system to attain additional maser gain, greater gain stability, and faster cooldown. However, this replacement did not solve the warm-up problems as there were three warm-ups the following week, the last of which resulted in a burned out crosshead drive motor. Extensive purging of the system, accompanied by a change of the compressor, followed by simultaneous vacuum pumping of the entire system was successful in eliminating the contamination problem, and the system was successfully cooled down in mid-January and has remained cold since that time.

II. Microwave Test Facility Activities

A. In Support of Section 333

Refurbishment of SMT cassegrain feedcone for DSS 14. Upon removal of the SMT cassegrain feedcone from DSS 14, the waveguide components were removed at the MTF while the cone shell and feedhorn were shipped to a vendor for installation of the reflector to be used with the multiple-frequency X- and K-band (MXK) feedcone. The waveguide system components were carefully cleaned, lapped, and sent to a vendor for a finishing process (iriditing) which provides a smooth surface resistant to oxidation. Upon receipt of the SMT feedcone with the reflector installed, the waveguide system was reinstalled and dual carrier testing accomplished at the dual 7-kW carrier level (the maximum which could be generated in that configuration). Good intermodulation performance was observed and the cone was reinstalled onto the DSS 14 64-m antenna. However, after reinstallation, dual 40-kW carrier testing was accomplished at DSS 14, and poor intermodulation performance was observed. At this time it is not certain whether the poor performance is due to the effects of the 64-m antenna, the higher power available for testing, or another manifestation of the diplexer problem discussed earlier in this article.

B. In Support of Section 335

1. **Non-interruptable waveguide pressurization manifold.** Working from plans and parts supplied by Section 333, a waveguide pressurization manifold designed to be supplied from two liquid-nitrogen dewars was fabricated for use at DSS 13 on the 26-m antenna. Continuous pressurization of the waveguide is important in maintenance of good intermodulation product performance.

2. **Dual carrier.** The majority of the available manpower continued to support dual-carrier testing at DSS 13. Disassembly and cleaning of waveguide components, including switches, reinstallation of cleaned components, and fabrication of special bracketry and mounts, are typical of the support given this project during this period.

Reference

1. Jackson, E. B., and Price, A. L., "Development Support Group," in *The Deep Space Network Progress Report*, Technical Report 32-1526, Vol. XIII, pp. 127–129. Jet Propulsion Laboratory, Pasadena, Calif., Feb. 15, 1973.

Universal Parallel Analog-to-Digital Encoder Module

T. O. Anderson
Communications Systems Research Section

As more and higher frequency DSIF receiver operations become digitized, the DSN requires higher speed, simpler and more cost-effective analog to digital converters. Besides meeting these requirements the converter described here is modular and lends itself to standardization.

The conversion method used is the all parallel method that is optimum for high speed. One comparator amplifier for each level of the resolution is used. The digital code converter that converts the output of the comparator amplifiers to binary code is included.

The module includes four levels. An eight-level converter is made up of two such modules connected externally, and a sixteen-level converter is made up of four modules externally connected.

I. Introduction

As more and higher frequency DSIF receiver operations become digitized, the DSN requires higher speed, simpler and more cost-effective analog-to-digital (A-D) converters. Besides meeting these requirements the converter described here is modular and lends itself to standardization.

The conversion method used is the all-parallel method, which is optimum for high speed. One comparator amplifier for each level of the resolution is used. The digital code converter from the output of the comparator amplifiers to binary code is included.

The module includes four levels. An eight-level converter is made up of two such modules connected externally and a sixteen-level converter is made up of four modules externally connected.

For reference, five fundamentally different analog-to-digital conversion methods are first reviewed. It will then be clear that the all-parallel conversion method is fundamentally the fastest. The modular code conversion method presented here will make parallel converters more efficient.

The universal converter module presented here includes a resistive ladder, four comparator amplifiers and four NAND gates. It will quantize an input signal to 2 bits. Two modules, connected externally in a simple manner, will quantize an input signal to 3 bits, four modules to 4 bits, and 8 modules to 5 bits. For higher resolution, a sequential scheme is suggested where universal modules are first connected in parallel, their outputs reconverted to analog form, and the outputs then used as an input to a second set of parallel modules. Most converter requirements can then be satisfied by converters simply implemented as indicated with the universal encoder module being the only component required.

II. A-D Converter Background

As mentioned, five fundamentally different analog-to-digital conversion methods are first reviewed. The parallel method and its features are then discussed. Different methods of code conversion are elaborated on and the optimum modular implementation is shown in detail.

The five fundamentally different types of analog-to-digital converters are:

(1) The chronologic, integration, or counter-ramp type.

(2) The successive approximation type.

(3) The tracking, up/down counter type.

(4) The n-bit, n-series comparator amplifier type.

(5) The n-bit, 2^n comparator amplifier all-parallel type.

Of the first three, each uses one comparator amplifier and one binary weighted D-A ladder network.

In the first type mentioned, the digital-to-analog converter (DAC) is connected to a unidirectional binary counter. The output of the DAC is one input to the comparator amplifier. The second input is the signal to be converted. The output of the comparator amplifier controls the clock gate to the counter. The conversion time is a function of the input signal. For n bits the conversion time is anywhere from zero to $2^n \cdot t_{cl}$ (t_{cl} = clock period). If the start conversion commands are unidistant, the actual sampling instants are not necessarily unidistant. They are however, computable. The sample at the time it is taken, on the other hand, is accurate to the resolution of the converter. This type of converter is inherently slow and cumbersome and not very efficient especially in comparison with more recent designs.

The second type mentioned, the successive-approximation-type converter contains a binary register, a weighted DAC, and a comparator amplifier. The output of the comparator amplifier forms a control bus for the register. The clock steps an n-position sequencer. Starting with the most significant bit in the register, it is turned on, left on, or turned off as a function of the control bus. In some designs a single set of flip-flops is used both as binary register and the sequencer, however with a more complex control logic. Successive approximation control logic designs are described in Ref. 1.

The conversion time for this type of converter is constant, $n \cdot t_{cl}$, however the sample accuracy is a function of the input signal bandwidth. A sample-and-hold amplifier is therefore often required. Nonetheless, this is a moderately fast and moderately efficient converter, and as such it is very popular.

The third type mentioned, the tracking converter, also contains a binary counter, a weighted DAC, and a comparator amplifier. This counter counts in either direction, up or down. Its clock is continuously on and the output from the comparator amplifier controls the counting direction for the counter.

This connection then forms a servo loop that tracks the input signal (as long as the loop slew rate is not exceeded). For a dc input, the output will "dither" between two adjacent states. It will track input changes of 1 least significant bit (LSB) at the rate of the service clock. Digital data can be extracted from the counter/register at any time, preferably in sync with the high-speed service clock that drives the counter. The tracking converter is usually fast, inexpensive, and very useful for the purpose for which it was designed.

The fourth type mentioned, the sequential-comparator-type converter or encoder uses n comparator amplifiers connected in series. The output of the first controls an analog weighting network that subtracts half the input signal from the summing node to the subsequent comparator. The output from the comparator is then directly the output in a binary code. The conversion time is $(n)^{1/2} \cdot t_s$; where t_s is the settling time for one comparator. To maintain a uniform scale factor between stages, the residue can be doubled between stages. This is the fastest of the four basic types of converters mentioned so far and moderately expensive with one comparator per stage.

The last type mentioned, the all-parallel converter or encoder shown in Fig. 1 divides a reference voltage in a resistive divider into 2^n unidistant levels. There are then 2^n comparator amplifiers each with one input from the divider and the other connected to the input signal, the same as for all the comparators. As the input increases, an increasing number of amplifiers turn on. For a half-scale signal, half of all the amplifiers are turned on (111 . . . 1000 . . . 0). This code is not usable as is, but must be converted to binary in a digital code converter.

The conversion time for this analog-to-digital converter is equal to that of the settling time for a comparator amplifier plus the propagation time through the code converter. It requires 2^n amplifiers, which becomes impractical for large n. For large n, a combination of the all-parallel type and the sequential type is then used. A single-parallel unit for smaller n can also be multiplexed between several analog inputs and digital output registers.

III. Possible Code Converters for the Parallel Encoder

Inspection of the truth tables in Fig. 2 may trigger the thought of connecting exclusive OR gates between A and B, B and C, C and D, etc., and thus first converting the shift code to a unary code. This code can then more easily be converted to binary with a unary-to-binary converter. Exclusive OR gates are available in large-scale integrated (LSI) chips and so is the unary-to-binary converter often called priority encoder. This scheme is not especially efficient. The chip count may be low, but the number of propagation levels high.

One may also discover however, to little avail, that the midway bit of the input code is equivalent to the most-significant bit (MSB) of the output code and that the LSB of the output code is the parity function of the input code, parity coders being readily available in medium-scale integrated (MSI) chips.

One may also discover to little avail that the entire output code is the weight function of the input code. Weighting networks have been explored in Ref. 2. They have usually many propagation levels. They are also too general for this application. They are designed so as not to matter where the ones are located, while in the present case this is known.

IV. Examples of Efficient Code Converters

Straightforward switching networks can be derived as follows: simply by inspecting the code conversion truth tables in Fig. 2, or, by any number of formal methods, one can devise a code converter such as shown in Fig. 3. It may be noticed that in this network, collector OR or wired OR gating is used. This will minimize the number of propagation levels. The implementation then requires open collector gates and common external collector resistors. It may also be noticed that the true output of the converter is the low level.

In Fig. 4 it is shown that the midway bit of the input code is equivalent to the most significant bit of the output code and how this bit partitions both truth tables into two equivalent parts. One can then devise and OR-wire two identical halves and access them with the midway bit. Such a converter is shown in Fig. 5. The access term is in effect an inhibit term for the lower half. Continuing this trend of thought one can of course again partition each half into two identical halves. This partition of the truth table is shown in Fig. 6, and a converter resulting from this strategy is shown in Fig. 7.

A number of other configurations are possible. One could, for example, multiplex one one-half network between two sets of inputs. And of course, one could multiplex one one-quarter network between four sets of inputs. Both of these configurations would take more gates with several more propagation levels.

V. The Universal Code Converter for the Parallel Analog-to-Digital Encoder

The quarter-truth table-converter, if it were to be made up in a special module, can be further streamlined to form a universal module such as shown in Fig. 8. In an iterative network this module can be used to form a code converter for any number of variables.

VI. The Universal Analog-to-Digital Encoder Module

Quad comparator amplifiers in a single module are presently available. The addition of the resistive ladder and the four-NAND-gate code converter will form a universal analog-to-digital encoder module such as shown in Fig. 9. In Fig. 10, four such modules are connected together to form a 4-bit A-D converter.

A 5-bit converter would use eight modules, etc. For greater resolution, a series of parallel converters would be used as discussed. Reconversion to analog form between sets of parallel converters for analog subtraction is then first performed.

VII. Conclusion

Five fundamentally different analog-to-digital conversion or encoding schemes have been reviewed. From this review it is clear that the all-parallel conversion method is the simplest and most efficient. The great variety of available comparator amplifiers allows for designs of encoders of a variety of speeds, resolutions and costs. The most important functional component besides the chain of comparator amplifiers is the code converter. Various designs of the code converter were explored. The optimum modular implementation was discovered.

It has then been shown how a resistive ladder network, four comparator amplifiers, and the optimum code converter module combine to form an optimum universal analog-to-digital encoder modules, which, in turn, combine to form analog-to-digital converters to meet the DSIF requirement stated in the introduction.

References

1. Anderson, T. O., "Optimum Control Logic for Successive Approximation Analog to Digital Converters," *Computer Design*, July 1972, pp. 81–86.
2. Anderson, T. O., "Modular Switching Network for Generating the Weight in Binary Notation of a Binary Vector," *Computer Design*, Apr. 1972, pp. 106–110.

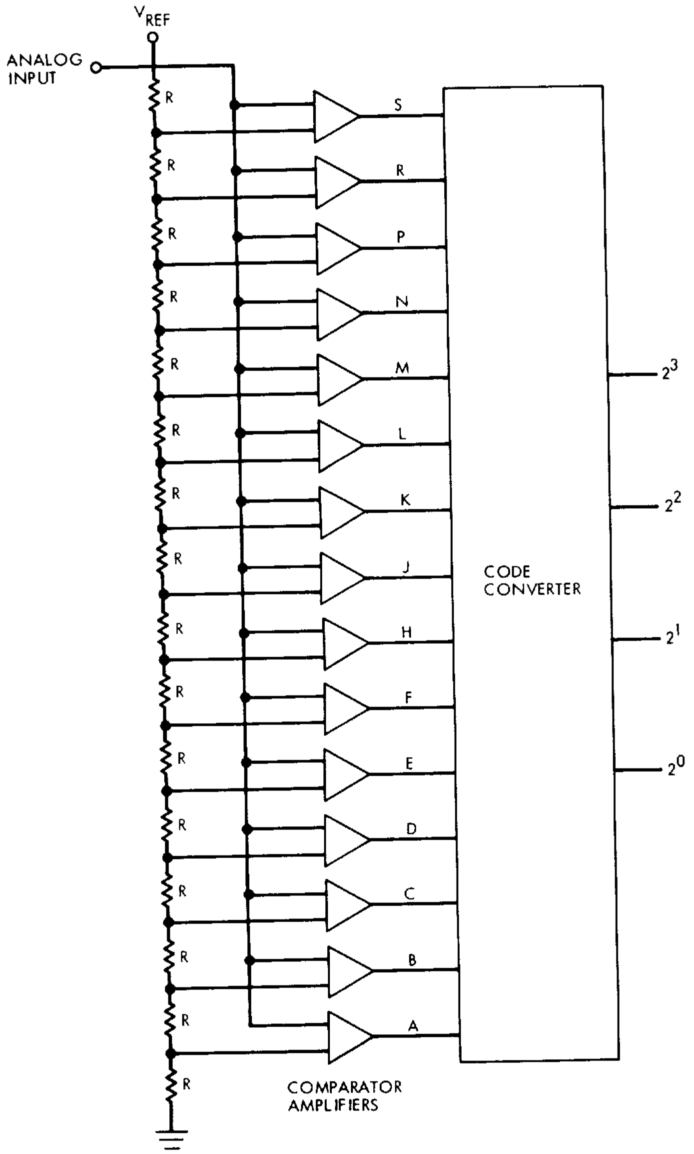

Fig. 1. All parallel code converter block diagram

A	B	C	D	E	F	H	J	K	L	M	N	P	R	S
0	0	0	0	0	0	0	0	0	0	0	0	0	0	0
1	0	0	0	0	0	0	0	0	0	0	0	0	0	0
1	1	0	0	0	0	0	0	0	0	0	0	0	0	0
1	1	1	0	0	0	0	0	0	0	0	0	0	0	0
1	1	1	1	0	0	0	0	0	0	0	0	0	0	0
1	1	1	1	1	0	0	0	0	0	0	0	0	0	0
1	1	1	1	1	1	0	0	0	0	0	0	0	0	0
1	1	1	1	1	1	1	0	0	0	0	0	0	0	0
1	1	1	1	1	1	1	1	0	0	0	0	0	0	0
1	1	1	1	1	1	1	1	1	0	0	0	0	0	0
1	1	1	1	1	1	1	1	1	1	0	0	0	0	0
1	1	1	1	1	1	1	1	1	1	1	0	0	0	0
1	1	1	1	1	1	1	1	1	1	1	1	0	0	0
1	1	1	1	1	1	1	1	1	1	1	1	1	0	0
1	1	1	1	1	1	1	1	1	1	1	1	1	1	0
1	1	1	1	1	1	1	1	1	1	1	1	1	1	1

2^3	2^2	2^1	2^0	
0	0	0	0	0
0	0	0	1	1
0	0	1	0	2
0	0	1	1	3
0	1	0	0	4
0	1	0	1	5
0	1	1	0	6
0	1	1	1	7
1	0	0	0	8
1	0	0	1	9
1	0	1	0	10
1	0	1	1	11
1	1	0	0	12
1	1	0	1	13
1	1	1	0	14
1	1	1	1	15

Fig. 2. Input/output code truth tables

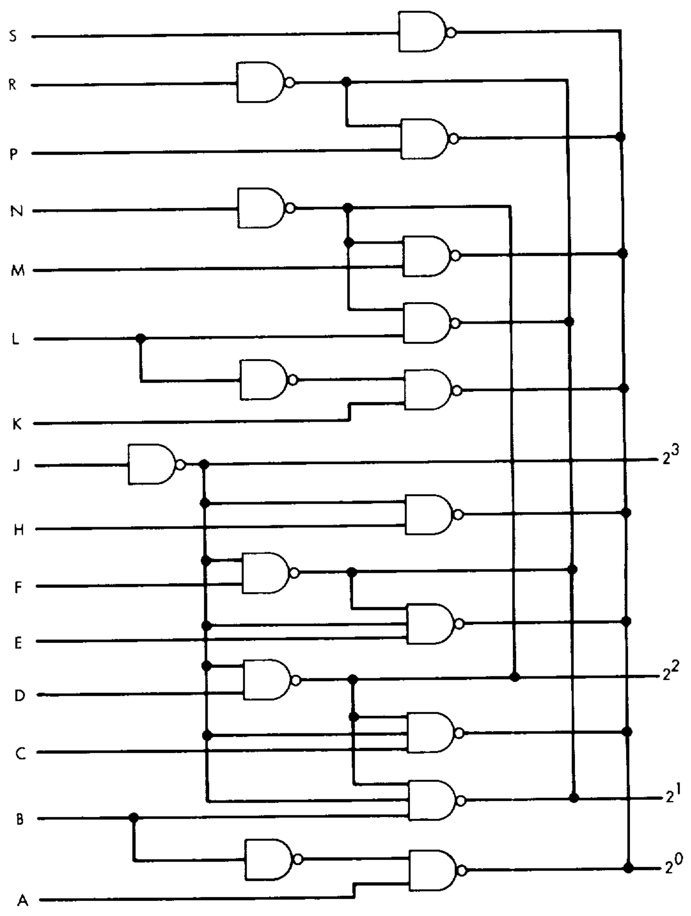

Fig. 3. Code converter logic

A	B	C	D	E	F	H	J	K	L	M	N	P	R	S	2^3	2^2	2^1	2^0	
0	0	0	0	0	0	0	0	0	0	0	0	0	0	0	0	0	0	0	0
1	0	0	0	0	0	0	0	0	0	0	0	0	0	0	0	0	0	1	1
1	1	0	0	0	0	0	0	0	0	0	0	0	0	0	0	0	1	0	2
1	1	1	0	0	0	0	0	0	0	0	0	0	0	0	0	0	1	1	3
1	1	1	1	0	0	0	0	0	0	0	0	0	0	0	0	1	0	0	4
1	1	1	1	1	0	0	0	0	0	0	0	0	0	0	0	1	0	1	5
1	1	1	1	1	1	0	0	0	0	0	0	0	0	0	0	1	1	0	6
1	1	1	1	1	1	1	0	0	0	0	0	0	0	0	0	1	1	1	7
1	1	1	1	1	1	1	1	0	0	0	0	0	0	0	1	0	0	0	8
1	1	1	1	1	1	1	1	1	0	0	0	0	0	0	1	0	0	1	9
1	1	1	1	1	1	1	1	1	1	0	0	0	0	0	1	0	1	0	10
1	1	1	1	1	1	1	1	1	1	1	0	0	0	0	1	0	1	1	11
1	1	1	1	1	1	1	1	1	1	1	1	0	0	0	1	1	0	0	12
1	1	1	1	1	1	1	1	1	1	1	1	1	0	0	1	1	0	1	13
1	1	1	1	1	1	1	1	1	1	1	1	1	1	0	1	1	1	0	14
1	1	1	1	1	1	1	1	1	1	1	1	1	1	1	1	1	1	1	15

Fig. 4. Truth table partitioning

A	B	C	D	E	F	H	J	K	L	M	N	P	R	S	2^3	2^2	2^1	2^0	
0	0	0	0	0	0	0	0	0	0	0	0	0	0	0	0	0	0	0	0
1	0	0	0	0	0	0	0	0	0	0	0	0	0	0	0	0	0	1	1
1	1	0	0	0	0	0	0	0	0	0	0	0	0	0	0	0	1	0	2
1	1	1	0	0	0	0	0	0	0	0	0	0	0	0	0	0	1	1	3
1	1	1	1	0	0	0	0	0	0	0	0	0	0	0	0	1	0	0	4
1	1	1	1	1	0	0	0	0	0	0	0	0	0	0	0	1	0	1	5
1	1	1	1	1	1	0	0	0	0	0	0	0	0	0	0	1	1	0	6
1	1	1	1	1	1	1	0	0	0	0	0	0	0	0	0	1	1	1	7
1	1	1	1	1	1	1	1	0	0	0	0	0	0	0	1	0	0	0	8
1	1	1	1	1	1	1	1	1	0	0	0	0	0	0	1	0	0	1	9
1	1	1	1	1	1	1	1	1	1	0	0	0	0	0	1	0	1	0	10
1	1	1	1	1	1	1	1	1	1	1	0	0	0	0	1	0	1	1	11
1	1	1	1	1	1	1	1	1	1	1	1	0	0	0	1	1	0	0	12
1	1	1	1	1	1	1	1	1	1	1	1	1	0	0	1	1	0	1	13
1	1	1	1	1	1	1	1	1	1	1	1	1	1	0	1	1	1	0	14
1	1	1	1	1	1	1	1	1	1	1	1	1	1	1	1	1	1	1	15

Fig. 6. Truth table quarter partition

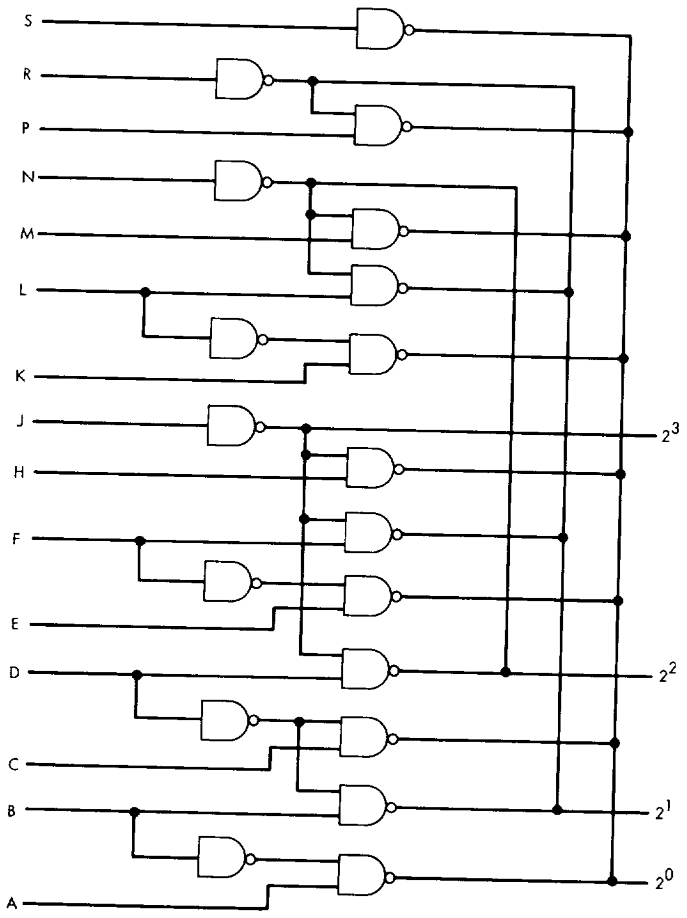

Fig. 5. Two-halves code converter

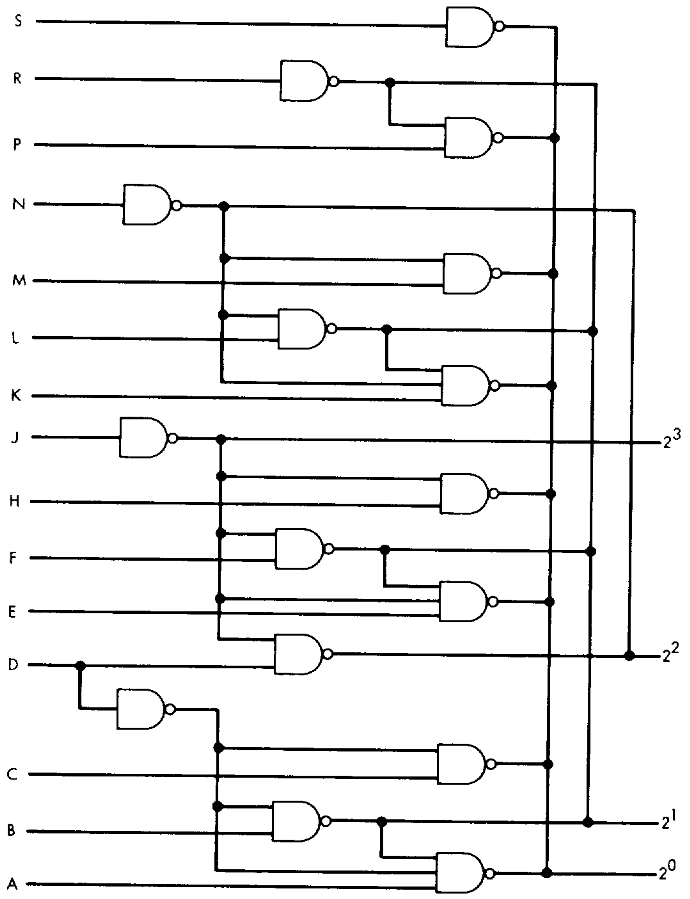

Fig. 7. Four-quarter code converter

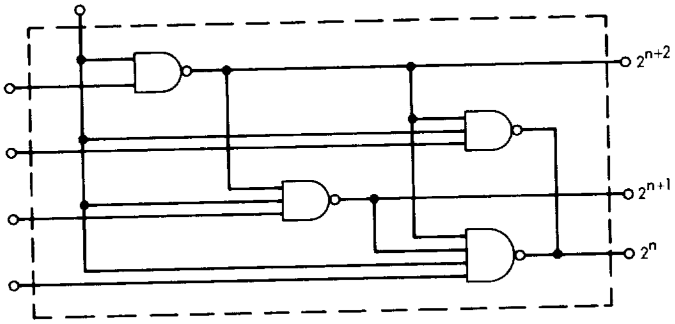

Fig. 8. Universal code converter module

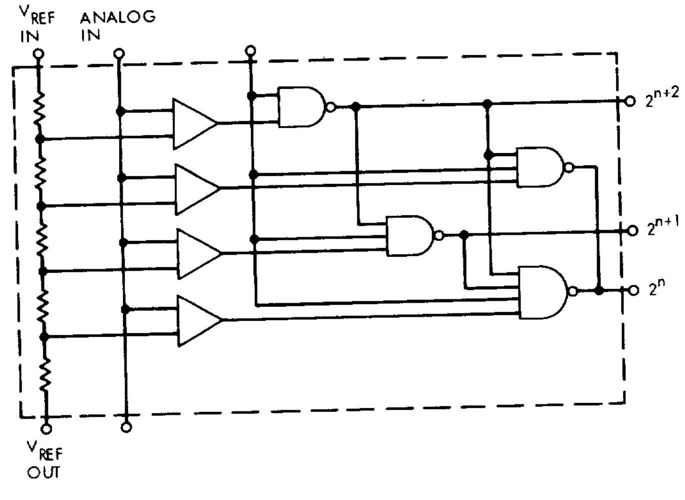

Fig. 9. Universal analog/digital encoder module

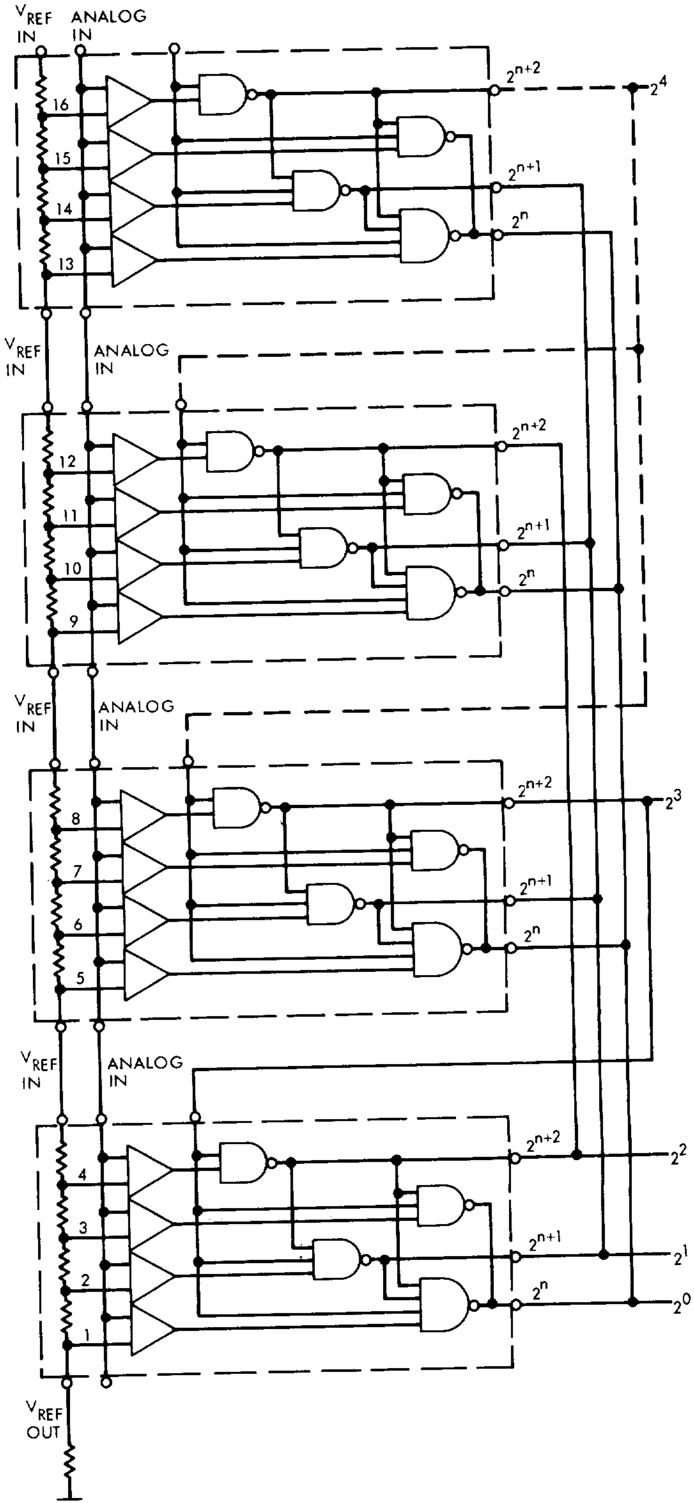

Fig. 10. 4-bit all-parallel A-to-D converter made up of four universal encoder modules

A Minicomputer Vector Generator

R. F. Emerson
Communications Systems Research Section

A vector generator was designed and built as a peripheral for a minicomputer. The vector generator is a device which accepts two endpoints and draws a straight line between them on some display device. While this could be done point-by-point by a minicomputer, it would use valuable computing power in an inefficient way. This generator is part of the Precision Signal Power Measurement (PSPM) System and is used to graph the power spectra of the signal measured to determine performance of spacecraft and ground telemetry transmitters and receivers. This hardware increases the graphing efficiency by an average of 4000 times over the point-by-point plotting method, requiring less than 15 μs of computer time per endpoint. The vectors are composed of points spaced 0.004 mm apart, providing excellent resolution and linearity.

I. Introduction

A vector generator was designed and built as a peripheral for the Lockheed Electronics Company MAC 16 minicomputer. The MAC 16 is being used as the control computer for the development of the Precision Signal Power Measurement (PSPM) System, a system which measures the downlink power of a spacecraft signal (Refs. 1 and 2). Measurement of the signal power is accomplished by computing the power spectrum of the signal and from this the signal-to-noise ratio. The signal-to-noise ratio is but one of many parameters available from the spectrum. The continuing demands on the PSPM System call for the utilization of other parameters contained within the spectrum. One of the techniques that can be used to measure other parameters is the graphing of the spectrum. In the past the graphing of the spectra has been done by hand, line printer, and slow computer-controlled mechanical plotting. These methods are no longer satisfactory because of the increasing data rates of the PSPM System. Replacing the mechanical plotter with a cathode-ray tube (CRT) display can improve the situation, but point-by-point plotting on a CRT has inherent speed limitations requiring that the line be broken into small segments and plotted incrementally. For each step in this process, the computer must calculate the increment and send it to the plotter. To maintain linearity and provide sufficient resolution, these calculations must be done hundreds of times even for lines of 1 to 2 cm. It will require, typically, 50 to 60 μs of computer processing time for each step during which time no other calculations can be done. A major portion of these calculations is now done by the hardware described in this report.

The vector generator, built as a peripheral to the MAC 16 computer, performs the computing necessary for plotting vectors and requires less than 30 μs of computer time for each vector regardless of length. This results in increasing the efficiency of plotting by an average of 4000 times with respect to point-by-point plotting. There is also an increase in plotting speed, averaging 60 times. The vector is drawn as a series of steps 0.004 mm in size, insuring a linearity of better than 0.02%. This is the theoretical limit and does not include the effects of the CRT, which limits the linearity to 1%.

Figure 1 presents the structure of the display system for which the vector generator was designed. Provisions were made to include a character generator within the display system by placing an analog interface multiplexer before the display unit. The display unit is a Tektronix Storage Display Unit, Type 611 (Ref. 3). Storage display units do not require refreshing. Both input and output interfaces handle data and control signals to and from the computer via the Programmed Data Channel (Ref. 4). The clock and control circuitry regulate the sequence of events within the vector generator. X and Y vector channels form the heart of the vector generator. It is here that the endpoints are stored and the calculations made to produce the straight line path between these endpoints. It is also necessary to position the beam without writing on the CRT; therefore, Z-axis control logic is provided. This logic interprets commands from the computer and turns the beam on or off.

II. Vector Generator Implementation

The vector generator was designed around the properties of a binary rate multiplier (BRM). The BRM circuit produces an output frequency that is a selectable rational fraction of the input frequency. The waveforms and logic diagram of Fig. 2 show this process. The binary counter divides the input pulse train of frequency f_i by two for each stage. AND gates (G_i) select unique transitions in this counting sequence, gating them with the input rate selection (X_i). The outputs of the AND gates are then ORed to produce the final pulse train (f_0). The average frequency of the output pulse train is

$$f_0 = \frac{\text{rate}}{2^n} f_i$$

where the rate is represented in binary by the X_i and n is the number of stages in the counter. To generate a vector, it is necessary to step from the initial point to the endpoint uniformly, or nearly so, in both axes. This can be done by counting pulses whose average rate is proportional to the difference between endpoints. For example, if it is desired to draw a vector from point $(-1, -1)$ to point $(0, +1)$, the pulse rate in the Y channel must be twice the pulse rate in the X channel.

The block diagram of Fig. 3 illustrates the functional units needed for a vector channel. A digital to analog (D-A) converter converts the digital representation of position to a voltage which deflects the writing beam of electrons in the CRT. The output register holds the instantaneous position for the D-A converter. This register is loaded from the interface with the initial point of the vector. It counts the pulse train from the BRM, thus stepping from the initial to the final point. A comparator controls the stepping process by indicating the direction to count, up or down, and by stopping the counting when the final point has been reached. The equality signal is also used by the control logic to determine when the vector is complete. The endpoint of the vector is stored in the temporary register, where it is available to both the comparator and the subtractor. Using the initial and final values stored in the registers, the subtractor computes the difference in 2's complement form. Since a BRM can accept only positive rates, the absolute value of the difference is formed using a conditional complementor.

The rate formed above could be used directly to control the BRM, but all vectors would take the same time to complete, thus making shorter vectors brighter than longer ones. To eliminate this problem, the rates for both X and Y channels are shifted left until the larger of the two reaches the most significant bit of its respective register. Since it is possible for both rates to be zero, a 1 is inserted in the least bit of each rate register to insure that the shifting process stops. The signals labeled "Load," "Shift," and "Max" control the operation of the rate register. After shifting stops, the clock is turned on, and the BRM begins producing output pulses at the proper rate. The clock is coherent with the computer clock and runs at 1 MHz. The time to draw a vector is proportional to its length on the axis plus the shifting time. Thus the minimum time will be 13 μs and the maximum will be 4099 μs.

The circuitry used for the above functions is of the medium scale integration type, packaged in dual-in-line form. These are inserted in a logic board where connections are made with wire-wrap (Fig. 4). Cascadeable BRM packages containing 6 stages, register packages of 4 bits each, and a computer word of 16 bits lead to the selection of 12 bits for register length. This was consistent with the required resolution and linearity.

III. Using the Vector Generator

The following section will assume that the reader is familiar with the MAC 16 computer and the MAC 16 assembly language, LEAP 8 (Refs. 4 and 5).

Commands to the display can be separated into two types: those that control the general display, such as "Erase," and those that refer to the vector generator itself. All of the commands are used in the following sequence:

```
LDA   DATA
EXO   UNIT,FUNCTION
JMP   *-1
```

Here EXO stands for either External Command Out (ECO), or External Data Out (EDO). The instruction following the EXO is skipped only when the device addressed has accepted the data and has acknowledged receipt of them, thus providing a ready test.

While general display commands use only the least three bits of the data word, all 16 bits are used to command the vector generator. Table 1 lists these two formats, enumerates the options included in each data type, and shows the instructions that can be used with each. The control bits, the least three for the general commands and the least four for the vector commands, operate independently and their functions will be merged. For the display commands it is necessary to specify all of the conditions required in one command as subsequent instructions will change all of these conditions. The nature of the vector commands does not place such a constraint upon their use. For these instructions the merging is for the convenience of the programmer. Bit 13 of the general display command data selects the input to the analog multiplexer. If it is a 1, the vector generator is connected to the display. A zero connects the character generator. Bit 14, when a 1, interchanges the roles of the X and Y channels producing a 90-deg rotation in the display. Bit 15 enables the interrupt pulse generated at the completion of vector generation to be sent to the computer. Bits 12 and 13 of the vector commands specify the destination for the point location data within the vector generator. This may be combined with the write/do not write (bit 14) and initiate vector generation (bit 15) subfunctions. The point location data have no meaning for these two subfunctions.

The expression field of the external command instruction is composed of two parts: the unit address or device number, which for the display system is a hexidecimal "D"; and the function or sub-address. Only 3 of the 16 possible function addresses are used with the vector generator: "3" calls for the display to be erased, "E" causes the display control bits to be accepted by the display interface, and "F" transfers the 12-bit position data to the vector generator as specified by the control bits of the word. When the data are transmitted with an EDO instruction, both the output and the temporary registers are loaded with the data. An ECO instruction only loads the data into the temporary register. Viewed in another way, the EDO instruction sets the initial point for the vector while the ECO sets the final point. It should be noted that the initial point must be loaded first as the temporary register is also loaded by the EDO command. The data formats of Table 1 and the summary of instructions in Table 2 provide a reference for the use of the vector generator. Further, it is important to note that the final point of the first vector can be used as the initial point of the next vector without reloading it, as it is remembered by the output register.

The sample program of Fig. 5 illustrates the use of all these commands. While the comments included in the program listing explain most of the points of the program, a description of the way in which these parts form a whole will aid in understanding the program. The "START" routine initializes the display system in the vector mode. It also sets it to operate under interrupt control, initializes the program for interrupt control, and forces the first interrupt from the display. This first interrupt shifts the computations to the display control level. "VECT" plots the first point on the display (as this is a unique point), and "VECTC" plots the remainder of the points. After all of the points have been plotted, the "VECTE" routine restores the computer to the normal level and disconnects the display from the vector generator. The points to be plotted are contained in a table, "TABLE," and have the control bits in the lower portion of the word as stored. The results of running this program are shown, simulated, with the points labeled, in Fig. 6. The numbers associated with each point refer to the data values in "TABLE" with the same number. A solid line indicates that a line was drawn and a dashed line indicates the path taken by the beam without writing on the scope.

IV. Conclusion

The equipment described in this report has been built, tested, and demonstrated in the laboratory in a form that can be installed in the field. The vector generator reduces the demand for computer processing time to less than 15 μs per endpoint. The high-speed, on-line display of graphic information will permit the real-time display of spectra used for signal power measurement and similar systems.

Further, this technique, with only minor hardware modifications, can be applied to a vector generator for the slower mechanical X–Y plotters, relieving a computer controlling such a device of vast amounts of processing time.

References

1. Winkelstein, R., "Precision Signal Power Measurement," in *JPL Quarterly Technical Review*, Vol. 2, No. 2, pp. 18–24. Jet Propulsion Laboratory, Pasadena, Calif., July 1972.
2. Newton, J. W., "Digital Device Development: Precise Measurement of Spacecraft Signal Power," in *The Deep Space Network*, Space Programs Summary 37-58, Vol. II, pp. 42–50. Jet Propulsion Laboratory, Pasadena, Calif., July 31, 1969.
3. *Instruction Manual for Type 611 Storage Display Unit*, Tektronix, Inc., Beverton, Oregon, 1968.
4. *MAC-16 Computer Reference Manual*, Lockheed Electronics Company, Los Angeles, Calif., Jan. 1970.
5. *LEAP Assembly Manual*, Lockheed Electronics Company, Los Angeles, Calif., Jan. 1970.

Table 1. Data format

Used with	Function	Data words						
		0 1 2 3	4 5 6 7	8 9 10 11	12	13	14	15
ECO $D,$E	General display commands							
	Select vector generator	←	Not used	→		1	x	x
	Select character generator					0	x	x
	Exchange X and Y outputs to display					x	1	x
	Enable interrupt from vector generator					x	x	1
ECO $D,$F or EDO $D,$F	Vector generator commands							
	Select X channel	S ←		Point location →	1	x	x	x
	Select Y channel			Point location	x	1	x	x
	Z on (write)			Point location	x	x	1	x
	Z off (do not write)			Point location	x	x	0	x
	Initiate vector generation			Point location	x	x	x	1

Notes: 1. S = sign bit (2's complement form)
2. x = don't care
3. Functions may be merged
4. For vector commands: EDO loads initial point
ECO loads final point

Table 2. Display instructions

Instruction	Function
ECO $D,3	Erase the display
ECO $D,$E	General display command
ECO $D,$F	Vector generator command load final point
EDO $D,$F	Vector generator command load initial point

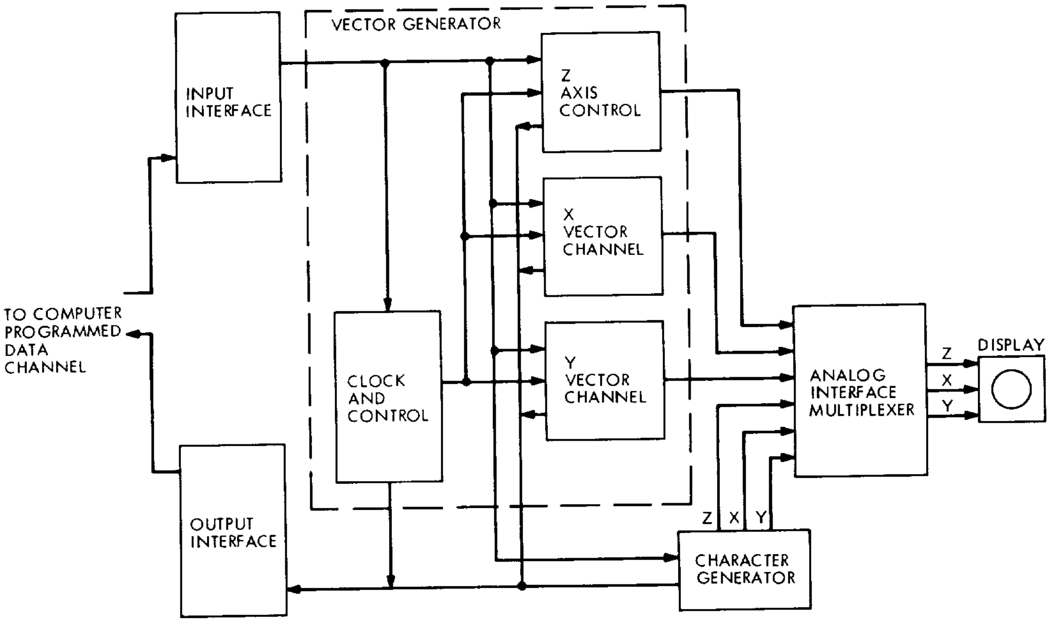

Fig. 1. Display system block diagram

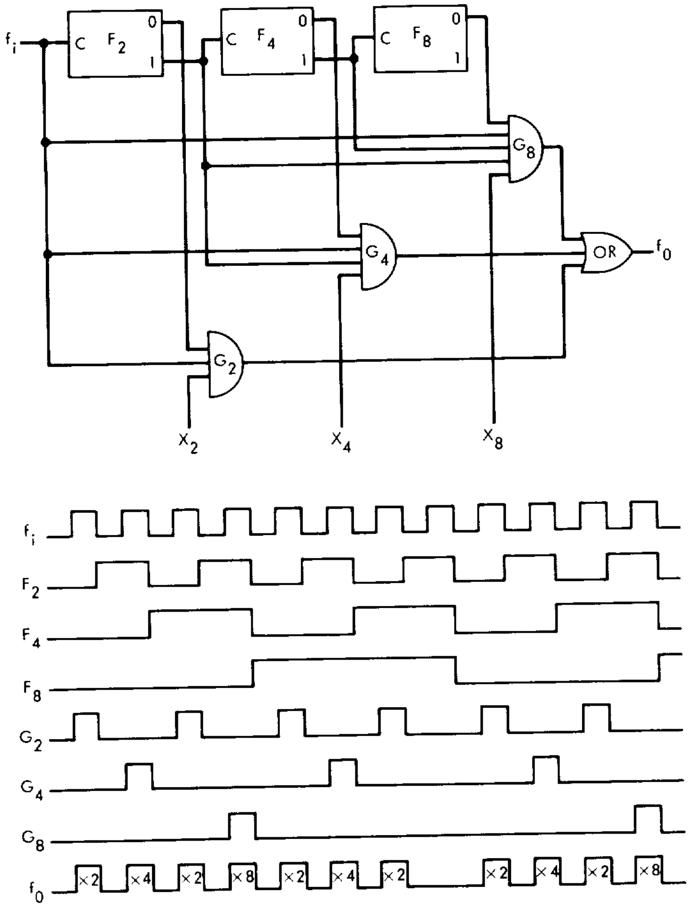

Fig. 2. Binary rate multiplier

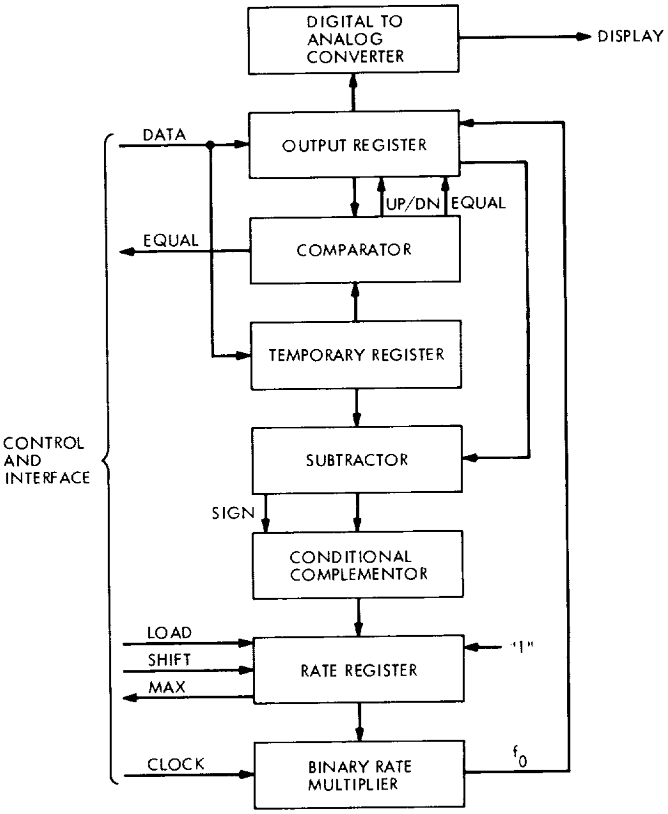

Fig. 3. Block diagram of vector generator channel

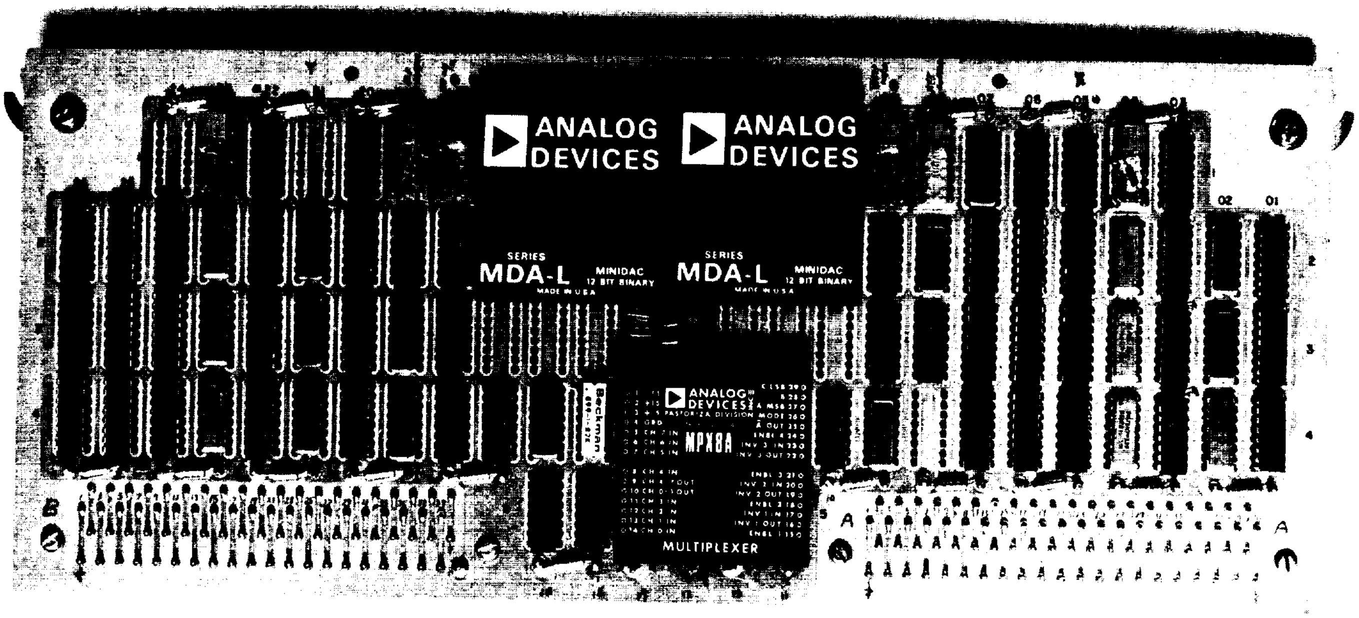

Fig. 4. Vector generator logic board

```
         BOOT
         ORG   $400
*SAMPLE PROGRAM FOR VECTOR GENERATOR
*RUN UNDER INTERRUPT
*
*INITIALIZE VECTOR GENERATOR
*
START    LDA   =VECT          ADDRESS OF VECTOR ROUTINE
         STA   *PILOC         INTERRUPT LOCATION POINTER
         ECO   $D,3           ERASE SCREEN
         JMP   *-1
         LDI   5              CONNECT VECTOR GENERATOR
         ECO   $D,$E          AND ENABLE INTERRUPT
         JMP   *-1
         LDI   1              FORCE AN INTERRUPT FROM THE
         ECO   $D,$F          VECTOR GENERATOR
         JMP   *-1
         JRL   *+1            PAUSE-HIT "SOP" TO CONTINUE
         JMP   START          GO AGAIN
*
*THE COMPUTER AND VECTOR GENERATOR ARE NOW WORKING IN CONSORT
*
VECT     LDX   MN2            (X) = -TWICE THE NO. OF POINTS
         LDA   ETABLE,1       GET THE INITIAL X POINT
         EDO   $D,$F
         JMP   *-1
         LDA   ETABLE+1,1     GET THE INITIAL Y POINT
         EDO   $D,$F
         JMP   *-1
QUIT     INX   2
         JRL   VECTC          CONTINUE PLOTTING
         JRL   VECTE          END PLOTTING
VECTE    CLA
         ECO   $D,$E          CLEAR DISPLAY FROM VECTOR
         JMP   *-1
         JRL   VECT           SETUP FOR NEXT VECTOR SET
*
VECTC    LDA   ETABLE,1       GET THE NEXT X POINT
         ECO   $D,$F
         JMP   *-1
         LDA   ETABLE+1,1     GET THE NEXT Y POINT
         ECO   $D,$F
         JMP   *-1
         JMP   QUIT
*TABLE OF PLOTTED POINTS
*
TABLE    DC    $8008,$8004    1 INITIAL POINT -- LL
         DC    $7FF8,$7FF7    2 DIAGONAL FROM LL TO UR
         DC    $0,$5          3 POSITION AT MR
         DC    $8008,$3       4 DRAW X AXIS
         DC    $0,$7FF5       5 POSITION AT UL
         DC    $7FF8,$8007    6 DIAGONAL FROM UL TO LR
         DC    $8,$1          7 POSITION AT LM
         DC    $0,$7FF7       8 DRAW Y AXIS
ETABLE   EQU   *
MN2      DC    TABLE-ETABLE
         END   START
```

Fig. 5. Sample program

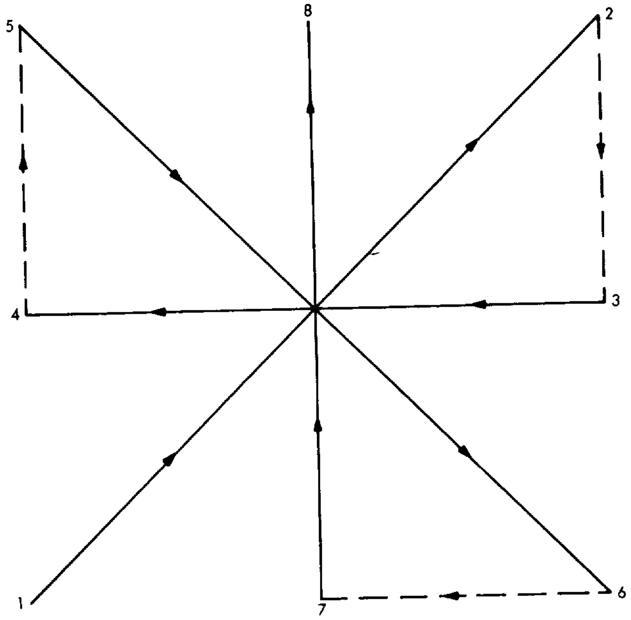

Fig. 6. Sample program output plot

Data Storage and Data Compression II

C. Lam
Communications Systems Research Section

In a recent article, Odlyzko showed that under certain idealized circumstances, a small increase in data storage capability can lead to a dramatic increase in the rate at which data can be communicated reliably. In this article a detailed investigation is made of the circumstances under which the maximum possible rate increase will occur.

I. Introduction

In a recent article, Odlyzko (Ref. 1) showed that under certain idealized circumstances, a small increase in data storage capability can lead to a dramatic increase in the rate at which data can be communicated reliably. In this article we will investigate in detail the circumstances under which the maximum possible rate increase will occur.

Let X be a set, whose elements are to be regarded as the possible outcomes of some experiment. Let S be a collection of subsets of X; we assume that when a sample $x \in X$ is obtained, the experimenter is satisfied in knowing only some $A \in S$ such that $x \in A$. The sets A of S are therefore sometimes called the *subsets of allowed uncertainty.* As explained in detail in (Ref. 1), if n_N denotes the minimum number of sets of the form $A_1 \times A_2 \times \cdots \times A_N$ needed to cover $X \times \cdots \times X$ (N copies of X), then if the data handling system can store N samples prior to transmission the data rate is proportional to $N/\log n_N$. Odlyzko showed that n_N can sometimes be as small as $Nn_1 - N$; i.e., the best possible increase in data rate is *linear* in the amount of storage. This is quite remarkable since for most systems $N/\log n_N$ is a constant, or nearly so, independent of N. Our goal here is to investigate the circumstances under which $n_N = Nn_1 - N$, and some related questions.

Let S be a collection of subsets of a set X such that their union is X. Define $c\,(X; S)$, the *covering number* of X with respect to S, to be the minimal number of elements of S

whose union is X, if this number exists, and infinity if no finite subcollection of S covers X. If $S_1, \cdots, S_N$ are collections of subsets of $X_1, \cdots, X_N$ respectively, define a collection $S_1 \times \cdots \times S_N$ of subsets of the Cartesian product $X_1 \times \cdots \times X_N$ by

$$S_1 \times \cdots \times S_N = \{A_1 \times \cdots \times A_N \,|\, A_i \epsilon S_i, \quad i = 1, \cdots, N\}$$

We will restrict ourselves to the case in which all the $c(X_i; S_i)$ are finite, since otherwise

$$c(X_1 \times \cdots \times X_N; S_1 \times \cdots \times S_N) = \infty$$

Odlyzko (Ref. 1) obtained an upper bound

$$c(X_1 \times \cdots \times X_N; S_1 \times \cdots \times S_N) \leq \prod_{i=1}^{N} c(X_i; S_i) \qquad (1)$$

and a lower bound

$$c(X_1 \times \cdots \times X_N; S_1 \times \cdots \times S_N) \geq \sum_{i=1}^{N} [c(X_i; S_i) - 1] + 1 \qquad (2)$$

The surprising result is that equality can be attained in Eq. 2, and in Ref. 1 Odlyzko gives a construction for it. In Subsection II of this paper, we will give an equivalent version of the problem in (0, 1)-matrix terms. In Subsection III, we will give a necessary and sufficient condition that the lower bound of Eq. 2 is obtained by a given partition. In particular, we will show that the Odlyzko constructions give essentially the only case that achieves the lower bound. In Subsection IV, we will give some conditions on when the upper bound of Eq. 1 is obtained.

II. Formulation of Problem as a (0,1)-Matrix Problem

A (0, 1)-matrix of size r by s is a matrix with r rows and s columns, in which all the entries are either 0 or 1. We now associate a (0, 1)-matrix with a set X and S, a collection of subsets of X.

Let $X = \{a_1, \cdots, a_r\}$, $S = \{A_1, \cdots, A_s\}$. Define

$$b_{ij} = \left\{ \begin{matrix} 1 & \text{if } a_i \epsilon A_j \\ 0 & \text{otherwise} \end{matrix} \right\}$$

Then $B = \{b_{ij}\}$ is a (0, 1)-matrix of size $r \times s$, and it represents the relationships between X and S.

We will call the minimum number of columns of a (0, 1)-matrix that has at least one 1 in each row the *1-width* of the matrix. So, $c(X; S)$ is just the 1-width of the matrix B representing X and S. We write $\epsilon(B)$ for the 1-width of B.

If B, C are (0, 1)-matrices, let

$$B = \left\{ \begin{matrix} b_{11} & \cdots & b_{1s} \\ \cdot & & \\ \cdot & & \\ \cdot & & \\ b_{r1} & \cdots & b_{rs} \end{matrix} \right\}$$

The Cartesian (tensor) product is

$$B \times C = \left\{ \begin{matrix} b_{11}C & \cdots & b_{1s}C \\ \cdot & & \\ \cdot & & \\ \cdot & & \\ b_{r1}C & \cdots & b_{rs}C \end{matrix} \right\}$$

where $b_{ij}C$ denotes multiplying all the entries of C by b_{ij}. The matrix $B \times C$ is obtained by placing these blocks of matrices side by side.

It can be easily shown that if B represents X_1 and S_1, and D represents X_2 and S_2, then the product $B \times D$ represents the product $S_1 \times S_2$. Therefore

$$\epsilon(B \times D) = c(X_1 \times X_2; S_1 \times S_2)$$

The results in Subsection I are now translated to

$$\epsilon(B_1 \times \cdots \times B_N) \leq \prod_{i=1}^{N} \epsilon(B_i) \qquad (3)$$

$$\epsilon(B_1 \times \cdots \times B_N) \geq \sum_{i=1}^{N} (\epsilon(B_i) - 1) + 1 \qquad (4)$$

From now on, we will work with the matrix version of the problem, which should be easier to visualize.

III. Conditions for Achievement of Lower Bound

We start this section off with some elementary observations about the 1-width of a (0, 1)-matrix.

A column (row) c_1 is said to *cover* another column (row) c_2 if whenever there is a 1 in the column (row) of c_2, there is a 1 in the corresponding position of c_1.

Property 1

If a row c_1 of a $(0,1)$-matrix A covers another row c_2 then the row c_1 can be removed without affecting $\epsilon(A)$.

Proof:

In any choice of columns of A which gives a 1 in each row, one of the columns must have a 1 in row c_2. Since row c_2 is covered by row c_1, a 1 must appear in row c_1 in the same column.

Property 2

If a column c_1 of a $(0,1)$-matrix A covers another column c_2, then c_2 can be removed without affecting $\epsilon(A)$.

Proof:

In any choice of columns which includes c_2, we could do as well or better by replacing column c_2 with c_1.

Note that the two processes above can be applied repeatedly to reduce the size of the matrix, which would make it easier to find the 1-width.

Given two integers ϵ, n with $n \geqq \epsilon > 0$, Odlyzko's construction gives a matrix of size

$$\binom{n}{n-\epsilon+1} \times n$$

with constant row sums $(n - \epsilon + 1)$, and the

$$\binom{n}{n-\epsilon+1}$$

rows represent all the possible ways of putting $(n - \epsilon + 1)$ 1s in n positions. We call such a matrix one of Odlyzko's type with parameters n and ϵ.

Example: $n = 5, \quad \epsilon = 3$

$$\binom{n}{n-\epsilon+1} = 10 \qquad \begin{array}{|cc|ccc|}
\hline
1 & 1 & 1 & 0 & 0 \\
1 & 1 & 0 & 1 & 0 \\
1 & 1 & 0 & 0 & 1 \\
\hline
1 & 0 & 1 & 1 & 0 \\
1 & 0 & 1 & 0 & 1 \\
1 & 0 & 0 & 1 & 1 \\
\hline
0 & 1 & 1 & 1 & 0 \\
0 & 1 & 1 & 0 & 1 \\
0 & 1 & 0 & 1 & 1 \\
\hline
0 & 0 & 1 & 1 & 1 \\
\hline
\end{array}$$

Theorem 1

The 1-width of a $(0,1)$-matrix of Odlyzko type is ϵ. Moreover, any choices of ϵ columns will have at least one 1 in each row.

Proof:

In every row, the row sum is $(n - \epsilon + 1)$, therefore there are only $(\epsilon - 1)$ 0's. So, in any choice of ϵ columns, it can at most contain $(\epsilon - 1)$ 0's in this row. Hence ϵ columns are enough to give at least one 1 in each row. On the other hand, if we take $(\epsilon - 1)$ columns, there is a row with all its $(\epsilon - 1)$ 0's in these columns. Hence $(\epsilon - 1)$ columns is not enough. Thus, the 1-width of the matrix is ϵ.

Odlyzko has proved the following theorem.

Theorem 2

If $B_1, \cdots, B_N$ are $(0,1)$-matrices with 1-width $\epsilon_1, \cdots, \epsilon_N$, then

$$\epsilon(B_1 \times \cdots \times B_N) \geqq \sum_{i=1}^{N} (\epsilon_i - 1) + 1 \qquad (5)$$

Proof: (See Ref. 1.)

We now investigate the conditions when equality in Eq. (5) is attained.

Theorem 3

Let $\epsilon_1, \cdots, \epsilon_N$ be positive integers, and let $B_1, \cdots, B_N$ be $(0,1)$-matrices with 1-width $\epsilon_1, \cdots, \epsilon_N$ respectively. The necessary and sufficient condition for

$$\epsilon(B_1 \times \cdots \times B_N) = \sum_{i=1}^{N} (\epsilon_i - 1) + 1 = n$$

is that for every B_i, there exists a submatrix of n columns which reduces, by repeated applications of property 1, to a submatrix of the Odlyzko type with parameters n and ϵ_i.

Proof:

Assume first that $\epsilon(B_1 \times \cdots \times B_N) = n$.

We focus our proof on matrix B_1, the others follow in a similar manner.

Let

$$B_1 = \begin{pmatrix} b_{11} & \cdots & b_{1s} \\ \cdot & & \\ \cdot & & \\ \cdot & & \\ b_{r1} & \cdots & b_{rs} \end{pmatrix}$$

We can write $B_1 \times \cdots \times B_N$ as

$$B_1 \times \cdots \times B_N =$$

$$\begin{bmatrix} b_{11}(B_2 \times \cdots \times B_N) & \cdots\cdot & b_{1s}(B_2 \times \cdots \times B_N) \\ \cdot & & \\ \cdot & & \\ \cdot & & \\ \cdot & & \\ \cdot & & \\ \cdot & & \\ b_{r1}(B_2 \times \cdots \times B_N) & \cdots\cdot & b_{rs}(B_2 \times \cdots \times B_N) \end{bmatrix}$$

We will call

$$[b_{i1}(B_2 \times \cdots \times B_N) \cdots b_{is}(B_2 \times \cdots \times B_N)]$$

the i-th row block and

$$\begin{bmatrix} b_{1j}(B_2 \times \cdots \times B_N) \\ \cdot \\ \cdot \\ \cdot \\ \cdot \\ b_{rj}(B_2 \times \cdots \times B_N) \end{bmatrix}$$

the j-th column block of $B_1 \times \cdots \times B_N$.

We are given a set of n columns such that there is a 1 in each row. We pick n columns of B_1 in the following manner. For every column in the set, we locate the column block that contains it. If the column is contained in block i, say, we take column i of B_1. Thus we can pick n columns, but at this point, there may be repeated columns among them.

We now prove that for the n columns of B_1, the row sums are at least $n - \epsilon_1 + 1$. If there is a row, say row 1, with row sum less than $n - \epsilon_1 + 1$, say α, we take the α columns which have a 1 in row 1. This in turn will give us α columns of the original n columns which gave us the 1-width of $B_1 \times \cdots \times B_N$. We focus our attention to the first row block. These α columns give us a 1 in each of the rows of the first row block. The same α columns will give us a 1 in each row for $B_2 \times \cdots \times B_N$, if we only take the first row block as $B_2 \times \cdots \times B_N$ copies many times (as many as the first row sum of B_1). Thus we have

$$\epsilon(B_2 \times \cdots \times B_N) \leqq \alpha < n - \epsilon + 1 = \sum_{i=2}^{n} (\epsilon_i - 1) + 1$$

contradicting Theorem 2. Therefore we have proved that the row sums of the chosen in columns of B_1 are all greater than or equal to $n - \epsilon_1 + 1$. In other words, there are at most $(\epsilon_1 - 1)$ zeros in each row.

We will now show that in these n columns of B_1 and for every possible choice of $(\epsilon_1 - 1)$ positions out of n, there is a row with $(\epsilon_1 - 1)$ zeros in these $(\epsilon_1 - 1)$ places. If this is not true, there will be a choice of $(\epsilon_1 - 1)$ columns with at least one 1 in each row. Then, the 1-width of B_1 is less than ϵ_1, a contradiction. This fact, by the way, also proves that there are no repeated columns among the n columns.

So, we have now n columns of B_1, and

$$\binom{n}{n - \epsilon_1 + 1}$$

rows of these columns with $(\epsilon_1 - 1)$ zeros in all the possible

$$\binom{n}{\epsilon_1 - 1} = \binom{n}{n - \epsilon_1 + 1}$$

positions. Let us call this submatrix B'. This is a submatrix of Odlyzko type.

In those n columns, if there were any other rows not yet contained in B', the row sum must still be at least $(n - \epsilon_1 + 1)$. Since we have all the possible

$$\binom{n}{n - \epsilon_1 + 1}$$

choices already, the extra row will cover one of the

$$\binom{n}{n - \epsilon_1 + 1}$$

rows. Thus by property 1, it can be removed without affecting the 1-width of the matrix.

Thus, we have proved half of the theorem.

We now assume that $B_1, \cdots, B_N$ contains a submatrix satisfying the conditions in the statement of the theorem.

We first show that the rows removed will not affect the 1-width of the product. Let us assume that the n columns are the first n columns of B_1. As before, we write

$$B_1 \times \cdots \times B_N = \begin{bmatrix} b_{11}(B_2 \times \cdots \times B_N) \cdots b_{1n}(B_2 \times \cdots \times B_N) \cdots b_{1s}(B_2 \times \cdots \times B_N) \\ \vdots \\ b_{r1}(B_2 \times \cdots \times B_N) \cdots b_{rn}(B_2 \times \cdots \times B_N) \cdots b_{rs}(B_2 \times \cdots \times B_N) \end{bmatrix} \tag{6}$$

Say, if row r covers row 1 in B_1, then the columns that cover the first row block will cover the r-th row block in Eq. (6). Hence it is enough just to consider the product of the submatrices of Odlyzko type. He proved that the 1-width of the product matrix is n. Anyway, if we write the n columns of B_i as $\{B_{i1}, \cdots, B_{in}\}$, it is not difficult to prove that the n columns given by

$$\prod_{i=1}^{N} B_{i1}; \cdots ; \prod_{i=1}^{N} B_{in}$$

will have at least one 1 in each row. Q.E.D.

IV. Conditions for Achievement of Upper Bound

We will now study the conditions when the upper bound

$$\epsilon(A \times B) = \epsilon(A) \times \epsilon(B) \tag{7}$$

is obtained.

Definition:

A (0, 1)-matrix A of size r by s is said to satisfy the *minimal condition* if its 1-width is also the value of the following linear program:

minimize

$$\sum_i y_i$$

subject to the conditions

$$\left. \begin{array}{l} AY \geq \begin{pmatrix} 1 \\ \vdots \\ 1 \end{pmatrix} \\ Y \geq \begin{pmatrix} 0 \\ \vdots \\ 0 \end{pmatrix} \end{array} \right\} \tag{8}$$

where $Y = (y_1, \cdots, y_s)^T$ is a column vector.

This definition is not as strange as it first seems. The 1-width of A is just the same linear program with the extra condition that components of Y are either 0 or 1. The minimal condition just states that among the solutions to the linear program, one can find a solution with the components of Y either a 0 or 1.

The following gives a sufficient condition for Eq. (7) to be true.

Theorem 4

If a (0, 1) matrix A satisfies the minimal condition then $\epsilon(A \times B) = \epsilon(A) \times \epsilon(B)$ for any (0, 1)-matrix B.

Proof:

Let

$$A = \begin{pmatrix} a_{11} & \cdots & a_{1s} \\ \vdots & & \\ a_{r1} & \cdots & a_{rs} \end{pmatrix}$$

and we write

$$A \times B = \begin{pmatrix} a_{11}B & \cdots & a_{1s}B \\ \vdots & & \\ a_{r1}B & \cdots & a_{rs}B \end{pmatrix}$$

We will define the i-th column block and j-th row block in the same way as before.

Suppose we have a set of columns of $A \times B$ that gives the 1-width, and suppose that x_i columns come from the i-th column block. Furthermore, assume that

$$\sum_{i=1}^{s} x_i$$

which is the 1-width of $A \times B$, is smaller than $\epsilon(A) \times \epsilon(B)$.

Consider, say, the first row of A,

$$\sum_{i=1}^{s} a_{1i}x_i$$

gives the number of columns of B picked up in the first row block. This number must be greater than the 1-width of B. Hence we have

$$A\begin{pmatrix} x_1 \\ \cdot \\ \cdot \\ \cdot \\ x_s \end{pmatrix} \geqq \begin{pmatrix} \epsilon(B) \\ \cdot \\ \cdot \\ \cdot \\ \epsilon(B) \end{pmatrix}$$

or

$$\frac{1}{\epsilon(B)} A\begin{pmatrix} x_1 \\ \cdot \\ \cdot \\ \cdot \\ x_s \end{pmatrix} \geqq \begin{pmatrix} 1 \\ \cdot \\ \cdot \\ \cdot \\ 1 \end{pmatrix}$$

or

$$A\left(\frac{1}{\epsilon(B)}\begin{pmatrix} x_1 \\ \cdot \\ \cdot \\ \cdot \\ x_s \end{pmatrix}\right) \geqq \begin{pmatrix} 1 \\ \cdot \\ \cdot \\ \cdot \\ 1 \end{pmatrix}$$

Since $\epsilon(A \times B) < \epsilon(A) \times \epsilon(B)$, we have

$$\sum_{i=1}^{s} x_i < \epsilon(A) \times \epsilon(B)$$

Thus

$$\frac{1}{\epsilon(B)} \sum_{i=1}^{s} x_i < \epsilon(A)$$

which implies that A does not satisfy the minimal condition.

Q.E.D.

In a way, the converse of the above theorem is true.

Theorem 5

If a (0, 1)-matrix A does not satisfy the minimal conditions, then there exists a (0, 1)-matrix B such that

$$\epsilon(A \times B) < \epsilon(A) \times \epsilon(B)$$

Moreover, B can be chosen so that it is symmetric, square, and has 1's in its main diagonal.

First of all, we will state the following lemma. The result is given in Ref. 3. It is also not difficult to construct the matrix.

Lemma

Given positive integers n and c with $n > c$, a symmetric (0, 1)-matrix E exists with the following properties:

(1) The order of E is at least n.

(2) E has 0s in the main diagonal.

(3) E has constant line sum c.

(4) E has no repeated rows.

Proof (of Theorem 5):

We need only construct a matrix B such that

$$\epsilon(A \times B) < \epsilon(A) \times \epsilon(B)$$

Since A does not satisfy the minimal condition, there exists a vector

$$\begin{pmatrix} x_1 \\ \cdot \\ \cdot \\ \cdot \\ x_s \end{pmatrix}$$

satisfying Eq. (8) such that

$$\sum_{i=1}^{s} x_i < \epsilon(A) \tag{9}$$

The vector

$$\begin{pmatrix} x_1 \\ \cdot \\ \cdot \\ \cdot \\ x_s \end{pmatrix}$$

can be obtained by the simplex method in linear programming. All the x_i's will be rational numbers. Hence there exists an integer k such that kx_i is an integer for all i, and

$$\sum_{i=1}^{s} kx_i < k\epsilon(A) \tag{10}$$

We will construct B such that $\epsilon(B) = k$, and

$$\epsilon(A \times B) \leqq \sum_{i=1}^{s} kx_i$$

$(=N$, say). It will have the properties promised by the theorem.

We first construct a (0, 1)-matrix E as promised in the lemma, with $n = N$ and line sum $c = k - 1$. The order of E will be M. In fact we can choose M as big as we like as long as $M \geqq n$. We will take $M > 3k - 4$ as well as $\geqq N$.

Now we take $(J - E)$. This is again a symmetric matrix with 1's in the main diagonal and $(k - 1)$ zeros on each row. Moreover, no two of the rows will have all its zeros in the same $(k - 1)$ places. So, the matrix $(J - E)$ is just a submatrix of an Odlyzko matrix with parameters M and k. We now construct B as

$$B = \begin{array}{cc} & \overbrace{\hphantom{J-E}}^{M} \\ M\left\{\vphantom{P^T}\right. & \left[\begin{array}{c|c} J-E & P^T \\ \hline P & I \end{array}\right] \end{array} \left.\vphantom{\begin{array}{c} J \\ P \\ I \end{array}}\right\}\binom{M}{k-1}$$

where P is the remaining rows of the Odlyzko matrix. Clearly B is a symmetric and square matrix. The first M columns of B has 1-width k. So,

$$\epsilon(B) \leqq k$$

Suppose the 1-width is less than k, then, there are $(k-1)$ columns that have one 1 in each row. At most $(k - 2)$ of these columns can be in the first M, or else it contradicts the fact that the 1-width of the first M columns is k. Considering the first M columns only, we will have at least $M - (k - 2)$ rows with no 1's in them. These rows had better be covered by the remaining columns. In the submatrix $(J - E)$, there are $(k - 1)$ zeros in each column. So there are at least $M - (k - 2) - (k - 1) = M - (2k - 3)$ rows that have no 1's in the part P. We can at most cover up $(k - 1)$ rows with columns from I. So, if we choose M so large that

$$M - (2k - 3) > (k - 1)$$

or

$$M > 3k - 4$$

we will have a contradiction. This explains the choice of M.

The last thing left to be proved is that

$$\epsilon(A \times B) \leqq \sum_{i=1}^{s} kx_i$$

To establish this, we only need to consider $A \times B'$ where B' is the first M columns of B. We write

$$A \times B' = \begin{bmatrix} a_{11}B' & \cdots & a_{1s}B' \\ \cdot & & \\ \cdot & & \\ \cdot & & \\ a_{r1}B' & \cdots & a_{rs}B' \end{bmatrix}$$

We now pick $\sum_{i=1}^{s} kx_i$ columns in the following manner:

column block number	number of columns picked	starting at
1	$k \times 1$	1
2	$k \times 2$	$kx_1 + 1$
3	$k \times 3$	$k(x_1 + x_2) + 1$
·	·	
·	·	
·	·	
s	$k \times s$	$k(x_1 + x_2 + \cdots + x_{s-1}) + 1$

Since the vector $\begin{pmatrix} x_1 \\ \cdot \\ \cdot \\ \cdot \\ x_s \end{pmatrix}$ satisfies Eq. (7), we have

$$Ak \begin{pmatrix} x_1 \\ \cdot \\ \cdot \\ \cdot \\ x_s \end{pmatrix} \geqq \begin{pmatrix} k \\ \cdot \\ \cdot \\ \cdot \\ k \end{pmatrix}$$

This means we have picked at least k different columns of B' in each row block of $A \times B'$. Thus the 1-width of $A \times B'$ is at most

$$\sum_{i=1}^{s} kx_i$$

In turn, it means

$$\epsilon(A \times B) \leqq \sum_{i=1}^{s} kx_i$$

Q.E.D.

V. Acknowledgments

I would like to thank R. J. McEliece for proposing these problems and for his help. I would also like to thank H. J. Ryser for many stimulating conversations.

References

1. Odlyzko, A. M., "Data Storage and Data Compression," in *The Deep Space Network Progress Report*, Technical Report 32-1526, Vol. VI, pp. 112–117, Jet Propulsion Laboratory, Pasadena, Calif., Dec. 15, 1971.
2. Ryser, H. J., *Combinatorial Mathematics*, Wiley, New York, 1963.
3. Fulkerson, D. R., Hoffman, A. J., and McAndrew, M. H., "Some Properties of Graphs with Multiple Edges," *Canadian J. Math.*, Vol. 17, pp. 166–177, 1965.

A Study of Varshamov Codes for Asymmetric Channels

R. P. Stanley[1] and M. F. Yoder[2]
Communications Systems Research Section

An important class of single-error-correcting codes for binary and nonbinary discrete asymmetric channels recently discovered by Varshamov is studied. Among other things, a wide generalization of Varshamov's construction is given, and the complete weight distribution of Varshamov's codes is calculated.

I. Introduction

Recently Varshamov (Ref. 1) discovered an impressive class of single-error-correcting codes for the binary asymmetric, or "Z" channel. (The reason for the letter "Z" appears in Fig. 1.)

In the Z channel, a 0 is always transmitted reliably but 1 may be received as either 1 or 0. Actual physical channels, in particular the Ground Communications Facility (GCF), usually exhibit some degree of asymmetry, and so a study of the Z channel provides insight into the effects of asymmetry on practical data-processing systems.

It is the object of this paper to extend Varshamov's work in several directions. In Subsection II, Varshamov's codes will be introduced, and a larger class of single-error-correcting codes will be described that contain Varshamov codes as a proper subset. Estimates on the number of codewords in these codes will be obtained, and a general upper bound on the number of words in *any* single-error-correcting code for the Z channel will be obtained. In Subsection III, the exact number of codewords in each of Varshamov's codes will be calculated; indeed the complete weight distribution of each code will be found. (In fact in Subsection III we will consider q-ary, rather than binary, codes, where q is an arbitrary integer.)

II. A Generalization of the Binary Varshamov Codes

Varshamov's single-error correcting codes for the binary Z channel may be described as the set of all vectors $(e_1, e_2, \cdots, e_n)$ with $e_i = 0$ or 1, such that

$$\sum_{i=1}^{n} ie_i \equiv d \pmod{n+1}$$

for a fixed d. There are, then, $n+1$ distinct Varshamov codes of length n, one for each choice of d. A generalization of this construction that immediately suggests itself is the following: let G be an arbitrary group of order $n+1$, and let $g_1, g_2, \cdots, g_n$ be an ordering of the non-identity elements of g. For a fixed $d \epsilon G$ consider the set of $\{0, 1\}$ vectors $(e_1, e_2, \cdots, e_n)$ such that

$$\prod_{i=1}^{n} g_i^{e_i} = d \tag{1}$$

---

[1] Consultant, University of California, Berkeley, Calif.

[2] Student at the California Institute of Technology, Pasadena, Calif.

Varshamov's codes are the special case where G is a cyclic group. Unfortunately in this generality the sets of $\{0,1\}$ vectors thus formed are not necessarily single-error correcting codes for the Z channel. We must restrict both the group G and the ordering of the elements of G, as in Theorem 1.

Theorem 1

Let G be a group of order $n+1$ such that every element commutes with all of its conjugates (e.g., if G is abelian or nilpotent of rank 2 this condition is satisfied). Let $g_1, g_2, \cdots, g_n$ be an ordering of the nonidentity elements of G with the property that the conjugacy classes appear serially; i.e., every conjugacy class appears as a set of consecutive elements $g_m, g_{m+1}, \cdots, g_{m+k}$ in the ordering. Then for every $d \in G$, the set of $\{0,1\}$ vectors $(e_1, e_2, \cdots, e_n)$ which satisfy Eq. (1) is a single-error correcting code for the Z channel.

Proof:

We first observe that no two vectors satisfying Eq. (1) differ in only one position; for if $(e_1, \cdots, e_i, \cdots, e_n)$ and $(e_1, \cdots, \bar{e}_i, \cdots, e_n)$ both satisfy Eq. (1), we would have

$$w_1 g_i w_2 = d = w_1 w_2$$

where

$$w_1 = g_i^{e_1} \cdots g_{i-1}^{e_{i-1}}, \qquad w_2 = g_{i+1}^{e_{i+1}} \cdots g_n^{e_n}$$

But then $g_i = 1$, a contradiction. Also, it is easy to prove that there cannot be two vectors such that a single error in one produces the same result as a single error in the other; for in such a case there would result an equation

$$w_1 g_i w_2 w_3 = d = w_1 w_2 g_j w_3$$

Then $g_j = w_2^{-1} g_i w_2$, and so w_2, being a product of elements that lie between the conjugates g_i and g_j commutes with g_i and so $g_i = g_j$, another contradiction.

Of course we would like to know the number of codewords in each of the codes constructed in Theorem 1. Unfortunately this is a very difficult problem, for which we have only partial solutions. If G is cyclic, i.e., for Varshamov's original codes, a complete solution will be given in Subsection III. In the general case, we make the observation that the 2^n $\{0,1\}$ vectors are distributed into $n+1$ codes and so at least one such code contains at least $2^n/(n+1)$ codewords. On the other hand, Hamming's bound says that a single-error-correcting code for the binary *symmetric* channel has at *most* $2^n/(n+1)$ codewords. Thus unless $n = 2^m - 1$ for some m the asymmetric channel will support a larger single-error-correcting code than the symmetric channel will. If $n = 2^m - 1$ for some m the assertion very probably remains true, but the codes of Theorem 1 cannot be used to demonstrate that fact, because of Theorem 2.

Theorem 2

If $|G| = 2^m$, then all of the codes defined in Theorem 1 contain 2^{2^m-1-m} codewords; i.e. no more than the Hamming codes of the same length.

Proof:

It is easier to prove the more general statement that if $(g_1, g_2, \cdots, g_r)$ is a sequence of elements of G such that every element with the possible exception of 1 appears at least once, then the number of $\{0,1\}$ vectors $(e_1, e_2, \cdots, e_r)$ such that

$$\prod_{i=1}^{r} g_i^{e_i} = d \tag{2}$$

is independent of d. To prove this fact we induct on m, the case $m = 1$ being easily treated. For $m > 1$, let $z \neq 1$ be an element of order 2 in the center of G. For convenience we assume $g_1 = z$. Then if ϕ is the homomorphism from $G \rightarrow G/\{z\}$, and if Eq. (2) holds, we have

$$\prod_{i=2}^{r} \phi(g_i)^{e_i} = \phi(d) \tag{3}$$

Furthermore, every element $\neq 1$ of $G/\{z\}$ occurs among the $\phi(g_i)$, and so by induction the number of vectors $(e_2, \cdots, e_r)$ which satisfy Eq. (3) is independent of d. But if Eq. (3) is satisfied it follows that

$$\prod_{i=2}^{r} g_i^{e_i} = d \quad \text{or} \quad dz$$

and so there is a unique choice of e_1 that forces Eq. (2) to hold.

Although Theorem 2 shows that the codes of Theorem 1 are unimpressive when $n = 2^m - 1$, there is good reason to believe that codes of these lengths do exist with more than $2^n/(n+1)$ codewords, if $m \geq 3$. For $n = 7$, a code with 18 codewords exists:

0 0 0 0 0 0 0
0 1 0 0 0 1 0
0 0 1 0 0 0 1
0 0 0 1 1 0 0
0 1 1 1 0 0 0
0 0 0 0 1 1 1
1 1 0 0 1 0 0
1 0 1 0 0 1 0
1 0 0 1 0 0 1
1 1 1 0 0 0 1
1 0 0 1 1 1 0
0 0 1 1 0 1 1
0 1 0 1 1 0 1
0 1 1 0 1 1 0
1 1 0 0 1 1 1
1 0 1 1 1 0 1
1 1 1 1 0 1 0
1 1 1 1 1 1 1

It is in fact possible to show that no single-error-correcting code of length 7 for the Z channel can have 19 words. The above code was found ad hoc by hand calculation. A computer search might yield an $n = 15$ code with more than 2^{11} words, but a general construction is desirable.

We conclude this section with a general upper bound on the number M_n of codewords in a single-error-correcting code for the Z channel.

Theorem 3

$$M_n \leq B_{n+1}$$

where B_{n+1} is the maximum number of words possible for a single-error correcting code for the symmetric channel.

Proof:

There are two asymmetric binary channels: one that changes 0's to 1's, and one that changes 1's to 0's. It is an odd but easily checked fact that a code which corrects t errors on one of these channels will also correct t errors on the other. We use this fact to obtain the upper bound of Theorem 3.

For a given code of length n for the Z channel, construct a new code of length $n + 1$ by adding a "parity" bit to each codeword that is 0 if the weight of the codeword is congruent to 0 or 1 (mod 4) and is 1 if the weight is $\equiv 2$ or 3 (mod 4). Now this extended code will correct 1 error on the *symmetric* channel, since an error in the parity bit will be obvious (the first n bits will be a codeword from the original code, but the parity bit will not check), and if an error occurs elsewhere the parity bit will indicate whether it was a $0 \rightarrow 1$ or a $1 \rightarrow 0$ transition, and thus the error can be corrected. Thus $M_n \leq B_{n+1}$, the maximum number of words in a single-error-correcting code for the symmetric channel.

Corollary

$$M_n \leq \frac{2^{n+1}}{n+2}$$

Proof:

$$B_{n+1} \leq \frac{2^{n+1}}{n+2}$$

by Hamming's bond.

Remark:

It is very probable that Theorem 3 is quite weak, and that

$$M_n \leq \sim \frac{2^n}{n+1}$$

for large n.

III. The Weight Distribution of Varshamov's Codes

Let q, m, and d be natural numbers satisfying $q > 1$, $m > 1$, $1 \leq d \leq m$. Set $n = m - 1$. Let $C(q, n, d)$ be the set of all n-tuples (*vectors*) $e = (e_1, e_2, \cdots, e_n)$, where $e_i \in \{0, 1, 2, \cdots, q-1\}$, and

$$\sum_1^n ie_i \equiv d \pmod{m} \tag{4}$$

Then $C(q, n, d)$ is a single-error-correcting asymmetric code in the sense of Varshamov. Since multiplying Eq. (4) by a unit modulo m merely permutes the e_i's, from now on we assume without loss of generality that d divides m (written $d \mid m$).

If $e = (e_1, e_2, \cdots, e_n) \in C(q, n, d)$, define the weight $|e|$ by

$$|e| = e_1 + e_2 + \cdots + e_n \text{ (real addition)}$$

Although this definition of weight differs from the usual Hamming or Lee weights (except when $q = 2$), it is in accordance with Varshamov's usage.

Let $c_i = c_i(q, n, d)$ be the number of vectors in $C(q, n, d)$ of weight i, and define the *weight enumerator* $W(y) = W(q, n, d; y)$ by

$$W(y) = \sum_{i=0}^{\infty} c_i y^i$$

$W(y)$ is actually a polynomial since $c_i = 0$ for $i > (q-1)n$. Finally let $c = c(q, n, d) = |C(q, n, d)|$, so $c = \sum c_i = W(1)$. Our object is to obtain an expression for $W(y)$ and for $c(q, n, d)$.

Theorem 4

We have

$$W(q, n, d; y) =$$
$$\frac{1-y}{m(1-y^q)} \sum_{f \mid d} f \sum_{g \mid \frac{m}{f}} \mu(g) \frac{(1 - y^{fgq/(fg,q)})^{m(fg,q)/fg}}{(1-y^{fg})^{m/fg}}$$

where (fg, q) is the g.c.d. of fg and q.

Before proving Theorem 4, we first discuss some consequences.

Corollary 1

Let k be the largest factor of m relatively prime to q. Then

$$c(q,n,d) = \frac{1}{m}\sum_{f\,|\,(k,d)} f \sum_{g\,|\,\frac{k}{f}} \mu(g)\, q^{(m/fg)-1}$$

Proof of Corollary 1:

Set $y = 1$ in Theorem 4. For a given choice of f and g, the factor $1 - y$ appears $1 + m(fg, q)/fg$ times in the numerator and $1 + m/fg$ times in the denominator. Hence the term corresponding to f, g will be 0 unless $(fg, q) = 1$. Hence we may assume $f\,|\,(k, d)$ and

$$g\,\Big|\,\frac{k}{f}$$

so

$$\begin{aligned} c(q,n,d) &= \frac{1-y}{m(1-y^q)} \\ &\quad\times \sum_{f\,|\,(k,d)} f \sum_{g\,|\,\frac{k}{f}} \mu(g) \left[\frac{(1-y^{fgq})^{m/fg}}{(1-y^{fg})^{m/fg}}\right]_{y=1} \\ &= \frac{1}{m}\sum_{f\,|\,(k,d)} f \sum_{g\,|\,\frac{k}{f}} \mu(g)\, q^{(m/fg)-1} \end{aligned}$$

Remark:

Let $M(q,r)$ be the number of q-symbol "necklaces" with r beads and with no symmetry. As is well-known

$$M(q,r) = \frac{1}{r}\sum_{d\,|\,r} \mu(d)\, q^{r/d}$$

Hence, by Corollary 1,

$$c(q,n,d) = \frac{k}{mq}\sum_{f\,|\,(k,d)} M\left(q^{m/k}, \frac{k}{f}\right)$$

where $M\left(q^{m/k}, \frac{k}{f}\right) > 0$. Hence we have:

Corollary 2

If $e\,|\,d\,|\,m$, then

$$c(q,n,d) \geqq c(q,n,e)$$

with equality if and only if every prime dividing d/e also divides q. In particular, $c(q,n,d)$ is maximized (for fixed q, n) at precisely those $d\,|\,m$ such that every prime divisor of m/d also divides q, and therefore for $d = m$.

Corollary 3

For fixed q, n, we have

$$\max_{d\,|\,m}\, c(q,n,d) = c(q,n,m) = \frac{1}{m}\sum_{h\,|\,k} \phi(h)\, q^{(m/h)-1}$$

where k as usual is the largest factor of m relatively prime to q.

Proof of Corollary 3:

By Corollary 2, $\max c(q,n,d) = c(q,n,m)$. By Corollary 1,

$$\begin{aligned} c(q,n,m) &= \frac{1}{m}\sum_{f\,|\,k} f \sum_{g\,|\,\frac{k}{f}} \mu(g)\, q^{(m/pg)-1} \\ &= \frac{1}{m}\sum_{h\,|\,k} q^{(m/h)-1} \sum_{f\,|\,h} f\,\mu\left(\frac{h}{f}\right) \qquad (h = fg) \end{aligned}$$

But

$$\sum_{f\,|\,h} f\,\mu\left(\frac{h}{f}\right) = \phi(h)$$

so the proof follows.

Remark 1:

The number $N(t,r)$ of inequivalent t-symbol necklaces with r beads is

$$\frac{1}{r}\sum_{h\,|\,r} \phi(h)\, t^{r/h}$$

Hence

$$c(q,n,m) = \frac{k}{qm} N(q^{m/k}, k)$$

This suggests that a combinatorial proof of Corollary 3 may be possible, especially in the case $(m, q) = 1$ (so $k = m$), but we have been unable to find one. More generally, if $(m, q) = 1$ and n_i is the number of q-symbol necklaces with m beads summing to i (where the symbols are $0, 1, \cdots, q-1$), then it follows from Theorem 4 that

$$n_i = c_i + c_{i-1} + \cdots + c_{i-q+1}$$

since

$$\sum n_i y^i = \frac{1}{m} \sum_{f|m} \phi(f) (1 + y^f + y^{2f} + \cdots + y^{(q-1)f})^{m/f}$$

This suggests that with each word $e \epsilon C(q, n, m)$ of weight i, one can associate a q-symbol necklace with m beads of weight $i + j$ for each $j = 0, 1, \cdots, q-1$, but we have been unable to find such a correspondence.

Remark 2:

The Hamming bound for *symmetric* q-ary single-error correcting codes of length $n = m - 1$ is q^{m-1}/m. Hence by Corollary 3, Varshamov's code in the optimum case $d = m$ does better than any symmetric code as long as m has a prime divisor not dividing q. As remarked in Subsection II, we have been unable to do better than the Hamming bound when every prime divisor of m divides q, except for the special cases for $q = 2$ listed there. The largest code has 18 elements (though $c(2, 7, 8) = 16$). There is also a 12-element binary code of length 6 and a 32-element binary code of length 8, both exceeding the cardinalities given by Corollary 3 of $c(2, 6, 7) = 10$ and $c(2, 8, 9) = 30$. These codes are:

$n = 6$:
0 0 0 0 0 0
1 1 0 0 0 0
0 0 1 1 0 0
0 0 0 0 1 1
1 0 1 0 1 0
1 0 0 1 0 1
0 1 1 0 0 1
0 1 0 1 1 0
1 1 1 1 0 0
1 1 0 0 1 1
0 0 1 1 1 1
1 1 1 1 1 1

$n = 8$:
0 0 0 0 0 0 0 0
1 1 0 0 0 0 0 0
0 0 1 1 0 0 0 0
0 0 0 0 1 1 0 0
0 0 0 0 0 0 1 1
1 1 1 1 0 0 0 0
1 1 0 0 1 1 0 0
1 1 0 0 0 0 1 1
0 0 1 1 1 1 0 0
1 0 1 0 1 0 0 0
1 0 0 1 0 0 1 0
1 0 0 0 0 1 0 1
0 1 1 0 0 0 0 1
0 1 0 1 0 1 0 0
0 1 0 0 1 0 1 0
0 0 1 0 0 1 1 0
0 0 0 1 1 0 0 1
0 1 0 1 0 1 1 1
0 0 1 1 0 0 1 1
0 0 0 0 1 1 1 1
1 1 1 1 1 1 0 0
1 1 1 1 0 0 1 1
1 1 0 0 1 1 1 1
0 0 1 1 1 1 1 1
1 1 1 1 1 1 1 1
0 1 1 0 1 1 0 1
0 1 1 1 1 0 1 0
1 0 0 1 1 1 1 0
1 0 1 0 1 0 1 1
1 0 1 1 0 1 0 1
1 1 0 1 1 0 0 1
1 1 1 0 0 1 1 0

Proof of Theorem 4:

Set

$$\begin{aligned} F(z) = {} & (1 + yz + y^2z^2 + \cdots + y^{q-1}z^{q-1}) \\ & \times (1 + yz^2 + y^2z^4 + \cdots + y^{q-1}z^{2(q-1)}) \\ & \cdots (1 + yz^n + y^2z^{2n} + \cdots + y^{q-1}z^{n(q-1)}) \\ = {} & \prod_{i=1}^{n} (1 - \omega z^i y)(1 - \omega^2 z^i y) \cdots (1 - \omega^{q-1} z^i y) \end{aligned}$$

where ω is a primitive q-th root of 1. Let $G(z)$ be the unique polynomial in z of degree $< m$ such that

$$F(z) \equiv G(z) \pmod{z^m - 1}$$

Then the coefficient of z^d in $G(z)$ is $W(g, n, d; y)$, since choosing a term $y^i x^{ij}$ from the i-th factor

$$1 + yz^i + y^2z^{2i} + \cdots + y^{q-1}z^{(q-1)i}$$

of $F(z)$ corresponds to choosing $e_i = j$ in Eq. (4).

Now $G(z)$ is the unique polynomial of degree $< m$ satisfying $F(\zeta) = G(\zeta)$ for every root ζ of $z^m - 1 = 0$ i.e., for every m-th root of unity ζ. We shall therefore now evaluate $F(\zeta)$. Suppose $e|m$ and ζ is a primitive e-th root of 1. Then

$$\begin{aligned} F(\zeta) & = \prod_{i=1}^{n} \prod_{j=1}^{q-1} (1 - \omega^j \zeta^i y) \\ & = \left[\prod_{j=1}^{q-1} (1 - \omega^i y)^{-1} \right] \cdot \prod_{j=1}^{q-1} \prod_{k=0}^{(m/e)-1} \prod_{i=1}^{e} (1 - \omega^i \zeta^{ke+i} y) \\ & = \frac{1 - y}{1 - y^q} \prod_{j=1}^{q-1} (1 - \omega^{je} y^e)^{m/e} \\ & = \frac{(1 - y)(1 - y^{eq/(e,q)})^{mq(e,q)/e}}{(1 - y^q)(1 - y^e)^{m/e}} \end{aligned}$$

since ω^e is a primitive $q/(e, q)$ root of 1.

We therefore have

$$G(z) = \sum_{e|m} \frac{(1 - y)(1 - y^{eq/(e,q)})^{m(e,q)/e}}{(1 - y^q)(1 - y^e)^{m/e}} G_e(z)$$

where

$$G_e(\zeta) = \begin{cases} 1, \text{ if } \zeta \text{ is a primitive } e\text{-th root of 1} \\ 0, \text{ if } \zeta^m = 1 \text{ but } \zeta \text{ is not a primitive} \\ \quad e\text{-th root of 1.} \end{cases}$$

We claim

$$G_e(z) = \frac{1}{m}(z^m - 1)\sum \frac{\zeta}{z - \zeta}$$

where the sum is over all primitive e-th roots of 1. Let

$$H(z) = \frac{z^m - 1}{z - \zeta_0}$$

(where ζ_0 is a primitive e-th root of 1). If $\zeta^m = 1$, $\zeta \neq \zeta_0$, then $H(\zeta) = 0$. Also $H(\zeta_0) = H'(\zeta_0) = m\,\zeta_0^{m-1} = m\,\zeta_0^{-1}$. Hence $G_e(\zeta_0) = (1/m)(m\,\zeta_0^{-1}\zeta_0) = 1$, while $G_e(\zeta) = 0$ if $\zeta^m = 1$ and ζ is not a primitive e-th root of 1. This proves the claim.

Summing a geometric series, we have

$$\frac{\zeta(z^m - 1)}{z - \zeta} = \frac{1 - z^m}{1 - \zeta^{-1}z}$$
$$= 1 + \zeta^{-1}z + \zeta^{-2}z^2 + \cdots + \zeta^{-m}z^m$$

Interchanging ζ with ζ^{-1} in the sum for $G_e(z)$ gives

$$G(z) = \sum_{e|m} \frac{1}{m}\frac{(1 - y)}{(1 - y^q)}\frac{(1 - y^{eq/(e,q)})^{m(e,q)/e}}{(1 - y^e)^{m/e}}$$
$$\times \sum_{\substack{\zeta = \text{primitive} \\ e\text{-th root} \\ \text{of } 1}} (1 + \zeta z + \cdots + \zeta^n z^n)$$

Hence

$$W(q, n, d; y) = \text{coefficient of } z^d \text{ in } G(z)$$
$$= \frac{1}{m}\frac{(1 - y)}{(1 - y^q)}\sum_{e|m}\frac{(1 - y^{eq/(e,q)})^{m(e,q)/e}}{(1 - y^e)^{m/e}}$$
$$\times \sum_{\substack{\zeta = \text{primitive} \\ e\text{-th root} \\ \text{of } 1}} \zeta^d$$

It is well-known that $\sum \zeta = \mu(e)$, where the sum ranges over all primitive e-th roots of 1. Now ζ^d is a primitive $e/(d, e)$ root of 1, so

$$\sum_{\substack{\zeta = \text{primitive} \\ e\text{-th root} \\ \text{of } 1}} \zeta^d = \mu\frac{e}{(d, e)}\frac{\phi(e)}{\phi\dfrac{e}{(d, e)}}$$

Hence

$$W(q, n, d; y) = \frac{1}{m}\frac{(1 - y)}{(1 - y^q)}\sum_{e|m}\frac{(1 - y^{eq/(e,q)})^{m(e,q)/e}}{(1 - y^e)^{m/e}}$$
$$\times \mu\frac{e}{(d, e)}\frac{\phi(e)}{\phi\dfrac{e}{(d, e)}}$$

To complete the proof we need the following result:

Lemma: (Brauer-Rademacher):

For all positive integers e, d,

$$\sum_{f|(e,d)} f\mu\left(\frac{e}{f}\right) = \mu\left(\frac{e}{(e, d)}\right)\frac{\phi(e)}{\phi(e/(e, d))}$$

Proof:

See Ref. 2.

References

1. Varshamov, R. R., "A Class of Codes for Asymmetric Channels and a Problem from the additive Theory of Numbers," *IEEE Transactions on Information Theory*, IT-19, pp. 92–95, Jan. 1973.
2. Subbarao, M. V., "The Brauer-Rademacher Identity," *Amer. Math. Monthly*, Vol. 72, pp. 135-138, 1965.

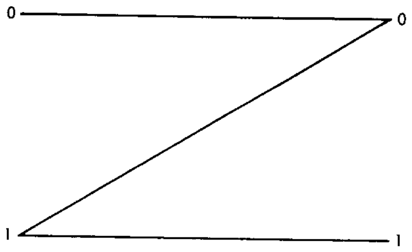

Fig. 1. The Z channel

Comment on Software Efficiency: Loops, Subroutines, and Interpretive Execution

J. W. Layland
Communications Systems Research Section

This article will discuss the relationship between the efficiency of software operation and the use within that software of conventional control structures such as loops and subroutines. These control structures 'fold' a program to reduce its storage requirements at the expense of increased execution time. The typical intuitive response to this consideration is one of "the faster, the better." In some contexts, this is far from correct. The extent to which folding should be done depends upon many factors, including especially the program's total size. The extent to which this folding can actually be done depends upon details of its operation, so the analysis presented in this article will of necessity retreat from reality, and assume that the program in question can be folded arbitrarily.

I. Introduction

This article will discuss the relationship between the efficiency of software operation and the use within that software of conventional control structures such as loops and subroutines. These control structures 'fold' a program to reduce its storage requirements at the expense of increased execution time. The typical intuitive response to this consideration is one of "the faster, the better." It will be seen shortly that in some contexts, this is far from correct. The extent to which folding should be done depends upon many factors, including especially the program's total size. The extent to which this folding can actually be done depends upon details of its operation, so the analysis presented in this article will of necessity retreat from reality, and assume that the program in question can be folded arbitrarily. We assume further that we are in a position to be able to pay for only as much storage and computing time as actually used. This implies either that we are using some small part of a fairly priced multiprogrammed computation center, or that we are assembling a computational facility that is being optimized for our particular task.

II. Problem Definition and Notation

Assume that a task has been defined in terms of a *Straight Line Machine Algorithm* (SLMA) of S steps on a standard computational resource. The label, SLMA, is a "corruption" of the logical straight line algorithms considered by Savage (Ref. 1), and implies only that each step is used exactly once in task execution, and no loops or other control strategies are employed that cause multiple usage of steps. No specific machine implementation is implied. It is the cost of various implementations of this task that is of interest. Were we, for example, to implement the task directly in the SLMA form, it would take S units of time, and S storage elements, resulting in a cost that is proportional to S^2 for the storage of the algorithm alone. This is not the only cost element in the machine. Other machine costs, denoted in total as M for the remainder of this article, will be assumed to be normalized by the cost of a single storage element. M consists of M_c, computer processor cost; M_d, task data cost; and M_p, external, or peripheral cost. For a medium-scale processor, M_c is currently on the order of 10^4 or larger. Common minicomputers have an M_c equal in cost to about 10^3 instruction storage elements, and the integrated circuit micro-computers have, or soon will have, an M_c below 10^2. The total cost of the directly implemented SLMA is

$$C_1 = S^2 + S \cdot M \tag{1}$$

The first term of Eq. (1) represents cost of storing the algorithm in a computer memory, and can be drastically reduced by use of the control structures of interest. At the same time, the execution time is increased by the overhead needed to perform the control function. For the remainder of this article, θ will be used to denote the amount of overhead, in machine steps, needed to perform one control operation in a folded implementation of an algorithm.

III. Loops

A loop exists in an algorithm implementation whenever some particular sequence of steps of the algorithm is executed repeatedly. This sequence of steps is followed by the θ overhead steps that determine whether the algorithm steps should be executed again, that modify pointers to the data manipulated by the algorithm, and do other house-keeping chores that are not inherent to the algorithm, but that are needed because of the way it is implemented.

Suppose that our task of S steps can be folded arbitrarily, and that it is to be implemented by repeated executions of a loop of β instructions. This loop must obviously be executed S/β times. Including overhead, the total time is $(\beta + \theta) \cdot S/\beta$, and the total storage is $\beta + \theta + M$. The total operating cost is

$$C_2 = (\beta + \theta + M) \cdot (\beta + \theta) \cdot S/\beta \tag{2}$$

We wish to determine a value for β such that Eq. (2) is minimized. For $M \approx 0$, the optimum β can be determined trivially by treating β as a continuous variable; differentiating by it, and solving the resultant equation. The optimum β is equal to the overhead θ. At this point ($M = 0$), the minimum task cost, C_2^* is

$$C_2^* = 4\theta \cdot S \tag{3}$$

which is a linear function of S.

For nonzero M, the optimum β is again approximately determined by treating β as continuous; differentiating by it, and solving

$$0 = \frac{\partial C_2}{\partial \beta} = \frac{S}{\beta}(\beta + \theta)(\beta + \theta + M) \times \left[\frac{-1}{\beta} + \frac{1}{\beta + \theta} + \frac{1}{M + \beta + \theta}\right] \tag{4}$$

To solve Eq. (4), make the change of variables $\eta = M/\theta$, and clear fractions, producing

$$[\beta + \theta(1 + \eta)](\beta + \theta) = \beta[\beta + \theta(1 + \eta)] + \beta(\beta + \theta) \tag{5}$$

After eliminating common terms from Eq. (5), its solution can be seen to be

$$\begin{aligned} \beta^* &= \theta(1 + \eta)^{1/2} \\ C_2^* &= S \cdot \theta \cdot [1 + (1 + \eta)^{1/2}]^2 \end{aligned} \tag{6}$$

Suppose that instead of being able to fold the algorithm into one loop, we were forced to use several, say N, with the i-th loop containing β_i steps. Each of the loops is executed for S/N total steps, causing $S/(\beta_i \cdot N)$ repetitions of the i-th loop. Hence total task time is

$$T = \sum_{i=1}^{N} \frac{S}{N} \cdot \frac{1}{\beta_i}(\theta + \beta_i)$$

and the storage required is

$$W = M + \sum_{i=1}^{N} (\theta + \beta_i)$$

since the overhead steps are required for each of the loops. The task operational cost is

$$C_3 = \left[M + \sum_{i=1}^{N} (\theta + \beta_i) \right] \cdot \left[\sum_{i=1}^{N} \frac{S}{N} \cdot \frac{1}{\beta_i} (\theta + \beta_i) \right] \tag{7}$$

By symmetry, $\beta_i = \beta_0$ for all i, so that

$$C_3 = \left[\frac{M}{N} + \theta + \beta_0 \right] \cdot S \cdot N \cdot \left[\frac{1}{\beta_0} \right] \cdot [\theta + \beta_0] \tag{8}$$

The solution to Eq. (8) can be determined by analogy with Eqs. (2) and (6) above. Let $\xi = M/(N \cdot \theta)$. Then

$$\begin{aligned} \beta_0^* &= \theta (1 + \xi)^{1/2} \\ C_3^* &= N \cdot S \cdot \theta \cdot [1 + (1 + \xi)^{1/2}]^2 \end{aligned} \tag{9}$$

For moderate M, the minimum C_3 represents an N-fold increase in cost over the minimum C_2. For large M, the minimum of both C_2 and C_3 approaches $S \cdot M$.

In an actual program, one would never have the option to fold a program as arbitrarily and completely as was done here. The option does exist to fold or not fold some particular sequence of steps, or perhaps to fold it partially. Suppose that the sequence of operations of current interest contains s_k steps that are to be folded (perhaps) into repeated execution of a loop of β_k steps. In Eq. (9), $1/N$ could be interpreted as the fraction of total algorithm steps performed by each of the loops. As such, $1/N$ corresponds to s_k/S in the present problem, and to a first-order approximation, the optimum β_k is given by

$$\beta_k^* = \theta \cdot \left(1 + \frac{M}{\theta} \cdot \frac{s_k}{S} \right)^{1/2} \tag{10}$$

If one of the allowed values for β_k falls close to this figure, then construction of the k-th loop at this figure is one portion of a minimum cost implementation. If allowed β_k values are below β_k^*, the s_k steps should almost certainly be implemented without the loop folding, because folding overhead adds proportionately more to task time than is saved in storage.

IV. Subroutines

Subroutines are a flexible means of causing multiple usage of specific steps within an algorithm implementation when these steps exist at scattered places within the algorithm. Just as with loops, a certain number of overhead steps must be executed to perform control operations of the subroutine linkage, and to establish data pointers for each distinct execution of the subroutine. As before, θ will denote the number of overhead steps per subroutine execution.

Suppose that our task of S steps can be folded arbitrarily, and that it is to be implemented by a sequence of calls to a subroutine of β instructions. There must obviously be S/β calls to this subroutine. Including overhead, the total time is $(\beta + \theta) \cdot S/\beta$, and the total storage is S/β for subroutine calls, $\beta + \theta$ for the subroutine, plus M for data, etc. The total operating cost is

$$C_4 = (M + \beta + \theta + S/\beta) \cdot (\beta + \theta) \cdot S/\beta \tag{11}$$

As before, we pretend that β is a continuous variable and locate the minimum of C_4 by differentiating with respect to β and solving for the zeros of that derivative. After some manipulation, we find that the minimizing β are the solutions to the cubic equation

$$\beta^3 = \beta (S + M\theta + \theta^2) + 2S\theta \tag{12}$$

For large S, the solution to Eq. (12) is approximately given by

$$\begin{aligned} \beta^* &\approx (S + M\theta)^{1/2} \\ C_4^* &\approx S \left[M + \frac{[2S + M \cdot \theta]}{(S + M\theta)^{1/2}} \right] \end{aligned} \tag{13}$$

The minimum cost is asymptotic to $2 \cdot S^{3/2}$ if $M << S$.

Subroutine structure is of course not limited to a single level. Subroutines can call subroutines that in turn call further subroutines ad infinitum. We would like to know how many levels can be used as well as how big each of the levels should be. Let β_i be the number of algorithm steps performed by one call to the i-th level subroutine, and let n be the number of subroutine levels. The n-th level subroutine then consists of β_n directly executed algorithm steps, and the i-th level subroutine (for $i \neq n$) consists of β_i/β_{i+1} calls to the $(i+1)^{st}$ level subroutine. Let $T(\beta_j)$ be the time to execute the steps at or below the β_j level. We consider $S = \beta_0$, $\beta_{n+1} = 1$. Then

$$\begin{aligned} T(S) &= \frac{S}{\beta_1} (\theta + T(\beta_1)) = \frac{S}{\beta_1} \left(\theta + \frac{\beta_1}{\beta_2} (\theta + T(\beta_2)) \right) \\ &= \cdots = \frac{S}{\beta_1} \left(\theta + \frac{\beta_1}{\beta_2} \left(\theta + \frac{\beta_2}{\beta_3} \right.\right. \\ &\quad \left.\left. \times \left(\theta + \cdots + \frac{\beta_{n-1}}{\beta_n} (\theta + \beta_n) \cdots \right) \right) \right) \\ &= S \cdot \theta \cdot \left(\frac{1}{\theta} + \frac{1}{\beta_1} + \frac{1}{\beta_2} + \cdots + \frac{1}{\beta_n} \right) \end{aligned} \tag{14}$$

The total storage for all subroutines with their entry overhead (disregarding base storage costs, M) is

$$W = \frac{S}{\beta_1} + \left(\theta + \frac{\beta_1}{\beta_2}\right) + \cdots + \left(\theta + \frac{\beta_{n-1}}{\beta_n}\right)$$

$$+ (\theta + \beta_n) = n \cdot \theta + \sum_{j=0}^{n} \frac{\beta_j}{\beta_{j+1}} \tag{15}$$

The task cost in this implementation is, as before, $W \cdot T(S)$. For fixed n, the minimum cost can be determined by treating the $\{\beta_i\}$ as continuous variables, and finding the zero(s) of the derivatives of cost with respect to each β_i.

$$0 = \beta_i \cdot \frac{\partial \ell n\,(c)}{\partial \beta_i} = \frac{\dfrac{\beta_i}{\beta_{i+1}} - \dfrac{\beta_{i-1}}{\beta_i}}{n\theta + \displaystyle\sum_{j=0}^{n} \frac{\beta_j}{\beta_{j+1}}} - \frac{\dfrac{1}{\beta_i}}{\dfrac{1}{\theta} + \displaystyle\sum_{j=1}^{n} \frac{1}{\beta_j}}, \quad \forall_i \tag{16}$$

Direct analytical solution of Eq. (16) appears hopeless, so the reasonable tactic is to search for upper and lower bounds to the $\{\beta_j\}$.

For an assumed fixed n, the lower bound is constructed quite simply as the solution to

$$0 = \frac{\beta_i}{\beta_{i+1}} - \frac{\beta_{i-1}}{\beta_i}, \qquad \forall_i \tag{17}$$

Any solution to Eq. (17) makes the right hand side of Eq. (16) negative for all i (since an always negative term was dropped from Eq. (16) to produce Eq. (17)). This in turn implies that minute increases in any or all of the β_i will decrease task cost, and hence that solutions to Eq. (17) are everywhere below the optimum $\{\beta_j\}$. Applying to Eq. (17) the boundary conditions that $\beta_0 = S$, and $\beta_{n+1} = 1$ produces the solution

$$\underline{\beta}_i = S^{(n+1-i)/(n+1)}, \qquad \forall_i \tag{18}$$

Rearranging Eq. (16) into the form of Eq. (17) plus an error term is a first step in developing an upper bound solution:

$$0 = \frac{\beta_i}{\beta_{i+1}} - \frac{\beta_{i-1}}{\beta_i} - \frac{1}{\beta_i}\left\{\frac{n\theta + \sum\limits_{j=0}^{n} \beta_j/\beta_{j+1}}{1/\theta + \sum\limits_{j=1}^{n} 1/\beta_j}\right\} \tag{19}$$

Substitution of Eq. (18) into the bracketed expression of Eq. (19) produces $n\theta S^{1/(n+1)}$. Thus at $\underline{\beta}_{n-j}$, Eq. (19) is approximately $n \cdot \theta \cdot S^{-j/(n+1)}$. For large S, moderate n, most j, this is much less than $\underline{\beta}_{j-1}/\beta_j = S^{1/(n+1)}$. Thus Eq. (17) is almost identical to Eq. (19) for most j, and it is only for j near n that significant error is introduced.

The subroutine depth, the value of n, for which task cost is minimum is yet to be determined. We restrict the $\{\beta_i\}$, the subroutine sizes, to be those of Eq. (18). For convenience, let $\beta \equiv \underline{\beta}_n = S^{1/(n+1)}$. Inserting Eq. (18) into Eq. (15) and Eq. (14), the storage cost W, and task time T are given by

$$\begin{aligned} W &= n\theta + (n+1)\,\beta \\ T &= S\theta \cdot \left(\frac{1}{\theta} + \frac{1 - \beta^{-n}}{\beta - 1}\right) \end{aligned} \tag{20}$$

The total task cost is $C = W \cdot T$. The expression can be simplified somewhat by assuming $n >> 1$, $\beta^{-n} << 1$:

$$C = n \cdot S \cdot (\theta + \beta) \cdot \left(1 + \frac{\theta}{\beta - 1}\right) \tag{21}$$

The value of n that minimizes C is found by setting its first derivative to 0:

$$0 = n \cdot c \cdot \frac{dC}{dn} = 1 - \beta\, \ell n \beta \left[\frac{1}{\theta + \beta} - \frac{\theta/(\beta - 1)}{(\beta - 1) + \theta}\right] \tag{22}$$

Equation (22) could be solved directly numerically to relate β, the smallest subroutine size, to the overhead, θ, but an approximate analytic answer may be obtained by assuming $\beta - 1 \approx \beta$:

$$0 = 1 - \ell n \beta \left[\frac{\beta - \theta}{\beta + \theta}\right] \tag{23}$$

Eq. (23) is made tractable by the approximation

$$2\left\{\frac{\beta - \theta}{\beta + \theta}\right\} \approx \ell n \beta - \ell n \theta$$

which is valid to within a few percent for $\theta > 10$. With this approximation, Eq. (23) becomes a quadratic in $\ell n\,(\beta)$ with the solution

$$\begin{aligned} \ell n\,(\beta) &= \ell n\,(\theta) \cdot \frac{1 + \left(\dfrac{1 + 8}{(\ell n \theta)^2}\right)^{1/2}}{2} \\ n &= \frac{\ell n S}{\dfrac{\ell n \theta}{2} + \left[\left(\dfrac{\ell n \theta}{2}\right)^2 + 2\right]^{1/2}} \end{aligned} \tag{24}$$

For large θ, β is approximately equal to θ, and task cost is given by

$$C \approx 4\theta S \ln(S)/\ln(\theta) \tag{25}$$

The overhead θ sets a lower bound to the smallest subroutine size, and hence places an upper limit to n. As the $\{\beta_j\}$ found in Eq. (18) represent a lower bound component-wise to the true minimizing $\{\beta_j\}$, we expect that the n, which minimizes cost at the true $\{\beta_j\}$, will be greater than the n found in Eq. (24).

To find an upper bound solution for the $\{\beta_i\}$, we must determine conditions under which $\{\partial C/\partial\beta_i\}$ is positive for all i. Equation (16) can be rearranged into the form

$$H^+(\beta)\frac{\partial C}{\partial\beta_i} = \beta_i^2 - \beta_{i+1}\cdot\left(\beta_{i-1} + \frac{n\theta + \sum\limits_0^n \beta_j/\beta_{j+1}}{1/\theta + \sum\limits_1^n 1/\beta_j}\right) \tag{26}$$

where $H^+(\beta)$ is an always positive function of $\{\beta\}$. Let us denote as $g(\theta, n, \beta)$ the fraction in parentheses in Eq. (26), and as g^+, an upper bound to $g(\theta, n, \beta)$. The lower-bound solution to $\{\beta_i\}$ is given in Eq. (18). We construct a tentative upper-bound solution from it as

$$\beta_i^0 = \left(\frac{n+1-i}{S^{n+1}}\right)^{\eta} S^{1-\eta} \tag{27}$$

where η is a small constant yet to be determined. A second tentative upper bound β_i^1 is constructed from the first by solving sequentially from $i = n$ down:

$$\begin{aligned} \beta_{n+1}^1 &= 1 \\ \beta_i^1 &= [\beta_{i+1}^1\cdot(\beta_{i-1}^0 + g^+)]^{1/2} \end{aligned} \tag{28}$$

With this solution, η is adjusted (if possible) so that

$$\beta_i^0 \geqq \beta_i^1, \qquad \text{all } i \tag{29}$$

This restriction implies that

$$\begin{aligned} \beta_i^1 &\geqq [\beta_{i+1}^1\cdot(\beta_{i-1}^1 + g^+)]^{1/2} \\ \beta_i^1 &\geqq [\beta_{i+1}^1\cdot(\beta_{i-1}^1 + g(\theta, n, \beta^1))]^{1/2} \end{aligned} \tag{30}$$

which in turn implies that

$$\frac{\partial C}{\partial\beta_i} \geqq 0, \qquad \forall_i, \qquad \text{at } \beta_i^1 \tag{31}$$

That is, $\{\beta_i^1\}$ is an upper-bound solution to $\{\beta_i\}$, but as $\beta_i^0 \geqq \beta_i^1$ for all i, $\{\beta_i^0\}$ is also an upper-bound solution for the selected η. It remains to determine η.

We expand the solution for β_i^1 by substituting Eq. (27) into Eq. (28) and iterating downward:

$$\beta_{n-K}^1 = \prod_{j=1}^{K+1} [S^{\eta(K+3-j)/(n+1)} + g_+]^{2^{-j}}$$

$$\beta_{n-K}^1 = S^{\eta(K+1)/(n+1)}\cdot S^{(1-\eta)(1-2^{-K-1})} \times \prod_{j=1}^{K+1}\left[1 + \frac{g_+}{S^{\eta(K+3-j)/(n+1)}\cdot S^{1-\eta}}\right]^{2^{-j}} \tag{32}$$

The product in Eq. (32) can be converted to a sum by the use of logarithms, and a summable upper bound to the sum of logarithms is generated by the use of $\ln(1+X) \leqq X$, for all X.

$$\beta_{n-K}^1 \leqq S^{\eta(K+1)/(n+1)}\cdot S^{(1-\eta)(1-2^{-K-1})} \times \exp\left\{\frac{g_+}{S^{1-\eta}}\sum_{j=1}^{K+1}\frac{1}{2^j S^{\eta(K+3-j)/(n+1)}}\right\} \tag{33}$$

The sum in Eq. (33) is a simple geometric progression. If the right hand side of Eq. (33) is forced to be below $\beta_{n-K}^0 = S^{\eta(K+1)/(n+1)}\cdot S^{1-\eta}$, then $\beta_{n-K}^1 \leqq \beta_{n-K}^0$, as desired. For convenience, denote $\beta \triangleq \beta_n^\eta = S^{\eta/(n+1)}$. The bound con-constraint becomes

$$S^{(1-\eta)(-2^{-K-1})}\exp\left\{\frac{g_+}{S^{1-\eta}}\beta^{-(K+3)}\frac{\beta^{K+2}-\beta}{\beta-1}\right\} \leqq 1 \tag{34}$$

or

$$g_+\cdot\frac{1-\left(\frac{2}{\beta}\right)^{K+1}}{1-\left(\frac{2}{\beta}\right)}\cdot\beta^{-2} \leqq S^{1-\eta}\ln S^{1-\eta}. \qquad \forall_K \tag{35}$$

If we assume $\beta > 2$, then the inequality of Eq. (35) is assured whenever

$$g_+ \leqq \beta(\beta - 2)\, S^{1-\eta}\ln S^{1-\eta} \tag{36}$$

A value for g_+ can be conveniently derived by manipulating $g(\theta, n, \beta^0)$: $g_+ = \theta(n\theta + n\beta + S^{1-\eta})$, thus

$$\theta(n\theta + n\beta + S^{1-\eta}) \leqq \beta(\beta - 2)\, S^{1-\eta}\ln S^{1-\eta} \tag{37}$$

Let us assume an n that varies with S as $n = \lambda \ln S$, for λ constant. This is consistent with past findings Eq. (24) at the lower bound. If n grows more rapidly than $\lambda\, \ell nS$, then task cost will grow more rapidly than $S \cdot \ell nS$, and it will be seen that this is achievable at $n = \lambda\, \ell nS$. Assuming η is approximately 1, substitution of $n = \lambda\, \ell nS$ into the inequality Eq. (37) produces

$$\theta \cdot (\lambda\, \ell nS\, [\theta + e^{1/\lambda}] + S^{1-\eta}) \leqq (e^{2/\lambda} - 2e^{1/\lambda}) \cdot S^{1-\eta}\, \ell nS^{1-\eta} \tag{38}$$

It can be shown that $S^{1-\eta}$ must grow at least as fast as $\mu \cdot \ell nS$ (for μ constant) to satisfy Eq. (38).

$$\theta \cdot \frac{\lambda}{\mu}\, [\theta + e^{1/\lambda}] + 1 \Big) \leqq (e^{2/\lambda} - 2e^{1/\lambda})\, \ell n\, (\mu\, \ell nS) \tag{39}$$

Equation (39) is satisfied for large S for any arbitrarily small constant μ since the right hand side is increasing with S. For $S^{1-\eta} = \mu\, \ell nS$, η converges to 1 for large S.

Using these forms for n and $S^{1-\eta}$, the task time and storage are given by

$$\left.\begin{aligned} T &= S \cdot \theta \left(\frac{1}{\theta} + \frac{1}{\mu\, \ell nS} \frac{1}{e^{1/\lambda} - 1} \right) \\ W &= \ell n\, (S)\, (\lambda\, [\theta + e^{1/\lambda}] + \mu\, e^{1/\lambda}) \end{aligned}\right\} \tag{40}$$

We are particularly interested in behavior at large S, so the second term of T may be ignored, as it converges to 0 for large S. The last term of W can also be ignored as μ can be an arbitrarily small constant, negligible with respect to λ. Thus

$$\begin{aligned} T &\approx S \\ W &\approx \ell n\, (S) \cdot \lambda\, [\theta + e^{1/\lambda}] \end{aligned} \tag{41}$$

The minimum of $C = T \cdot W$ is at that λ that minimizes storage, i.e., at

$$\theta = \beta\, (\ell n\beta - 1), \qquad \text{where } \beta = e^{1/\lambda} \tag{42}$$

The minimum cost is thus

$$C = S \cdot \ell n\, (S) \cdot \beta \tag{43}$$

and

$$C \lesssim S \cdot \ell n\, (S) \cdot \frac{\theta}{\ell n\theta - 1} \tag{44}$$

The value of β defined from Eq. (42) is below the lower-bound β for all values of θ. Hence the value of n which corresponds to Eq. (42) is larger than that of Eq. (24), and it may be argued that this n is an upper bound to the true n.

From the form of the upper- and lower-bound solutions, it may reasonably be inferred that the subroutine depth n for minimum task cost is given by $n = \lambda\, \ell n\, S$, for λ some small constant which makes $S^{1/n} \approx \theta$, and that minimum task cost is equal to $\nu \cdot S \cdot \ell n\, S \cdot \theta / \ell n\theta$ where ν is a small constant on the order of 1.

V. Interpretation

One can perform almost the same sequence of analysis for execution with an interpreter as for multiply-nested subroutines. The interpreter is another tool with which a software system designer can reduce storage at the expense of increased execution time. The interpreter requires some fixed minimum overhead in storage to hold the interpretive mechanism itself, and a smaller amount of storage associated with subroutine linkage via the interpreter. There is a time overhead associated with interpreted subroutine linkage which is greater than the corresponding storage overhead, and there is a time overhead associated with each interpreted step. To counterbalance these effects, the storage required for an interpreted step is reduced by a factor of 2 to 10 (or more) from what it would be without the interpreter. Although the specific parameters are different from those of the multilevel subroutines, the conclusion reached is certain to be quantitatively the same as just presented for subroutines: that the decision to fold the program is a good one provided the work performed in the lowest level routines is roughly equal to the overhead work encountered in getting there.

There are a wide variety of other options that have not and will not be covered here. Both program code and data may be stored in a secondary memory, and called to main storage when needed, instead of being assumed to all reside in main storage as was done here. This call for secondary memory data may be either program controlled, or under system control as part of a virtual memory structure. In the latter case, both processor and swapping scheduling algorithms affect the task cost, as does the installation's pricing policies. Another piece of this massive "jigsaw puzzle" called computational efficiency is the effect of memories and processors with a variable cost that is some function of the innate device speed. These are some of the open questions.

VI. Implications for Reality

The analysis just presented has attempted to reveal the efficiency implications of some conventional software structures. The actual problems solved are abstractions of the real programming questions of how much a program should be folded by loop and subroutine control structures. Such questions are of direct interest to two types of people: to system designers who can build or buy exactly the right amount of hardware to do their job, and to users of large-scale, time-sharing, multiprogramming systems where one pays only for resources used. Our departure from reality consists of the drastic assumption that the programs can be folded arbitrarily, i.e. without regard to content. While this is clearly false, and hence degrades the quantitative conclusions, the qualitative conclusion should remain valid, namely: whenever the storage for a task is dominated by program rather than data, the decision to fold that program to reduce its storage, by any available means, is a good one provided that the work performed in the lowest level routines is roughly equal to the overhead involved in the control structures of the higher levels.

The Structured Programming and "levels of abstraction" techniques (Ref. 2) is currently growing in popularity for the development of complex software systems that are transparent and readily understandable. The technique leads naturally to extensive use of multiple level subroutines. Are such programs efficient? The analysis presented above says *yes*.

References

1. Savage, J. E., and Harper, L. H., "Contributions to a Mathematical Theory of Complexity," in *The DSN Progress Report,* Technical Report 32-1526, Vol. V, Jet Propulsion Laboratory, Pasadena, Calif., Oct. 15, 1971.
2. Baker, F. T., "System Quality through Structured Programming," *AFIPS Conference Proceedings,* Vol. 41, Part I, pp. 339–343, 1972 Fall Joint Computer Conference, Los Angeles, Calif., Dec. 5–7, 1972.

An Input/Output Processor for the XDS 930: An Exercise in Micro-programmed Design

A. I. Zygielbaum
Communications Systems Research Section

A micro-programmed stored logic input/output (I/O) processor has been developed to evaluate micro-programming as a digital design technique. This I/O processor can be used for investigating DSN standard computer/computer interfaces as well as for experimentation with external control of the XDS 930 in emulation of multiple computer systems.

I. Introduction

A micro-programmed stored logic I/O processor has been developed to evaluate micro-programming as a digital design technique. The processor was specifically designed as an I/O processor for an XDS 930 to minimize loading of the CPU when driving the digital video display system (Ref. 1). This flexible I/O processor can be used for investigating DSN standard computer/computer interfacing, and for experimentation with external control of the XDS 930 in emulation of the control of satellite minicomputers in a multiple-computer DSIF tracking station.

Micro-programming was found to provide an orderly straightforward design process, simplifying digital system debugging, maintenance, and documentation. This article will discuss micro-programmed stored logic and the minicomputer-like I/O processor (Mini-proc).

II. Definitions

To clarify the terms to be used, the following definitions are applicable. "Stored logic" shall imply a digital system where system states are contained in the address counter of a sequencing memory (control store) rather than in the conventional conglomeration of gates and flip-flops. "Micro-instruction" will refer to a particular system state transition function stored in this memory. A "micro-program" is a sequence of micro-instructions. An "instruction" is a word stored in a computer's memory for the purpose of controlling that computer through its central processor. A "command" is a word stored in a computer's memory for the purpose of controlling an input/output processor.

III. Background

In 1951, M. V. Wilkes (Ref. 2) proposed a computer controlled by the output of a diode matrix memory. Each word of this memory controlled the gating structures of the computer's functional units (adders, registers, etc.) in some particular way. Each bit of the word controlled a unique gate in the structures. This scheme allowed the independent design of functional units and the straightforward sequencing of data transfers.

Using one bit per function in the micro-instruction is known as "horizontal format." A simple example is shown in Fig. 1. A simple micro-program can, for instance, subtract register 2 (R2) from register 1 (R1); then double the result. Assume a synchronizing clock for each step:

ADDRESS	WORD	
000	10011001	Subtract R2 from R1. Store result in R1 and go to NEXT INSTRUCTION.
001	00111011	Add R1 to itself, store result in R1 and Step
010	00000000	HALT (NO STEP, NO FUNCTION)

It is unlikely that gates G1, G2, G3, and G4 will need to be enabled at once. The only likely possibilities are G1, G2; G3, G4; G1, G4; and G2, G3. These four conditions can be encoded into two bits thus reducing the word size from 8 bits to 6 bits. This is an example of "vertical format."

Vertical formating breaks the micro-instruction into encoded fields. There are two primary disadvantages relative to horizontal format. First, the system loses flexibility because some logic states are disallowed. Second, decoding involves extra hardware and design time. However, the advantages of vertical format are a shorter micro-instruction, coupled with easier microprogram development and documentation, since mnemonics can be assigned for each field. Usual design involves a combination of both formats as shown in Fig. 2.

One can establish a hierarchy of levels where a "nano-instruction" mechanizes the execution of a micro-instruction just as a micro-instruction mechanizes a computer instruction. The unique vertically formatted micro-instruction of the Nanodata QM-1, for instance, is essentially an address which selects a nano-instruction in a nano-memory (Ref. 3). The nano-instruction, which has a horizontal format, controls gate level functions. Consequently, the QM-1 offers an extremely flexible combination of both formats.

One must note that, no matter what the format, the present state of the system is contained in the current micro-instruction address, and the next state is easily determined. In a conventional system the current state is spread over many locations.

The states of the stored logic machine need not be sequential. Branching on condition and subroutining can be easily implemented. Repetitious or conditional functions are a simple extension to the stored logic. This offers additional logic efficiency to the digital system. In the example of Fig. 1, branching can be accomplished by leaving the low-order control store address bit unspecified and allowing that bit to be set by some condition, like adder carry. The higher order bits would merely step sequentially.

The development of integrated circuits and medium/large-scale integrated (MSI/LSI) circuits encourages the modularization of digital system design. Modularization lends itself quite readily to stored logic which offers a simple way to control data transfers between MSI/LSI modules. Further, MSI/LSI read-only memories (ROMs) and random-access memories (RAMs) offer attractive storage for micro-programs. MSI/LSI circuits make stored logic an economically feasible choice for digital system design.

Current use of micro-programming in computers is well known. Most popular mini-computers as well as the IBM System/360 are micro-programmed. The 360 uses a vertically formatted micro-instruction to implement a fixed computer instruction set which reaches across a compatible line of computers. As the System/360 is a business data machine, IBM will not support a user micro-programmed machine. This restriction is necessary to insure software compatibility between installations. Minicomputers can be micro-programmed by the user to specialize machine capabilities as was done in the DSN data decoder assembly (Ref. 4). In this application, an

Interdata 4 mini-computer was microprogrammed to perform sequential decoding of the Pioneer 10 telemetry at data rates adequate to support the Pioneer Program.

IV. Rationale for Stored Logic

On the XDS 930, direct memory access is typically through the data multiplex system (DMS) which operates through the multiple access to memory (MAM). The DMS can transfer a block of up to 512 words without central processing unit (CPU) intervention. The CPU must, however, update word count and data location between each block.

The digital video display system (DVDS, Ref. 1) uses blocks on the order of 30 words. For this block length the CPU is 50% occupied with the job of updating the data multiplex system (DMS) control words. To reduce this load, an I/O processor was designed for the XDS 930. This I/O processor, controlled by a command program in memory, must transfer data at full memory bandwidth (570,000 words/s) and perform system status tests, both independent of the CPU.

Initial design proceeded in the usual manner. Several block diagrams were tried. Each worked but each had its limitations. Typically a design which was optimal for the DVDS was not efficient for other I/O. Compromises and the inability to include all contingent I/O requirements lead to the abandonment of conventional logic in favor of stored logic.

V. Functional Units

The Mini-proc is made up of independent functional units (Fig. 3). These units are interconnected by a single 8-bit bus. This two-way path allows the output of any functional unit to be connected to any combination of functional unit inputs.

The functional units were designed independently. The only specifications were: (1) logic level delays from enable to output of 100 ns maximum, (2) transistor-transistor logic (TTL) compatible 5-V logic levels, and (3) 8-bit wide data input and output. The control store word was not defined until after the basic design was completed.

The manipulator is the data modifier in the Mini-proc. Referring to Fig. 4, the primary operand enters the manipulator through a shifter into the arithmetic logic unit (ALU). The shifter can shift data one bit right cyclic, left cyclic or left noncyclic. The shifter's output supplies the "A" input of the ALU. The second operand is stored in the arithmetic logic buffer which is routed to the B input of the ALU. In the ALU, two Texas Instrument SN74181 (arithmetic logic units) provide 16 logic functions and two sets of 16 carry dependent arithmetic functions for eight bit bytes. The ALU can also be used to compare two numbers. A special A = B signal is available to the status functional unit. The output carry, saved in a flip-flop for the status unit, can be routed back into the ALU to facilitate multi-byte arithmetic. The output of the ALU is stored in the accumulator for distribution on the bus. Sixteen 8-bit words of storage are available in a semiconductor scratch pad. The scratch pad address is supplied by the control store.

Direct communication to the Mini-proc from the XDS 930 CPU is by way of the parallel output (POT) channel. The CPU can start or stop the processor. A *channel status dump* is available to the CPU on request. The *interface control* decodes the necessary XDS 900 series EOMs and signals the status functional unit as required. Two EOMs override control store. The *unconditional activate* forces the Mini-proc to reinitialize and start. The *stop immediate* halts the processor no matter its current status. The interface control can interrupt the CPU using two interrupt channels. In case the CPU tries to activate an already active Mini-proc, one interrupt channel provides a warning. The second interrupt is under the control of control store.

Primary data and command transfers between the XDS 930 memory and the Mini-proc is by way of the MAM. The interface control synchronizes all data and address transfers on this channel. The unit also generates word parity to the XDS 930 and checks parity from the XDS 930. The address buffer supplies the memory location address to the MAM. Sixteen bits of storage are available although only fifteen are used for the address. Two Mini-proc cycles are required to transfer address data in or out by way of the 8-bit bus. The data buffer assembles 24 bits of data in three Mini-proc cycles for transfer to the XDS 930 via the MAM. Conversely the buffer unpacks 24 bits into 8-bit bytes in three cycles for distribution on the bus.

Communication to the outside world is through the external control functional unit. Besides providing synchronizing signals for XDS 930 memory access, this unit has four special-purpose timing lines available to control store. These lines can be used for arbitrary control line simulation.

The Mini-proc's single bus can be gated to the outside world for direct I/O. This facilitates simulating XDS 930 EOM-type instruction. Special status conditions can be input in this manner. The external control also provides a test line which is routed to the status functional unit.

The status unit keeps track of various internal and external conditions. Its primary function is the control of conditional jumps. Any of the following three specific conditions can be tested: Manipulator A = B, Manipulator carry, and External test. The status unit can also provide an interrupt-like jump, that is, a jump to a specific address if any condition is set. The conditions are tested on a priority scheme and are reset once handled. The jump addresses, one for each condition, are defined by an eight diode dual in-line package (DIP) carrier on the status board.

The control address buffer selects the active micro-instruction. This micro-instruction is stored in the control buffer. The address buffer can be reset to zero or incremented by one. To facilitate micro-program branching, the control address buffer can also copy jump addresses from the bus.

In the initial version of the Mini-proc, the control store is a diode matrix memory with a 100-ns access time. Diode matrices, though cumbersome, are easily changeable and therefore amenable to experimentation. The control store operates in parallel with the functional units. The next micro-instruction is fetched while the current one is being processed. A conflict occurs with a jump micro-instruction. Here the fetched word is not the next one to be processed. The usual solution is to ignore the fetched word and thus lose a machine cycle. The Mini-proc, however, handles a jump by allowing one sequential micro-instruction to be executed after the jump micro-instruction occurs. The programmer would then put a jump instruction one step earlier than necessary or follow the jump with a clear word (no-operation).

The format of the micro-instruction is a combination vertical/horizontal format. An explanation of the format appears in Figs. 5 and 6. Basically the output of any functional units can be connected to any combination of inputs under control of the control field.

VI. Micro-Programming

The sample micro-program (Fig. 7) is the start up routine for the Mini-proc. The XDS 930 stores a command program starting address in location 0234 of its memory. The Mini-proc is enabled and accesses that location. The micro-program then jumps to the routine called for by the command in the starting address location. This micro-program was written with the aid of a Meta-symbol procedure deck written for the XDS 930. The assembly language has fields as shown in Table 1.

The card image corresponds to the input data for the assembler. The label field is an address locator. The device field corresponds to the micro-instruction device field. (AORG sets the absolute origin. END implies an end to the program.) The control/input field uses the input mnemonics previously given in Figs. 5 and 6. A control function is written by giving a name and its corresponding value such as ('L', 234). This places the value 234 in the label subfield of the control field. Additional field definitions are found in Table 2. The assembler produces a binary tape of the 27 bit micro-instruction words for later implementation.

Each command of the processor program calls a specific micro-programmed routine. The initial command list will consist of the following:

LOAD IMMEDIATE BLOCK COUNT

LOAD IMMEDIATE WORD COUNT

LOAD IMMEDIATE DATA STARTING ADDRESS

JUMP

DECREMENT, JUMP IF LOC. < 0

INPUT ONE WORD

OUTPUT ONE WORD

TRANSFER DATA (according to word, block count)

VII. Summary

Design of the Mini-proc has demonstrated the value of stored logic. Micro-programming offers the digital system designer an orderly method to produce logical controls. The efficiency of design, along with simplified documentation and debugging, suggests that stored logic is an attractive and viable alternative to ad hoc design.

References

1. Zygielbaum, A. I., "Information Systems: Range Doppler Display System," in *The Deep Space Network*, Space Programs Summary 37-60, Vol. II, pp. 22–28. Jet Propulsion Laboratory, Pasadena, Calif., Nov. 30, 1969.
2. Wilkes, M. V., "The Best Way to Design an Automatic Calculating Machine," presented at the Computer Inaugural Conference, Manchester University, North Manchester, Ind., July 16–18, 1951.
3. Rosen, R. F., et al., "An Environment for Research in Microprogramming and Emulation," presented at the 4th Annual Workshop on Microprogramming, ACM-Sigmicro-IEEE, Santa Cruz, Calif., September 13–15, 1971. Also appears in *Communications of the ACM*, Vol. 15, No. 8, pp. 748–760, August 1972.
4. Grauling, C. R., "Data Decoder Assembly," in *The Deep Space Network*, Technical Report 32-1526, Vol. IV, pp. 170–177. Jet Propulsion Laboratory, Pasadena, Calif., Aug. 15, 1971.

Bibliography

Leis, C., "Microprogramming Features of a 16-bit Mini," Preprint of the 4th Annual Workshop on Microprogramming, ACM-Sigmicro-IEEE, Santa Cruz, Calif., Sept. 13–15, 1971.

McDermott, J., "Suddenly, Everybody is Building Micro-Programmed Computers," *Electronic Design*, Vol. 24, pp. 23–28, Nov. 25, 1971.

Redfield, S. R., "A Study in Microprogrammed Processors: A Medium Sized Microprogrammed Processor," *IEEE Transactions on Computers*, Vol. C-20, No. 7, pp. 743–750, July 1971.

Rosin, R. F., "Contemporary Concepts of Microprogramming and Emulation," *Computing Surveys*, Vol. 1, No. 4, pp. 197–212, December 1969.

Wilkes, M. V., "The Present States and Potential of Microprogramming," *IEEE Convention Record*, pp. 131–133, March 25, 1971.

Table 1. Assembly language format

Relative location	Assembled code			Card number	Card image		
	Tag	Device	Control/input		Label	Device	Control/input
XXXXX	X	XX	XXXXXXX		(INIT)	(RT B)	('L', O), BTADB

Table 2. Field definitions

Mnemonic	Corresponding 'field'	Remarks/sub-class
MCM	B	ALU Control
BTSP	A	Scratch Pad
SP	A	Used with SPTB
TIC	D	HALT – Stop RIN – Request Input RAC – Request Access RDCS – Request Dump Channel Status ENINT – Fire Interrupt
TAG	TAG	
ST	E	STATUS
X	C	EXTERNAL
L	F	LITERAL

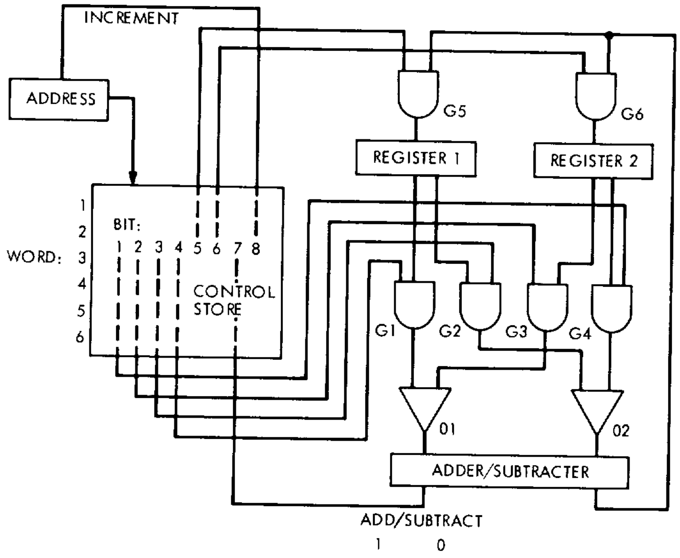

Fig. 1. Simple digital system, horizontal format

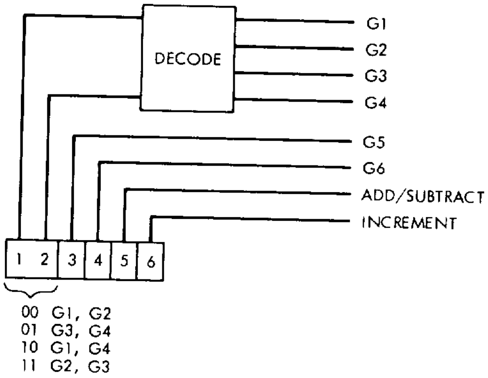

Fig. 2. Simple digital system, vertical format

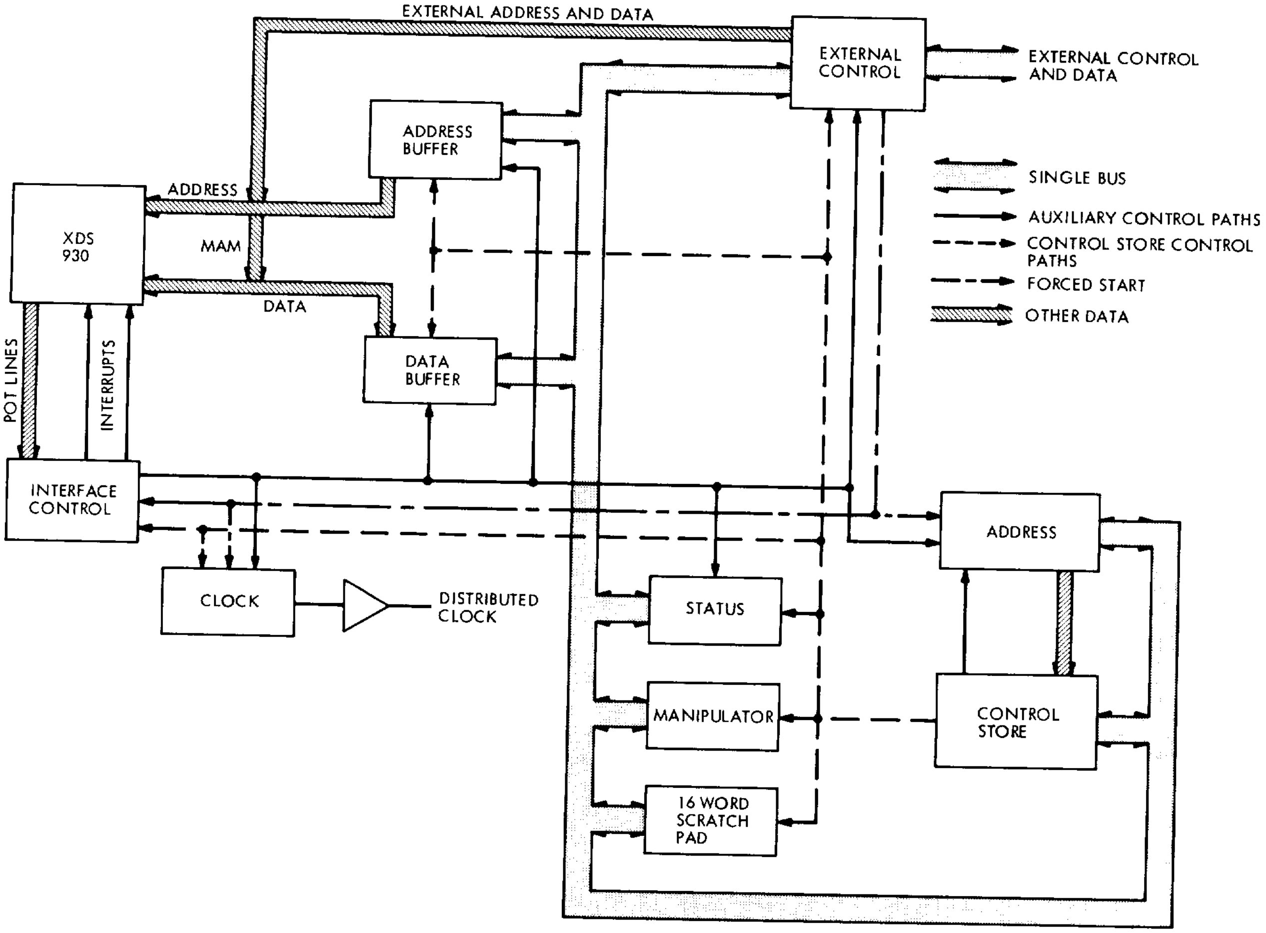

Fig. 3. Block diagram of Mini-Proc

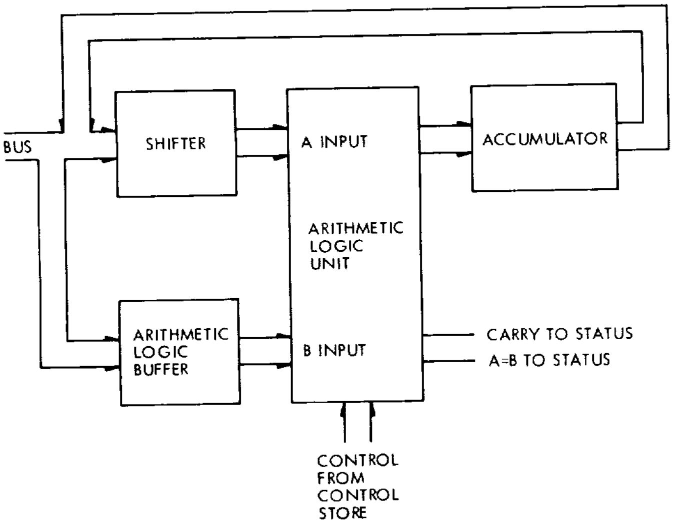

Fig. 4. Manipulator

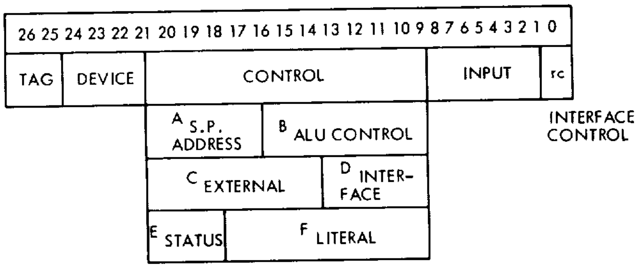

TAG FIELD

VALUE	MNEMONIC	ACTION
01	LRC	LOAD CONTROL MODIFY
10	RC	MERGE CONTROL MODIFY

DEVICE, CONTROL

VALUE	MNEMONIC	CONTROL FIELD ENABLED	ACTION
0000	NOB		NO ACTION
0001	RA↑B		CONTROL ADDRESS TO BUS
0010	AC↑B		ACCUMULATOR TO BUS
0011	DB↑B		DATA BUFFER TO BUS
0100	C↑DB		COMPUTER TO DATA BUFFER
0101	DB↑C		DATA BUFFER TO COMPUTER
0110	ADB↑B		ADDRESS BUFFER TO BUS
0111	SP↑B	A	SCRATCH PAD TO BUS
1000	ST↑B	E	STATUS TO BUS
1001	EX↑B		EXTERNAL TO BUS
1010	EXTCTL	C	EXTERNAL CONTROL
1011	R↑B	F	CONTROL STORE LITERAL TO BUS
1100	EXTRST		OPTIONAL TIMING RESET
1101	STOP		DEACTIVATE MINI-PROC
1110	EXPY		SUPPLY EXTERNAL PARITY

INPUT

BIT	MNEMONIC	CONTROL FIELD ENABLED	ACTION
8	JP		JUMP (BUS TO CONTROL ADDRESS)
7	XJP	E	JUMP ON CONDITION
6	MCM	B	MANIPULATOR CONTROL
5	B↑ALB		BUS TO ARITHMETIC LOGIC BUFFER
4	B↑DB		BUS TO DATA BUFFER
3	B↑ADB		BUS TO ADDRESS BUFFER
2	B↑SP	A	BUS TO SCRATCH PAD
1	B↑EX		BUS TO EXTERNAL

INTERFACE CONTROL

INTERFACE CONTROL FIELD (D) ENABLED IF BIT 0 (RC) IS A ONE.

Fig. 5. Control store micro-instruction format

ALU CONTROL (B)

BIT	ACTION
16 15	SHIFT CONTROL
14 13	LOGICAL MODE: ARITHMETIC MODE: 01 INPUT CARRY = 0 10 INPUT CARRY = 1 11 INPUT CARRY = LAST OPERATION RESULT CARRY
12 11 10 9	ACTION CONTROL

S.P. ADDRESS (A)

SCRATCH PAD ADDRESS

EXTERNAL (C)

BIT	ACTION
20	ENABLE EXTERNAL MEMORY ACCESS REQUEST LINE
19	ENABLE EXTERNAL MEMORY INPUT REQUEST LINE
18	ENABLE EXTERNAL MEMORY ADDRESS REQUEST LINE
17	TOGGLE OPTIONAL TIMING LINE A
16	TOGGLE OPTIONAL TIMING LINE B
15	TOGGLE OPTIONAL TIMING LINE C
14	TOGGLE OPTIONAL TIMING LINE D

INTERFACE (D)

BIT	ACTION
13	FIRE INTERRUPT
12	RESET DUMP CHANNEL STATUS REQUEST
11	REQUEST MEMORY ACCESS
10	REQUEST MEMORY INPUT
9	HALT -- STOP CLOCK (WAIT)

STATUS (E)

BIT 20	19	XJP (BIT 7)	ACTION
0	0	1	JUMP IF MANIPULATOR A = B IS 1
0	1	1	JUMP IF MANIPULATOR CARRY IS 1
1	0	1	JUMP IF EXTERNAL TEST = 1
1	1	1	JUMP TO PRIORITY ADDRESS
1	1	0	STATUS TO BUS

Fig. 6. Control fields

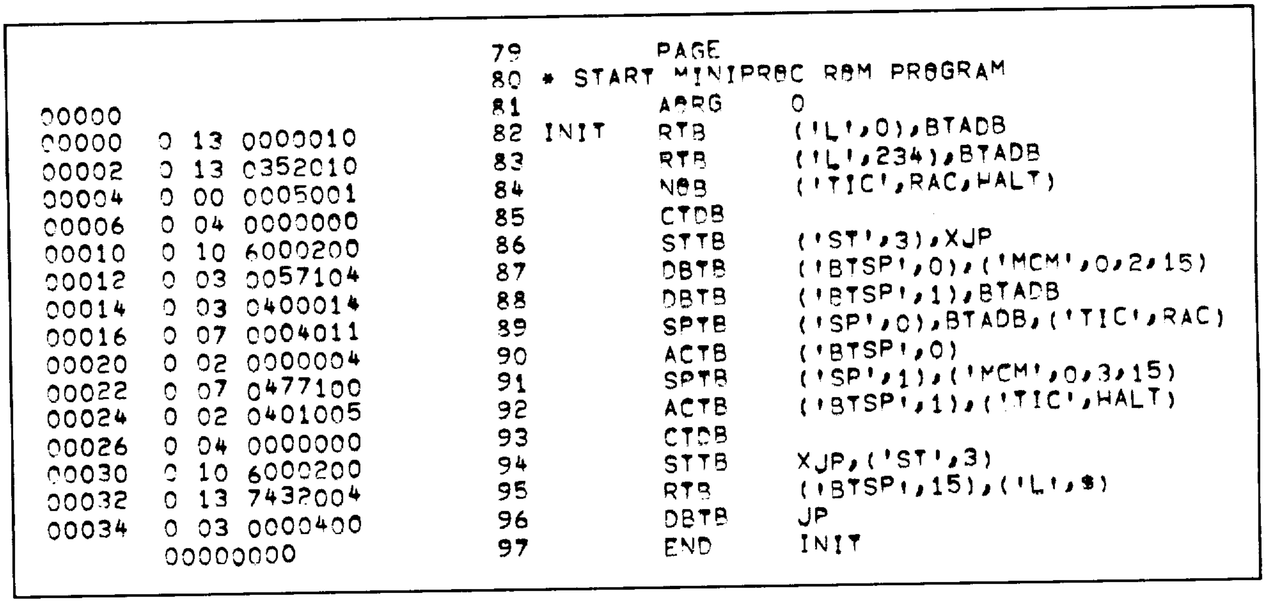

```
                                  79         PAGE
                                  80 * START MINIPROC ROM PROGRAM
00000                             81         AORG     0
00000   0 13 0000010              82 INIT    RTB      ('L',0),BTADB
00002   0 13 0352010              83         RTB      ('L',234),BTADB
00004   0 00 0005001              84         NOB      ('TIC',RAC,HALT)
00006   0 04 0000000              85         CTDB
00010   0 10 6000200              86         STTB     ('ST',3),XJP
00012   0 03 0057104              87         DBTB     ('BTSP',0),('MCM',0,2,15)
00014   0 03 0400014              88         DBTB     ('BTSP',1),BTADB
00016   0 07 0004011              89         SPTB     ('SP',0),BTADB,('TIC',RAC)
00020   0 02 0000004              90         ACTB     ('BTSP',0)
00022   0 07 0477100              91         SPTB     ('SP',1),('MCM',0,3,15)
00024   0 02 0401005              92         ACTB     ('BTSP',1),('TIC',HALT)
00026   0 04 0000000              93         CTDB
00030   0 10 6000200              94         STTB     XJP,('ST',3)
00032   0 13 7432004              95         RTB      ('BTSP',15),('L',$)
00034   0 03 0000400              96         DBTB     JP
        00000000                  97         END      INIT
```

Fig. 7. Sample micro-program

Network Control System

J. N. Edwards
DSIF Digital Systems Development Section

The Network Control System (NCS) is being implemented for the Deep Space Network. This report includes progress activities for (1) final NCS hardware implementation, (2) NCS data formats and Mission Operations Control interfaces, (3) software development summary, and (4) interim NCS hardware and software development summary.

I. Introduction

This is the third report describing the JPL Deep Space Network (DSN) Network Control System (NCS). The previous reports (Refs. 1 and 2) described the project plan and resources, system functions and interfaces, data flow, and hardware allocations for the interim and final NCS configurations. This report describes progress toward implementation of the interim and final NCS.

II. Final NCS Hardware Implementation

The revised DSN 822-series System Requirements Documents are the basis for the NCS configuration which has been defined for hardware implementation. Detailed functional requirements documents and hardware block diagrams are in preparation for subsystems with approved configuration and budget.

Extensive effort has been directed to design maximum uniformity into the mini-computer subsystems. This design includes processors, memory, input/output, communication link interfaces, peripherals, NCS standard data transfer interfaces, direct memory access, operating modes, and on-line/off-line spares compatibility. An automatic data processing equipment (ADPE) plan has been prepared and approved for the NCS subsystem mini-computers.

A reassessment of budgets and functional requirements has delayed procurement of the Network Support Controller midi-computer. The support functions, of diminished scope, will be provided by two Sigma 5 computers transferred from the interim NCS. Additional memory and functions will be required above that provided by the interim NCS Sigma 5 configuration.

The development of a standard data transfer interface for computers and peripherals, to reduce related obsolescence costs when selected equipments are updated, has been a DSN goal. Various interfaces have been evaluated for NCS/DSN standards. The NCS data interfaces are:

(1) NASCOM GCF, 1200/2400-bit serial data block.
(2) RS232, serial ASCII.
(3) Standard parallel byte, 8 bits with 6 control lines.

The byte format provides efficient computer-to-computer controlled transfers, adaption to common data processing peripherals, optimum interface to a Bus Switch Controller (BSC), and data transfer rates well in excess of current requirements.

The BSC is a hardware device for multiple-port data routing between various NCS computers. The BSC configuration will provide routing priorities, subsystem functional addressing, computer-controlled data transfers, and multiple-path full-duplex data routing. The hardware will be of modular configuration to provide cost-effective implementation of the same basic unit in several NCS computer interfaces.

The Display Subsystem requirements for the final NCS have been revised, and will be implemented in a standalone configuration. Features include improved data selection modes, hard copy, simplified video distribution, and higher reliability at reduced cost.

The Network Control System to Mission Control and Computing Center (NCS to MCCC) communications link provides for bilateral transfer of operations and administrative data, and for NCS Ground Communications Facility (GCF) log recall to MCCC. The NCS/MCCC link can be switched for backup to several of the existing GCF lines from Central Communications Terminal (CCT) to MCCC. The MCCC interface to the NCS is the same as to a DSS and requires no MCCC hardware implementation.

The NCS will provide for the operation of a Remote Mission Operations Control (RMOC) for project control to a DSS. The data path via the NCS GCF filler multiplexer will provide NCS access to the high-speed data line (HSDL) synchronized by the RMOC data set. The GCF filler multiplexer will synchronously substitute local NCS data blocks for GCF filler blocks on the line from RMOC to DSS. The GCF filler multiplexer will be used in conjunction with the normal GCF equipment as shown in Fig. 1.

III. Final NCS Software Development

The software design effort for the final NCS has involved extensive negotiation and interpretation of implementation details related to the basic functional requirements. Overall software system block diagrams have been completed. Detail Software Requirements Documents, including diagrams and detail functions, are in preparation and review for each NCS subsystem. Project reviews are in progress to establish accuracy and uniformity of common elements. In addition, benchmark test criteria have been generated to evaluate mini-computer features applicable to all the NCS subsystems. They include:

1. Linking and addressing.
2. External interrupt characteristics.
3. Word synchronization.
4. Macro algorithm computation time.
5. Operating system priority features.
6. Fortran alpha-numeric manipulation.
7. Accuracy and execution time of calculations.
8. Fortran compiler evaluation.
9. Bit, byte, word, doubleword, manipulation.
10. Direct memory access data transfers.

A contract for software design support for the final NCS has been negotiated. Contract start time is estimated to be early March 1973.

A computer model study has been implemented to evaluate line loading, processing, and memory requirements as applied to the CCT Communications/Log Processor (CLP). This processor, with attendant input/output and data logging, is being reviewed for its stringent functional requirements and associated memory requirements.

IV. Interim NCS Hardware Implementation

The interim NCS will provide selected control and monitoring functions for the DSN from July 1973 to July 1974. These functions will be provided by the realtime and backup Sigma 5 computers described in the previous DSN progress report.

The interim system will be installed in JPL Building 202 as shown in Fig. 2. The facility has an existing raised floor for interequipment cabling. The realtime Sigma 5 processor, printer, seven- and nine-track magnetic tapes, paper tape reader/punch, teletype, disk memory and card reader are installed, tested, and being used for software development. Remaining operator terminal display, communications controllers, and remote line printer are scheduled for installation in March. The complete backup Sigma 5 equipment will be installed in May 1973.

The PDP-8 input/output equipment is temporarily located in Building 202 to facilitate testing with the Sigma 5. Interface buffer circuits for two GCF channels have been fabricated and are being tested with the PDP-8. The line drivers, data sets, and data lines for communication between Buildings 202 and 230 have been delivered and are in test.

The NCS to MCCC high-speed data (HSD) link will be implemented for the interim NCS with functional interfaces as described above for the final NCS.

The interim NCS will also provide for operation of an RMOC with a GCF filler multiplexer as described above for the final NCS. The logic design is complete, and two prototypes of the GCF-FM are being fabricated at JPL for use in the interim NCS.

V. Interim NCS Software Development

The software design for the interim NCS is based on an approved subset of the final NCS JPL 822-series functional requirements documents.

Preliminary analysis has shown the need for additional memory in the Sigma 5. An ADPE plan has been approved and procurement is being expedited. The system software block diagram and requirements document have been completed. Subsystem detail requirements and software design are in progress.

Software design personnel, provided by a support contract, are assigned to support the JPL subsystem task leaders. Project design reviews have facilitated uniformity of subsystem design, applicability to final NCS, requirements revisions and guidelines, and expedited schedule milestones.

References

1. Hall, J. R., "Network Control System," in *The Deep Space Network Progress Report*, Technical Report 32-1526, Vol. XI, pp. 5–11. Jet Propulsion Laboratory, Pasadena, Calif., Oct. 15, 1972.
2. Edwards, J. N., "Network Control System," in *The Deep Space Network Progress Report*, Technical Report 32-1526, Vol. XIII, pp. 209–218. Jet Propulsion Laboratory, Pasadena, Calif., Feb. 15, 1973.

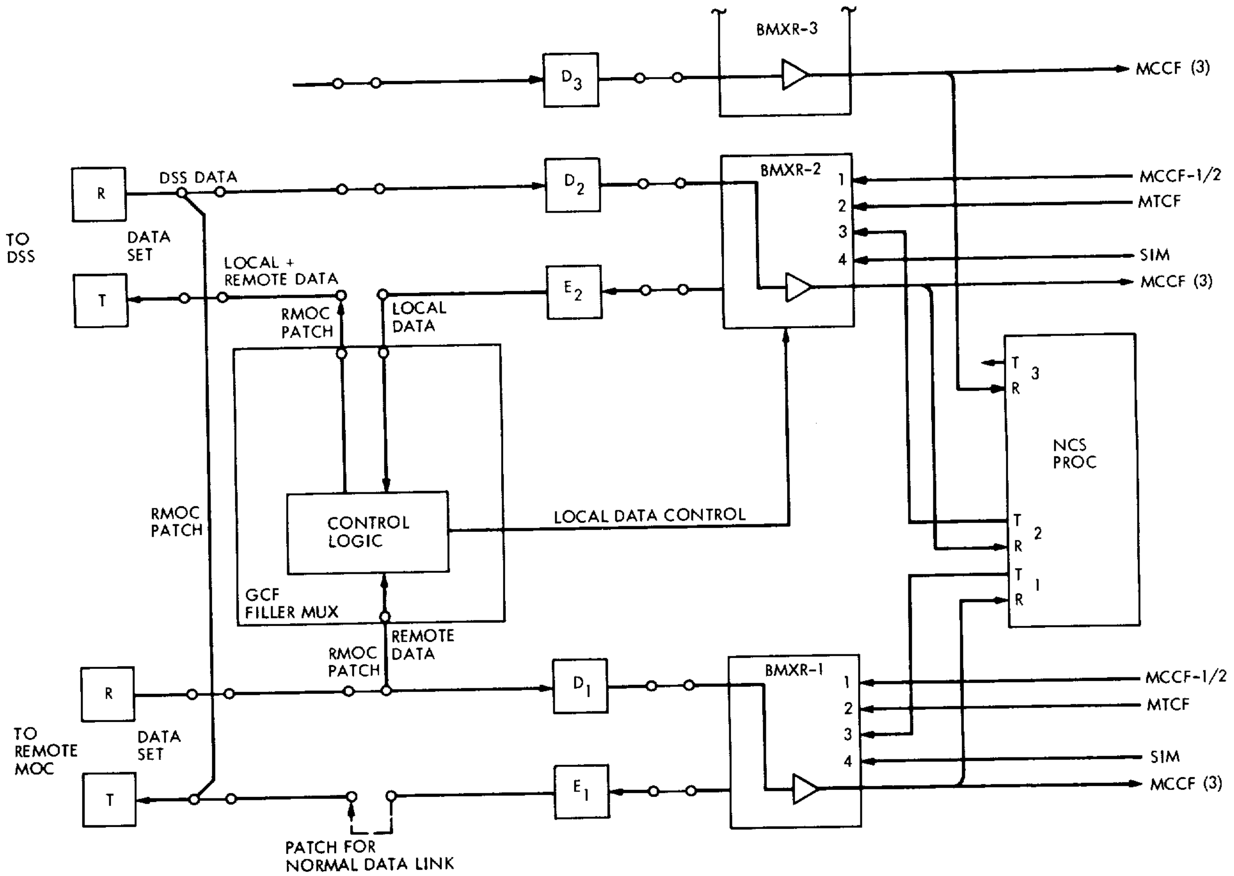

Fig. 1. NCS/Remote Mission Operations Control link

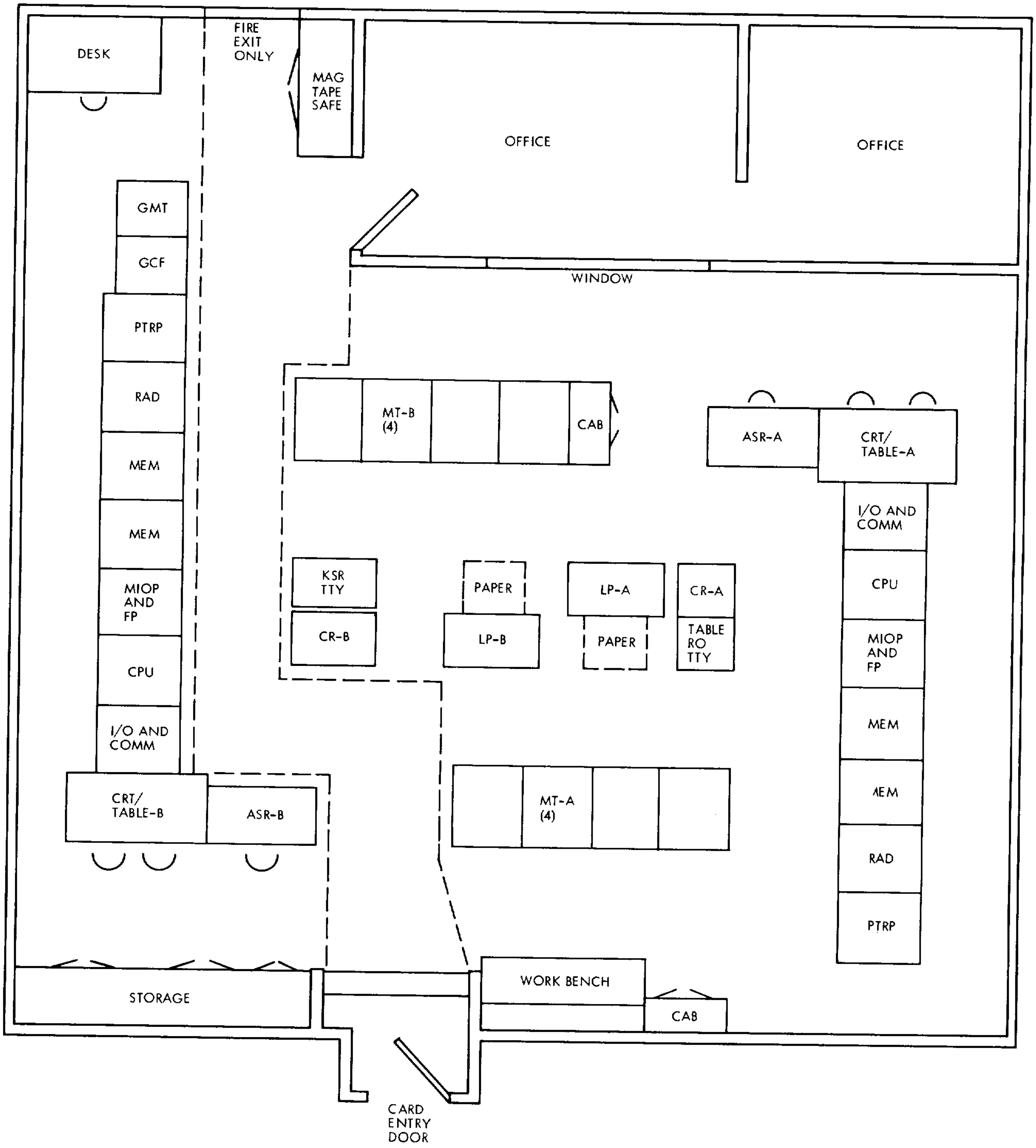

Fig. 2. Interim NCS data processing area

Overseas 64-m Station Implementation Status

R. C. Rydgig
DSIF Engineering Section

Activities associated with implementing the overseas 64-m-diam antenna stations in Australia (DSS 43) and Spain (DSS 63) are presented. The article gives the current status of the project, describes the system configuration as implemented, and discusses the activities involved in reaching the desired configuration.

I. Purpose

The purpose of this article is to present the activities associated with implementing the overseas 64-m-diam antenna stations: DSS 43 in Australia and DSS 63 in Spain. The article will show the current status of the project, describe the system configuration as implemented, and discuss the activities involved in reaching the desired configuration.

II. Implementation Status at DSS 43

The DSS 43 antenna was completed in July 1972. Subreflector and multicone installation and control room electronic equipment installation are in process with a scheduled completion date of April 1973. Subsystem testing is accomplished as the equipment is installed, and system testing will start in March 1973 and be completed by April 30, 1973. This completes the mission-independent implementation.

III. Implementation Status at DSS 63

The DSS 63 antenna was accepted in January 1973. Subreflector and multicone installation is in process and scheduled for completion on May 2, 1973 with an additional weather allowance of up to 30 days.

The Angle Data Assembly will be installed in parallel with the multicone installation and should be completed by May 30, 1973. Control room electronics installation and subsystem testing are in process and should be completed by June 30, 1973. System testing is scheduled for completion by August 30, 1973.

In the event that weather does not unduly impact installation of equipment upon the antenna, the mission-independent operational readiness date could improve by as much as 30 days.

IV. System Configuration

The system configuration, as shown in Fig. 1, consists of separate 26-m and 64-m antennae and associated servo systems. The 64-m antenna is controlled by an Antenna Pointing Subsystem and the 26-m antenna is controlled by a combination of a Spaceflight Tracking and Data Network (STDN) Antenna Position Programmer and the Simulation Conversion Assembly, which provides simulation for both the 26-m and 64-m stations. A Tracking Data Handling Subsystem processes radio metric data for the

64-m antenna and an STDN Tracking Data Processor handles the 26-m radio metric data. Each station has separate antenna microwave, receiver/exciter, ranging and monitor subsystems. Each station has one telemetry and command functional system and shares a second system by means of a switching network. Additional shared electronic equipment consists of frequency and timing, communications (tactical intercom, teletype, high-speed data, and voice), system control, and monitor and simulation. Shared facilities equipment consists of power generation and distribution, heating, ventilation, and air conditioning.

JPL drawing 9456098, "Functional Block Diagram 1973 Model Conjoint Stations" functionally depicts the configuration. With this configuration, each station can track a spacecraft simultaneously, and at the completion of the implementation, both stations will be capable of supporting the Pioneer Project. Additional equipment and testing will be required to support Mariner and Viking. Note that the configuration of DSS 61/63 is identical to DSS 42/43.

V. Implementation Activities

Because of the interrelationship between the 26-m and 64-m stations, a description of the implementation activities must include both stations. As the 64-m antennae were being built, the 26-m stations were being prepared for the new configuration. This was a two-step process.

Step one, as described in Ref. 1, consisted of removing the Deep Space Network (DSN) equipment from the DSN control room and installing sufficient equipment in the Manned Spaceflight Network (MSFN) (now identified as STDN) control room to allow the 26-m stations to continue to support the Apollo, Pioneer, and Mariner Projects while the 64-m stations were being built. This Integration Program also provided some equipment and facilities which were needed for the 64-m station. When the 26-m stations resumed tracking, the empty control rooms at DSS 42 and DSS 61 were upgraded and expanded to provide room for the equipment needed to support projects through 1975. At the same time, the power generation and distribution, heating, ventilation, and air conditioning modifications were made for simultaneous two-station support.

After the facility modifications were completed, step two of the implementation activities was initiated. The 26-m stations were shut down and DSN equipment was removed from the 26-m control room and reinstalled in the 64-m control room. This move was conducted in a manner which would allow the 26-m stations to return to an operational status, for Apollo support only, when required by STDN. The modifications to existing equipment and installation of new equipment which was needed to allow the 26-m station to return to a DSN as well as STDN operational condition was then implemented. In November 1972, DSS 42 became a fully operational station. In addition, the implementation of DSS 43 had progressed to the point where the 64-m station successfully supported Apollo 17 on a best effort basis. DSS 61 became operational for Apollo support in November 1972 and DSN support in January 1973.

With both 26-m stations operational, the implementation of the 64-m stations continues on a noninterference basis to the 26-m stations in accordance with the schedule outlined in the status section of this article.

Reference

1. Weber, R., "MSFN/DSN Integration Program for the DSS 11 26-m Antenna Prototype Station," in *The Deep Space Network Progress Report,* Technical Report 32-1526, Vol. III, pp. 197–202. Jet Propulsion Laboratory, Pasadena, Calif., June 15, 1971.

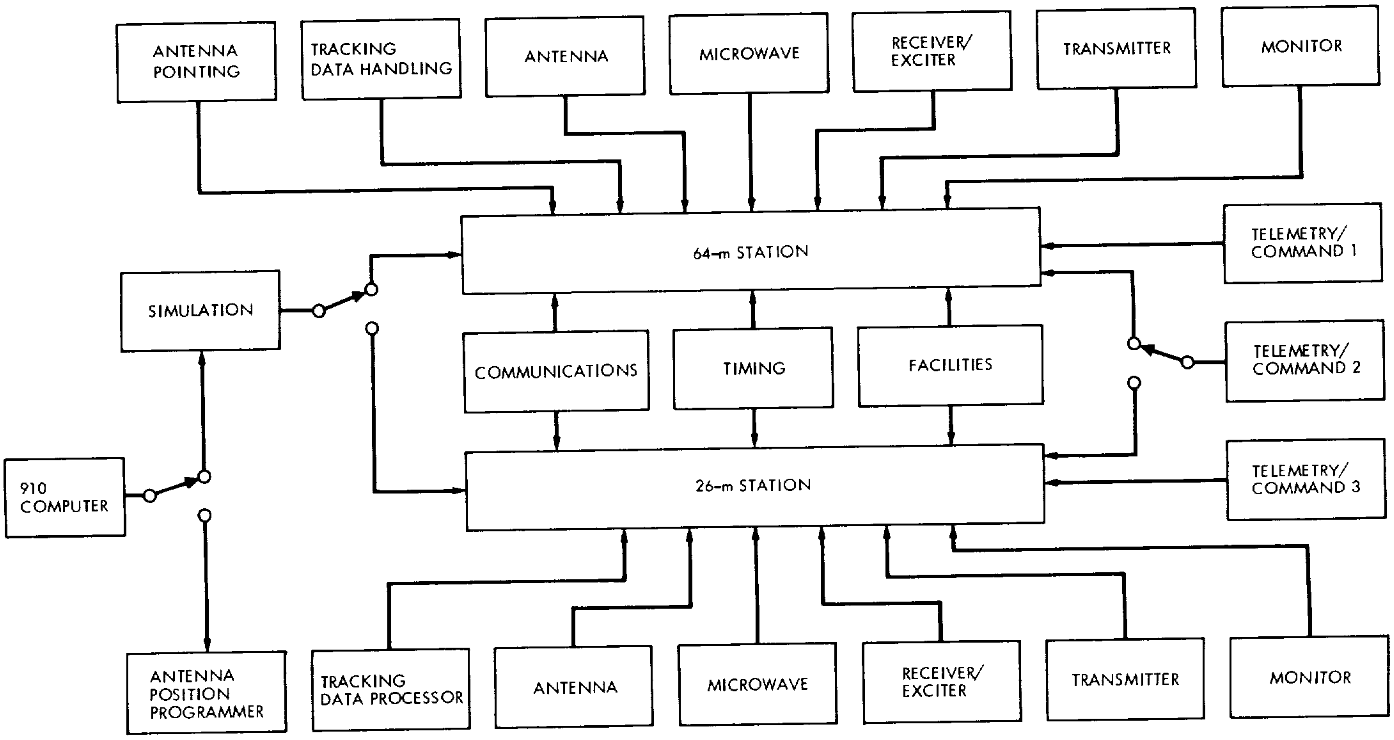

Fig. 1. Conjoint station configuration of DSS 42/43 and DSS 61/63

Amplitude and Frequency Modulation Effects to Telemetry Link Reception

N. C. Ham
R. F. Systems Development Section

A spin-stabilized spacecraft can produce an amplitude and phase variation to the normally phase-modulated downlink carrier signal due to its antenna characteristics. The manifestation of these variations is equivalent to an amplitude and frequency modulation to the carrier signal, and the effects to the telemetry link must be considered. The Helios spacecraft and mission is a typical case, and means for simulating a certain portion of the flight profile, which will create such conditions, was utilized to test and evaluate the effect upon the DSIF Telemetry System. Initial test results indicated that the Telemetry System was more sensitive to the phase variation than to amplitude variations in increasing the detected symbol error rate for a given telecommunication link situation.

I. Introduction

Spin-stabilized-type spacecraft can alter the telecommunication link between the spacecraft and ground systems, particularly if the spacecraft RF antenna subsystem's physical placement is not coincident to the spacecraft spin axis and its radiation pattern is non-symmetrical containing lobes and deep nulls.

Typical is the case of the Helios spacecraft in its construction (Ref. 1) and mission flight maneuver phases. The spacecraft omni-directional antenna, which is comprised of simultaneously driven top dipole and bottom horn antenna elements, as shown in Fig. 1, produces a combined pattern envelope that is non-symmetrical on each side of the spin axis and for a radial polar revolution within the axis plane. The non-symmetry of each side of the axis is due to the horn antenna, which is displaced 6λ (wavelength at the transmitted frequency) from the spin axis. The polar asymmetry results from the linearly polarized, top dipole antenna and circularly polarized bottom horn antenna, where the top null is the top antenna "end-fire" characteristic and lower portion nulls result from the interferometric effects of the combined top and bottom antennas.

During a spacecraft attitude maneuver (Step I: when the spacecraft aligns its axis normal to the Sun) early in the mission, the signal could possibly traverse through the lower antenna interference zone. The effect to the telecommunication link can be seen to vary the signal amplitude which is further compounded by the spacecraft rotation producing a periodic signal phase variation. A similar effect will occur during a later maneuver phase (Step II) when the spacecraft is commanded to align its spin axis perpendicular to the ecliptic plane.

The manifestation of these conditions is a phase variation expressed by $A_\lambda \sin 2\pi f_s t$ superimposed upon the normal phase-modulated, S-band, downlink signal, and an amplitude variation affecting this same signal to modify the carrier ($E_c \cos \omega_c t$) expressed as

$$e(t) = E_c (1 + A_m \cos 2\pi f_m t) \cos \omega_c t$$

where A_λ is related to the offset antenna distance of the horn antenna, f_s is related to the spacecraft rotation rate, A_m is related to the null depth in the antenna interference zone, and f_m is related to the omni-antenna pattern for one spacecraft revolution multiplied by the spacecraft rotation rate and "look angle."

Consider first the rotating spacecraft, with its offset antenna, traveling in a radial direction away from Earth with a radial velocity v. If the "look angle" is taken as being normal to the spin axis (a possible condition during Step II), as shown in Fig. 2, then the full value of the 6λ offset can be considered as the largest magnitude value for the rotating vector spinning within the plane of the radial velocity direction (see Fig. 3). The projected lateral component due to this rotating vector, parallel to the direction of radial velocity, is then $6\lambda \cos \Phi$, where Φ is the included vector angle. The spacecraft is revolving at an angular velocity ω of one revolution per second or, with an angular rate of change $d\Phi/dt = \omega = 2\pi f_s t = 2\pi t$; thus, the lateral component becomes $6\lambda \cos (d\Phi/dt)$ or $6\lambda \cos 2\pi t$ expressed as a function of time.

The radial velocity v imparts a Doppler frequency to the RF signal by the relation

$$F_{\text{Doppler}} = F_T \frac{c + v}{c - v}$$

where F_T is the frequency of the transmitted signal and c is the speed of light.

The displacement 6λ is also related to the transmitted frequency by $\lambda = c/F_T$. Since there are 2π radians per cycle of revolution, the above lateral component expression becomes $12\pi \cos 2\pi t$ and for one cycle of revolution $\Delta F_{\text{Doppler}} = 12\pi \cos 2\pi t$. The instantaneous doppler is the sum of the rotating component, with a magnitude of ±37 Hz varying at a one-cycle rate, and the doppler due to the radial velocity v. This is shown in Fig. 4.

The rate of change of the component due to the spinning spacecraft can be obtained by the derivative of the above equation:

$$\frac{dF_D}{dt} = \frac{d}{dt} 12\pi \cos 2\pi t = -24\pi^2 \sin 2\pi t$$

or $\dot{F}_D = 240$ Hz per second. Thus, the phase variation of the ground received frequency results in a peak frequency deviation of ±37 Hz about the radial velocity Doppler frequency, occurring periodically every second, with a 240-Hz per second rate change due to the spinning spacecraft.

The gain variation of the antenna produces an amplitude-modulated carrier signal with an envelope that is cusp-serrated, as shown in Fig. 5 modeled from a typical spacecraft antenna pattern for one revolution and specific "look angle" of Fig. 6. This can be approximated as a time varying function where $f_m = 20$ Hz and $A_m = 10$ dB when considering only the higher frequency components of the Fig. 6 rotation-time function characteristics.

It becomes a concern for the mission operation as to the degree of additional degradation to the normal telemetry telecommunication link that may be contributed from this condition. The Deep Space Station Telemetry System is comprised of the receiver subsystem which phase and amplitude tracks the modulated carrier using electronic servo loops, the Subcarrier Demodulator Assembly (SDA) for creating a local estimate of the bi-phase modulated subcarrier for data demodulation of the sideband energy, the Symbol Synchronizer Assembly (SSA) for data synchronization, and a Data Decoder Assembly (DDA) for sequentially decoding the convolutional-encoded telemetry when the coded mode is utilized.

Based on the postulated conditions and modeled signal variations, a quick analysis of the Telemetry System performance is presented in the following discussion.

II. Receiver Automatic Gain Control Loop Response

The Automatic Gain Control (AGC) closed loop $H(j\omega)$ amplitude response is shown in Fig. 7 for the widest bandwidth (BW) value with a resulting -3-dB amplitude value corresponding to 6 Hz (Ref. 1). With the postulated 20-Hz periodic amplitude-variation input applied, the AGC response curve indicates a -10-dB value, and consequently the gain control loop cannot track or follow this rate but instead responds only to the average of the signal variations. This average value is approximately 1 dB higher in value than the non-amplitude-modulated condition and due to the variations produces a resultant carrier and sideband fluctuation at the IF amplifier output as shown in Fig. 8. The variation is a periodic $+3$-dB increase and -7-dB decrease from the average or control level value.

The only AGC loop anomaly that may result from this instantaneous -7-dB carrier decrease is that the receiver loop "in-lock" detector, which reacts to the carrier amplitude, may momentarily disengage if the decrease in signal and duration approaches the "in-lock" circuit time constant. An instantaneous disengagement can produce an erroneous "flag" to the telemetry data stream block.

III. RF Loop Response

The receiver carrier phase-locked loop employs a bandpass limiter whose input-signal level "set point" is related to the absolute value of the carrier as established by the AGC loop. The "set point" is well beyond the limiter "knee" such that a -8-dB (-7 dB plus -1 dB due to AGC control level change) instantaneous decrease, at strong signal conditions, will still develop a constant limiter output value (see Fig. 9). Since the RF loop bandwidth determination involves an amplitude parameter which is still maintained constant by the limiter, the loop will remain "in-lock" and develop a normal operating bandwidth.

The above condition applies regardless of the RF loop bandwidth value; however, the input Doppler and Doppler rate will produce phase errors within the loop and to the local estimate of the carrier phase. For example, if the bandwidth of 152 Hz is used, an additional phase error due to the rotating 6λ offset horn of no more than 3-deg peak will result (Ref. 1).

IV. Subcarrier Demodulator Response

The SDA, which utilizes a phase-locked loop, should be operated in the medium loop bandwidth value for reducing phase tracking errors. This loop has a "soft limiter" circuit, as contrasted to the carrier loop "hard limiter," and although the SDA limiter output varies proportionally to the input value (at strong signal levels), the loop will remain "in-lock" and maintain a constant loop BW since the loop low-pass filter averages the variations (Ref. 2). The Doppler rate-to-SDA loop BW ratio at the subcarrier frequency is considerably lower than for the carrier case and since the SDA loop is also a second-order type, it produces only a small resultant phase error when tracking the input-signal phase variations.

The SDA data-demodulation channel achieves the demodulation by a phase-coherent amplitude detector circuit; hence, the demodulated data have the same signal amplitude variations. The momentary data amplitude increase, during high signal-to-noise ratio (SNR) conditions, will not encounter signal suppression since the dynamic range of the circuits possesses ample amplitude linearity range. See Fig. 10, which also illustrates the time relationship of the signal duration (128 symbols per second (sps)) to the amplitude variation envelope and null depth. The SDA is also equipped with an "in-lock" detector, similar to the carrier AGC circuit, but it reacts instead to the data amplitude; therefore, its response to the varying sideband amplitude follows a similar consideration.

V. Symbol Synchronizer Response

The SSA is similarly comprised of a phase-locked, symbol-tracking loop for symbol synchronization and a symbol-detection channel (Ref. 3).

The symbol-tracking loop will remain "in-lock" to the input variation, where again the Doppler rate is low at this symbol frequency. Since the loop integration occurs symmetrically about the symbol transition point, the loop is unperturbed by the amplitude variations or noise at a high input SNR.

The symbol detection channel will operate with only slight degradation because its data-type selector uses the sign bit of the symbol value (from the channel integrate-and-dump circuit) to determine whether the symbol is a logical 1 or a logical 0 and the amplitude linearity is adequate to handle the amplitude increases. Also, should it be necessary to increase the overall level of the symbols (an SDA operational adjustment) to insure that the minimum value of the symbol is always above the threshold value, this can be easily accommodated to enhance its performance capability.

VI. Data Decoder Response

In the coded-mode case the symbol duration time must be considered, for here the symbol rate is 256 symbols per second and the SSA, which outputs the detected symbols to the DDA for decoding the convolutional encoded data, now has a shorter symbol duration-to-envelope variation time ratio (see Fig. 10). As far as the DDA performance is concerned, only relatively slight degradation is expected since the symbol value output from the SSA is a binary number related to the polarity and amplitude of the voltage in the SSA integrator (at the end of the symbol time) and the expected amplitude will be above the DDA threshold designed value. If an occasional symbol error due to amplitude variations randomly occurs (at a frequency no greater than one in ten), then no degradation is expected – especially at high SNR.

VII. Simulated System Test

Figure 11 is a block diagram of the test configuration that was used at the JPL Compatibility Test Area (CTA 21) to simulate the above conditions and evaluate the Telemetry System performance. The signal generator (shown driving the exciter VCO) simulates the phase variation, where the amplitude of the generator signal relates to the 6λ offset or frequency deviation, and the generator frequency to the spacecraft rotation rate. The function generator, and circuitry following the translator output, simulates the amplitude variation due to the antenna interference zone, where the generator frequency and signal level set these parameters. The function circuitry is a simple diode-bridge rectifier which accepts the sine-wave signal from the generator and develops a full-wave rectified output waveform simulating the amplitude cusp-serrated envelope. The power amplifier amplifies this signal and modulates the PIN (P-intrinsic-N) modulator. The PIN modulator contains a number of PIN diodes mounted as shunt elements across a transmission line. Because of their appreciable storage time, they do not rectify the S-band signal; however, when a dc forward bias is applied, the diode conducts, reducing their resistance with low reactance, and shunts the transmission line. This functions as an absorption modulator, with virtually no incidental frequency modulation, and a simulated amplitude-variation signal is thereby achieved.

The variable attenuator is used to establish the average signal level which is used as the independent variable parameter for the test conditions. The Simulation Conversion Assembly (SCA) generates a 128-symbol per second PN sequence pattern (uncoded mode test configuration) for modulating the exciter simulating the spacecraft telemetry stream, and simultaneously a reference stream to the Telemetry and Command Processor (TCP) for a symbol-by-symbol comparison with the detected data to compute symbol-error-rate (SER) statistics. A typical test run procedure was to establish a particular signal-level margin M above the RF loop threshold value and observe the SER (computed for a sampling size of 10^4 symbols) with various combinations of simulated amplitude and frequency modulation applied.

Although a high SNR setting (when no AM and FM is applied) results in a low probability of SER, the value of 1×10^{-4} was set as a minimum value for evaluation comparison when modulation is applied. Thus, any degradation that may occur due to the simulation would produce nearly instantaneous symbol errors occurring at a periodic rate of the simulation FM and AM frequencies. The criterion for system failure is orders-of-magnitude SER increase during simulation modulation. The ratio of the 10^4 symbol time duration to the AM/FM frequencies duration (50 seconds to 50 milliseconds and 1 second) was considered adequate for gathering error statistics. The rationale was to reduce extremely long test runs at this low symbol rate for each adjusted signal level setting.

The same procedure was followed for the coded-mode test configuration except that frame erasures were used as the parameter for comparative purposes.

The monitor equipment was used to calibrate and monitor the various points throughout the Telemetry System to insure that the results were correct and to validate the simulation. For example, a base band signal of 1 kHz was used to calibrate the modulation depth of the AM simulation by observing the phase-demodulated envelope pattern at the receiver phase detector output (normally used for pre-detection recording) after bypassing the detector limiter circuit.

VIII. Test Results

The following conditions were used for the system test:

RF loop BW	152 and 48 Hz
AGC loop BW	Wide
SDA loop BW	Medium
SSA loop BW	Medium
SDA mod index attenuator	Normal setting
Modulation index	68.2° (−8.6-dB carrier suppression)
Subcarrier frequency	32,768 Hz
Symbol rate (uncoded)	128 bps
Symbol rate (coded)	256 sps
Bit rate (coded)	128 bps
AM (period)	20 Hz
FM (deviation)	±37 Hz
FM (period)	1 Hz
Data Format:	
Uncoded	2047-bit PN sequence
Convolutional coded	192 bits/frame

Tables 1 through 7 are tabulations of the results obtained from the various test combinations.

Table 1 is the resulting SER for 128-bit per second (bps) uncoded data and an AM null depth of 10 dB applied with an RF loop BW of 152 Hz and the remaining test conditions as stated above. This table indicates that the FM phase variation produced only slight degradation when the signal level is 10 dB or greater above the RF loop threshold value, as expected, since the additional loop phase error contributions were analyzed to be approximately 3 deg at a 10-dB margin; similarly, the degradation is slight with AM applied in addition to FM.

Table 2 is the SER for 128-bps uncoded similar to conditions of Table 1 except that an RF BW of 48 Hz was used. Here it is seen that FM has quite an effect upon the degradation since an evaluation of the RF loop indicates that the phase error is approximately 20 deg (at a signal margin of 10 dB), with the applied 240-Hz per second Doppler rate, as compared to only 3 deg for the 152-Hz BW (Ref. 1).

Figure 12 is a plot of the SER versus the signal margin M from this same test run.

Table 3 is a direct comparison of the RF loop BW of 152 Hz versus 48 Hz showing the doppler rate effect to the lower BW value for the combined AM/FM applied case.

Table 4 conditions are similar to Table 1 except that the AM depth was increased from 10 dB to 13.6 dB and shows that this null depth contributes very little additional degradation compared to the FM-only condition.

Table 5 compares the 10-dB AM depth to the 13.6-dB depth for the RF BW value of 152 Hz for both AM/FM applied and shows surprising identical results indicating that the Telemetry System is not sensitive to AM over this range of AM depth when the margin is 10 dB or greater.

Table 6 tabulates the results of the convolutional-coded mode similar to the uncoded mode test conditions of Table 1. The sample run time was 10 minutes for each of the signal margin levels.

Table 7 combines the results shown in Table 1 and Table 6, uncoded versus coded mode simply to show that the 10-dB RF loop margin value appears to a "criteria point" below which degradation begins to become apparent.

IX. Conclusions

As stated previously, a 10-dB margin above RF loop design threshold value (for this particular modulation index and BW settings) was the signal level where detection error changes became noticeable. A signal margin of 15 dB or greater would insure that the postulated signal variation would produce negligible degradation to the DSS Telemetry System performance.

The Telemetry System was more sensitive to the phase variations than to the amplitude variations as shown by Tables 3 and 5. This is a particularly important factor since these results are applicable to the "uplink" signal transmission to the spacecraft if similar type demodulation/detection systems are employed. Briefly stated, the most severe Doppler and Doppler rate values occur at the carrier frequency, and RF loop circuits that must track this signal could produce phase errors which contribute largest to the overall degradation. Since the amplitude variations below the AGC average value were of short duration, the "in-lock" circuits did not fluctuate or develop erroneous "flags" as first assumed.

The performance to either the coded or uncoded mode for these specific formats produced comparable results.

The foregoing analysis and Telemetry System test, based on the modeled input condition, were not intended to be rigorous but was structured to observe the first-order effects; hence, a more detailed analysis would be required for a complete performance evaluation covering more facets of possible conditions. Suffice it to say, the test method and results appear valid and support the quick analysis; furthermore, information presently available pertaining to performance characteristics of the individual subsystems can be used as an intuitive guide for evaluating the expected systems performance – or, at least, to formulate a system test method.

It should be clarified here that these results were the effects due to the rotating offset spacecraft antenna and a typical omni-antenna pattern and should be considered as additional factors that would contribute to any specific condition. Thus, the Doppler effects resulting from trajectory dynamics must certainly be included for a complete performance evaluation.

References

1. *Deep Space Network/Helios Spacecraft Telecommunication Interface Definition*, Document 613-6, Dec. 1, 1972 (JPL internal document).
2. Brockman, M. H., "MMTS: Performance of Subcarrier Demodulator," in *The Deep Space Network*, Space Programs Summary 37-52, Vol. II, pp. 127–141. Jet Propulsion Laboratory, Pasadena, Calif., July 31, 1968.
3. Frey, W., Petrie, R., and Greenberg, R., "Multiple-Mission Telemetry System Project," in *The Deep Space Network*, Space Programs Summary 37-61, Vol. II, p. 125. Jet Propulsion Laboratory, Pasadena, Calif., Jan. 31, 1970.

Table 1. SER comparison of FM against AM/FM applied

Test mode	$M = 27$ dB	$M = 17$ dB	$M = 12$ dB	$M = 10$ dB
With FM	$<10^{-4}$	$<10^{-4}$	$<10^{-4}$	4.8×10^{-4}
With AM/FM	$<10^{-4}$	$<10^{-4}$	1.6×10^{-4}	4.5×10^{-4}

RF BW = 152 Hz, 10-dB AM depth, 128 bps uncoded

Table 2. SER comparison of AM against AM/FM applied

Test mode	$M = 15$ dB	$M = 12$ dB	$M = 10$ dB	$M = 5$ dB
With AM	$<10^{-4}$	$<10^{-4}$		
With AM/FM	2.47×10^{-3}	4.5×10^{-2}	1.0×10^{-1}	2.2×10^{-1}

RF BW = 48 Hz, 10-dB AM depth, 128 bps uncoded

Table 3. SER comparison of RF BW 152 Hz versus 48 Hz

Test mode	$M = 16$ dB	$M = 15$ dB	$M = 12$ dB	$M = 10$ dB
152 Hz AM/FM	$<10^{-4}$	$<10^{-4}$	1.6×10^{-4}	4.5×10^{-4}
48 Hz AM/FM	3.5×10^{-3}	2.47×10^{-3}	4.5×10^{-2}	1.0×10^{-1}

10-dB AM depth, 128 bps uncoded

Table 4. SER FM versus AM/FM comparison with 13.6-dB AM

Test mode	$M = 28$ dB	$M = 20$ dB	$M = 16$ dB	$M = 10$ dB
With FM		$<10^{-4}$	$<10^{-4}$	3.3×10^{-4}
With AM/FM	$<10^{-4}$	$<10^{-4}$	$<10^{-4}$	4.1×10^{-4}

RF BW = 152 Hz, 13.6-dB AM depth, 128 bps uncoded

Table 5. SER comparison of 10-dB versus 13.6-dB AM depth

Test mode	$M = 28$ dB	$M = 20$ dB	$M = 16$ dB	$M = 10$ db
10-dB AM depth	$<10^{-4}$	$<10^{-4}$	$<10^{-4}$	4.5×10^{-4}
13.6-dB AM depth	$<10^{-4}$	$<10^{-4}$	$<10^{-4}$	4.1×10^{-4}

RF loop = 152 Hz, AM/FM applied, 128 bps uncoded

Table 6. Frame erasure comparison for coded mode

Test mode	$M = 20$ dB	$M = 15$ dB	$M = 10$ dB	$M = 7$ dB	$M = 3$ dB
No AM, FM	None	None	None	8 Erasures	>100 Erasures
With AM/FM	None	None	None	9 Erasures	>100 Erasures

RF BW = 152 Hz, 10-dB AM depth, 128 bps coded

Table 7. Comparison of uncoded versus coded with AM/FM

Test mode	$M = 15$ dB	$M = 10$ dB	$M = 7$ dB
Uncoded SER	$<10^{-4}$	4.5×10^{-4}	
Coded erasure	No erasures	No erasures	9 erasures

RF BW = 152 Hz, 10-dB AM depth

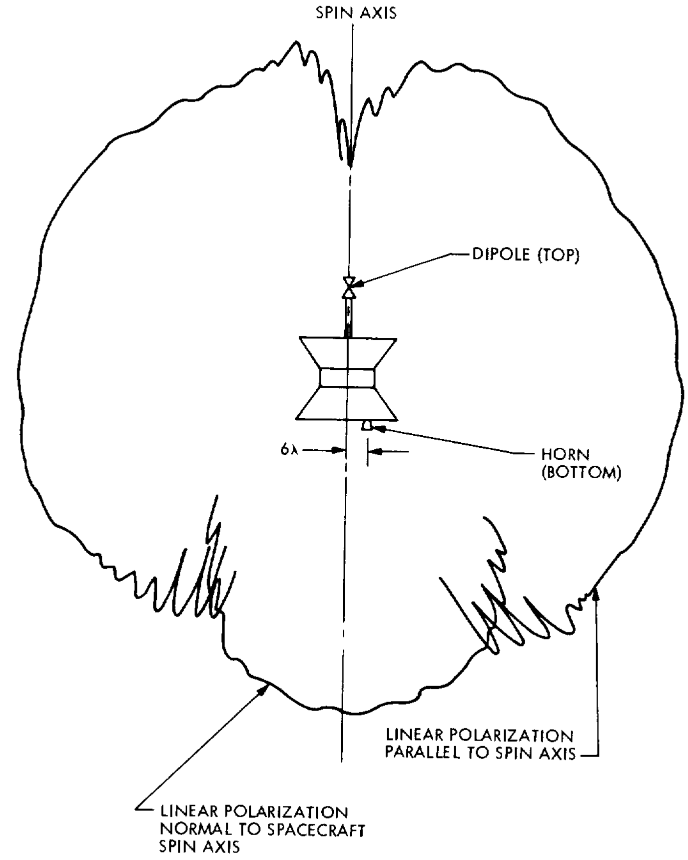

Fig. 1. Spacecraft omni-antenna pattern in plane through spin axis

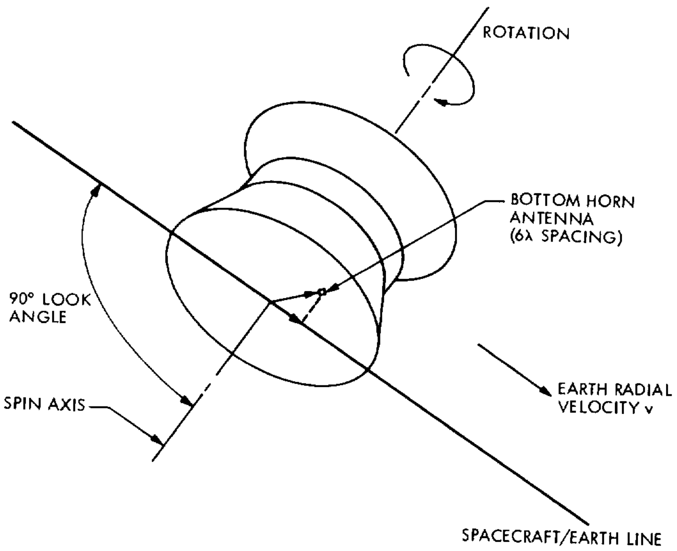

Fig. 2. Rotating spacecraft with off-axis RF antenna as seen from Earth

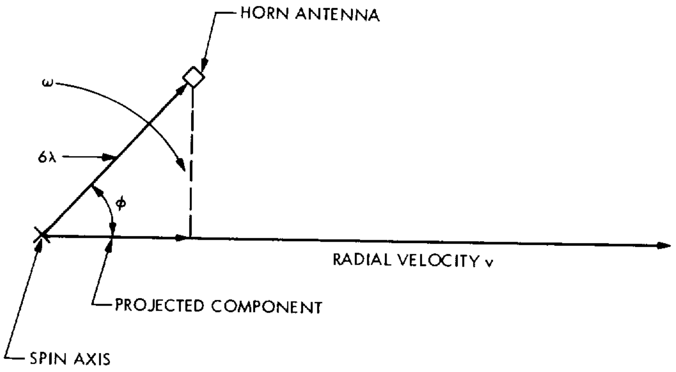

Fig. 3. Rotating spacecraft with off-axis RF antenna in plane normal to spin axis

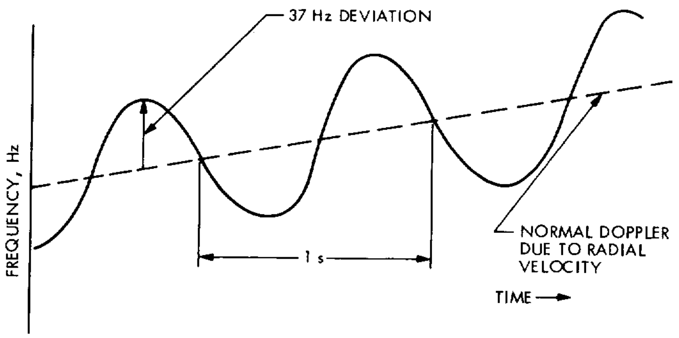

Fig. 4. Resultant instantaneous Doppler frequency due to rotating spacecraft traveling at a radial velocity

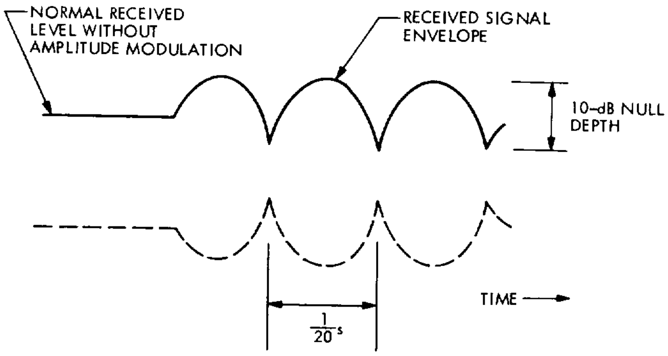

Fig. 5. Modeled amplitude-modulated signal due to low-gain antenna characteristic

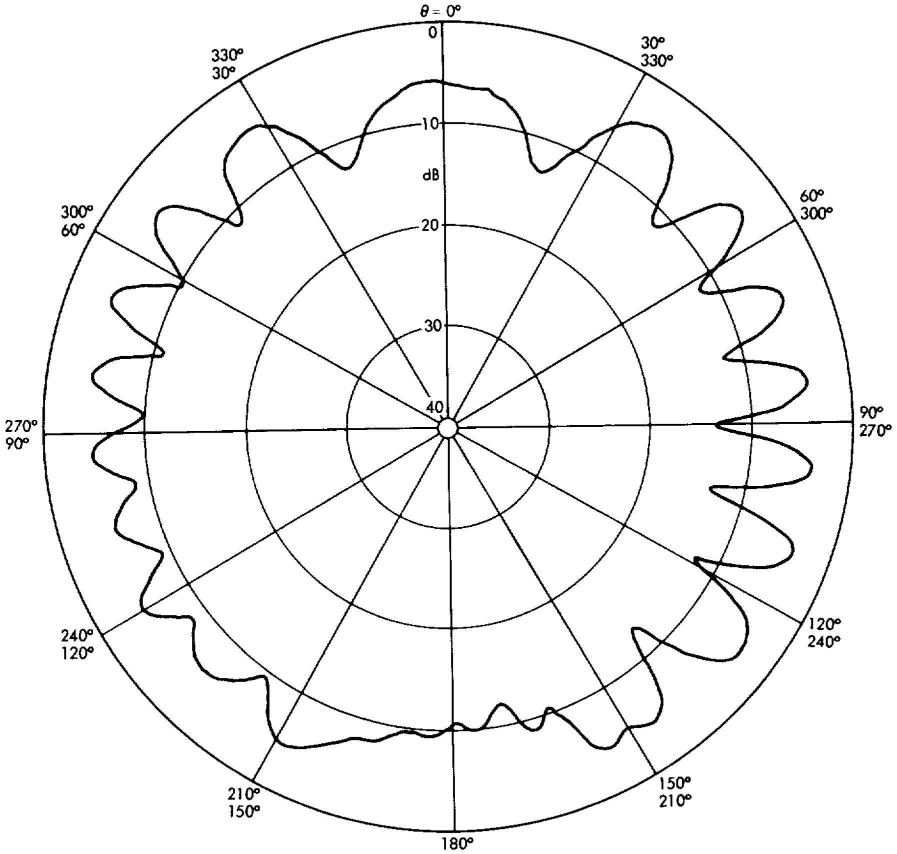

Fig. 6. Typical combined LGA pattern plotted through interference zone for one revolution

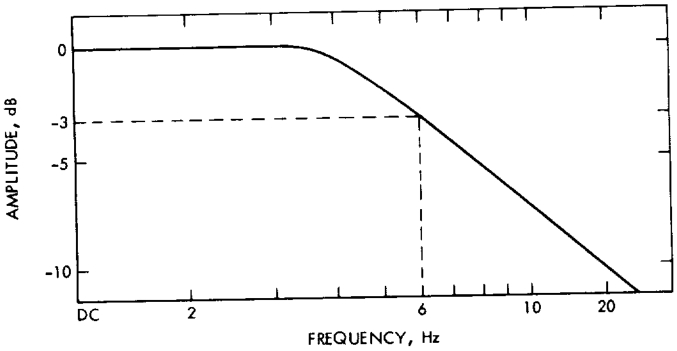

Fig. 7. Closed loop H(jω) AGC amplitude response

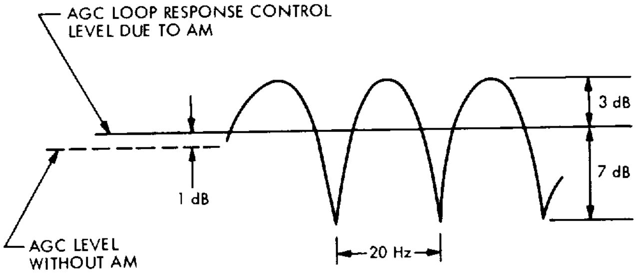

Fig. 8. Gain control level of AGC loop to modulated signal

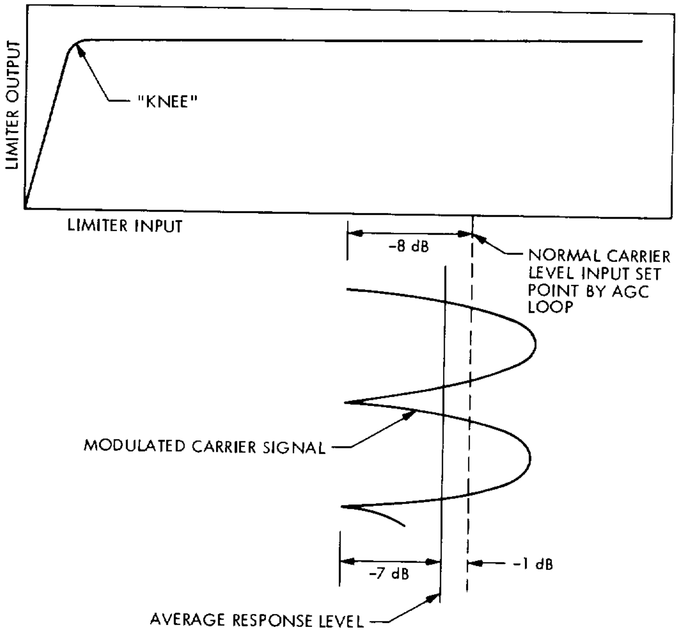

Fig. 9. RF loop limiter characteristic

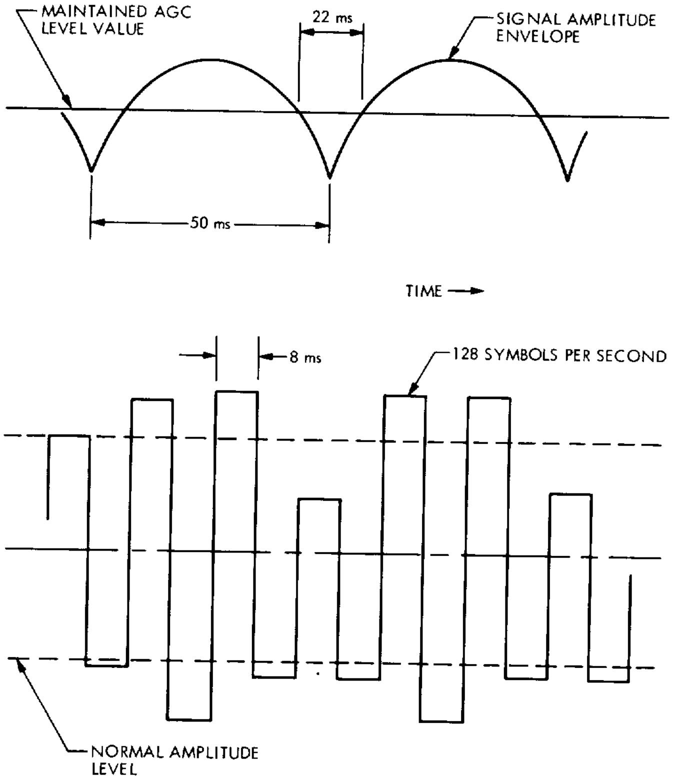

Fig. 10. Resultant SDA demodulated data amplitude and time relationship

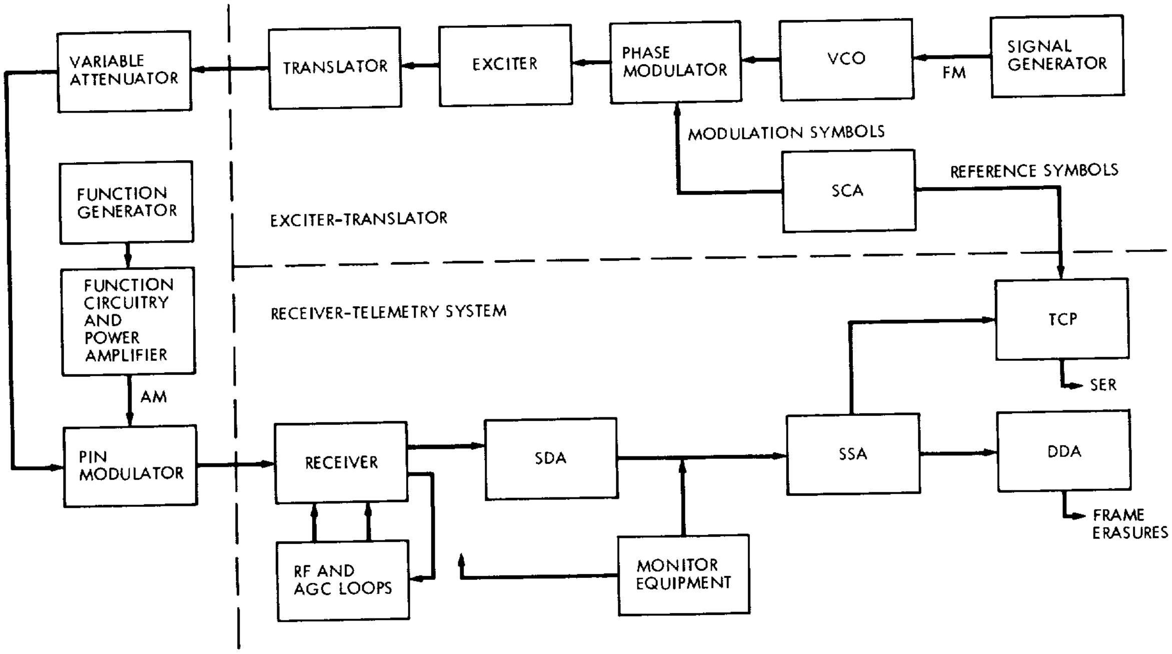

Fig. 11. Block diagram of simulation system test

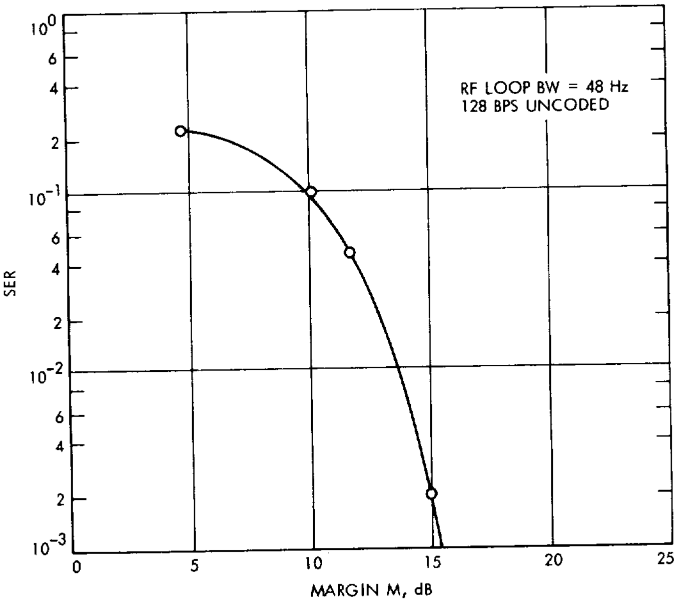

Fig. 12. SER versus M with AM/FM applied as obtained from Table 2 data

Block IV Ranging Demodulator Assembly

R. C. Coffin
R. F. Systems Development Section

The Block IV Ranging Demodulator Assembly is a 10-MHz ranging receiver operating on the automatic-gain-controlled output of either a Block III or Block IV DSIF receiver. It demodulates the 10-MHz carrier that has been phase modulated with range code to provide two range correlation voltages to the Planetary Ranging Assembly. The design of the Ranging Demodulator Assembly, which encompasses range code correlation and demodulation of the 10-MHz carrier, is compatible with either composite or sequential range code schemes. Manual control of the Block IV Ranging Demodulator Assembly is straightforward and easy to comprehend, which will serve to minimize operator expense and operator errors. Computer control capability is provided and may be implemented as soon as a suitable interface is developed.

I. Introduction

The planetary ranging system is a two-way radio link employing an active transponder in the spacecraft. Basically, the system operates by transmitting a carrier signal modulated by a suitable code. Upon receipt of the ranging signal, the spacecraft detects the code and then modulates it onto a downlink carrier. The ground station receives the downlink signal from the spacecraft and detects the code. The two-way spacecraft range, in time units, is determined by comparison of the phase of the received code with that of the transmitted code.

II. Block IV Ranging Demodulator Assembly

The Ranging Demodulator Assembly (RDA) is a 10-MHz special-purpose receiver whose function is to demodulate the range code modulated IF signal from the DSIF receiver. Historically, there have been two planetary ranging systems, both built as developmental tasks. The two systems differ in several ways, but fundamental among the differences is the coding scheme employed. One system (Refs. 1, 2, and 3) uses a composite pseudo-random code scheme and was termed alternatively the Tau, MV67 or PN system. The other system (Refs. 4, 5, and 6) utilized a sequential binary code and was called the Mu or SQ Wave system. The two distinct ranging systems exhibit unique advantages. The sequential system, because all of its energy is concentrated in one component at any given time, has a signal-to-noise ratio advantage (18 dB) which results in shorter clock acquisition times. The composite system, because its code is pseudo-random, spreads its energy over a wide spectrum and creates less interference for other signals. The Block IV RDA is independent of coding schemes and will operate equally well with either.

The Block IV RDA is designed in accordance with the requirements set forth in the DSIF Data System Development Plan (DSDP), 803-3. It will operate from either the Block III or Block IV DSIF receiver and will therefore perform ranging demodulation for either S- or X-band frequencies. The construction, packaging, and design philosophy followed in the Block IV RDA results in a very compact receiver (12¼ in. of standard rack) as may be seen from Fig. 1.

Future performance requirements, explicit as well as implicit, indicate that operator expense should be minimized and that ultimate computer control should be planned. As may be seen from Fig. 1, the Block IV RDA manual controls are convenient and easy to comprehend. The phase calibration operation, which is adjustment of the reference signal, is achieved by depressing a single button. Confirmation indicators for each module as well as one representing the quality of the reference signal are provided. The simplified operation of the Block IV RDA will result in lower operator costs and also fewer operator errors.

In the future it will be necessary to operate ground stations, to the extent possible, by remote control. System configuration, failure analysis, and fault location will be controlled by computers. The Block IV RDA is fully compatible with computer control, providing computer accessible configuration and monitor points. The gating to select between computer or manual control is designed into the Block IV RDA and a manual/computer select switch is provided on the control panel.

III. Functional Specifications

The functional specifications of the Block IV RDA are shown in Table 1. The range modulation delay variation for the entire DSS (12 h) is specified at 1 m or less. Range delay variation has been allocated to the various DSS components such that when root-sum-squared the total is less than 1 m. The range delay allocated to the combined RDA/Planetary Ranging Assembly (PRA) is 30 cm. The RDA/PRA division of delay is equal, meaning that the RDA is allocated 15 cm, or less. This allocation is in units of apparent spacecraft position; therefore, because the ranging system operates over a two-way link, the range delay variation in units of electrical path length for the RDA is 30 cm or less.

Digital dumping (Ref. 7) is a technique which provides a practical alternative to integrate and dump, without the attendant hardware constraints. The digital dump time constant (single RC) of the final dc amplifier is 0.36 ±0.2 s.

The interface between the RDA and PRA is through an analog-to-digital converter located in the RDA. Output correlation voltages are converted, upon command from the PRA, to an 8-bit digital word having an offset binary code. There are two A-D converters, one for each channel, and they are employed by the phase-calibrate circuitry during calibration.

IV. Operation

The input to the RDA is a 10-MHz carrier, phase modulated with a binary code. The code may be either pseudorandom (composite) or sequential binary. Figure 2 is a functional-level block diagram of the RDA. The phase-modulated signal from the receiver (selected by the Control Unit from two receiver outputs) is applied to a digital attenuator. Attenuation is set according to the ratio of ranging sideband power to carrier power and serves to maintain the full output of the RDA (at the A-D converter input) at 5 Vdc. After attenuation, the phase-modulated signal is divided into two channels in order to facilitate dual channel tracking. The phase-modulated signal is then demodulated with the local model of the transmitted code. The result is a 10-MHz signal, orthogonal to the carrier, whose amplitude is proportional to the correlation of the received code by the local model. Further amplification and bandlimiting is achieved before the signal is applied to a coherent amplitude detector (CAD). The CAD is a mixer having a reference of 10 MHz that is orthogonal to the carrier. This arrangement will amplitude detect the correlation signal which is then passed through a dc amplifier before presentation to the A-D converter.

The Block IV RDA Control Unit serves two main functions. First, it provides for input selection from one of two DSIF receivers or one of two test signals. Secondly, upon command, it adjusts (phase calibrates) the phase shifters in the CADs. Phase calibration is achieved through a digital feedback loop encompassing the A-D converters (Ref. 8).

References

1. Tausworthe, R. C., "Digital Communication and Tracking: Ranging Measurement," in *The Deep Space Network*, Space Programs Summary 37-42, Vol. III, p. 52. Jet Propulsion Laboratory, Pasadena, Calif., Nov. 30, 1966.
2. Foster, C. F., "Receiver Subsystem Development," in *The Deep Space Network*, Space Programs Summary 37-45, Vol. III, p. 70. Jet Propulsion Laboratory, Pasadena, Calif., May 31, 1967.
3. Brown, D. W., "Planetary Ranging Demodulator," in *The Deep Space Network*, Space Programs Summary 37-64, Vol. II, pp. 71–72. Jet Propulsion Laboratory, Pasadena, Calif., Aug. 31, 1970.
4. Goldstein, R. M., "Ranging With Sequential Components," in *The Deep Space Network*, Space Programs Summary 37-52, Vol. II, p. 46. Jet Propulsion Laboratory, Pasadena, Calif., July 31, 1969.
5. Martin, W. L., "Information Systems: A Binary Coded Sequential Acquisition Ranging System," in *The Deep Space Network*, Space Programs Summary 37-57, Vol. II, p. 72. Jet Propulsion Laboratory, Pasadena, Calif., May 31, 1969.
6. Martin, W. L., "Information Systems: Performance of the Binary-Coded Sequential Acquisition System," in *The Deep Space Network*, Space Programs Summary 37-62, Vol. II, p. 55. Jet Propulsion Laboratory, Pasadena, Calif., March 31, 1970.
7. Winkelstein, R. A., "Digital Equipment," in *The Deep Space Network,"* Space Programs Summary 37-48, Vol. II, p. 111. Jet Propulsion Laboratory, Pasadena, Calif., Nov. 30, 1967.
8. Coffin, R. C., "Firmware Control of Block IV Ranging Demodulator Assembly," in *The Deep Space Network Progress Report*, Technical Report 32-1526, Vol. IX, pp. 188–195. Jet Propulsion Laboratory, Pasadena, Calif., June 15, 1972.

Table 1. RDA performance parameters

Functional characteristic	Required capability
Input center frequency	10 MHz ±10 Hz
Power in (AGC'd carrier)	−55 dBm
Noise power density (max)	−55 dBM/Hz
Bandwidth (pre-correlation)	8 MHz at −1 dB
Gain	124 ±1 dB
Modulation index control range	51 dB in 0.2-dB steps
Number of correlation channels	2
Channel gain balance ($G_{chan\ 1} - G_{chan\ 0}$)	$\leq \pm 1$ dB
Modulation phase stability (in 12 h)	$\leq$30 cm (electrical path)
Control/monitoring	Computer/manual
Output voltage	±5V (into 50 Ω)
Output offset voltage	0 ±50 mV
Output integration time constant (final)	0.36 ±0.02 s
Output interface	8-bit A-D converter
Computer control interface	NASA/JPL Standard

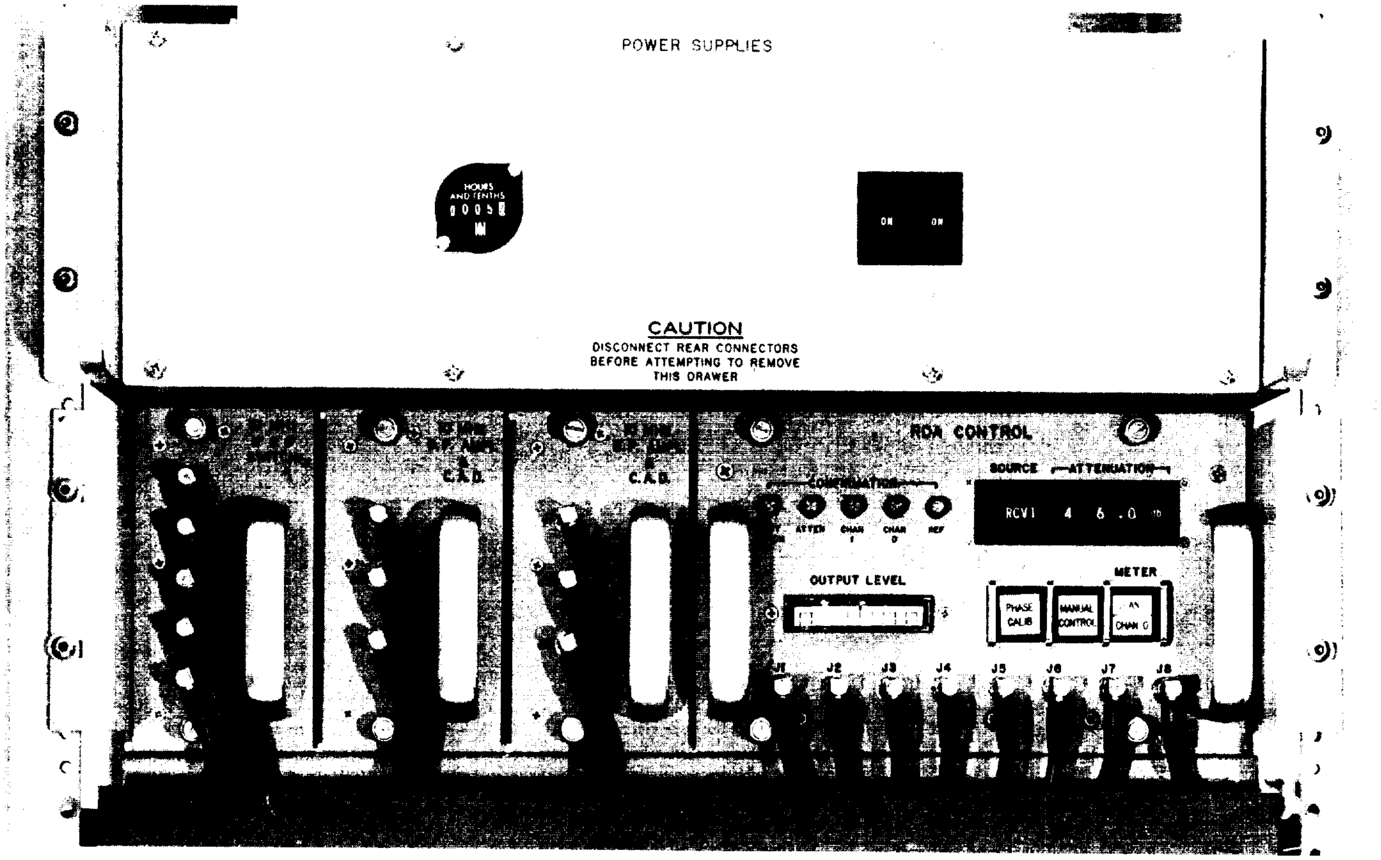

Fig. 1. Ranging demodulator assembly

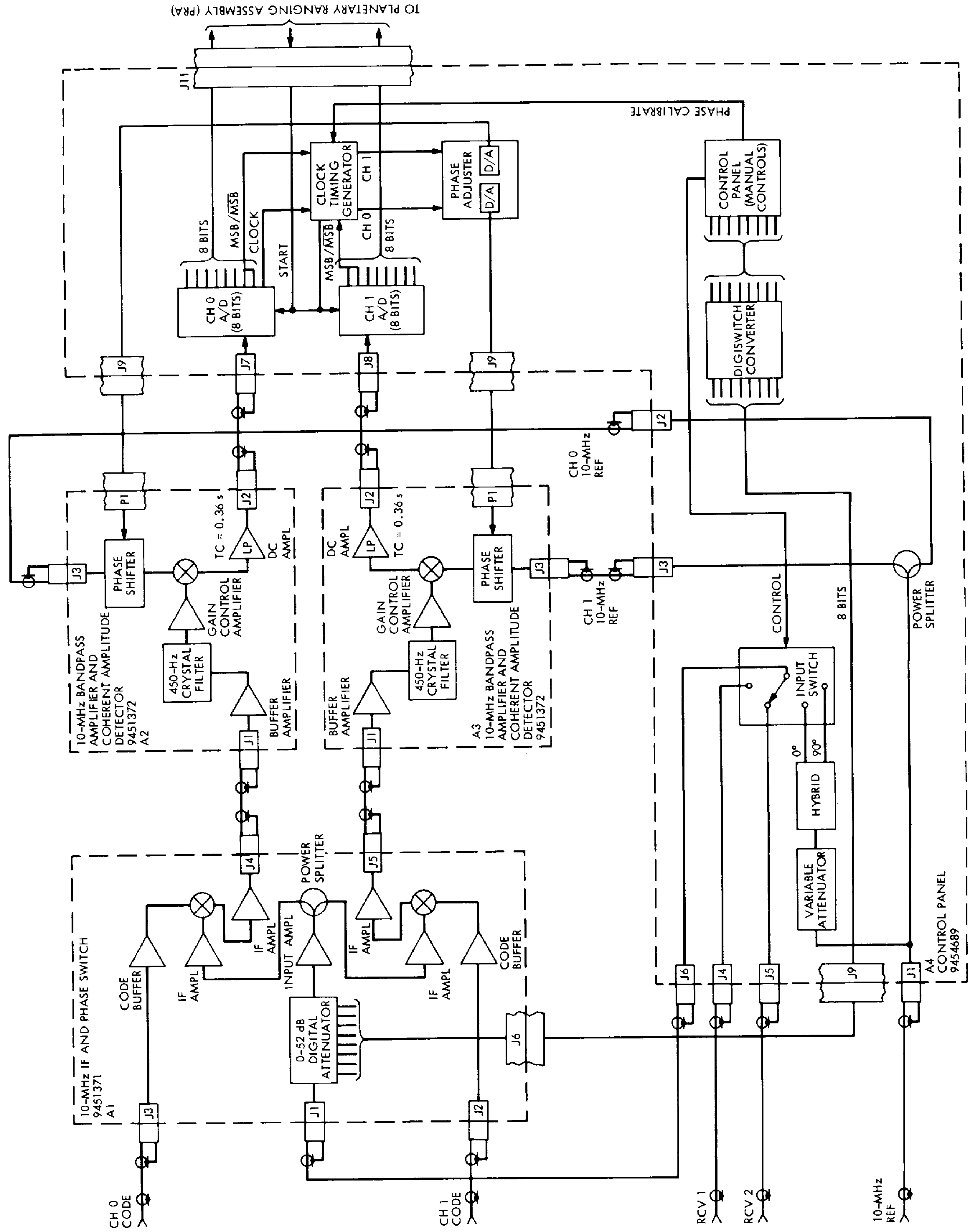

Fig. 2. Functional block diagram—ranging demodulator assembly

Motor Run-Up and Control Unit

J. J. Daeges
R.F. Systems Development Section

A motor generator set is used to convert 60-Hz line voltage to 400-Hz voltage for use in the high-power transmitter. The motors used in the motor generator sets are either 1750- or 3500-hp synchronous motors. They must be brought up to speed before line voltage can be applied to avoid severe power-line transients. The present unit being used to bring the motor up to speed is an open-loop analog device and cannot compensate for drift, temperature changes, or line frequency changes. The design of the new unit will compensate for all variations and is simple to set up and maintain.

I. Introduction

A motor generator (MG) set is used to convert 60-Hz line voltage to 400 Hz for high-voltage use on the high-power transmitters. The motors used in the MG sets are either 1750- or 3500-hp synchronous motors. They must be brought up to speed before line voltage can be applied (Fig. 1) to avoid severe power-line transients. The present unit being used to bring the motor up to speed is an open-loop analog device. It does not compensate for such things as drift, temperature changes in the motors or magnetic clutch, or changes in the line frequency. The new unit has been designed using digital circuits to compare the motor speed to the line and compensate for speed variations without any adjustment. The motor run-up and control unit serves three functions: speed control, voltage control, and power factor control.

II. Speed Control

The synchronous motor is brought up to speed by varying the magnetic coupling of an eddy-current clutch, which connects it to an induction starter motor. To prevent the magnetic coupling from becoming excessive and overloading the starter motor, the current of the starter motor is monitored. This signal is used as a feedback to limit the coupling when the current approaches the maximum rating.

The speed of the synchronous motor is monitored by use of a tachometer that produces a frequency and voltage proportional to its speed. As this frequency approaches 55 Hz, the motor field voltage is applied. The motor acts as a generator producing a voltage having a frequency proportional to its speed. This frequency is then used for speed control to synchronize the motor frequency with the line frequency.

III. Voltage Control

While the motor is acting as a generator, the voltage it produces must be matched to the line voltage. This is done by comparing voltages and producing an error voltage that will vary the field current to match the motor voltage to the line voltage.

IV. Power Factor Control

After the motor has been matched to the line in frequency, phase, and voltage, the motor contactor is closed and the motor is "on line." The power factor of the motor must then be maintained near unity. This is done by comparing the input voltage phase to the current phase and varying the motor field voltage to keep the voltage and current in phase.

V. Design

In order to compare the frequency of the 60-Hz line to that of the motor, an up/down counter (C1) was utilized (Fig. 2). This counter is counted up or down depending on the speed of the motor. After one complete cycle of both the line and motor, the value of the up/down counter is transferred to a latch (L1) and the up/down counter is again preset. This allows a comparison to be made up to 30 times a second. The output of L1 goes to a digital-to-analog (D-A) converter (D-A1), whose output is held high until a frequency of 55 Hz is obtained. As the motor speed increases beyond 55 Hz, the output of D-A1 will decrease, causing the acceleration rate to slow until approximately 58 Hz is obtained. At this time the output of D-A1 has decreased to the point where acceleration stops. The output of L1 also goes to another latch (L2) and two comparators (CM1 and CM2). L1 and CM1 are used to determine if motor speed is increasing or decreasing. This is done by comparing the latest value of C1 with a value taken one second earlier.

CM2 compares the latest value of the up/down counter to its preset value. This comparison will show the frequency of the motor to be low, high, or equal to the line. If the frequency of the motor is low and the speed of the motor is not increasing, another up/down counter (C2), which has been held preset until 55 Hz, will be counted up. The output of this counter goes to a second D-A converter (D-A2) whose output is in parallel with D-A1. Since the outputs of the D-A converters are paralleled, the output to the clutch will be increased, increasing the speed of the motor.

If the speed of the motor is found to be fast and not decreasing, C2 will be counted down. A safety overspeed sensor (not illustrated) will remove all drive to the clutch if the motor frequency exceeds the line frequency by more than 0.8 Hz. Drive is restored when the motor frequency drops below 0.8 Hz above the line.

Voltage control of the motor takes place after the motor reaches a speed of 55 Hz. The motor field contactor is closed and the motor acts as a generator. The voltage it produces is compared to the line voltage with a resistor divider network (Fig. 3). The error voltage from this comparison is amplified and sent to the field power supply. If the motor voltage goes low, the error voltage will go high, causing the field power supply to increase the field current. As the field current increases, the motor voltage increases. If the motor voltage goes high, the error voltage will go low, causing the field current to decrease, lowering the motor voltage. In this manner the motor voltage and line voltage will be matched when the motor is placed "on line."

When the motor is placed "on line," a relay is activated which switches the motor field power supply input from the voltage comparator to a phase comparator. This comparator compares the phase of the voltage to the motor with the phase of the current of the motor. An error voltage goes to the field power supply and will vary the field current to keep the motor current in phase with the voltage. In this way a power factor of near unity is maintained under varying loads.

VI. Conclusion

Tests made using this new control unit show a marked improvement in speed control. A complete unit is now being built which will be installed at DSS 14.

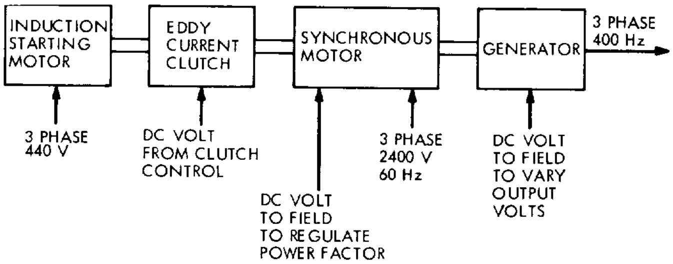

Fig. 1. Motor generator set

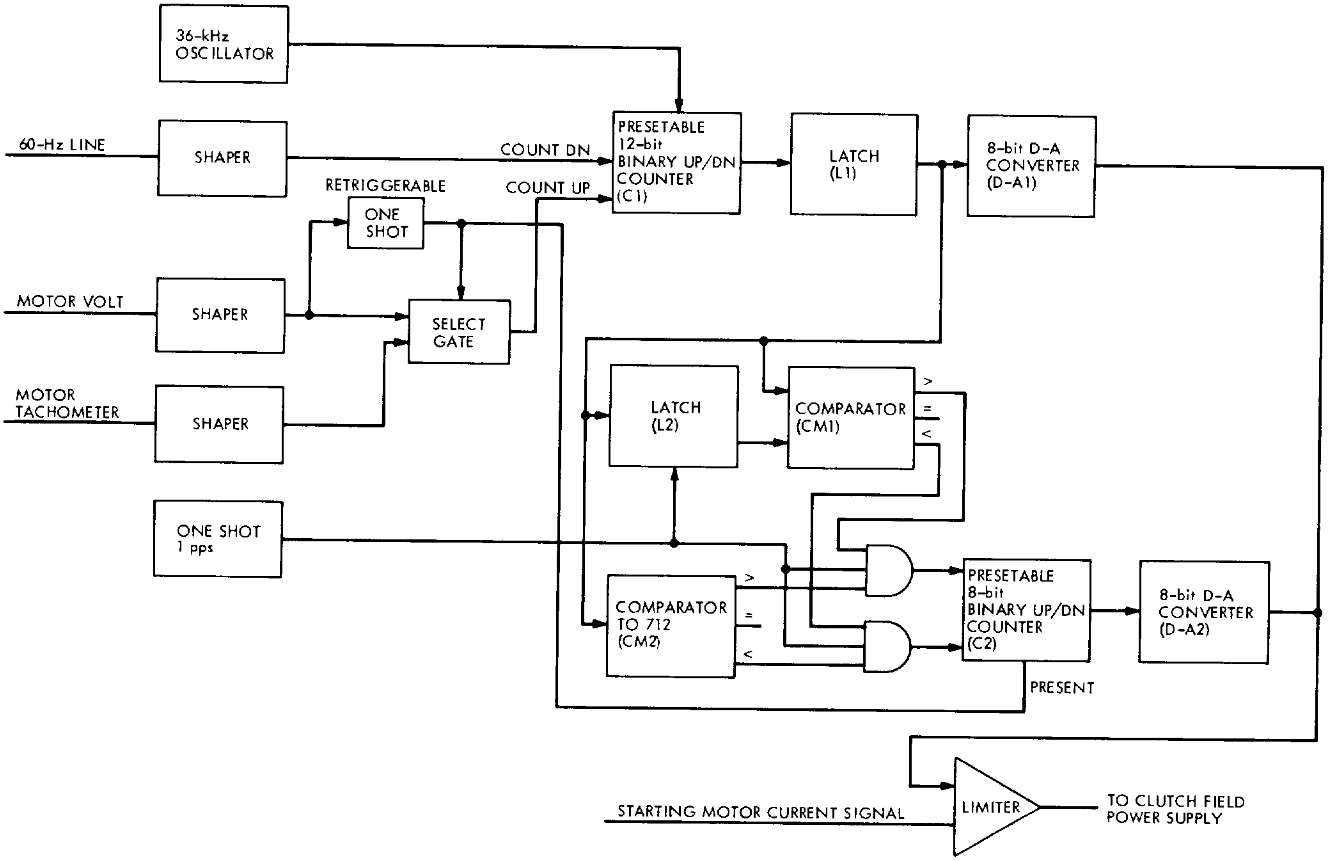

Fig. 2. Speed control

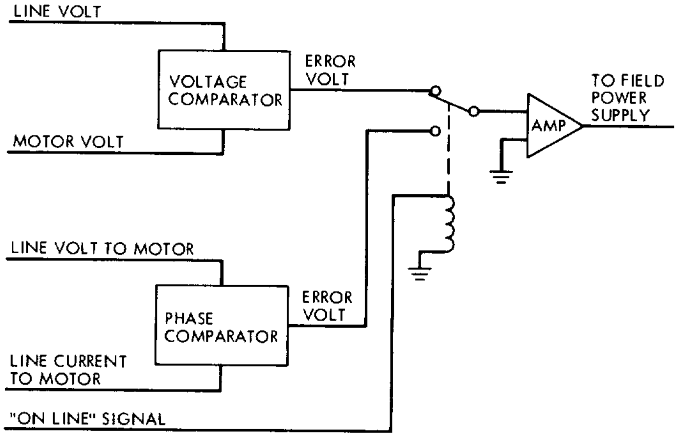

Fig. 3. Voltage and power factor comparators

New Arc Detector

E. J. Finnegan and R. A. Leech
R. F. Systems Development Section

During this reporting period a new arc detector was constructed and tested both on the bench and at the Venus Deep Space Station. Test data show that the new arc detector meets or exceeds the performance of the existing arc detector and has the advantages of being simpler in construction and half the physical size.

I. Introduction

The arc detector is used to protect the 100/400 kW klystrons presently used in the DSIF. It optically senses arcs that can occur in either the klystron window or further down the waveguide. The arc detector also monitors voltage standing wave ratio (VSWR), and if the reflected power increases above a set level, the circuitry will automatically remove RF drive power in less than 10 μs and beam voltage in less than 1 ms, which is more than sufficient to prevent klystron damage. Figure 1 is a block diagram of the arc detector.

The present arc detectors now in use at DSS 14 have several problems. The arc detecting circuitry (light detector)is mounted in the waveguide where it is subjected to strong RF fields and high temperature variations. The RF fields have caused false trips in the existing light detector. The old arc detector assembly utilizes a large number of components and eight relays which would sometimes fail. It is housed in two large chassis.

II. Description

The new arc detector just developed will overcome the above problems by using fiber optics (light pipes). The use of light pipes allows the light detector to be mounted in the instrument cabinet away from the klystron and in a more constant temperature environment. The light pipe consists of quartz fibers arranged into a bundle that is split into two bundles at each end. One end is split so the pipe can view both directions in the waveguide. The opposite pipe end is split so that two identical light sensing amplifiers can be illuminated. The new arc detector occupies half the physical size of the old one.

The waveguide is viewed optically for arcs using fiber optics (light pipes). One light pipe is aimed at the klystron RF output waveguide window, and the other light pipe is directed down the waveguide away from the window. The opposite ends of the light pipes are coupled to a sensitive fast-operating solid-state light detector. The light (arc) detector that is used in this unit is a silicon photodiode/operational amplifier. This device has several advantages over the photo pin diode or the photomultiplier tube (PMT). It is almost as sensitive as the PMT and much more sensitive than the pin diode used in the old arc detector. It requires a ±15 V power supply rather than 1500 V for the PMT. Finally, it is small and easy to package and its reliability and life expectancy greatly exceed other devices. The light detector uses a pin-type silicon photodiode and a selected low-noise high-speed operational amplifier in a single hybrid package. Sensitivity is controlled by selecting the proper feedback resistor. The output voltage of this unit is linearly related to the input light power. To test this part of the arc detector a small calibrated light is activated in the waveguide near the fiber optics. For reliability there are two identical light detector channels.

Reflected power is monitored from a waveguide directional coupler. This RF power (less than 10 mW) is divided and drives two crystal detectors. The dc output from each crystal is applied to the input of a voltage comparator. This dc voltage represents the VSWR (reflected power). When the VSWR is 1.2, the reflected power is approximately 4 kW in the waveguide. The reference voltage to the comparator is set to the value corresponding to 4 kW of reflected power. When the reference and monitor voltages are equal, the protective logic circuit is activated. There are two identical reflected power channels for reliability.

The arc detector logic which the above amplifiers drive, with the exception of three transistors, utilizes all digital integrated circuits. The output from both light detectors and both reflected power amplifiers is fed to two edge-triggered flip-flops (Fig. 1). The output from the flip-flops is fed through buffer amplifiers to two pin diode drivers. They are used to control the crystal switches that turn on and off the drive to the klystrons. The crystal switches are mounted in a stripline circuit and "turn-on" is when they are conducting (forward biased). For maximum switching speed they are reverse biased (negative voltage) for turn off instead of just being allowed to decay. When both crystal switches are turned off they will provide 40 dB of attenuation. If only one is turned off, it provides 25 dB of attenuation which is more than enough to reduce the RF output from the klystron; therefore extinguishing the arc or reducing the reflected power in the waveguide. If a fault occurs in one or all channels, one or both crystal switches will be turned off, removing the drive power and, at the same time, indicating both locally and remotely which channel fired. The crystal switches are reactivated by a system interlock reset command, and can be reactivated only if the faults have been corrected. When the unit is reset, it will automatically test itself. The light detectors are test fired by turning on a small light aimed into the waveguide, and reflected power amplifiers are tested by a ramp voltage from the logic circuit. If all the channels do not test fire, the arc detector cannot be reset.

III. Conclusion

The present arc detector which this is going to replace is packaged in two chassis each 7 in. high. One chassis contains the power supply; one chassis contains the logic; and a third waveguide mounted module contains the light detector. It has several critical adjustments, several of which are on the front panel where they can be accidentally disturbed. It uses all discrete components and eight relays.

The new arc detector will be housed in one chassis approximately 7 in. high, completely self-contained, including power supplies and light detector. It uses no relays and has only three adjustments which are not panel mounted. It will be cheaper to produce and more reliable.

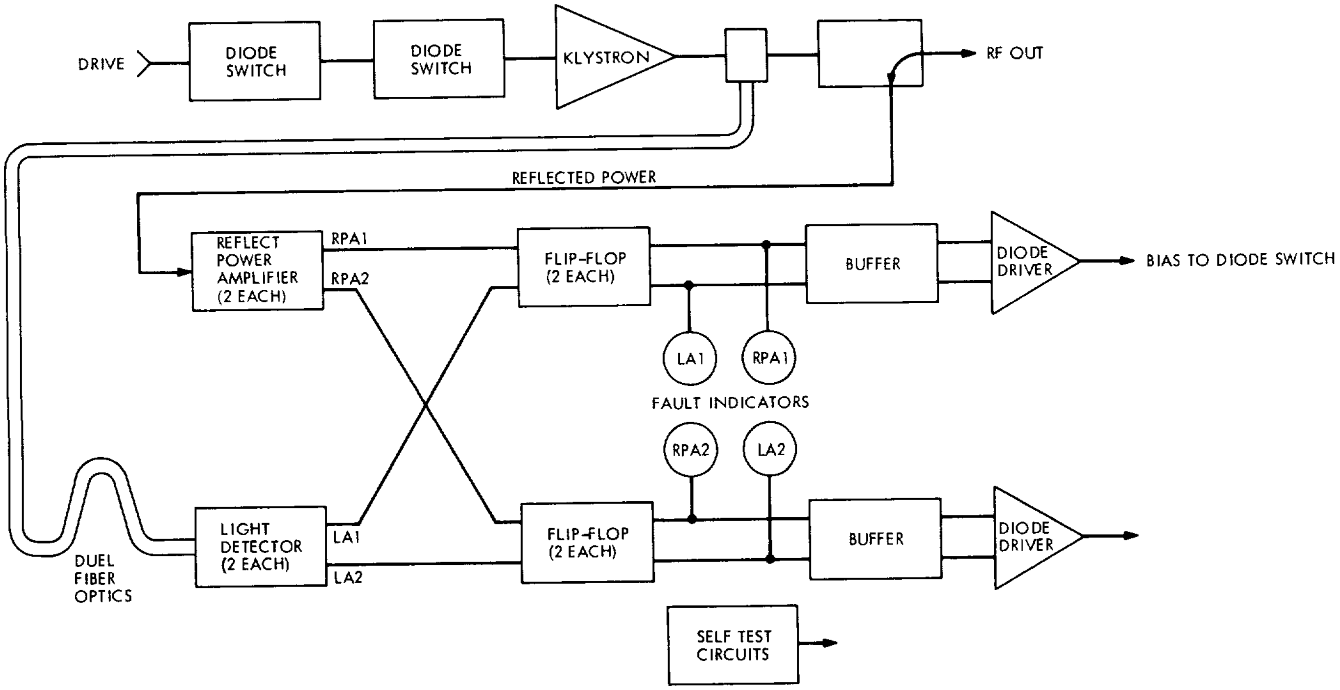

Fig. 1. Arc detector

DC Current Sensor

R. Perez
R.F. Systems Development Section

A current sensor has been developed having capabilities for measuring a differential dc current and also, within a few microseconds, detecting the burst of current caused by a high-voltage arc. This sensor was designed to measure the klystron body current and, in conjunction with a crowbar, protect the tube against internal high-voltage arcs. This article describes the operational characteristics of the current sensor and the results of the characteristics that were investigated.

I. Introduction

When the 100/400-kW transmitters were being developed, it became obvious that a protective device was necessary to guard the RF (body) section of the klystron against serious damage from high-voltage energy; therefore, a crowbar, a device that removes the high voltage in a few microseconds, was designed to protect the klystron. The crowbar needed a signal to gate it *on* whenever an arc (high body current) occurred in the klystron; thus the dc current sensors were developed for this purpose.

The body of the klystron is grounded through its mechanical structure. Because of this, body current is measured by comparing the difference between the cathode current and the collector current (the current leaving the cathode that does not arrive at the collector has been intercepted by the body).

The classical approach to measuring body current is to float the dc power supply using a meter shunt. The output of the shunt then drives an analog body current monitor. The separation of the components on a 64-m-diam antenna makes this approach impractical due to the fast (microsecond) protection requirement of the klystron body. The dc current sensor is now located near the klystron for fast response and the dc power supply is grounded.

One- and two-ampere dc current sensors, models PM1594-1 and PM1594-A2, respectively, have been developed for JPL and have been used in the Deep Space Network for a few years. However, certain abstract characteristics of the current sensors needed additional investigation.

A new procurement was initiated to provide current sensor probes for the DSS 43 and DSS 63 overseas transmitters. Since the newly purchased current sensors had to be tested, the opportunity was seized to make further studies of the current sensor's characteristics. The current sensors have analog and digital outputs that are referred to as the slow and fast outputs, respectively. The fast output has a level control that sets the current level at which the unit will produce a pulse train.

The parameters measured include the slow output linearity and the fast output pulse parameters—rise time, pulse width, pulse amplitude, and, most important, the time delay for the current sensors to produce a pulse after being excited (triggered).

The characteristics investigated include the relationship between the test pulse amplitude and the time delay for various current level settings. Also investigated was the effect on delay time by a test pulse with and without a quiescent current. The test pulse was a 10-microsecond pulse of variable amplitude. It was run through the current sensor with the purpose of triggering the fast output.

II. Current Sensor Operation

The current sensors consist of two units each: a magnetic unit and an electronic unit. The magnetic unit consists of a magnetic core with several coils of wire wound around it—in other words, a magnetic amplifier (MAGAMP). A coaxial high-voltage cable carrying the differential dc current to be measured is passed through the magnetic core and thus is the MAGAMP gate winding. The center conductor carries the cathode current at −70 kVdc, and the shield carries the collector current. The output from this unit is ac, which is rectified and amplified by the electronic unit. This is the analog output of the electronic unit. To achieve fast response, the MAGAMP is excited by a high frequency generated by the electronic unit. The electronic unit will produce a pulse train (Fig. 1) when the current being measured reaches a preset current level set by the fast control. Input and output specifications are listed in Table 1.

III. Slow Output Measurements

The slow output is used to directly drive panel meters to monitor the klystron body current. In order to achieve accuracy, the output must be linear within 5% of full scale. Figure 2 illustrates a typical test result.

IV. Fast Output Measurements

Klystrons operate at very high voltages (−70 kVdc); therefore, they are subject to internal high-voltage arcs that may destroy the tube. The test pulse used in this test simulates the current attributed to an arc. Once triggered the current sensor generates a fast output pulse that goes to the crowbar logic. The crowbar logic is part of a system to protect the klystron (Ref. 1); therefore, the time delay must be minimized.

Figure 3 illustrates the type of test performed. The lower pulse is a test pulse through the current sensor as viewed across a one-ohm resistor. The pulse above it is the fast output pulse which the current sensor produces within 10 microseconds after being triggered. An actual arc will be sensed by the current sensor as a large current pulse. The relatively low current used in this test (15 amperes maximum) was for the purpose of measuring the fast output parameters and also for researching the current sensor's response characteristics.

In the system it is possible for the high-voltage supply to be ON and the body current to vary from a minute amount to as high as 1.25 amperes; therefore, it is possible to have an arc under either of these circumstances. A test was conducted to study the effect on time delay at each of these conditions. The current sensor was fired by a test pulse with and without a quiescent current. The results are discussed in the conclusion.

V. Conclusions

All six of the units tested displayed a linearity within the specifications. The maximum deviation for each unit of full scale from a linear output ranged from 4.62 to 0.42%. The average for this range is 1.78%, which is lower than the design goal of 2%. The average percentage deviation for each unit ranged from 2.71 to 0.28%, and the average for this range is 1.08%.

The output pulse parameters of all the units tested are within the specifications. Typical values are amplitude 18 volts, pulse width 125 microseconds, and rise time 0.4 microseconds.

The time delay varied with the current level setting and test pulse amplitude. Figure 4 illustrates the relationship between the test pulse amplitude and the time delay for various current level settings. From the graph, it can be seen that the time delay is shortest when the fast control is at its lowest possible setting.

There is a limit as to how low the units can be set. The current sensors will produce a pulse train when the dc current being monitored reaches the preset current level;

however, when a current sensor is set below its stable point, the unit may produce a pulse train even though the current being sensed is below the preset level. Most of the units tested become unstable below 0.3 amperes. The actual point of stability varied from 0.5 amperes down to one unit that was completely stable.

The amplitude of the test pulse has an effect on time delay in the following manner: the larger the test pulse, the shorter the time delay. It can be seen in Fig. 4 that for any current level setting as the test pulse increases, the time delay decreases.

The effect on time delay by a test pulse with and without a quiescent current is very small. The difference measures in tenths of microseconds. The shorter time delay occurs when there is a quiescent current present. The presence or absence of a quiescent current has the greatest effect on time delay when the fast control is set low. The effect is then steadily reduced as the current level setting is raised.

The most notable relationship between the test pulse and the current level setting is that even though the fast output will produce a pulse train when the steady-state dc current being monitored reaches the preset current level, it may not do so when a pulse reaches that same preset level. A test pulse of from 1 to 4 amperes greater than the current level setting is required before the current sensor responds. The amount greater than the setting that is required depends on the setting itself and the width of the test pulse. The higher the setting the more current above the setting is needed. The test pulse width used in this test was 10 microseconds wide. A wider pulse reduces the amount of over current required by the current sensor.

This phenomenon is not detrimental to the protection of the klystron because an arc in the tube will produce a body current of much greater amplitude and width than these test pulses.

Reference

1. Finnegan, E. J., "A New Crowbar Logic Unit," in *The Deep Space Network Progress Report*, Technical Report 32-1526, Vol. VII, pp. 136–138. Jet Propulsion Laboratory, Pasadena, Calif., Feb. 15, 1972.

Table 1. Electrical specifications

Input current range:	
Model 1594-1	0 to 1 Adc
Model 1594-A2	0 to 2 Adc
Fast level set:	Capable of producing a pulse at input current level adjustable from:
Model 1594-1	0.5 to 1 A
Model 1594-A2	0.5 to 2 A
Analog output:	
Range	0 to 5 Vdc
Linearity	±5% of full scale over entire range with design goal of ±2%
Ripple	10 mV rms maximum
Load	5 kΩ
Pulse output:	
Amplitude	Design goal of 20 V
Rise time	<1 μs
Time delay	<10 μs with design goal of 1 μs
Load	50 Ω
Power required:	28 Vdc ±5%

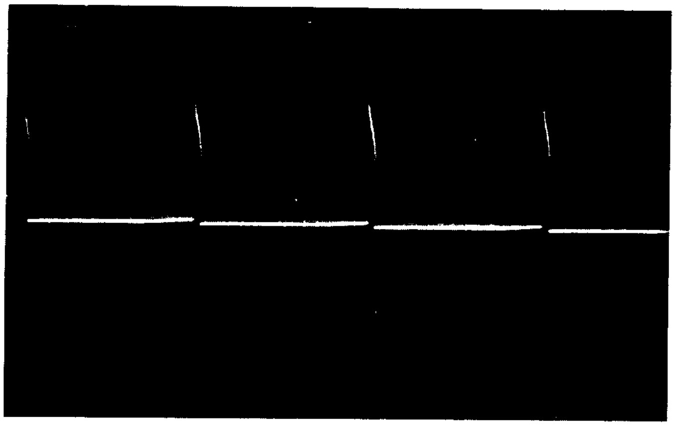

PULSE: 10 V/division
TIME: 1 ms/division

Fig. 1. Fast output pulse train

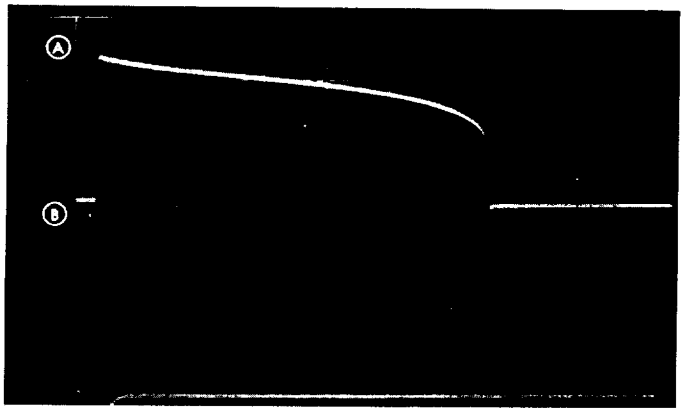

Ⓐ FAST OUTPUT PULSE: 10 V/division
Ⓑ TEST PULSE: 5 V/division
TIME: 20 μs/division

Fig. 3. Test pulse and corresponding fast output pulse

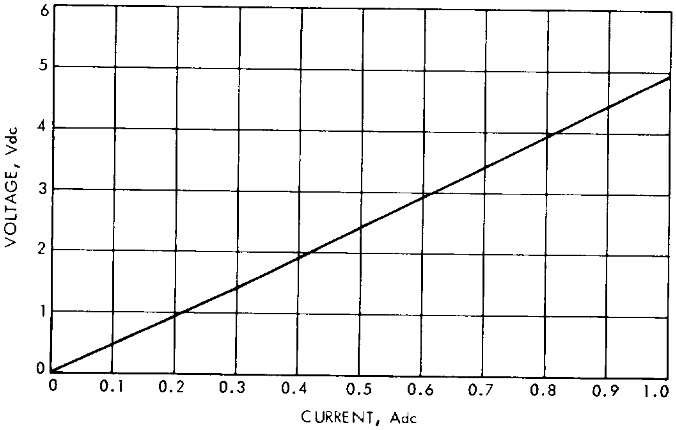

Fig. 2. Graph of slow output linearity

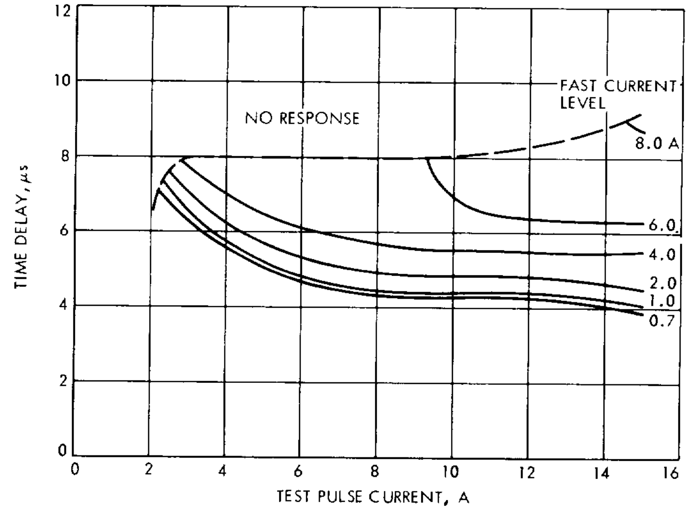

Fig. 4. Graph of time delay vs test pulse amplitude

Dual Carrier Preparations for Viking

D. A. Bathker
Communications Elements Research Section

D. W. Brown
R. F. Systems Development Section

The problem of receive band interference resulting from both single and dual carrier transmission from a deep space station has been synthesized and, to a large extent, resolved at the Venus Deep Space Station. Although there are remaining problems, the application of this experience to 64-m-diam antenna stations, the Mars Deep Space Station in particular, is discussed.

I. Introduction

Receive band interference resulting from high power diplexing with dual carrier uplink has been the subject of intensive investigation in recent months. A description of the problem was given in a recent report (Ref. 1) along with a brief summary and references to background experience and related work. This report will be more specific; a review of DSS 14 performance will be given as well as related progress achieved at DSS 13 (Refs. 2, 3) through the end of calendar 1972.

II. Description

The interference consists of two types: (1) broadband noise bursts (NB) which occur with single *or* dual carrier transmission and are observed as impulsive increases in receiving system temperature and, (2) intermodulation products (IMPs) whose frequencies may be predicted by the expression:

$$F_{IMP} = (N + 1)\,F_2 - NF_1$$

where F_2 and F_1 represent the upper and lower uplink carrier frequencies and N takes positive integral values. The intermodulation order (IO) is defined as the sum of the absolute values of the coefficients above, that is:

$$IO = 2N + 1$$

However, for convenience, the first expression may be written as:

$$F_{IMP} = F_2 + N(F_2 - F_1)$$

where N is clearly the index of the Nth spectral line at interval $(F_2 - F_1)$ appearing above the upper carrier frequency F_2.

Because the DSN receive band (2290 to 2300 MHz) lies at a more or less fixed interval (180 MHz) above the transmit band (2110 to 2120 MHz) in the spacecraft transponder ratio of 240/221, it is apparent that the value or values of N appearing in the receive band may be approximated as follows:

$$N_{rcv} = \frac{180 \pm 5\,\text{MHz}}{(F_2 - F_1)}$$

For instance, if the uplink channel separation were 6 MHz, one would expect N = 30 (as well as 29 and possibly 31) to appear within the receive band. Indeed, this is the case, and for each pair of the four Viking channel assignments (9, 13, 16, 20), the representative indices are N = 48 (channels 9, and 20), 75 (channels 9 and 16 or 13 and 20), 133 (channels 9 and 13 or 16 and 20) and 175 (channels 13 and 16). Although none of the several IMPs falling in the receive band may lie within an active receive channel for a particular pair of uplink frequencies, these IMPs will walk through the receive band as N times the differential uplink tuning, and thereby impact any and all receive channels as the uplinks are operationally tuned as a function of uplink doppler.

Experience has shown that, while these IMPs are entirely predictable regarding center frequency, they appear to have a spectral width of 10 Hz or so, as if modulated by the random noise burst effect. The overall interference then appears throughout the receive band with clusters of noise energy at the IMP frequencies. In fact, recordings of the usual instrumentation—receiving system temperature (T_{op}) and receiver AGC voltage—show a strong correlation in time between the magnitude and time density of noise bursts and the AGC estimate of IMP power. This is especially true in the short term (seconds), but also generally true in medium (minutes) or long (hours, days) term. Similarly, the noise burst activity and IMP effect appear to be somewhat correlated in magnitude as a function of system condition as if they both arise from the same basic mechanisms (microarcs or other nonlinearities). And yet, there are some clues that internal waveguide mechanisms may generate noise bursts in somewhat weaker proportion to the IMP mean than do external antenna sources. One clue to support this view is the observation that, while operating in an internal mode (without the antenna), the IMP is characterized as having less AGC voltage variance, for a given mean, than a complete antenna system.

III. Review of DSS 14 Performance

Considering for a moment the uplink low-order (N = 1, 2) intermodulation products generated primarily in the klystron, the aforementioned Viking channels were selected such that these IMPs would not fall within an assigned uplink channel. In addition, the power per carrier has been nominally established at 10% of single carrier klystron rating (Ref. 4), in order to limit the uplink IMPs to at least 20 dB below each carrier as based upon tests early in 1972 (Ref. 5). This results in dual 40-kW nominal capability at DSS 14 and dual 10-kW rating at DSS 13 and overseas 64-m-diam antenna stations.

Early concerns regarding suspected receive band interference in the Viking mode led to preliminary testing at DSS 14 with carrier separations yielding values of N as low as 31 and as high as 75. First results showed mean values of receiver AGC (when locked to the IMP) to be typically −140 dBmW for N = 31, somewhat weaker values for N as high as 45, and no lock for the higher values of N. These data suggested a model of monotonically weaker IMPs for increasing N, with the projection of near threshold (and therefore potentially degrading) interference at least for N = 48 and possibly for N = 75 in the Viking mode. Repeated testing confirmed this by demonstrating N = 48 receiver locks with IMP means in the vicinity of −168 dBmW. The full significance of these values has not yet been established, but any consideration of these mean levels of IMP must recognize the short-term fluctuations which have been typically ±10 dB for 0.1 Hz AGC bandwidth (narrow) and perhaps as much as ±20 dB for wide AGC bandwidth. Figure 1 presents typical mean values of IMP for several values of N and attempts to depict the medium- and long-term variations as well. During these tests, noise burst activity was typically of the order of 100 K peaks and, for a given system condition, was consistently more noisy for dual 40 kW than for single carrier powers of 100 to 400 kW. The reason for dual carriers being more effective than a single carrier of equal or greater power level in stimulating noise bursts is not understood. The effectiveness is consistently evident in both amplitude and time density of the noise bursts.

While examining potential tradeoffs and clues to the IMP behavior, several attempts were made to evaluate mean IMP levels as a function of transmitted power per carrier. Incidental equipment problems as well as medium term variations have clouded the result. Figure 2 depicts some of the data which suggest a possible 3-dB IMP per dB of balanced transmitter power relationship. Whether or not this is true and whether or not operational use of this effect could be exploited depends strongly upon certain assumptions and conditions of medium term fluctuation of the IMP at a given power level.

IV. DSS 13 Dual Carrier Implementation and Performance

Although the Viking dual carrier commitment (Ref. 1) specifies 64-m station support, any major effort in terms of extensive experimentation with dual carriers at a 64-m station would be extremely difficult. In the past, significant single carrier noise burst and dual carrier (restricted to uplink intermodulation product) testing had been accomplished at the Goldstone DSCC Microwave Test Facility (MTF) and Venus (DSS 13) 26-m Deep Space Station (Refs. 6, 7). Early in June 1972, a management decision was made which would significantly impact DSS 13. The obvious needs of typical DSN antenna reflecting surfaces, together with a 100- to 400-kW class transmitter and low noise receiver could be most easily achieved by committing DSS 13 to a dual carrier test program. The results and conclusions obtained from that program could then be assessed with regard to impact upon the 64-m network.

Considerable planning was required to outfit DSS 13 with a dual carrier test capability, both in terms of the capability itself, and ancillary test features such as observation ports, air and water terminations and the like. Figure 3 shows the block diagram arrived at after much consultation among various groups involved. A 100-kW klystron was made available. It is interesting to note, for the nominal dual 10-kW carriers, that the power density incident on a 26-m antenna is comparable to dual 40-kW carriers on the DSS 14 64-m-diam antenna. Standard 400-kW DSN filtering was made available from 64-m network spares. Initially a Block II traveling wave maser (TWM) was made available as preamplifier for the DSS 13 receiver. Receivers in use at DSS 13 included the 2295-MHz R&D receiver operated both open loop and 455 kHz closed loop. Open-loop T_{op} instrumentation was available with 1-MHz bandwidth. The XDS 930 computer was used as a digital spectrum analyzer. A low-noise transistorized preamplifier was used with an analog spectrum analyzer (LNSA), for example, to examine receive band IMPs, if any, directly from the klystron or from the test probes. A high-power waveguide directional coupler was available to sample forward and reverse transmitter power over a broad band. Four terminations were initially selected; the complete 26-m antenna with S-band Radar Operational (SRO) feedcone, the 26-m antenna SRO feedcone without antenna, by way of a flat plate reflector over the feedhorn, a water load, and an air load termed side-looking horn (SLH). A view of the DSS 13 side-looking horn installation is seen in Fig. 4. This termination provides the simplest possible radiator, closely coupled in terms of numbers of waveguide flanges to the transmitter/filtering/receiver system, housed within the DSS 13 26-m antenna electronics room seen in the upper portion of Fig. 4.

Additional work accomplished at this time (September 1972) was to remove all questionably bonded hardware from the exterior reflecting surfaces of the DSS 13 26-m antenna. This hardware included conduits, lights, clamps, ladders, and other peripheral equipment. The reflecting surface was completely retaped using newly available corner patches, as seen in Fig. 5. Also shown in Fig. 5 are the two surface probes seen in the block diagram (Fig. 3). One probe is broadband (waveguide bandwidth) while the other is a highpass filter, cutoff at 2200 MHz. With it, the receive band can be observed without simultaneously coupling in the strong transmitted signals near 2115 MHz.

Figure 6 shows the DSS 13 antenna, completed around Oct. 1, 1972, as initially configured for dual carrier work. During the latter stages of reconfiguration, tests of the transmitter output spectrum using the water load were simultaneously possible. Those data proved the 100-kW transmitter with dual carrier excitation was operating properly, and that transmit-band IMPs were as anticipated from previous tests, or better. In addition, the receive band was checked for possible IMPs. Under no conditions could receive band IMPs be detected. The tangential sensitivity of the instrumentation was -35 dBmW referred to the transmitter output port, through use of the high-power waveguide directional coupler. After consideration is given for the 160 dB of microwave filtering, to be used later, an excess of ~ 55 dB sensitivity was available to detect an IMP of -140 dBmW. Considerable attention was given at this time to possible spurious, harmonic, or other mechanisms to explain the previously observed DSS 14 performance. Most, if not all of the possible complex mechanisms proposed were checked, including sensitivity to maser idler frequencies (fundamental and subharmonic), accomplished in the laboratory. None of these possible mechanisms were identified. On the basis of the above transmitter testing, it was further determined that several standard microwave components (klystron, high-power coupler with associated terminations and cables, harmonic filter, and one type of water load) were receive band IMP-free at least down to the levels indicated above.

Proceeding with confidence, from the data base that noise burst and intermodulation products at 2290 to 2300 MHz were not sufficiently generated by the 100-kW klystron (<195 dBmW at the TWM input), all four terminations were first tested on Oct. 15, 1972. Nominal test conditions of dual 10-kW carriers with N = 31 were adopted.

The SLH mode showed (via XDS 930 spectrum analyzer) relatively steady −175 ±5 dBmW IMP with NB less than 1 K at the predicted receive band frequency. The water load (Fig. 3) provided comparable performance with the observation that it tended to be mildly microphonic, i.e., shock sensitive (produced NB and presumably transient IMP under vibration). While not ignoring these low level signals, the stronger −135 ±10 dBmW IMP with NB > 500 K in a 1-MHz bandwidth observed on the total antenna system, for the dual 10-kW N = 31 standard conditions adopted, received priority attention. These intermodulation products were, on the average, only a few decibels worse than present at DSS 14, (Fig. 1) even though it was considered that significant structural cleanup had been accomplished at DSS 13 (Fig. 6). A hint of the problems to be later encountered was observed when the flat-plate reflector was used; no repeatable difference in performance between the flat plate mode and the total antenna system mode was detectable.

There were many questions as to whether the flat plate would be an effective switch (Fig. 7) in providing isolation from the antenna reflecting surfaces. Tertiary mechanisms, such as support arm arcing, spillover, diffraction and others, could indeed support the observed intermodulation, in view of the tremendous dynamic range between uplink (+76 dBmW peak) and downlink (−135 dBmW average), which is greater than 200 dB.

In order to provide a high reliability answer to such questions, a more effective switch was employed. The subreflector and quadripod were removed as a unit (Fig. 8). Performance, with or without the flat plate reflector, remained essentially the same with the possibility that the mean level dropped 3 dB (−138 dBmW). Samples of the T_{op} and AGC instrumentation recordings made during this initial period are available in Fig. 9.

By using a manual waveguide switch rotation (SW3 in Fig. 3), the water load was relocated on the unused SW4 port. Performance remained quite poor (∼−140 dBmW, 500 K). The waveguide run connecting the 26-m antenna electronics room with the SRO feedcone (SW1 to SW3) was next disassembled, cleaned, acid etched, relapped, and flanges lightly greased according to current DSN standards (Ref. 8). With the exception of startup burn in or “rf processing,” and mild microphonics, the waveguide cleanup was considered successful as measured on the relocated water load.

Performance was also significantly improved when radiating out the SRO feed cone, although nowhere near acceptable (−155 dBmW), and quite variable, microphonic, and intermittent. The variability was apparently a function of many things; shock, vibration, solar illumination, rain and polarization, as a minimum accounting.

Because the SRO feedcone polarizer and SW3 were the only waveguide-like components not having undergone cleanup recently, these too were next serviced according to the standard. There was no observable change in performance. Finally, the SRO feedhorn was removed and also serviced.

While the main feedhorn was being serviced it was possible to install a water load on top of the polarizer, in place of the feedhorn. Performance was of the (then acceptable) −175 ±5 dBmW class. By use of a clean 2-m long waveguide, it was further possible to try two other horn radiators on top of the long waveguide, approximately 0.5 m above the feedcone top surface. One horn was low-gain (+6 dBi) while the other was medium-gain (+16 dBi). Both provided intermittent NB and accompanying IMP of the −145 dBmW class until microwave absorber was tried about the feedhorn exterior throat regions. While not eliminating the problem, significant (∼15 dB) reduction was observed.

The serviced main feedhorn was reinstalled without change in the −145 dBmW intermittent class performance. The microwave absorber continued to provide significant improvement. One characteristic of all three horns used was that of dominant or single mode excitation. Dominant mode operation is known to diffract significant energy into the rear hemisphere, as a result of untapered E-plane excitation. Power density surveys in amplitude and polarization about the dominant mode SRO feedhorn, and about the hybrid or effectively dual mode SLH confirmed the expected significant density difference as well as expected field orientations. Two main conclusions were drawn from these tests; (1) dominant mode horn diffraction with normally constructed feedcone exteriors is sufficiently strong to excite poorly bonded metal joints and cause a portion of the microphonic NB/IMP phenomena, but more importantly, (2) a comparison of the power density due to diffraction, and the density to be expected later with hyperboloid illumination shows the hyperboloid illumination to be stronger. Therefore, the feedcone exterior requires sound bonding, independent of horn type, since the hyperboloid illumination dominates.

During all the above testing, the SLH performance remained consistent at the −175 ±5 dBmW level, on a daily reference basis. It was decided impractical to appropriately bond the SRO feedcone exterior within the available time. An approach utilizing an existing partially welded feedcone, which was to be more fully welded, with the SLH reference horn mounted within, was selected. A simple interior was agreed upon, the only components being a fixed quarterwave plate polarizer and a waveguide connection to the floor interface. The joint between the SLH and the feedcone roof surface was prepared much like a waveguide flange, with approximately five bolts per wavelength, flat, well contacting corrosion-free surfaces, protected with grease. The feedcone doors were insulated rather than welded. Thought was given to the feedcone/reflector interface (an aluminum to steel joint), but nothing practical was devised prior to installation (Fig. 10).

Performance using the prepared exterior feedcone was as expected; NB less than 1 K, with IMP −172 ±5 dBmW for an extended test period including shock, vibration, solar illumination, and microphonic tests. A second-generation flat plate, with all joints either welded or insulated was then tested, with identical results. It should be noted, however, that such a flat plate test is necessary, but not sufficient. Diffraction and spillover might be possible problems after the quadripod is installed. In view of the large dynamic range involved, the question arises, what would the isolation of this switch be with the quadripod *in situ*?

Although earlier cleanup work on the main reflector surface and quadripod legs had been done, results to date indicated not enough had been accomplished. It was possible, through a parallel effort, to thoroughly bond the subreflector while the new feed cone was being proofed. The vertex plate, beamshaping flange, and to some extent, hardware behind the rim of the flange, were bonded together by welding. This parallel effort eliminated obtaining a pre-calibration on the "as-received" condition of the subreflector. A review of the anticipated power densities on the subreflector and physical condition, compared with earlier experience with feedcone exterior power densities, physical condition, and poor performance, showed that, by a factor of 30 dB, the subreflector would have failed. Figure 11 shows the bonded subreflector being reinstalled in the quadripod; meanwhile testing of the new feed cone is under way (begun around Dec. 7, 1972).

After a high degree of confidence was obtained on the new feed cone, the quadripod was reinstalled (Fig. 2). Questions requiring answers at this point were:

(1) Is the feedcone base to reflector (aluminum to steel) joint adequate under increased illumination stress from the subreflector?

(2) Are the joints between the steel quadripod legs and the aluminum reflector adequate?

(3) Is there sufficient diffracted illumination behind the subreflector to stress the myriad of joints located there which are extremely difficult to bond/insulate/shield?

(4) Is the aluminum tape treatment of reflecting panel joints, found adequate for a single carrier NB solution, sufficient under dual carrier stress?

(5) Are any or all of the above weather or solar illumination dependent (intermittent)?

Reinstallation of the quadripod included retaping of the joints about the reflecting panels which had been removed for access (Note Figs. 6 and 10). Additionally, attempts were made to shield the aluminum to steel interfaces, at both the bases of the quadripod legs and the feedcone base, using aluminum tape. Because of the physical complexity of these joints, many overlapping and/or wrinkled tape joints became evident on visual inspection leading one observer to comment on the probability of overdoing otherwise good practice.

Indeed, a strong indication that this was correct was immediately obtained upon turn-on of the standard conditions; N = 31 dual 10-kW carriers. NB with accompanying IMP at −135 ±5 dBmW were observed, which had the impact of returning the project to initial poor performance levels. Furthermore, the SLH reference facility was no longer available (used within new feedcone). Wind precluded use of the flat plate at that time. It was decided to remove the complex of tape in the regions surrounding the quadripod leg bases. Performance returned to an encouraging −168 dBmW level. The tape was reinstalled to determine repeatability. The −135 dBmW level repeated. The tape was removed a second time. The

−168 dBmW level repeated. Confidence was gained in two areas; (1) the tape quality indeed was a problem area, and (2) a few (possibly singular) poorly bonded joints can cause essentially the entire problem. In retrospect, team members witnessing all of the above tests are of the judgement that the initial −135 dBmW levels probably represent a saturated effect, i.e., a singular addition to, or subtraction from, a large number of poorly bonded joints goes unnoticed. The strong suggestion here is that a single uncontrolled installation of some peripheral device on the illuminated portion of DSN antenna reflecting surfaces will probably cause an unacceptable noise impulse and intermodulation interference.

Next, tests of dual 5, 10, and 20 kW pairs with N = 31 were conducted. Total operating noise temperature and AGC traces are seen in Fig. 13. A few small intermittents are noticed, increasing with power level. Holding the power level constant at dual 10-kW carriers, other (narrower uplink frequency separation) pairs were tried. N = 48, 75 (Channels 9 + 16 and 13 + 20), 130, 134, and 177 all showed the expected acceptable performance (Fig. 14).

Figure 15, a and b, are less encouraging. Apparently weather, particularly heavy fog or rain, impacts the otherwise good performance severely, and in a complicated way. A suggestion was seen that a totally wetted antenna surface provided a continuous noise-free reflector. An antenna drying out is apparently quite intermittent and noisy. These effects, however, are not yet well understood. Even common environmental effects such as solar radiation remain to be more fully examined.

V. DSS 13 Summary

An approximate 5-month program (3 months at DSS 13) has resulted in much improved understanding of causes and cures for noise impulse and intermodulation phenomena within the DSN. Problems have been observed, identified, and either eliminated or substantially reduced, both within the internal bounded waveguide and external free space wave portions of a typical DSN antenna. Figure 16 summarizes the milestones reached at DSS 13 by the end of this reporting period. While the problems are difficult and dwell on a large number of small details, initially no exotic nor cost prohibitive measures appear necessary. On the other hand, the possibility of a difficult and/or costly follow-on maintenance regimen may be needed, and weather independence may not be possible.

The investigation is not complete. A low-level problem (−175 dBmW) at N = 31, dual 10-kW operation has continually existed. Although this level is acceptable, in the Viking context, given the repeatable decay observed with larger N numbers, the unknown long-term stability of this level is worrisome. Whether this is a waveguide flange or diplexer effect is presently unknown. A high-level problem exists during inclement weather.

VI. Status at Year End

Overall results at DSS 13 by mid-December were such that confidence was building that it would be possible to achieve comparable results on a 64-m antenna, fully appreciating the problems attendant to a much larger structure. Significant unknowns, including the residual intermittence at DSS 13, as well as the scheduled S/X band feed hardware on the 64-m antennas, remained unresolved.

Notwithstanding these difficulties, the outcome of the December 20 meeting with the Viking project was the continued intent to use dual uplinks from each 64-m station. Plans were then made to take advantage of the February-March down time at DSS 14 to make whatever tests and modifications as were judged feasible. In the meanwhile the investigation at DSS 13 was to be completed in a few areas and followed by a long-term evaluation of noise burst and IMP performance.

As of this writing, progress is being made as planned, although recent guidelines suggest that for reasons beyond the control of the DSN, the Viking project plan will be revised to place the dual carrier (from one 64-m station) capability in a mission enhancement classification.

Acknowledgment

The conscientious efforts and unusual contributions from many individuals associated with JPL Sections 331, 332, 333 and 335, as well as Philco Ford, are acknowledged.

References

1. Bathker, D. A., and Brown, D. W., "Dual Carrier Preparations for Viking," in *The Deep Space Network Progress Report*, TR 32-1526, Vol. XI, pp. 146–149. Jet Propulsion Laboratory, Pasadena, Calif., Oct. 15, 1972.
2. Mudgway, D. J., "Viking Mission Support," in *The Deep Space Network Progress Report*, TR 32-1526, Vol. XII, pp. 14–15. Jet Propulsion Laboratory, Pasadena, Calif., Dec. 15, 1972.
3. Jackson, E. B. and Kolbly, R. B., "DSN Research and Technology Support," in *The Deep Space Network Progress Report*, TR 32-1526, Vol. XII, pp. 124–126. Jet Propulsion Laboratory, Pasadena, Calif., Dec. 15, 1972.
4. Smith, R. H., "Dual Carrier," in *The Deep Space Network Progress Report*, TR 32-1526, Vol. XII, pp. 200–201. Jet Propulsion Laboratory, Pasadena, Calif., Dec. 15, 1972.
5. *High Power Transmitters and Dual Carrier Uplink Support for Viking '75*, IOM 3300-72-176, April 17, 1972 (JPL internal document).
6. Jackson, E. B., and Kolbly, R. B., "DSN Research and Technology Support," in *The Deep Space Network Progress Report*, TR 32-1526, Vol. IX, p. 149. Jet Propulsion Laboratory, Pasadena, Calif., June 15, 1972.
7. Jackson, E. B., "DSN Research and Technology Support," in *The Deep Space Network Progress Report*, TR 32-1526, Vol. III, p. 156. Jet Propulsion Laboratory, Pasadena, Calif., June 15, 1971.
8. *Installation Procedure, WR430 Waveguide Assemblies, IP506254A*, Feb. 18, 1972 (JPL internal document).

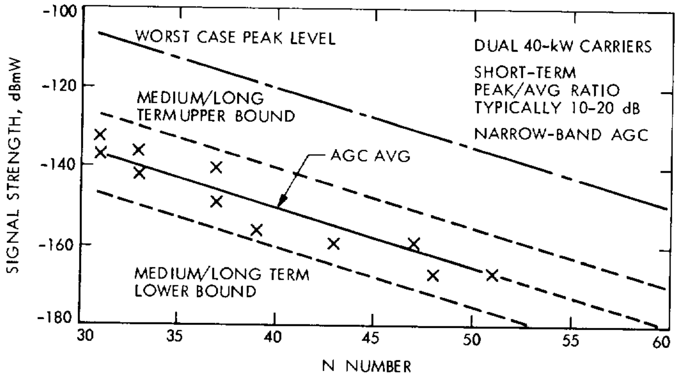

Fig. 1. DSS 14 IMP amplitude as a function of N (1972)

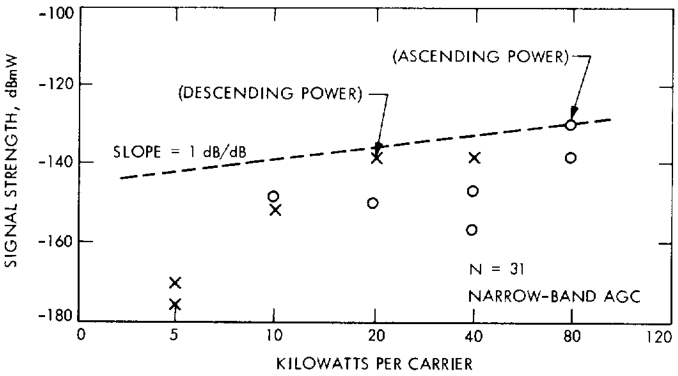

Fig. 2. DSS 14 IMP amplitude as a function of power (1972)

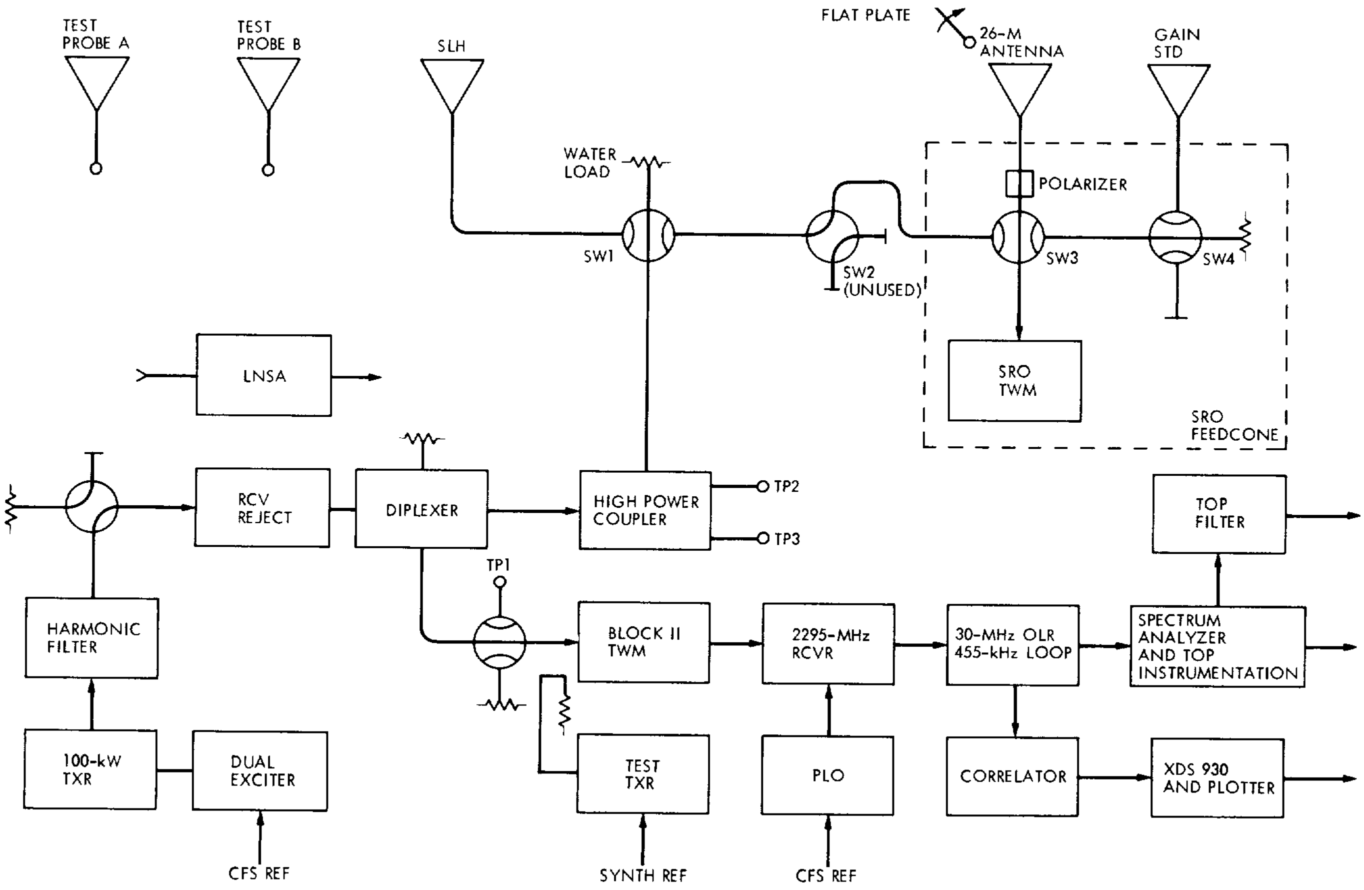

Fig. 3. DSS 13 dual carrier reconfiguration block diagram

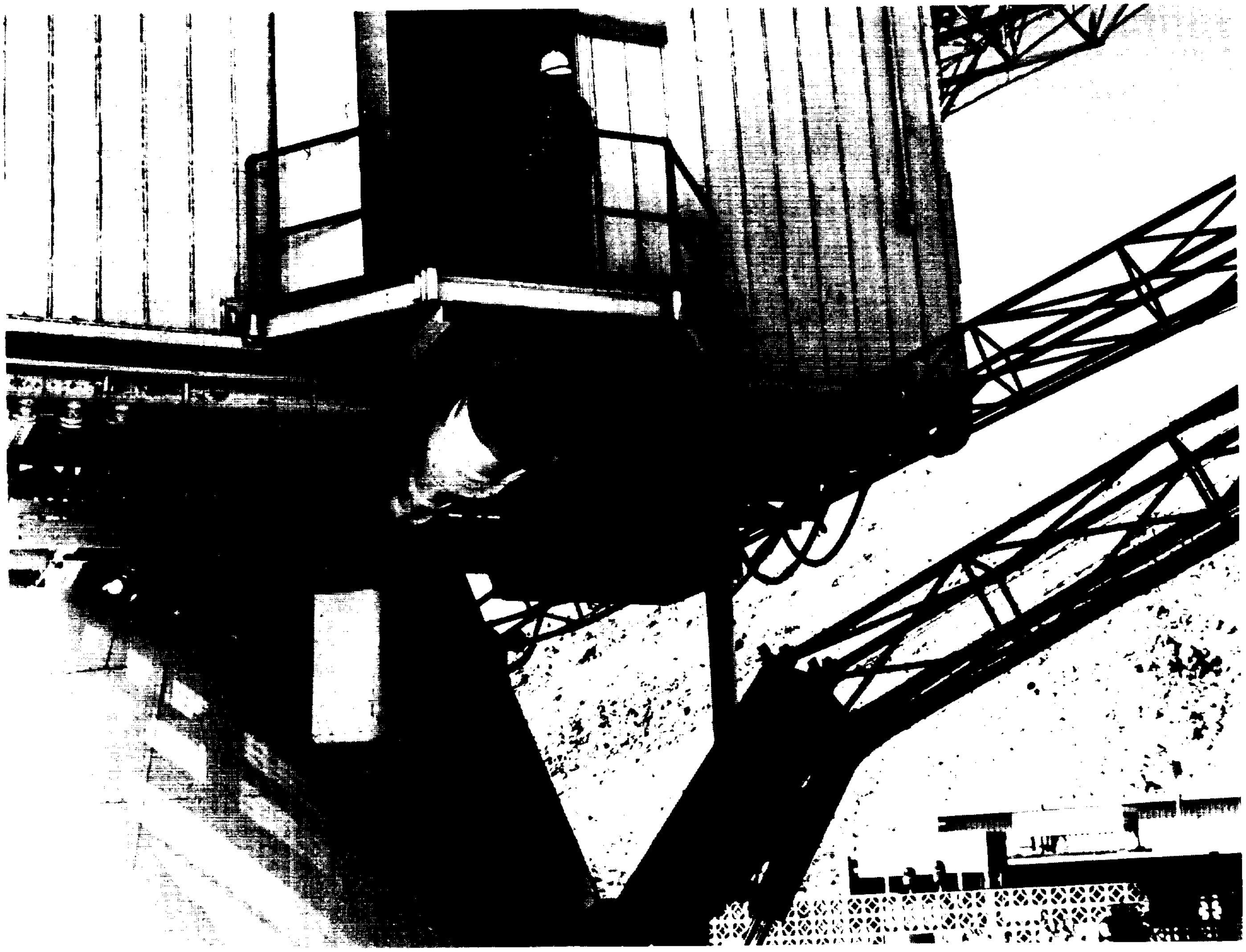

Fig. 4. DSS 13 side-looking horn installation

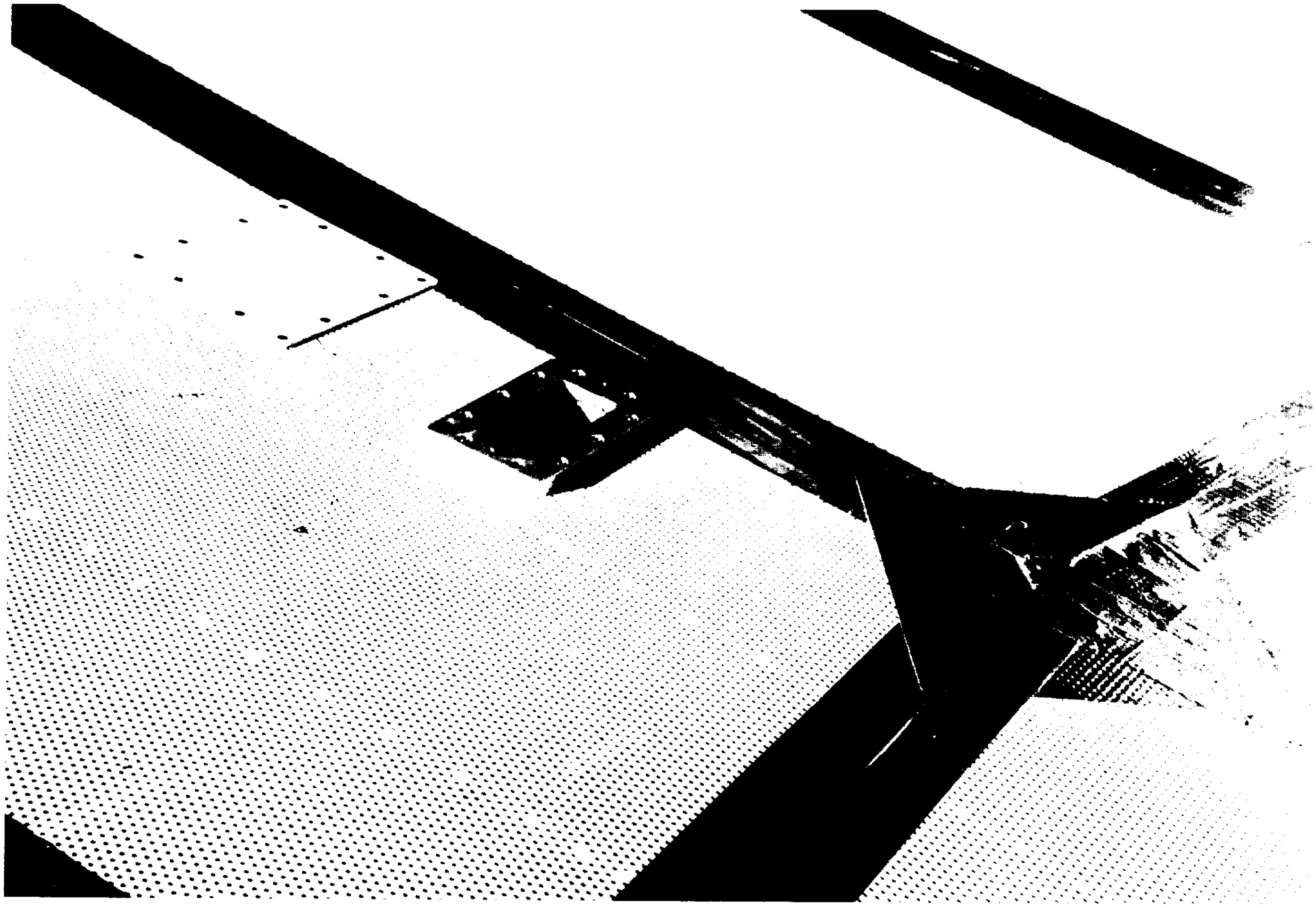

Fig. 5. DSS 13 retaped main reflector and test probes

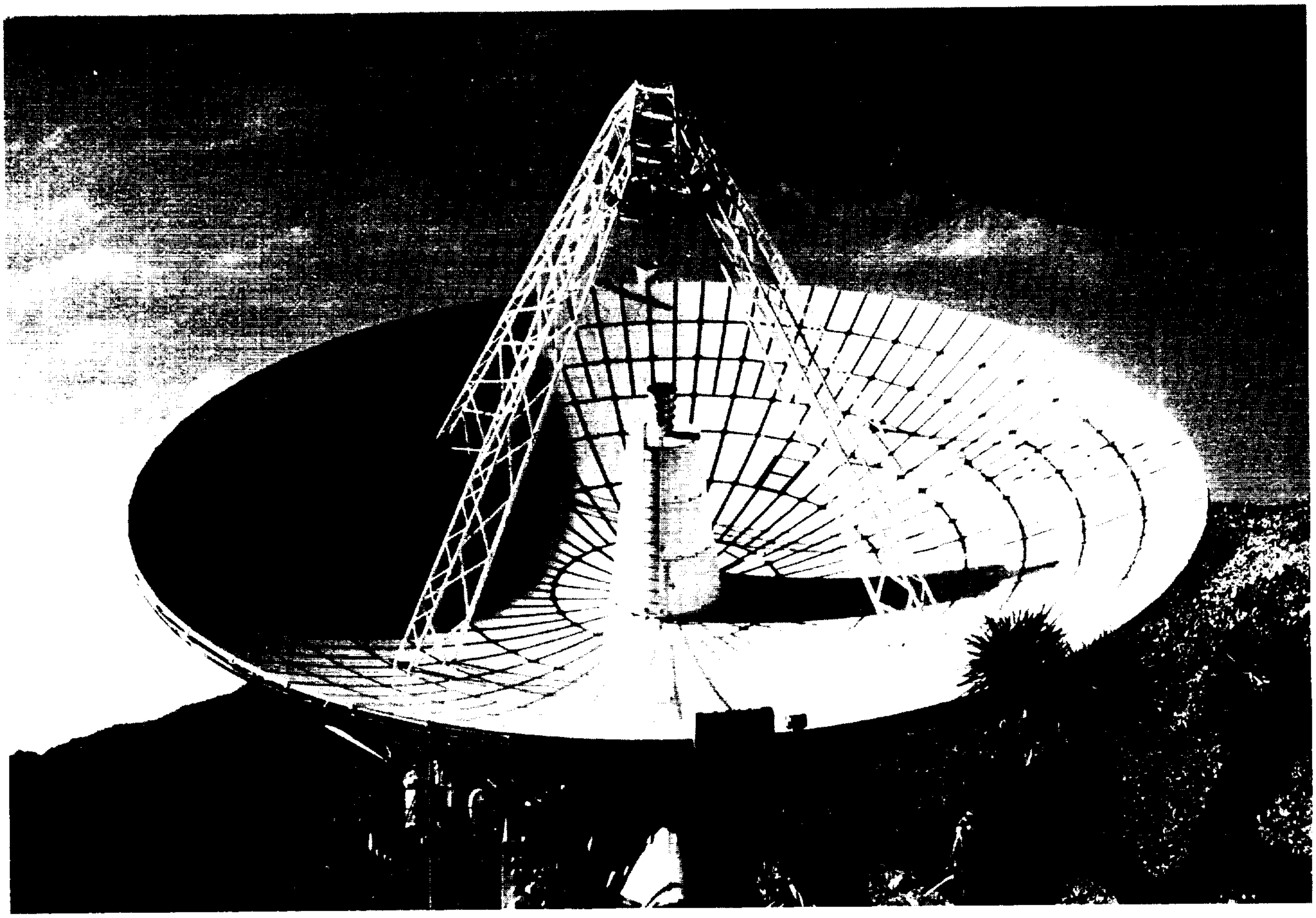

Fig. 6. DSS 13 initial dual carrier configuration

Fig. 7. DSS 13 flat plate reflector on SRO feed cone

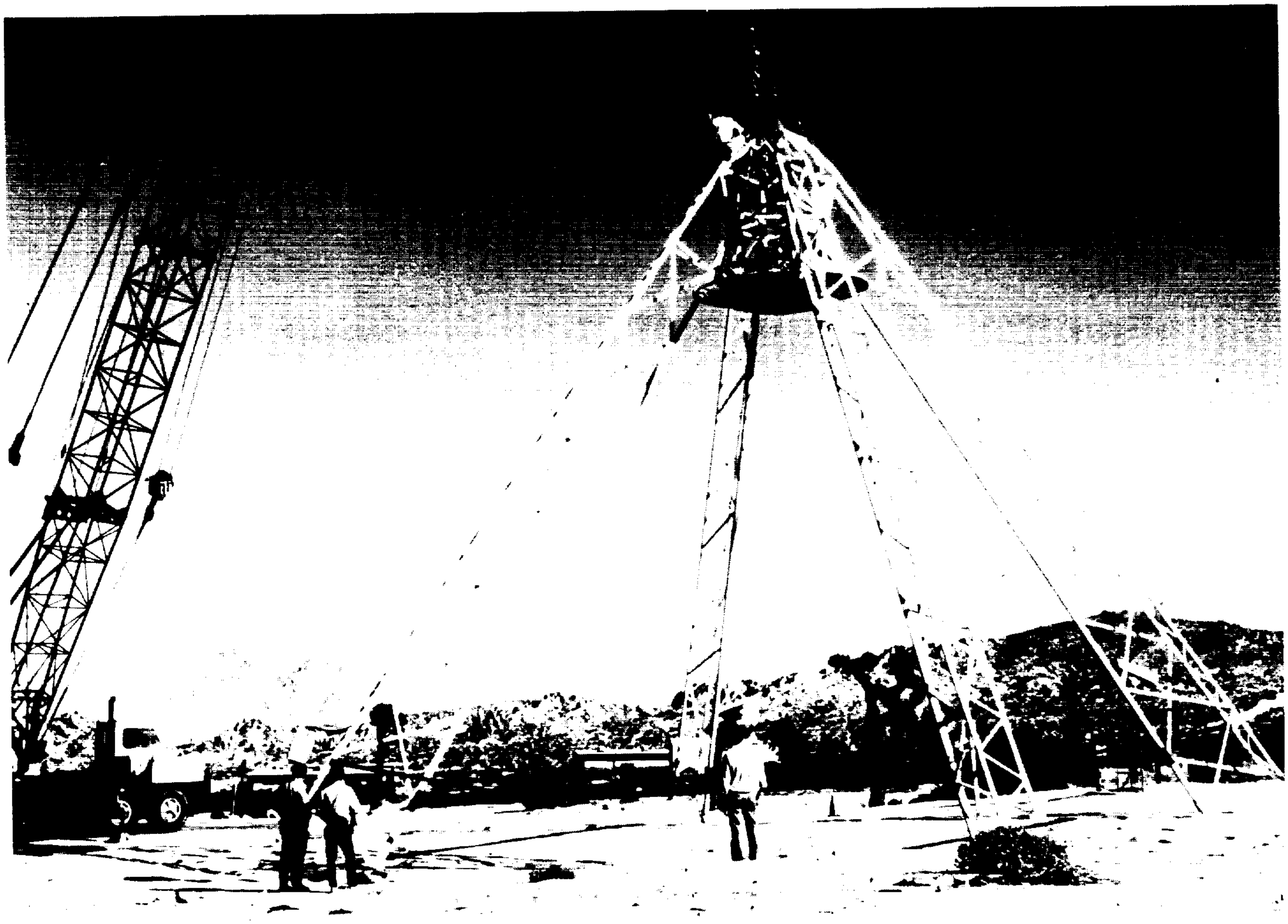

Fig. 8. DSS 13 subreflector and quadripod removal

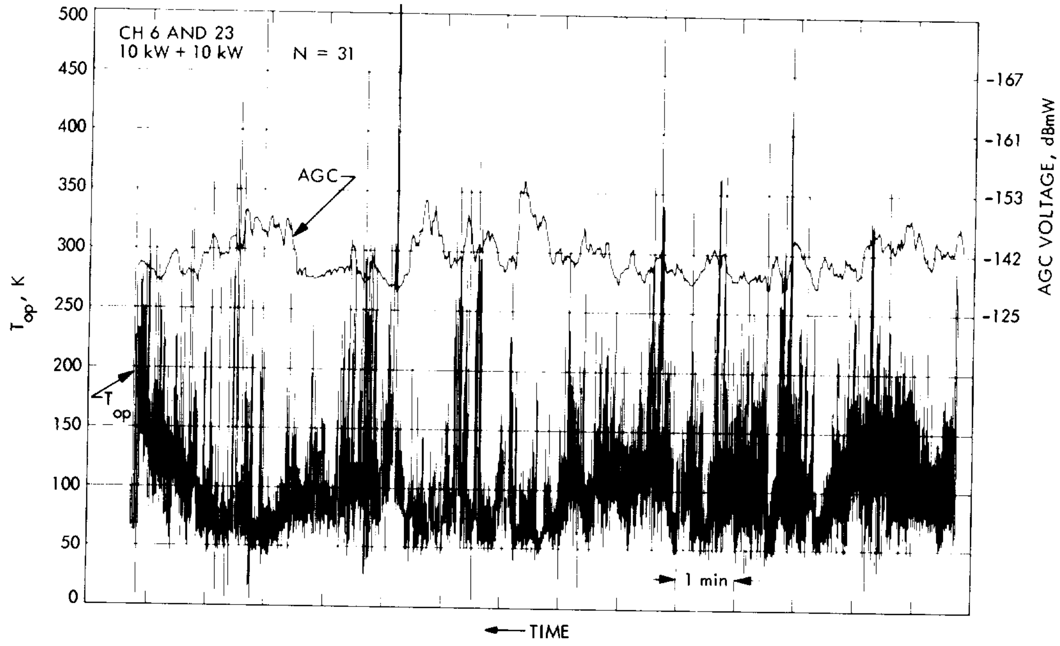

Fig. 9. System temperature and AGC performance, DSS 13 antenna system Oct. 15 to Nov. 1, 1972

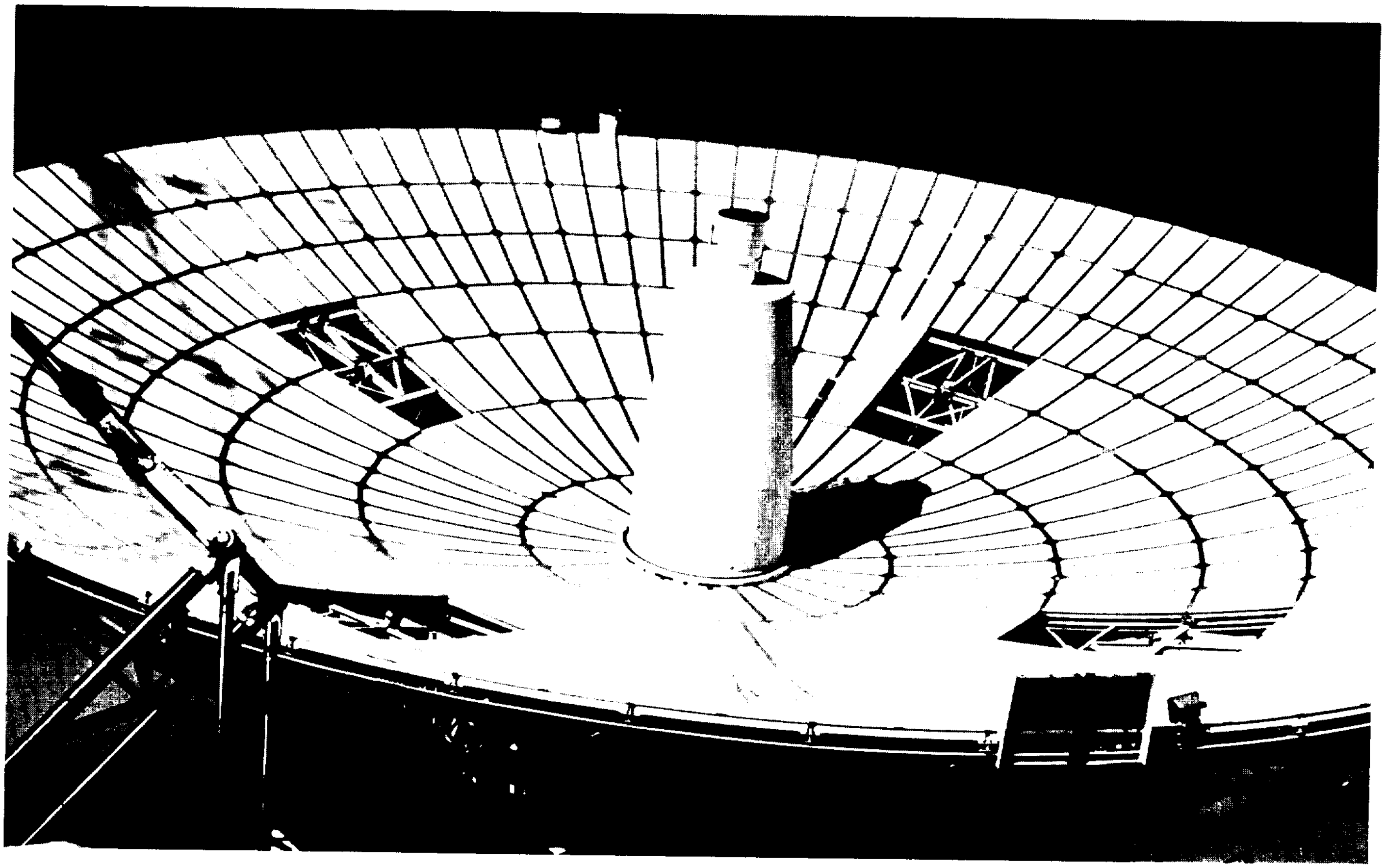

Fig. 10. DSS 13 welded feed cone with SLH horn

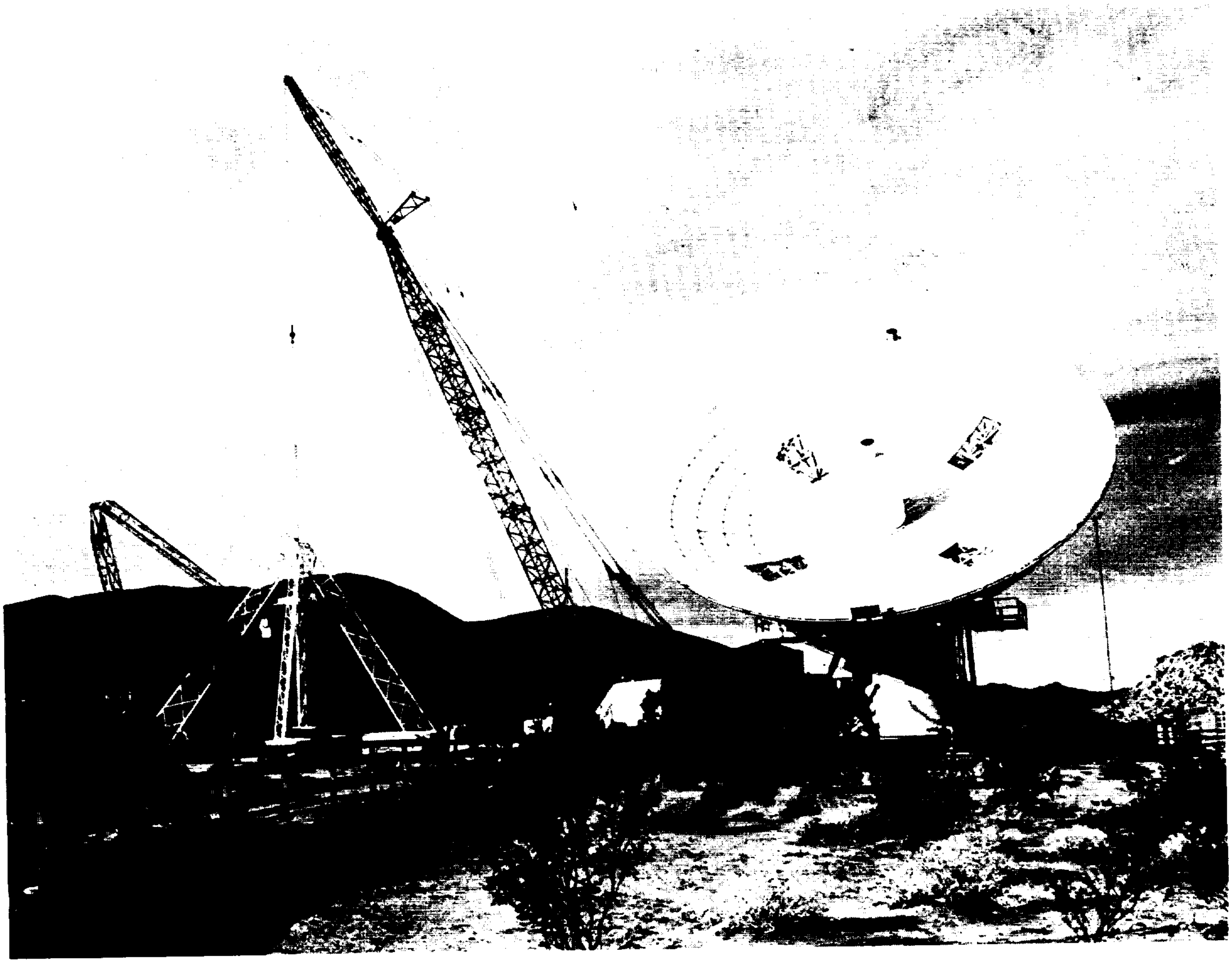

Fig. 11. DSS 13 subreflector installation

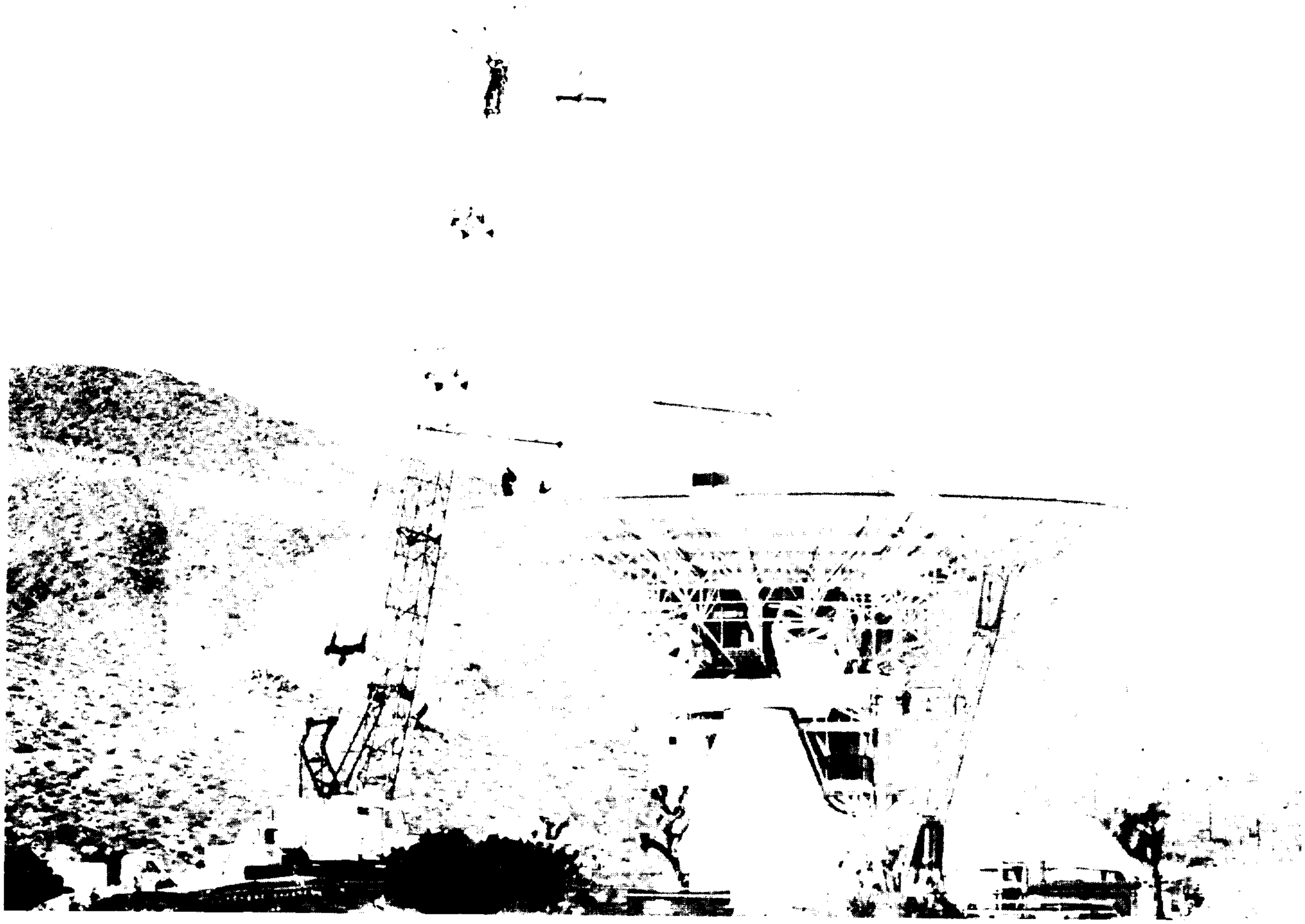

Fig. 12. DSS 13 quadripod installation

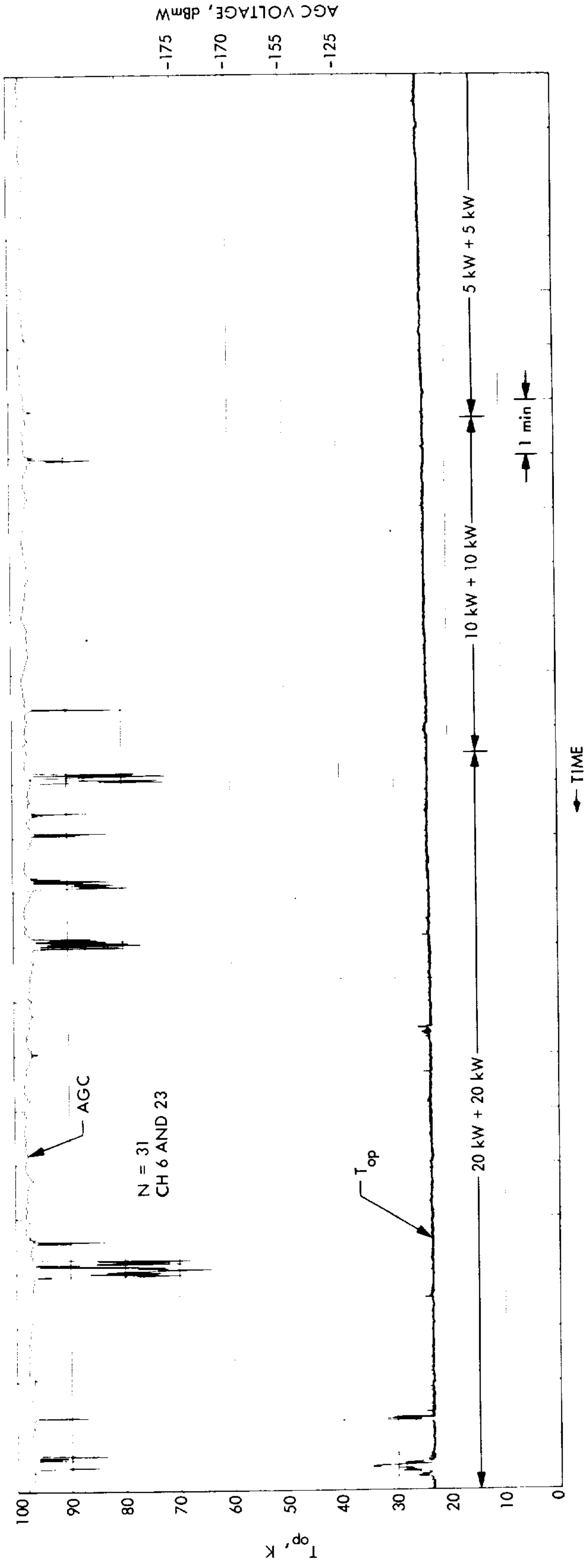

Fig. 13. System temperature and AGC performance, DSS 13 antenna system, Dec. 7, 1972

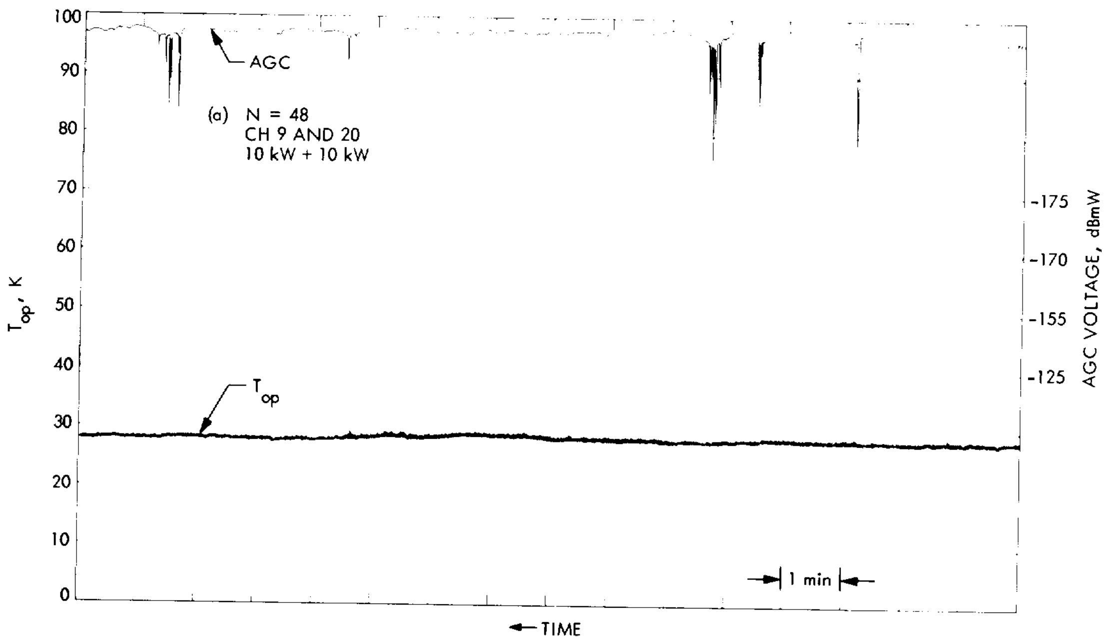

Fig. 14. System temperature and AGC performance as functions of N, DSS 13 Antenna System, Dec. 7, 1972

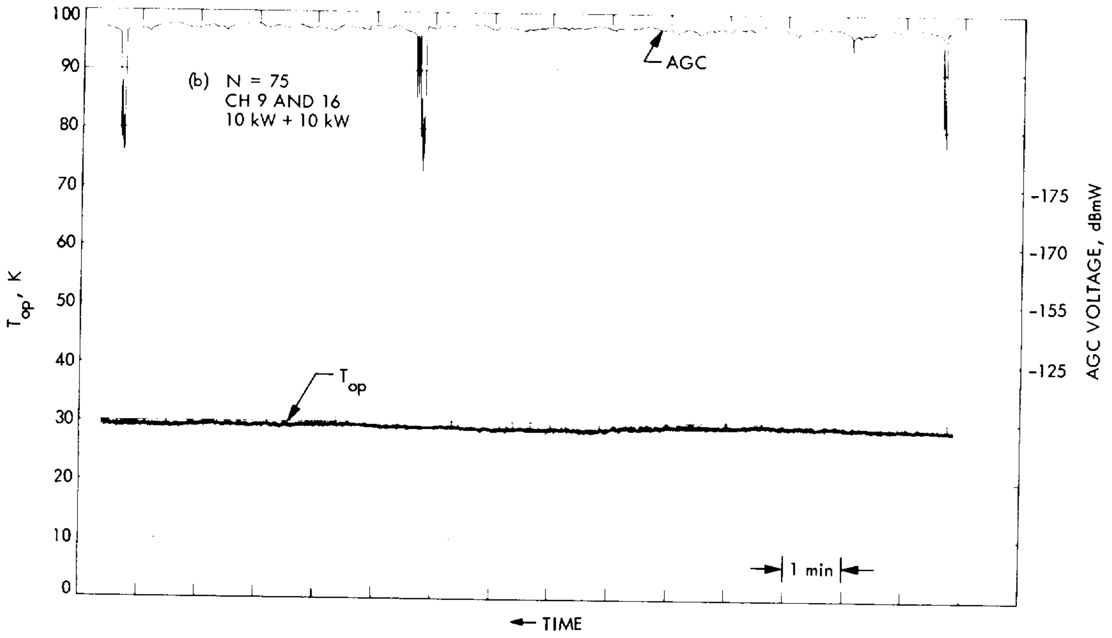

Fig. 14 (contd)

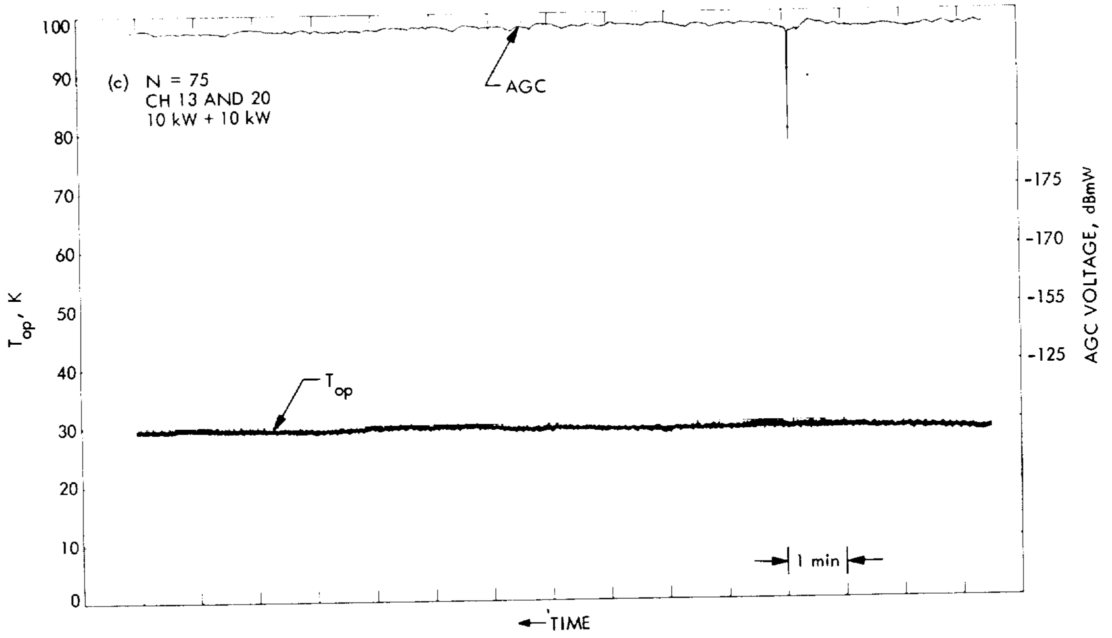

Fig. 14 (contd)

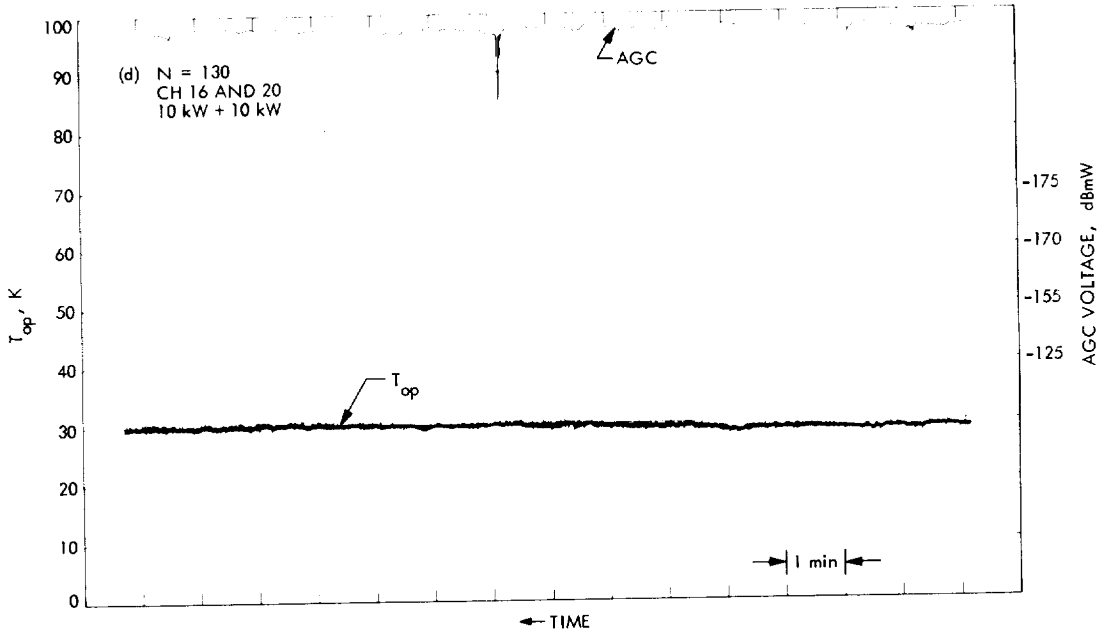

Fig. 14 (contd)

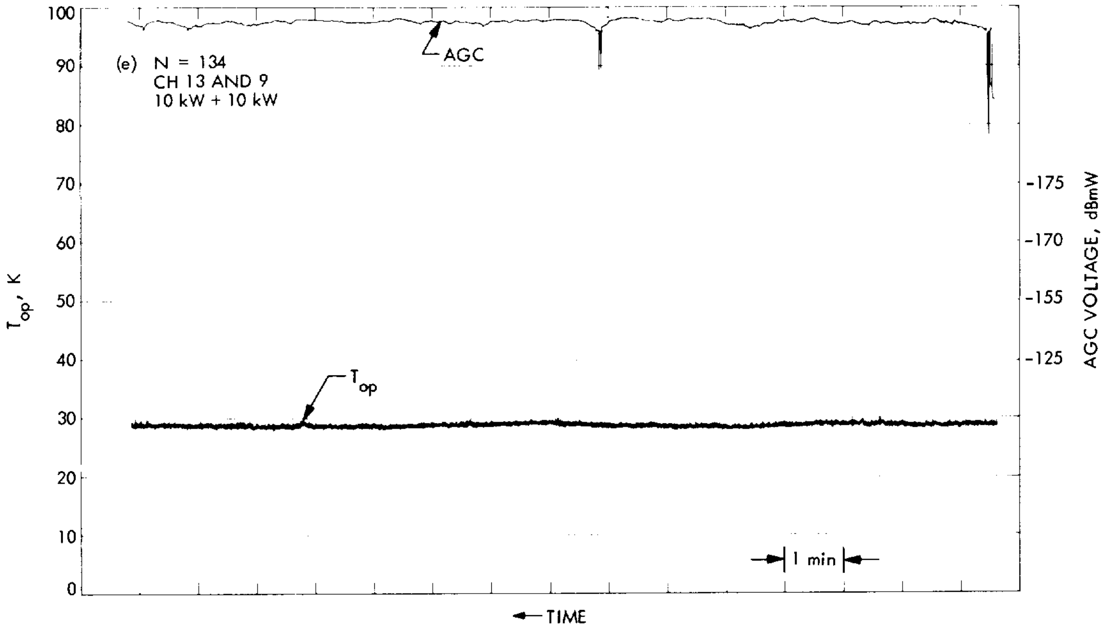

Fig. 14 (contd)

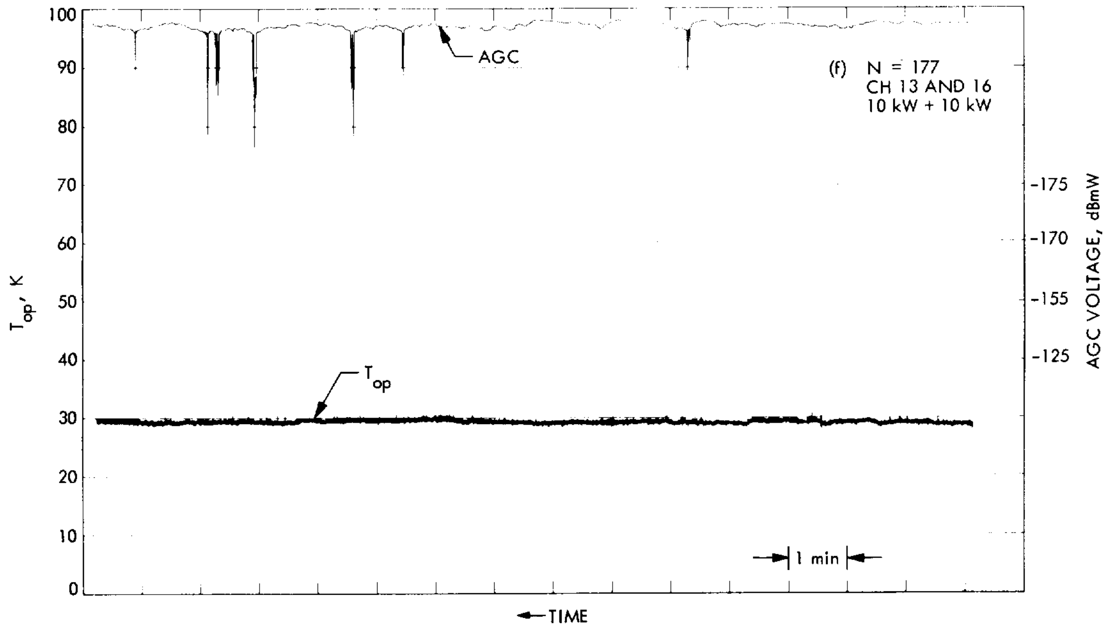

Fig. 14 (contd)

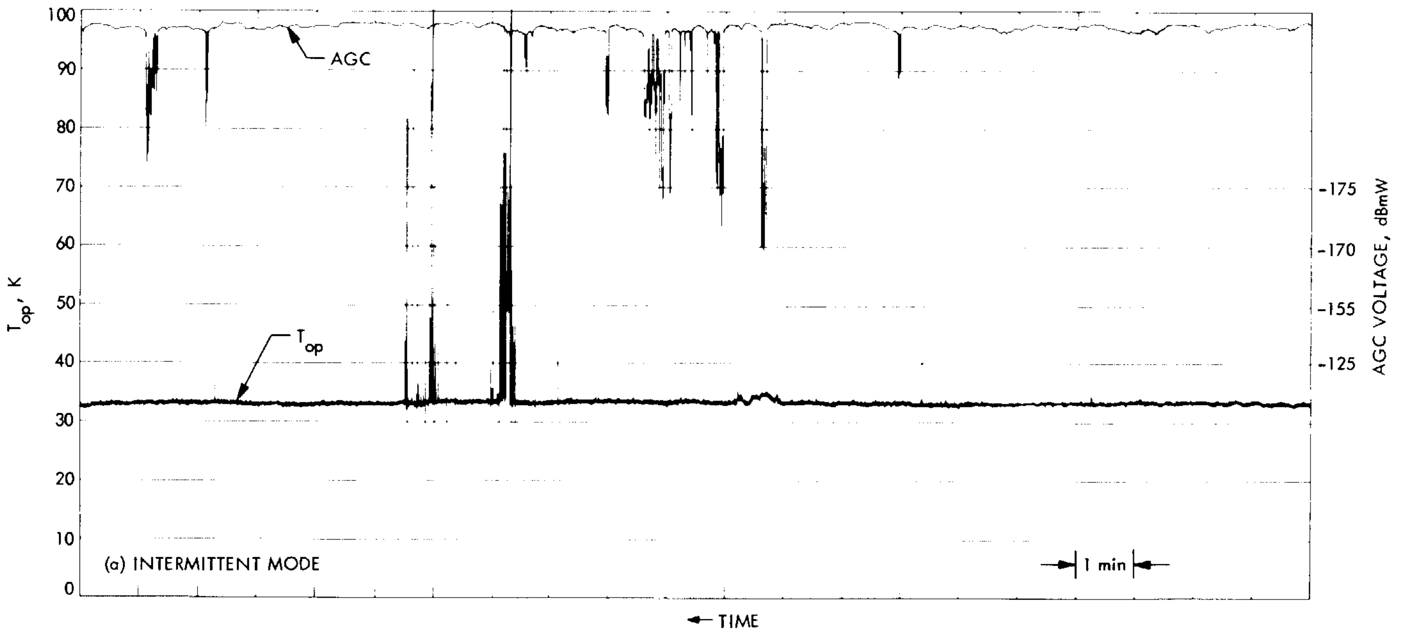

Fig. 15. DSS 13 antenna system temperature and AGC performance on Dec. 8, 1972
(a) during intermittent mode (b) during probable weather effects

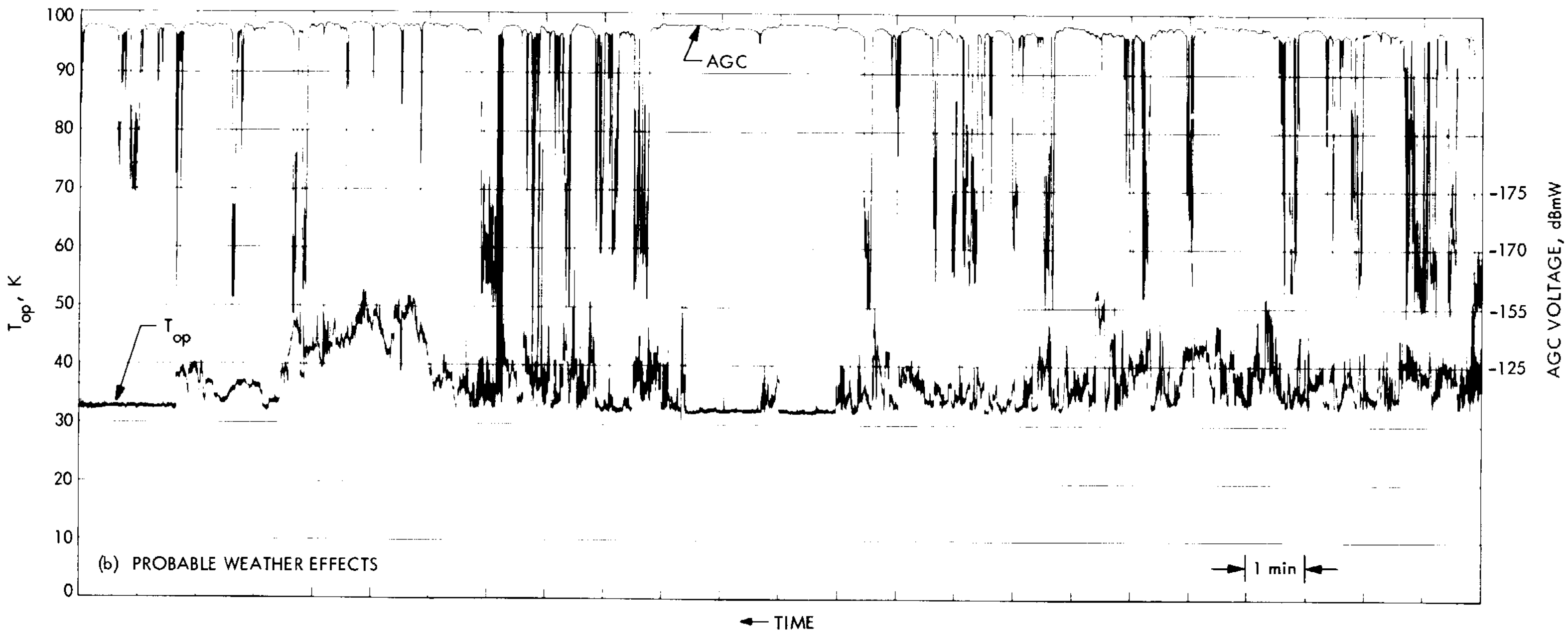

Fig. 15 (contd)

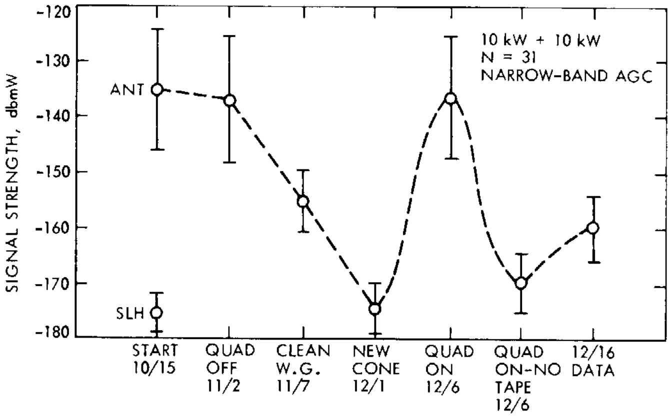

Fig. 16. DSS 13 milestones of IMP performance, 1972

Effects of Doppler Rate on Subcarrier Demodulator Assembly Performance

G. L. Dunn
Network Operations Section

A time dependent, steady-state static phase error equation that includes doppler rate effects has been incorporated into the Subcarrier Demodulator Assembly efficiency program. With the program in its present form, the optimum possible bandwidths, bit rate, amount of nulling of static phase error, and degradation expected can be obtained for the tracking of a given two-way doppler shift profile by various manipulations of the program.

I. Introduction

The presence of significant doppler rate in future DSN missions raises the following questions with respect to Subcarrier Demodulator Assembly (SDA) performance:

1. What loop bandwidths should be used for the various data rates?
2. How often should the SDA static phase error (SPE) be nulled?
3. What degradation should be expected for periods of significant doppler rate?

This article presents analysis to help answer the above questions. What follows is the derivation of a steady-state, time dependent, static phase error equation that includes error terms due to doppler rate and higher order effects. A computer program is then presented that incorporates the new static phase error equation and finally an example of the use of the computer program is given using Pioneer 10 data.

II. Derivation of Static Phase Error Equation

Using the linear SDA model as presented in Brockman (Ref. 1) (Fig. 1) the error ratio is given by:

$$\frac{E(s)}{\Theta(s)} = \frac{1}{1 + \dfrac{G}{s}\left(\dfrac{1+\tau_2 s}{1+\tau_1 s}\right)} = \frac{s + \tau_1 s^2}{G + (\tau_2 G + 1)s + \tau_1 s^2} \tag{1}$$

from which, if we perform a series expansion by dividing the numerator polynomial by the demoninator polynomial, we obtain:

$$\frac{E(s)}{\Theta(s)} = C_0 + C_1 s + C_2 s^2 + C_3 s^3 + \cdots \tag{2}$$

Therefore:

$$E(s) = C_0\Theta(s) + C_1 s\Theta(s) + C_2 s^2\Theta(s) + C_3 s^3\Theta(s) + \cdots \tag{3}$$

Neglecting initial conditions and impulses at $t = 0$, we obtain the steady state error equation:

$$E_{ss}(t) = C_0\Theta(t) + C_1\Theta'(t) + C_2\Theta''(t) + C_3\Theta'''(t) + \cdots \tag{4}$$

Assuming contributions of higher order terms are negligible, the steady-state static phase error equation is:

$$E_{ss}(t) \cong C_0\Theta(t) + C_1\Theta'(t) + C_2\Theta''(t) + C_3\Theta'''(t) + C_4\Theta^{iv}(t) \tag{5}$$

Evaluation of Eq. 1 gives the following values for C_i's:

$$C_0 = 0$$

$$C_1 = \frac{1}{G}$$

$$C_2 = \frac{G(\tau_1 - \tau_2) - 1}{G^2}$$

$$C_3 = \frac{2G(\tau_2 - \tau_1) + G^2(\tau_2^2 - \tau_1\tau_2) + 1}{G^3}$$

$$C_4 = \frac{-(\tau_2 G + 1)^3 + (2\tau_1(\tau_2 G + 1) + \tau_1(\tau_2 G + 1)^2)G}{G^4} - \frac{\tau_1^2 G}{G^4}$$

since $C_0 = 0$,

$$E_{ss}(t) \cong C_1\Theta'(t) + C_2\Theta''(t) + C_3\Theta'''(t) + C_4\Theta^{iv}(t) \tag{6}$$

where

$E_{ss}(t)$ = steady-state static phase error

$\Theta'(t)$ = input doppler shift function

$\Theta''(t)$ = input doppler rate function

$\Theta'''(t), \Theta^{iv}(t)$ = input higher order effects

Equation 6 gives the steady-state static phase error as a function of time for a given doppler shift curve and its respective derivatives, $\Theta'(t)$, $\Theta''(t)$, etc.

Close agreement is found between Eq. 6 and published results by Tausworthe (Ref. 2) for second order loops with doppler shift and doppler rate inputs. For example, if the input phase function with phase offset Θ_0 and frequency offset Ω_0 is:

$$\Theta = \Theta_0 + \Omega_0 t$$

then Eq. 6 predicts, for a passive integrator, second order loop, the steady-state static phase error to be:

$$E_{ss}(t) = \frac{\Omega_0}{G}$$

which is the same value or that predicted by Tausworthe. For an input phase function with doppler rate Λ_0 given by:

$$\Theta = \Theta_0 + \Omega_0 t + \frac{\Lambda_0 t^2}{2}$$

Eq. 6 predicts, for a passive integrator, second order loop, the steady-state static phase error to be ($\tau_1 >> \tau_2$):

$$E_{ss}(t) \cong \frac{(\Omega_0 + \Lambda_0 t) + \tau_1\Lambda_0}{G}$$

This compares favorably with Tausworthe's result:

$$E_{ss}(t) \cong \frac{(\Omega_0 + \Lambda_0 t)}{G}$$

Two assumptions in the above analysis were made. First, it is assumed that the static phase error can be described using a steady-state equation. This assumes the SDA loop dynamics are such that any transients introduced into the loop die out quickly. Second, the above analysis assumes that the steady-state error equation can be approximated by four terms, which implies that the error series converges rapidly. For the doppler data used for Pioneer this is a good assumption. However, for another doppler profile and different subcarrier/carrier ratios, this assumption would have to be further tested.

III. Computer Program

To use the static phase error equation as given by Eq. 6 in the current SDA efficiency program, a curve fit of doppler shift predict data must first be obtained. The coefficients, $a_0, a_1, a_2, \cdots$ of a curve fitting polynomial of the form

$$y = a_0 + a_1 x + a_2 x^2 + \cdots a_n x^n$$

are then inputted into the program in ascending order. At least 5 coefficients, starting with a_0 must be specified.

If fewer than five coefficients are necessary to describe the fitted polynomial, then the remaining coefficients must be inputted as

$$a_i = 0_{i=n,4}$$

The current program is set up to accept only two-way doppler shift profiles given in MHz with time scales given in minutes.

The following information is supplied by the user to the SDA efficiency program:

(1) Data bit rate (bps), BRATE.
(2) Number of bits/symbol for data, RN.
(3) The time interval of interest for doppler study (minutes), LTMIN and LTMAX.
(4) Sampling time interval (minutes), INCRE.
(5) The maximum allowable degradation in the SDA (dBs), ADMAX.
(6) The modulation index (radians), TMOD1.
(7) The system temperature (Kelvin), TEMP.
(8) The appropriate carrier and subcarrier frequencies (Hz), FCAR and FSUBC.
(9) The carrier power (dBM), PCDBM.
(10) SDA loop design bandwidth (Hz), I = narrow, medium, or wide.
(11) The doppler shift curve fitted polynomial coefficients, $a_0, a_1, \cdots, a_n$.

The program computes, first nulling out the static phase error at time LTMIN, all static phase error for times LTMIN to LTMAX at increments of time INCRE. The overall static phase error (doppler plus phase noise) is then calculated along with SDA degradation,

$$\left(\frac{\text{demod} \dfrac{ST_{sy}}{N_0}}{\text{input} \dfrac{ST_{sy}}{N_0}} \right)$$

in dBs.

The following information is outputted by the program for time increments of INCRE.

(1) Values of doppler shift, DELF1, (Hz) for LTMIN to LTMAX.
(2) Doppler rate, DELF2 (Hz/s), for LTMIN to LTMAX.
(3) Second and third order derivatives values, DELF3 (Hz/s^2), and DELF4 (Hz/s^3).
(4) Time T (min) at which static phase error is computed.
(5) SDA Efficiency

$$\left(\frac{\text{demod} \dfrac{ST_{sy}}{N_0}}{\text{input} \dfrac{ST_{sy}}{N_0}} \right)$$

(6) Degradation as defined in Eq. (5) (phase noise + doppler) in dBs, DEGDB.
(7) Added degradation as defined in Eq. (5) due to doppler alone (dB), DEGDB.
(8) Static phase error due to doppler (radians), SPESDA.
(9) Nulling factor (radians), SPET.

The SPET is the amount of static phase error that has accumulated when the SPE is nulled on the SDA.

The computer deck setup follows:

```
@RUN

@FOR

User supplied information (BRATE,RN,LTMIN,
LTMAX,INCRE,ADMAX,TMOD1,TEMP,FCAR,
FSUBC,PCDBM,I=NARROW,MEDIUM, or WIDE)

PROGRAM

END

@MAP

LIB LIB*JPL$

@XQT

±X.XXXXXX±XX ←DATA FORMAT  }
     .                      }  Doppler
     .  (at least 5 coefficients)  }  profile
     .                      }  coefficients
     .                      }
```

From the computer program the number of times the SDA SPE must be nulled for some ADMAX is easily found by counting the number of times during tracking the SPE is nulled so SDA degradation is never greater than ADMAX.

The user can obtain the maximum amount of degradation expected for a tracking period without constant nulling by setting ADMAX to some arbitrarily large number that would never occur during a tracking period. For example set ADMAX = 100.

The SDA efficiency program can be used to select optimum design bandwidths for a given doppler profile as a function of time by iterating over the set of available bandwidths for a given bit rate and carrier power, then storing the degradation as a function of time, and finally searching the stored values for optimum bandwidths.

IV. Example of the Computer Program—Pioneer 10

Using the SDA efficiency program with the new static phase error equation, a doppler shift curve was obtained for Pioneer 10, DSS 12 predicts for a Jupiter encounter. Using a least squares polynomial fit routine, PFIT in the JPL Subroutine Library, an eighth order doppler shift equation was produced for time −420 to +74 min before and after encounter. A sampling interval of 5 min was used. A bit rate of 128 bps with narrow bandwidth and a carrier power of −152 dBm was used. ADMAX, the maximum allowable degradation before nulling, was set to 0.1 dB. The above inputs necessitate the nulling of the static phase error three times, and the maximum predicted overall degradation (doppler + phase noise) was 0.16 dB.

References

1. Brockman, M. H., "MMTS: Performance of Subcarrier Demodulator," in *Supporting Research and Advanced Development*, Space Programs Summary 37-52, Vol. II, p. 131, Jet Propulsion Laboratory, Pasadena, Calif., July 31, 1968.
2. Tausworthe, R. C., *Theory and Practical Design of Phase-Locked Receivers*, Technical Report 32-819, Vol. I, p. 36. Jet Propulsion Laboratory, Pasadena, Calif., Feb. 15, 1966.

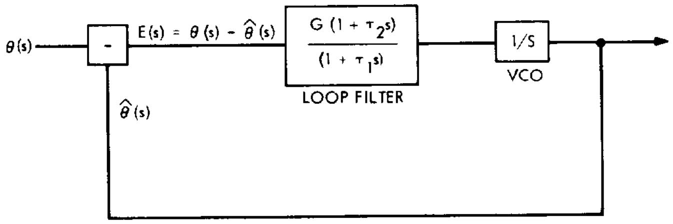

$\theta(s)$ = INPUT PHASE FUNCTION
$\hat{\theta}(s)$ = ESTIMATED PHASE FUNCTION
$E(s)$ = ERROR SIGNAL
G = OPEN LOOP GAIN AT DC
τ_1, τ_2 = TIME CONSTANTS OF LOOP FILTER

Fig. 1. Linear model of subcarrier phase–tracking loop (Laplace representation)

Viewperiod Generator for Spacecraft and the Planets

W. D. Diemer
Network Operations Office

This article describes a method, and the supporting software, developed to provide an inexpensive means of generating spacecraft and planetary viewperiods for the Deep Space Stations over a long period of time. In the past, the only method for obtaining this information was an expensive and complex computer program which provided these data as a secondary output to the actual station look angles.

The task of receiving and transmitting signals from and to spacecraft in solar orbits poses many observational problems which are unlike those of conventional astronomy.

Conventional telescopes are most frequently targeted on stellar objects whose positions are fixed on the celestial spheres. Less often, they are aimed at planets and other objects within the solar system, whose varying positions in the heavens are known with great accuracy for long into the future.

In contrast, tracking antennae are targeted most frequently on spacecraft whose paths across the sky can only be estimated in advance of launch. Once aloft and en route, their paths can be determined with sufficient accuracy for tracking purposes by using not only the laws of celestial mechanics but also those of propulsion physics. Unlike natural objects, their trajectories can be altered on command to achieve desired observational objectives.

As a consequence of these uncertainties in spacecraft trajectories, it is more difficult to make long-range plans for efficient use of the tracking antenna in the NASA Deep Space Network (DSN) operated by the Jet Propulsion Laboratory (JPL).

The efficient use of these expensive scientific instruments requires that long-range planners have reasonably accurate estimates of the times during which particular spacecraft will be in view (i.e., above the horizon) for long periods into the future. With these data, they can determine whether two spacecraft are in view during the same period, during overlapping periods, or during non-overlapping periods. (The word *view* must be interpreted here in a radio sense rather than in an optical sense.) If two spacecraft of interest are above the horizon during the same period, but not within the beam width of one antenna, then only one can be tracked on a given day by a given station (though, of course, it is possible to use a portion of the "viewperiod" for each, rather than devoting the entire period to one and ignoring the other). On the other hand, if two spacecraft have non-overlapping viewperiods, the antenna can be aimed at the second after the first has set.

Such information (i.e., the rise and set times for each spacecraft at each station) also reflects back on other planning activities. The projected workloads developed by long-range planners may influence budgetary allocations and requests in future years, as well as manpower loading, equipment requests, and maintenance and training needs. For several years, the Jet Propulsion Laboratory has been using two partial solutions to this problem: highly accurate short-range predictions and approximate long-range predictions.

Every few days, a computer run is performed which generates precise aiming coordinates for use in tracking particular spacecraft from each station. This program, constructed on iterative principles, produces coordinates for five-minute intervals throughout the day. Rise and set times are only one of the products of these calculations. This program, known as PREDIX, is very time-consuming and expensive to operate; it requires nearly one hour of computer time (IBM 360/75) to generate two weeks of aiming coordinates. Because of convenience and need for frequency updates, these programs are rarely executed more than a few weeks in advance of need, as the results are used for actual tracking and must be as accurate as possible.

For longer future projections, a semi-graphical method has been used. JPL's Navigation and Mission Design Section has the responsibility for developing approximate trajectories and alternatives for proposed missions and maintaining accurate flight paths for vehicles already launched, using actual positional fixes. This section has developed a digital plot program, using both the Univac 1108 and a Calcomp Plotter. The output of this program (Fig. 1) is a graph containing three superimposed plots. All plots use time as one dimension, along the length of the continuous forms, so that trajectories of any time span can be shown. The other dimensions are:

(1) *Declination*—the angular distance between the spacecraft and the celestial equator. This variable almost always has values ranging between $-25°$ and $+25°$, since to date all spacecraft have been directed in orbits close to the ecliptic.

(2) *Range*—the distance from the Earth to the spacecraft. Since all spacecraft launched to date (except Pioneer 10) have had orbits not farther than that of the planet Mars, this variable usually ranges between zero and 400 million kilometers. This value can be used directly to calculate round-trip signal times at the speed of light.

(3) *Local Meridian Crossing Time*—the time at which the spacecraft crosses the local meridian at the observing station. (The meridian is the line that bisects the sky as seen from any point on Earth. It starts at the north horizon, passes through the zenith, and ends at the south horizon.) The point at which any celestial object crosses the local meridian, as Earth rotates, is also the point of maximum elevation. It is rising from the horizon until it crosses the meridian; thereafter its elevation decreases until it sets. This variable can have any value between zero and 24 hours. Objects that are close to a celestial pole never rise nor set. If they are in the same hemisphere as the observing station, they trace a circle in the sky around the pole, crossing the meridian twice each day. The higher crossing is termed the superior crossing, the other is the inferior crossing. Conversely, objects close to the pole opposite the observing station never rise at all. Their circles in the sky never reach above the horizon. To date, no spacecraft have been sent in orbits so close to the poles that they are in constant view (or constant eclipse) from any station.

Using these plots as a starting point, we have developed a computer method for generating rise and set times for any spacecraft, as viewed from any point on Earth, for any period and as far into the future as trajectories have been calculated. This program can produce these times for every single day, if desired. For practical purposes, however, it is usually sufficient to produce them at weekly or monthly intervals, since the day-to-day changes are quite small (2–5 minutes), and may be determined by interpolation when closer intervals are required.

In addition to the data from these plots, two other data inputs are required: the geocentric coordinates of each station (i.e., latitude and longitude on Earth's surface), and the profile of the local horizon around each station.

The phrase that JPL uses to describe this local horizon profile is "horizon mask," the term implying that a celestial object is masked from view (whether visual or radio) until it rises above the surrounding hills and mountains. This horizon mask is most conveniently represented graphically by a chart termed a "stereographic projection" (see Fig. 2).

This chart is representative of the charts developed for each station. The outer circle represents the entire sky as seen from the observation point. The shaded area around the circumference of the circle represents that portion of the sky which is not visible due to the neighboring hills, and shows the irregularity characteristic of natural topographic features. The numerous intersecting lines, circles and arcs on the chart represent the two different coordinate systems used for celestial observation. One of these systems is Earth-centered, the other is sky-centered.

Though these charts do represent the entire visible sky as seen from each of the stations in the DSN, they include some portions of the celestial sphere which are outside the observational range of the antennae. These further restrictions on viewing are a consequence of the manner in which the antennae are supported, and moved to compensate for the apparent motion of the spacecraft across the sky as Earth rotates.

These mechanical limitations on spacecraft tracking are shown on the stereographic projections represented in Fig. 2. The heavy blocked line around the figure indicates the tracking limits. The small arc near the celestial pole indicates that celestial objects close to that pole cannot be observed throughout the 24 hours. The jagged balance of this line, generally outside the circle, indicates that in these regions the antenna can be pointed below the horizon—or actually at the ground.

We shall now use the stereographic projection in Fig. 2 to illustrate the principles upon which our viewperiod generator computer program was constructed.

Let us start with an object whose declination is 0°, i.e., it lies precisely on the celestial equator. If we examine the chart closely, we see that the equator crosses the horizon mask about 1° from the eastern horizon, or 89° from the meridian. Since Earth rotates a full 360° in one day, a point on the celestial sphere seems to move equally 360° in a day, or, most simply, it takes four minutes for an object to move 1°. We therefore determine that the object will rise above the horizon (if it is on the equator) 5 hours and 56 minutes before it crosses the meridian (89° × 4 minutes = 356 minutes = 5h 56m). Similarly, we observe that the celestial equator crosses the western horizon mask exactly at sea level. The object will therefore remain in view while Earth rotates 90°. We thus determine that the object will set 6h 0m after it crosses the meridian. The total view-period duration will be the sum of these two times, or 11h 56m. The actual local times of rise and set are determined by subtracting and adding these two time intervals to the time of local meridian crossing. For example, if the object crosses the meridian at 09:52 local time, its rise is at 03:56 and its set is at 15:52.

However, local times are not adequate for the operation of the DSN. Being a worldwide operation, it must use a uniform time standard for all its stations, and has selected Greenwich Mean Time (GMT) as that standard. The local time can be easily converted to GMT by adding or subtracting the time required for Earth to rotate from the Greenwich meridian to the local meridian, which time is a direct function of the longitude of the station. Since DSS 12 is approximately 118° west of the Greenwich meridian, its time difference from GMT is 7h 52m. Therefore, the GMT rise time for the above example is 20:04 of the previous day, its GMT set time is 08:00 of the same day.

For a second example, let us choose an object whose declination is −24°, or 24° south of the celestial equator. Examining the stereographic chart, we see that at this declination, the angular distance from the meridian to the eastern horizon mask is 72°. The time equivalent of this angle is 4h 48m (72° × 4m = 288m = 4h 48m). Similarly, the angular distance from the meridian to the western horizon is 65°, and its time equivalent is 4h 20m. The duration of the viewperiod is the sum of these two, or 9h 8m. Note that this viewperiod is substantially shorter than for an object at the celestial equator. Also note that an object whose declination is greater than 48° south does not rise above the horizon at all.

For a final example, let us choose an object whose declination is +10°, or north of the celestial equator. The chart shows that the angular distance between the meridian and the eastern horizon is 100°, for a time equivalent of 6h 40m. However, we also observe that this declination arc intersects the heavy line representing the mechanical limits imposed by the HA–dec mounting of the antenna. The angular distance from the meridian to this limit is only 90°, for a time equivalent of 6h 0m. This difference illustrates the fact that, for celestial objects at this declination, observation cannot begin when the object rises above the horizon, but must wait until it comes within pointing range of the antenna, some 40 minutes later. Assuming, again, a local meridian crossing time of 09:52, such an object rises above the horizon at 03:12, but cannot be observed until 03:52. Similarly, the angular distance along the +10° declination arc from the meridian to the western horizon is 97°, for a time equivalent of 6h 27m. Again, the mechanical limits imposed by the mounting restrict the actual viewing angle to 90° or 6h 0m. (Note that at high declinations, the angular distances east and west are equal. This is a consequence of the fact that the mounting is symmetrical.) Thus the object passes out of practical viewing range some 27 minutes before it actually drops below the horizon.

These three examples illustrate the three variables required to calculate local rise and set times:

(1) The time of the local meridian crossing.

(2) The declination of the object.

(3) The angular distance along the declination arc from the meridian to each horizon, or to the mechanical antenna limits in extreme latitudes.

A fourth variable, the longitude of the station, is all that is further required to convert these local times to GMT.

An interesting aspect of this approach to the solution of determining long-range rise and set times is the fact that the local meridian crossing time is the same for all stations, regardless of longitude. We are aware that when the Sun crosses the local meridian, it is local noon. Another celestial object on the Sun's meridian will also cross the local meridian at local noon. An object (say the moon whose angular distance is 30° in advance of the Sun's meridian will cross the local meridian 2 hours in advance of noon, or 10:00. And any object whose angular distance from the Sun's meridian is known will cross the local meridian at a time before or after noon, which is a direct function of the time equivalent of that angular distance.

This point must not be taken too literally. The position of an object on the celestial sphere does vary slightly from day to day. For a stellar object, this variation is the difference between a solar day and a sidereal day, or about 4 minutes. For an object pursuing a solar orbit in the same direction as Earth (i.e., a spacecraft), this variation is somewhat less. For Pioneer 10, it is about 2.5 minutes. For objects pursuing a solar orbit within Earth's orbit, the variation is somewhat greater than 4 minutes per day. As a consequence, the local meridian crossing time of a spacecraft is not precisely identical for all stations in the DSN, but the difference is seldom more than a minute or two. This variation is not of sufficient significance to affect long-range planning data, and this refinement has not been included in the program we have developed.

The declination of a celestial object also varies slightly from day to day, though this variation is even smaller than the variations in local meridian crossing time. If we again examine the sterographic projection in Fig. 2, we see that as an object moves from one declination level to another, the angular distance along the declination arc from the meridian to the horizon increases as the object approaches the pole, and decreases as it recedes from the pole. The observational consequence is that the viewperiod lengthens as the object approaches the pole, and decreases as it recedes.

If there were an object in the solar system whose position was fixed, its declination would vary as the Earth made its annual trip around the Sun, reaching a maximum of about +23° at one point in the year, and a minimum of −23° six months later. There is, of course, no such stationary object. The nearest approximation is the planet Pluto, whose annual motion across the sky is somewhat less than 2°, since it requires 248 Earth years to complete its single solar circuit. Thus, the declination plot (see Fig. 1) of the planet Pluto would show a cycle of about 367 days, just slightly more than a year. The nearer superior planets (Neptune, Uranus, Saturn, Jupiter, and Mars) would have declination plots showing progressively larger cycles: almost 400 days for Jupiter and over 600 days for Mars. The two inferior planets (Venus and Mercury) speed around the Sun much faster than Earth. Their declination plots show cycles of much less than a year: about 200 days for Venus and about 100 days for Mercury.

The declination plots of the planets are not precisely repeated in each cycle. The nominal maximum and minimum values of +23° and −23° are for objects which are precisely in the ecliptic, the plane of Earth's orbit. All the planets have orbits whose planes are inclined at varying (though small) degrees to the ecliptic. The actual plots over long periods may show variations as great as +30° to −30° or as little as from +16° to −16°. The declination pattern is never precisely repeated, since the revolution times of all the planets are incommensurable with Earth's year. This cyclical variation in local meridian crossing time and declination should be kept in mind when interpolating values from the tables we have produced.

Interpolation will provide rise and set times with errors usually less than those inherent in the approximate method used. These errors will be smallest when the declination plot is straight or nearly so. They will be largest when the plot is sharply curved, i.e., near the times of maximum and minimum declination. Interpolations will show the largest errors for plots which oscillate rapidly (those of Mercury and Venus) and the smallest for the slowly oscillating plots, particularly Mars.

The computer program has been designed to provide rise and set times for any object anywhere in the celestial sphere, i.e., for any object with a declination between −90° (south celestial pole) and +90° (north celestial pole). Since the horizon mask at each station varies irregularly, the program includes a set of tables for each station defining this mask. Table 1 is a sample set for DSS 12. It gives, for each degree of declination, the angular distance to the east and to the west horizon masks. These values were obtained by visual scaling from the stereographic projection shown in Fig. 2. Note that the table gives zero values for declinations between −90° and −49°, indicating that celestial objects at these southern latitudes can never be viewed from Goldstone. Between −48° and +81°, the table shows gradually increasing values (sharply at first, then more slowly), indicating that as an object climbs northward, its viewperiod lengthens. Above +16° to 81°, the values are constant, indicating that in this range, the mechanical antenna limits rather than the topographic horizon determine the bounds of the viewperiod. Finally, from +82° to +90°, the values revert to zero, indicating that the polar mounting of the antenna prevents aiming it this close to the north celestial pole.

The accuracy of this table is limited by the scale of the stereographic projection from which it was derived. We have used one degree as our scale interval, which corresponds to a time interval of 4 minutes. The accuracy of our calculations is thus on the order of ±2 minutes, perhaps more if the actual declination is between scale points. This accuracy can, of course, be improved if declination points were chosen more closely than one degree, and if the declination arcs are measured to a finer degree of accuracy than one degree.

Though this table lookup feature can be used to determine viewperiods for the az–el stations as well as the HA–dec stations, the horizon mask of the former is amenable to a straightforward mathematical solution rather than a table lookup. The declination arc of a celestial object is part of a small circle on the celestial sphere, parallel to the great circle that is its equator. The length of this arc (β) is a function of three angles:

(1) λ, the latitude of the station

(2) δ, the declination of the object

(3) β, the minimum elevation for observation (the DSN uses 6°) and can be found by a trigonometric analysis of the sphere:

$$\cos \beta = \frac{\sin \beta}{\cos \delta \cos \lambda} - \tan \delta \tan \lambda$$

This equation is used to determine rise and set times at the three 64-m Deep Space Stations. Since it is an exact formula, the rise and set times at these stations are not subject to the table lookup errors of the times at the other stations.

Data are input to the program via a card deck. Each card contains:

(1) Date.

(2) Local meridian crossing time.

(3) Declination.

From each card, the program computes the local rise and set times at each station, using either table lookup or trignometric formula as appropriate. These are then converted to GMT using the station longitude. This array is then printed out, along with the date.

This logic is repeated for each data card until the entire deck is read. Thus, the date intervals may be regular or irregular. Also, the cards may be in order, though any order other than strictly chronological would be confusing to a user.

A sample input data deck listing is shown in Table 2, and a sample output listing is shown in Table 3. The first three columns of the output simply repeat the input, for visual verification in situations where there is suspicion of error.

We are continuing to develop this program to increase its speed, economy, timeliness, and accuracy. We are adapting the trajectory program which now produces the declination and local meridian crossing plots, to produce digital output in a form suitable for input to this program. This step will save the time now required to read and interpolate the plots, and reduce the possibility of error in transferring these data to punched cards. When this step is completed, it will be necessary only to enter basic trajectory parameters (position, velocity, and acceleration) and have the computer generate declinations and local meridian crossing times first at specified intervals and then the viewperiods themselves.

Somewhat further downstream, we would like to develop the capability of showing these plots graphically, rather than numerically, on a remote terminal display. It will then be possible to punch a few buttons to identify the time period, station(s), and spacecraft and get an instant visual display of conflicts and overlaps.

Though this program was developed primarily to support the spacecraft tracking responsibilities of the DSN, it appears to have broader uses. Other radio astronomy sensors at other locations around the globe can use it to generate their own viewperiods for planetary and even stellar objects.

Optical astronomy may be able to use the program, after modifying it to include periods of darkness and daytime for similar planning of their observing schedules. Such modifications would be particularly useful, where

(1) The observatory has a non-uniform horizon mask.

(2) Atmospheric conditions prevent adherence to a planned schedule, and instant readjustments must be made.

Table 1. Sample horizon mask for DSS 12

Declination	Rise	Set	Declination	Rise	Set	Declination	Rise	Set
−90	0	0	−30	67	59	30	94	95
−89	0	0	−29	68	60	31	94	95
−88	0	0	−28	70	61	32	94	95
−87	0	0	−27	70	62	33	94	95
−86	0	0	−26	70	64	34	94	95
−85	0	0	−25	72	64	35	94	95
−84	0	0	−24	72	65	36	94	95
−83	0	0	−23	73	66	37	94	95
−82	0	0	−22	75	67	38	94	95
−81	0	0	−21	76	68	39	94	95
−80	0	0	−20	76	70	40	94	95
−79	0	0	−19	76	71	41	94	95
−78	0	0	−18	77	72	42	94	95
−77	0	0	−17	77	72	43	94	95
−76	0	0	−16	77	73	44	94	95
−75	0	0	−15	78	74	45	94	95
−74	0	0	−14	78	75	46	94	95
−73	0	0	−13	80	76	47	94	95
−72	0	0	−12	81	77	48	94	95
−71	0	0	−11	82	79	49	94	95
−70	0	0	−10	82	80	50	94	95
−69	0	0	−9	83	81	51	94	95
−68	0	0	−8	83	82	52	94	95
−67	0	0	−7	84	83	53	94	95
−66	0	0	−6	85	84	54	94	95
−65	0	0	−5	85	84	55	94	95
−64	0	0	−4	86	85	56	94	95
−63	0	0	−3	86	85	57	94	95
−62	0	0	−2	88	86	58	94	95
−61	0	0	−1	89	87	59	94	95
−60	0	0	0	89	90	60	94	95
−59	0	0	1	90	90	61	94	95
−58	0	0	2	90	90	62	94	95
−57	0	0	3	90	90	63	94	95
−56	0	0	4	90	90	64	94	95
−55	0	0	5	90	90	65	94	95
−54	0	0	6	90	90	66	94	95
−53	0	0	7	90	90	67	94	95
−52	0	0	8	90	90	68	94	95
−51	0	0	9	90	90	69	94	95
−50	0	0	10	90	90	70	94	95
−49	0	0	11	90	90	71	94	95
−48	40	7	12	90	90	72	94	95
−47	43	30	13	90	90	73	94	95
−46	44	31	14	90	90	74	94	95
−45	45	32	15	90	90	75	94	95
−44	46	34	16	94	95	76	94	95
−43	48	37	17	94	95	77	94	95
−42	50	40	18	94	95	78	94	95
−41	51	42	19	94	95	79	94	95
−40	52	43	20	94	95	80	94	95
−39	54	45	21	94	95	81	94	95
−38	56	47	22	94	95	82	0	0
−37	58	50	23	94	95	83	0	0
−36	60	52	24	94	95	84	0	0
−35	61	52	25	94	95	85	0	0
−34	63	52	26	94	95	86	0	0
−33	64	53	27	94	95	87	0	0
−32	65	56	28	94	95	88	0	0
−31	66	58	29	94	95	89	0	0
−30	67	59	30	94	95	90	0	0

Table 2. Sample input data deck listing

```
72 227PN-F     90-15
72 327PN-F     43-32
72 426PN-F     20-29
72 525PN-F    231-25
72 625PN-F    212-23
72 725PN-F    195-23
72 824PN-F    182-24
72 923PN-F    168-25
721023PN-F    157-25
721123PN-F    144-24
721222PN-F    132-23
73 121PN-F    119-22
73 220PN-F    107-19
73 320PN-F     91-17
73 421PN-F     73-16
73 520PN-F     57-16
73 620PN-F     34-16
73 719PN-F     11-17
73 819PN-F    229-19
73 918PN-F    206-20
731018PN-F    187-20
731117PN-F    167-19
731220PN-F    151-17
74 120PN-F    138-15
74 220PN-F    123-12
74 320PN-F    108- 9
74 419PN-F     94- 6
74 518PN-F     78- 3
74 618PN-F     60- 1
74 718PN-F     41. 1
74 818PN-F     22. 1
74 917PN-F      1. 0
741016PN-F    220- 1
741115PN-F    220- 1
741215PN-F    182. 0
75 115PN-F    166. 2
75 215PN-F    148. 4
75 315PN-F    131. 6
75 415PN-F    117. 8
75 514PN-F     99.10
75 614PN-F     80.12
75 713PN-F     72.13
75 813PN-F     47.14
75 912PN-F     24.14
751011PN-F      1.13
751110PN-F    221.12
751210PN-F    200.12
76 1 9PN-F    182.12
76 2 9PN-F    163.13
76 3 9PN-F    145.14
76 4 8PN-F    130.15
76 5 8PN-F    112.16
76 6 7PN-F     93.17
76 7 7PN-F     77.18
76 8 7PN-F     58.18
76 9 6PN-F     39.19
7610 5PN-F     17.18
7611 4PN-F    235.17
7612 4PN-F    217.17
77 1 4PN-F    195.17
77 2 4PN-F    176.17
```

Table 3. Sample output listing for Pioneer 10[a]

Limit	Declination	Date	Week	DSS 11		DSS 12		DSS 14		DSS 42		DSS 51		DSS 61		DSS 62	
				Rise	Set	Rise	Set	Rise	Set	Rise	Set	Rise	Set	Rise	Set	Rise	Set
0900	−15	2/27/72	9	1154	2146	1134	2142	1203	2131	1703	0523	0112	1308	0436	1348	0416	1408
0418	−32	3/27/72	13	0832	1524	0744	1548	0833	1537	1129	0109	2030	0826	0106	0758	0046	0806
0200	−29	4/26/72	17	0558	1330	0514	1346	0559	1335	0911	2251	1812	0608	2236	0556	2216	0608
2306	−25	5/25/72	21	0240	1108	0204	1108	0245	1101	0641	1957	1518	0314	1930	0314	1906	0334
2112	−23	6/25/72	25	0038	0922	0006	0922	0043	0915	0455	1755	1324	0120	1724	0128	1708	0148
1930	−23	7/25/72	30	2256	0740	2224	0740	2301	0733	0313	1613	1142	2338	1542	2346	1526	0006
1812	−24	8/24/72	34	2142	0618	2110	0618	2147	0611	0151	1455	1024	2220	1432	2224	1412	2240
1648	−25	9/23/72	38	2022	0450	1946	0450	2027	0443	0023	1339	0900	2056	1312	2056	1248	2116
1542	−25	10/23/72	42	1916	0344	1840	0344	1921	0337	2317	1233	0754	1950	1206	1950	1142	2010
1424	−24	11/23/72	47	1754	0230	1722	0230	1759	0223	2203	1107	0636	1832	1044	1836	1024	1852
1312	−23	12/22/72	51	1638	0122	1606	0122	1643	0115	2055	0955	0524	1720	0924	1728	0908	1748
1154	−22	1/21/73	3	1516	0008	1440	0008	1521	0001	1945	0837	0406	1602	0758	1614	0742	1634
1042	−19	2/20/73	8	1348	2312	1324	2312	1357	2301	1837	0721	0254	1450	0634	1518	0614	1530
0905	−17	3/20/73	12	1204	2144	1144	2140	1217	2129	1701	0537	0118	1314	0450	1350	0430	1406
0718	−16	4/21/73	16	1012	2000	0956	1956	1025	1945	1517	0345	2330	1126	0258	1206	0238	1222
0542	−16	5/20/73	20	0836	1824	0820	1820	0849	1809	1341	0209	2154	0950	0122	1030	0102	1046
0324	−16	6/20/73	25	0618	1606	0602	1602	0631	1551	1123	2351	1936	0732	2304	0812	2244	0828
0106	−17	7/19/73	29	0404	1344	0344	1340	0417	1329	0901	2137	1718	0514	2050	0550	2030	0606
2254	−19	8/19/73	33	0200	1124	0136	1124	0209	1113	0649	1933	1506	0302	1846	0330	1826	0342
2035	−20	9/18/73	37	2350	0902	2318	0902	2355	0851	0427	1715	1248	0044	1628	0104	1612	0120
1842	−20	10/18/73	42	2156	0708	2124	0708	2201	0657	0233	1521	1054	2250	1434	2310	1418	2326
1642	−19	11/17/73	46	1948	0512	1924	0512	1957	0501	0037	1321	0854	2050	1234	2118	1214	2130
1506	−17	12/20/73	50	1804	0344	1744	0340	1817	0329	2301	1137	0718	1914	1050	1950	1030	2006
1348	−15	1/20/74	3	1642	0234	1622	0230	1651	0219	2151	1011	0600	1756	0924	1836	0904	1856
1218	−12	2/20/74	8	1504	0120	1440	0112	1513	0057	2033	0829	0434	1626	0738	1718	0726	1730
1048	−9	3/20/74	12	1330	2358	1302	2358	1331	2339	1911	0647	0308	1456	0552	1556	0548	1608

[a]View periods 1972–1976.

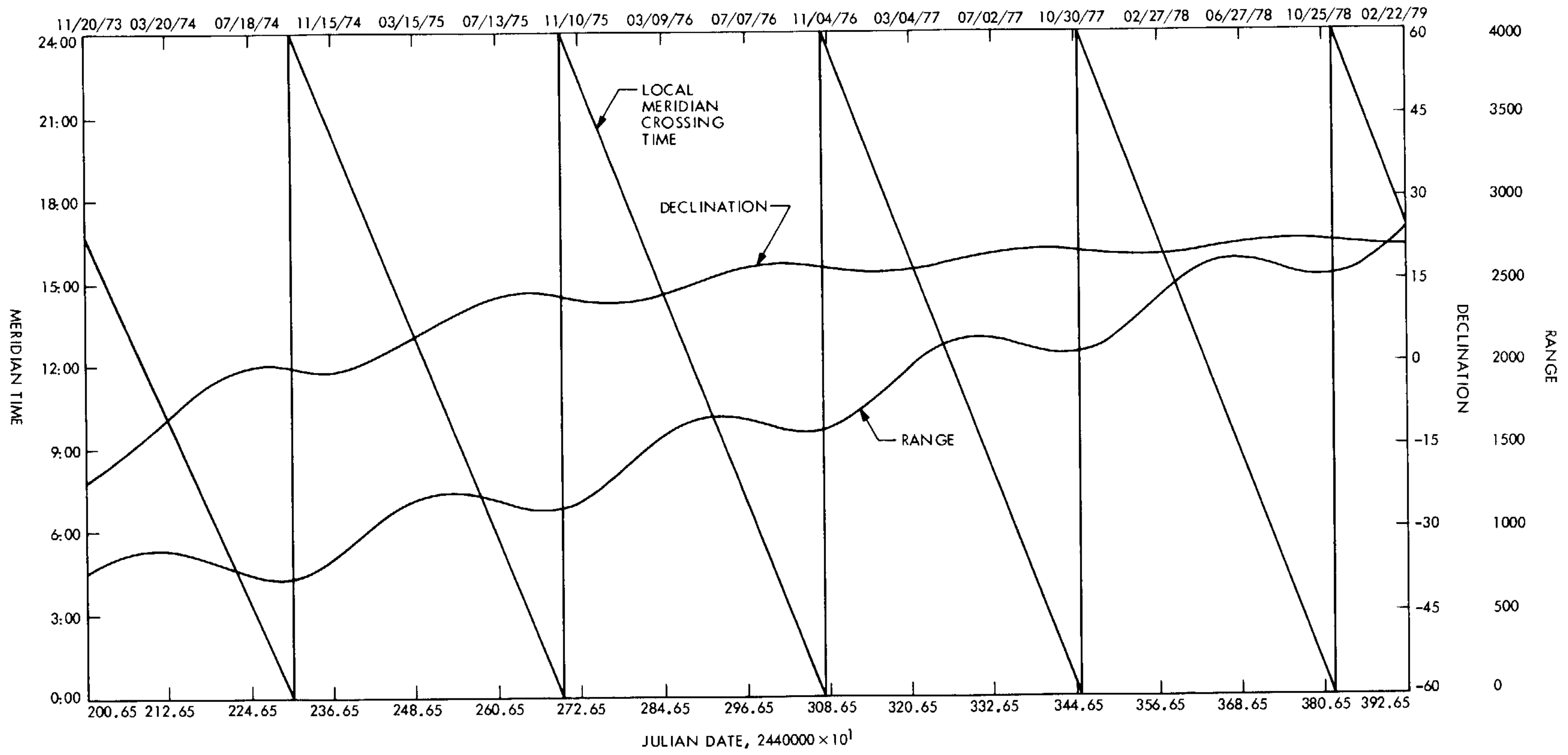

Fig. 1. LMCT–declination–ranging plots

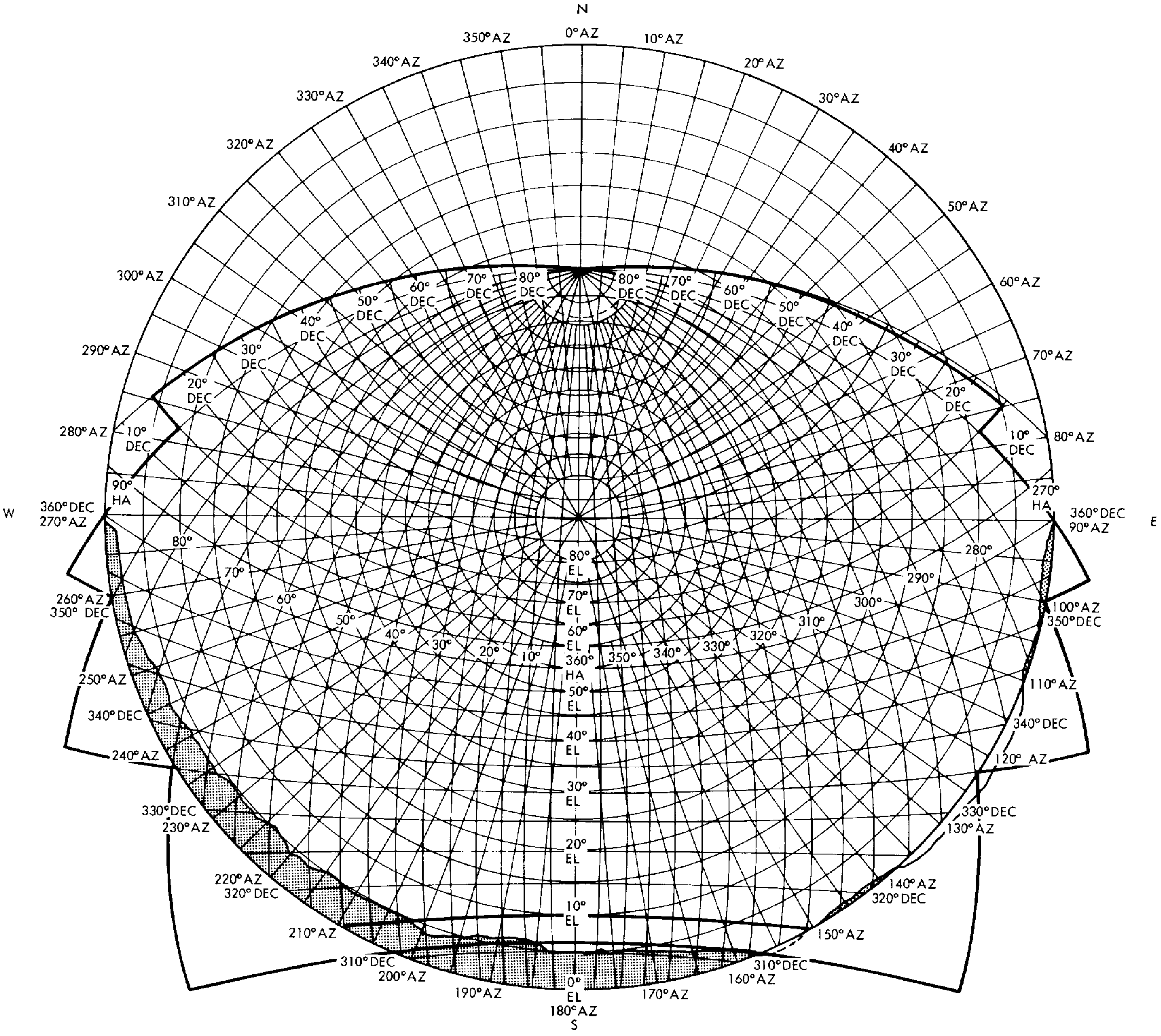

ANTENNA LIMITS					
DEC	PRE	FINAL	HA	PRE	FINAL
DN	082.590	083.560	H1E	267.560	266.840
D2E	015.072	013.958	H2E	270.942	270.050
D3E	352.958	351.176	H3E	276.066	275.008
D4E	334.870	333.850	H4E	290.668	290.076
D2W	015.072	013.958	H1W	095.162	096.012
D3W	352.958	351.176	H2W	088.978	089.486
D4W	334.870	333.850	H3W	083.818	084.702
DS	312.540	311.450	H4W	069.010	069.878

Fig. 2. Sample stereographic projection

The DSN Hydromechanical Equipment Service Program

I. D. Wells and R. M. Smith
DSN Facility Operations Office

Operational experience from the first 64-m-diam antenna (DSS 14) indicated that the increase in quantity of spares required to support the system was becoming prohibitive. With additional antennas becoming operational, it was obvious that an efficient controllable program was necessary to support the DSN. A study was conducted to determine the optimum method for providing repair, test, and calibration service in support of hydromechanical equipment. Several possible sources of service were considered; the governing factors throughout the comparison phase of the study were cost and reliability. Major consideration was given to conservation of skilled personnel, control of service environment, turnaround time, and the adoption of an oil sampling and contamination control program. This article summarizes the results of the study and the present and future status of the program.

I. Introduction

In 1970 a detailed study was performed by I. D. Wells (DSN Antenna Servo-Mechanical Cognizant Operations Engineer) to determine the optimum method for providing repair, test, and calibration services in support of hydromechanical equipment. The study was performed because the advent of the first 64-m-diam antenna (DSS 14) had indicated that the quantity of spares required to support the system would soon become prohibitive (one 64-m antenna contains more hydromechanical subassemblies than the entire net of 26-m antennas). With two more 64-m antennas planned and a possible total of six, it was obvious that an efficient controllable program was necessary to support the DSN.

II. Study Summary

The study considered several possible sources of service: Manufacturers and vendors, a single DSN service facility, and a service facility at each major DSN geographic location. The governing factors throughout the comparison phase of the study were cost and reliability. Major consideration, in support of these two factors, was given to: (1) conservation of skilled personnel, (2) control of service environment, (3) turnaround time, and (4) the adoption of an oil sampling and contamination control program.

Figure 1 portrays the past, present (1971), and projected replacement costs of all items comprising the equipment population. Pumps, motors, and servo-valves are considered as major items because they (1) constitute 87% of the replacement costs, (2) require more servicing actions, (3) are the most expensive to repair, and (4) have the longest turnaround time under present servicing methods. The remaining items (gauges, accumulators, pressure valves, and miscellaneous items) are defined as minor items. If the present method of "servicing on demand" is continued, the useful life of these items will be shortened due to the extended service without periodic overhaul. This will be particularly true of the major items. Even a conservative attrition rate of 2% per annum would mean a replacement cost of approximately $5500 yearly on major items placed in service prior to 1971.

The least biased approach to equipment failure prevention is scheduled servicing using experienced mean time between failures (MTBF) data. Research in this area revealed that data available at the present time would not support such a program with the accuracy that is required. The next most logical approach appeared to be equipment servicing on a periodic recall basis. The expected equipment failure rates were established by (1) using manufacturer's recommended overhaul times (expressed in thousands of hours), (2) assuming the adoption of an oil sampling/contamination control program, and (3) a careful examination of failures noted on various DSN records over 4 years prior to 1971. These rates were then equated into the yearly recycle rates shown on Fig. 2. These rates may be adjusted based on wear rates derived from oil analysis and measured in recalled equipment.

Figure 3 compares the cost differential between servicing by the DSN Maintenance Center (DMC) on a periodic basis and the equivalent service performed by a vendor. The DMC costs, shown in the foreground of the figure, detail the breakdown of costs on an annual basis. The annual manhour requirements to repair the various items of equipment are shown on Fig. 2. The cost of establishing the facility is written off in the first year instead of the usual amortization practice. This accounts for the disparate cost of the first year as contrasted to the succeeding years.

To lend credence to the cost of "servicing on demand" shown prorated to 1971 and also projected through 1972, the records for the period January 1, 1966 through November 15, 1969 were analyzed. The prorated annual cost for the period was $37,000. Assuming that this cost would remain fairly constant through 1972, plus the previously assumed 2% replacement attrition, a conservative annual cost of approximately $45,000 was given to continue the "on demand" type of vendor servicing.

Oil sampling by the DMC would result in a saving of over $17,000 during the 6-year period covered by this study (1970–1976).

The probability of equipment servicing on the complex level was evaluated and deemed as being too costly ($60,000 annually) and would result in inefficient utilization of personnel.

Figure 4 recapitulates the annual savings that can be expected by graphically comparing the costs between periodic servicing performed by a vendor and a hydromechanical facility in the DMC. The light dash line represents the facility costs and the heavy dash line represents the vendor costs, projected through 1976.

III. Results of the Study and Present Status

The study revealed that a central DSN Hydromechanical Service Facility would be the most effective method of rendering support. The recommendations to DSN management were:

(1) Establish periodic recall and service of all hydromechanical equipment, except servo-valves, at a central facility by July 1, 1971.

(2) Establish periodic service of servo-valves by July 1, 1975.

(3) Perform oil sampling and analysis as soon as possible after September 1, 1970 (the date the report was submitted).

The first services of hydromechanical equipment were performed during mid-1972. There was no recall established at this time because budget constraints had limited the growth rate of the facility. By January 1973 enough of the facility had been installed to begin recalling hydromechanical equipment. DSS 12 was the first station to be serviced and during 1973 the remainder of the Deep Space Stations will be included.

The first oil samples were taken at DSS 61 during February 1972. Since then samples have been taken at other stations and subsequently analyzed and reported. This effort has already proven effective by disclosing, in several instances, a buildup of contaminants and in one instance a breakdown of hydraulic oil, in another a failing bearing in a main pump. As a result the stations were given specific instructions to correct the situations.

The fluid analysis capability provides the DSN with a direct method of monitoring the online status of fluid systems, whether they are antenna servo hydraulics, power generator diesel engines or water coolant systems.

The initial efforts at recalling and overhauling hydromechanical subassemblies has revived interest in a phenomenon called "hitching." This is an effect where two apparently identical hydraulic motors in the antenna drive, supposedly working in concert, tend to bind or impede each other because of difference in their respective flow rates. The normal tolerances in the flow rate specifications of new motors apparently allows enough of a difference between two motors to allow "hitching" to occur. All motors that work in pairs in the system will be provided in matched sets to improve the "hitching" problem.

IV. The Future

During the next one to two years, the hydromechanical service facility is to be developed for full coverage of both the 26-m and 64-m antenna hydromechanical service. Because of the similarity of support requirements, the analysis of power generator lubricating oil has been considered as a possible task.

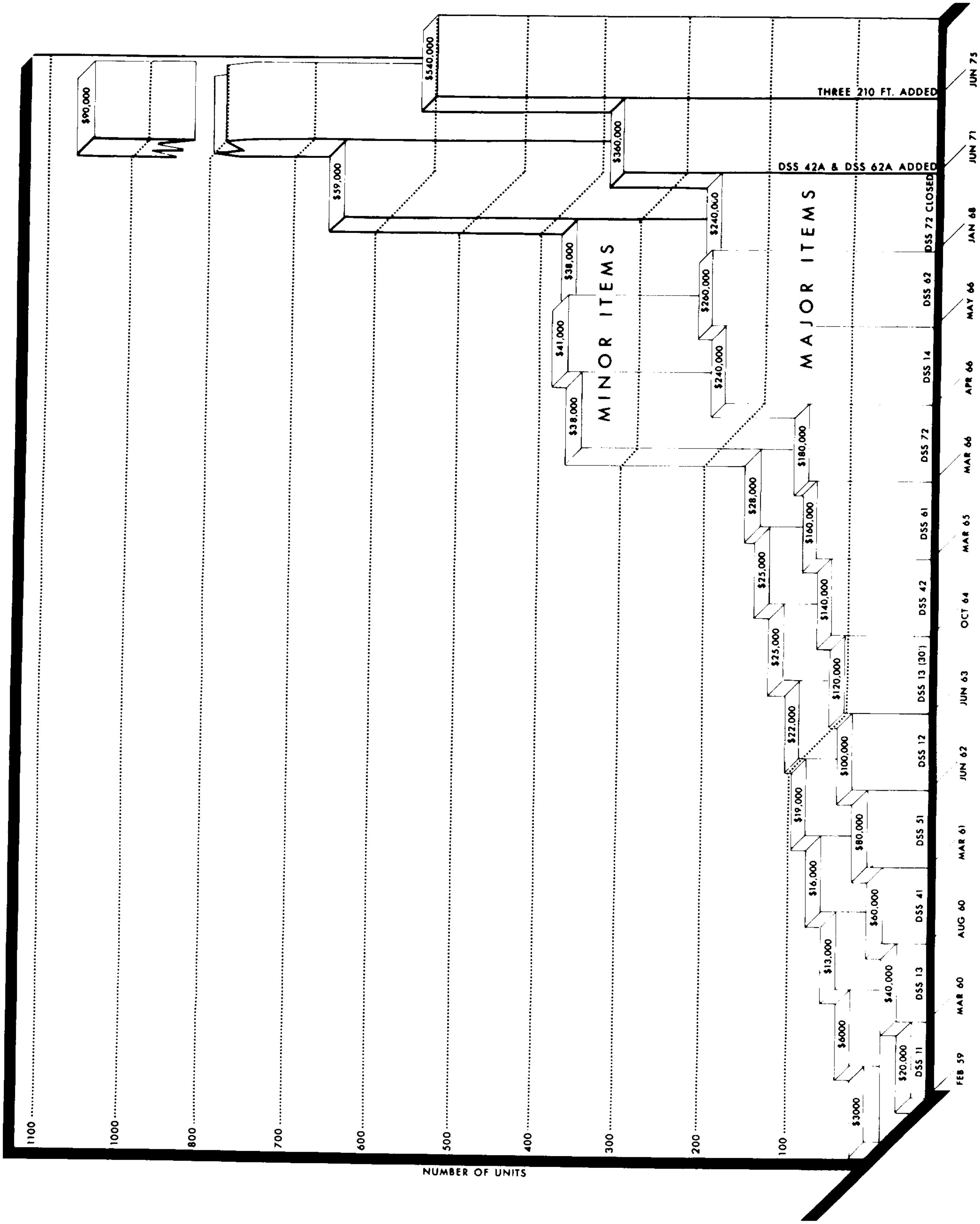

Fig. 1. Equipment population and replacement cost

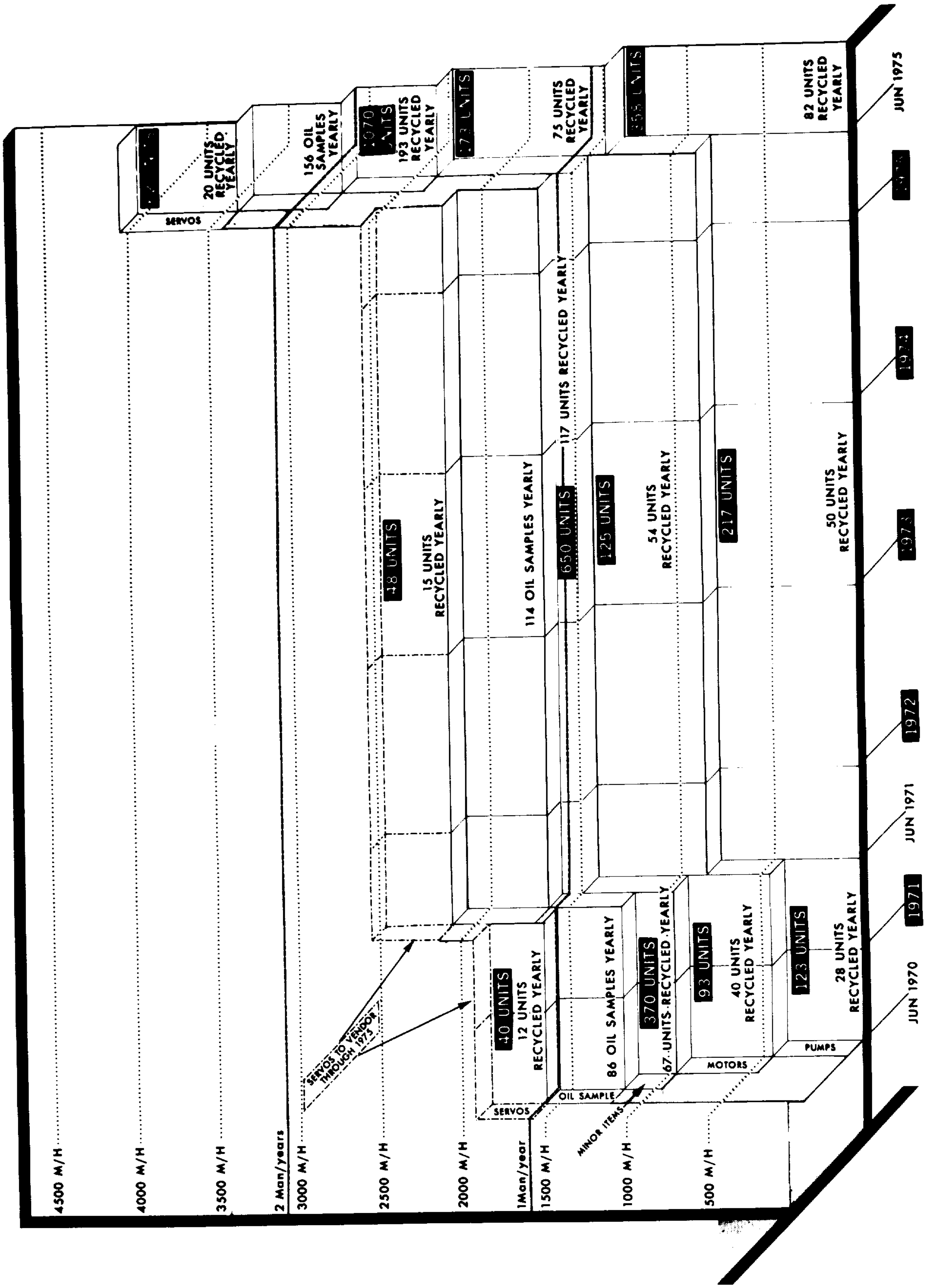

Fig. 2. Equipment recycle rate (yearly) and manhours to repair, including oil sampling

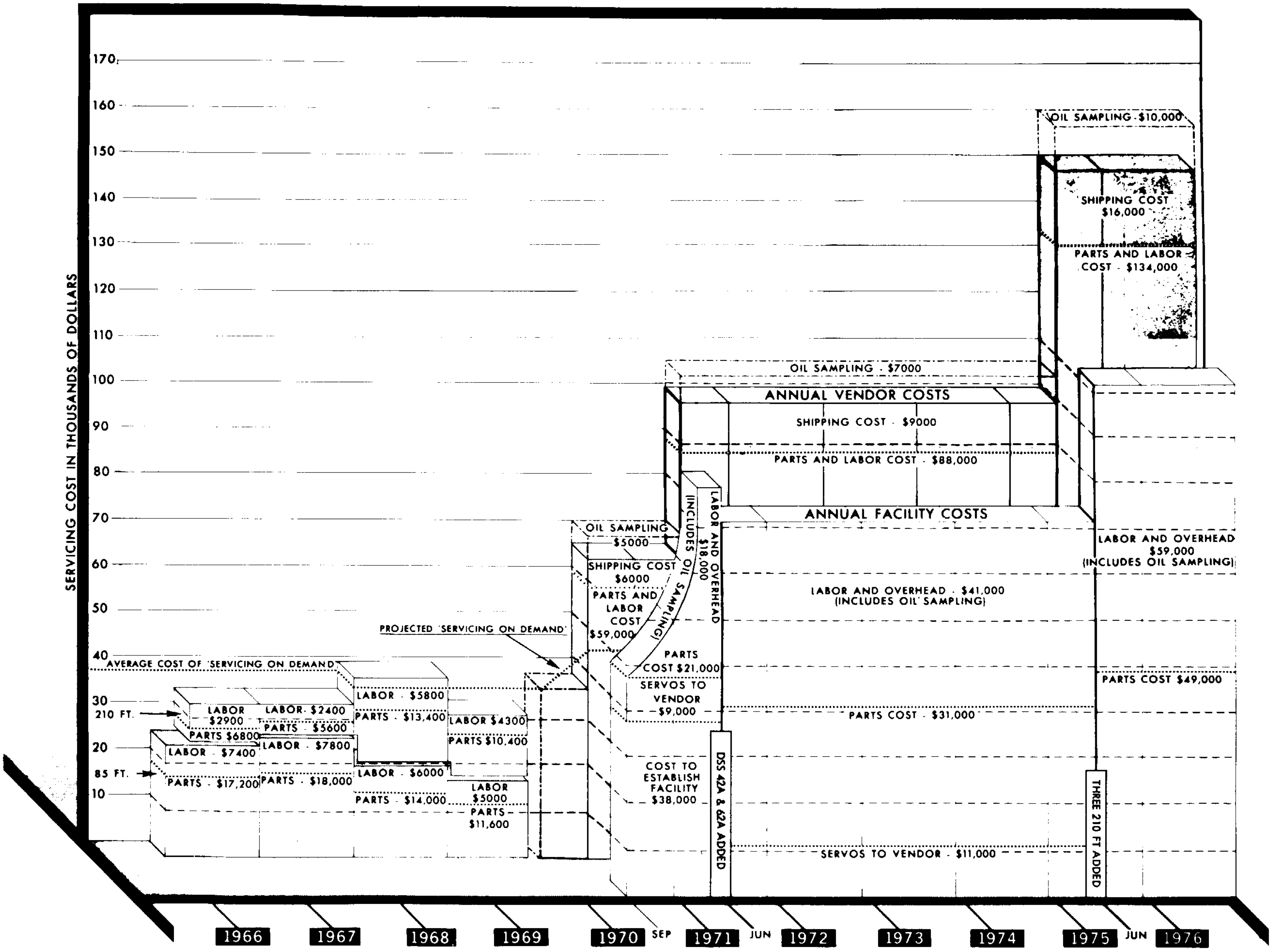

Fig. 3. Comparison of vendor and DMC facility servicing costs

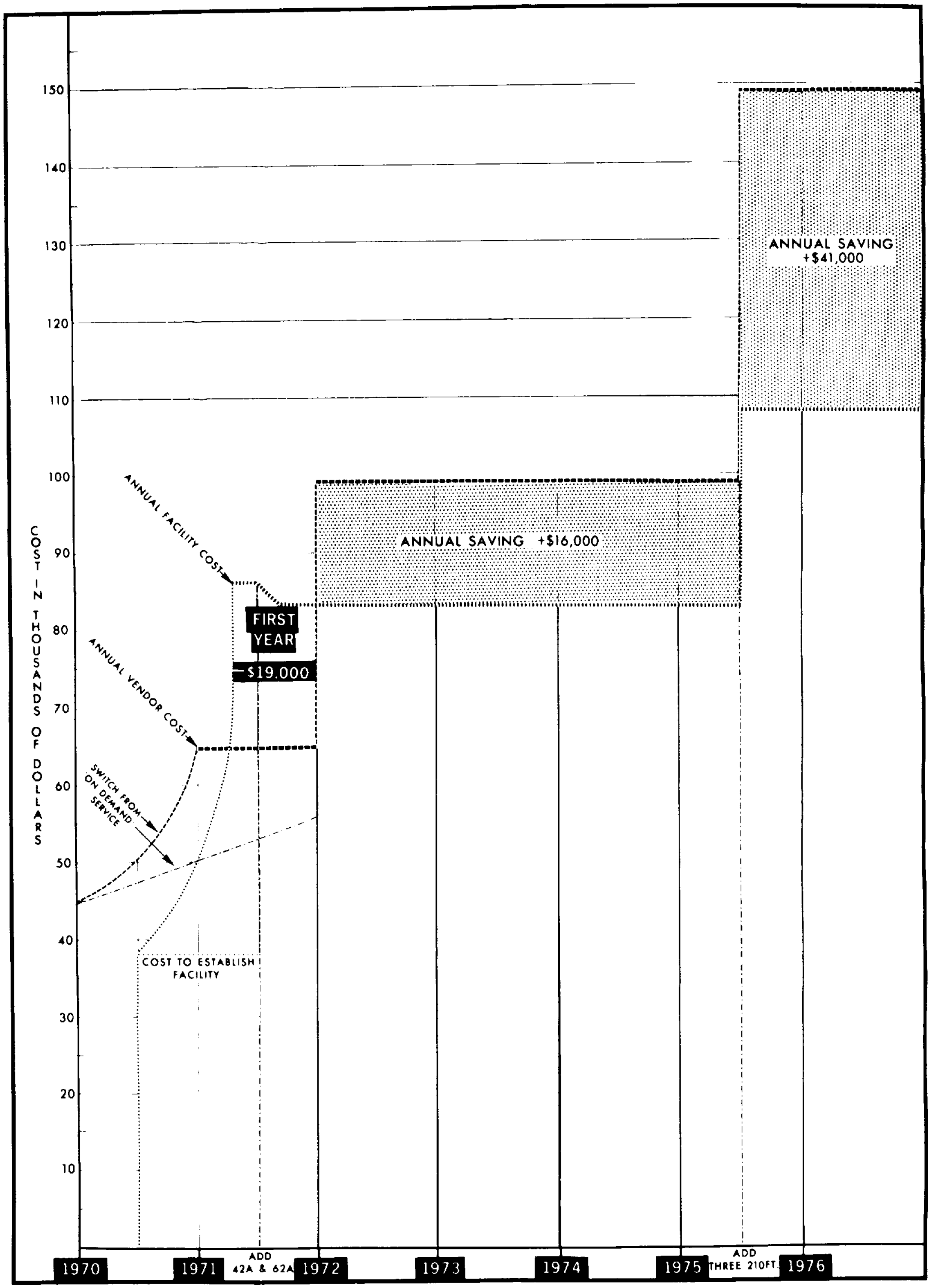

Fig. 4. Recapitulation of annual savings

Simulated Deep Space Station Control Console Study

H. C. Younger
DSN Facility Operations Section

This article describes a study of deep space station operations with the aid of a simulated control console. This is currently being used to evaluate operations at the Echo Deep Space Station. This study is intended to improve performance and reduce operating costs by allowing the station to be operated on a system basis by system engineering personnel. Study approach and current status are presented.

I. Introduction

A study of deep space station control room operations is currently being conducted at DSS 12. The purpose of this study is to improve operational performance of the DSS. Investigations are concentrated in three areas:

1. Centralization of subsystem controls to optimize the operational efficiency and number of operators required
2. Improvement of the man-machine interface
3. Provision of a more rewarding position for operational personnel, thereby reducing attrition and overall operating costs.

The eventual result of this study is intended to be a specification for an improved station monitor and control console. This specification will define the functions required at the station control and monitor console to meet DSN operations requirements for operation of the DSS on a system basis, by system engineers. The operations control specification will be used by DSN development personnel for incorporation into future design.

This represents a significant change in operational philosophy. It should improve station reliability and reduce response time and operating costs, by allowing the station to be operated by a smaller number of more highly qualified personnel on each crew.

II. Implementation

Based on information obtained from station personnel and from cognizant operations engineers, a simulated control console has been assembled and installed at DSS 12. This is shown in Fig. 1. This console is intended to serve as a test bed for further investigations. The console was assembled primarily from spare assemblies and existing surplus hardware, at very low cost, and is definitely not an optimum configuration.

The following criteria governed the development of the simulated console:

(1) No function that required high cost or considerable engineering design would be included

(2) No function that is mission dependent would be included

(3) Only those functions that are necessary for station operations from the completion of countdown through the tracking and post-calibration period would be included

(4) Only those functions that are regularly used during tracking would be included

(5) Within space limitations, all functions would be located for easy access by the operator in a seated position

(6) Functions would be grouped to aid in the reduction of human errors

(7) A local/remote operations switch would be included, to allow operation from either the console or the normal operating position

The basic functions required to implement these criteria are grouped in six areas as listed below and as shown in Fig. 2.

(1) Antenna positioning

(2) Spacecraft communications

(3) Data communications

(4) System monitoring

(5) Analog instrumentation, recording, and TTY

(6) Voice communications

III. Current Activities

The console is operational at DSS 12. It has been the normal control point for DSS 12 operations since mid-January, although "local" control of some subsystems has been used on occasion.

A number of changes in the console have been suggested as a result of the operational experience to date. Some of these have been incorporated, and others will be as soon as feasible. Some desirable changes cannot readily be included in the present console.

A major side benefit of the DSS 12 installation has been the reduction of personnel required in the control room during normal Pioneer cruise mode operations. Ordinarily only one person is required to control the station between acquistion and end of track. This allows intensive training of other station personnel to be conducted at the same time.

IV. Future Activities

During the next few months, continued operation of the console is anticipated. This will release most station personnel for training in operation of the station on a system basis, coinciding with an increase in staffing required for three-shift operation later in the year. Effects of long-term operation using the console will be observed. An analysis of procedures will be made, to determine changes which may be desirable for more efficient operation under the system philosophy. The analysis of station operations functions will be continued, to determine which functions should be remoted and which are amenable to automation. The results of these analyses will be included in the operations control specification.

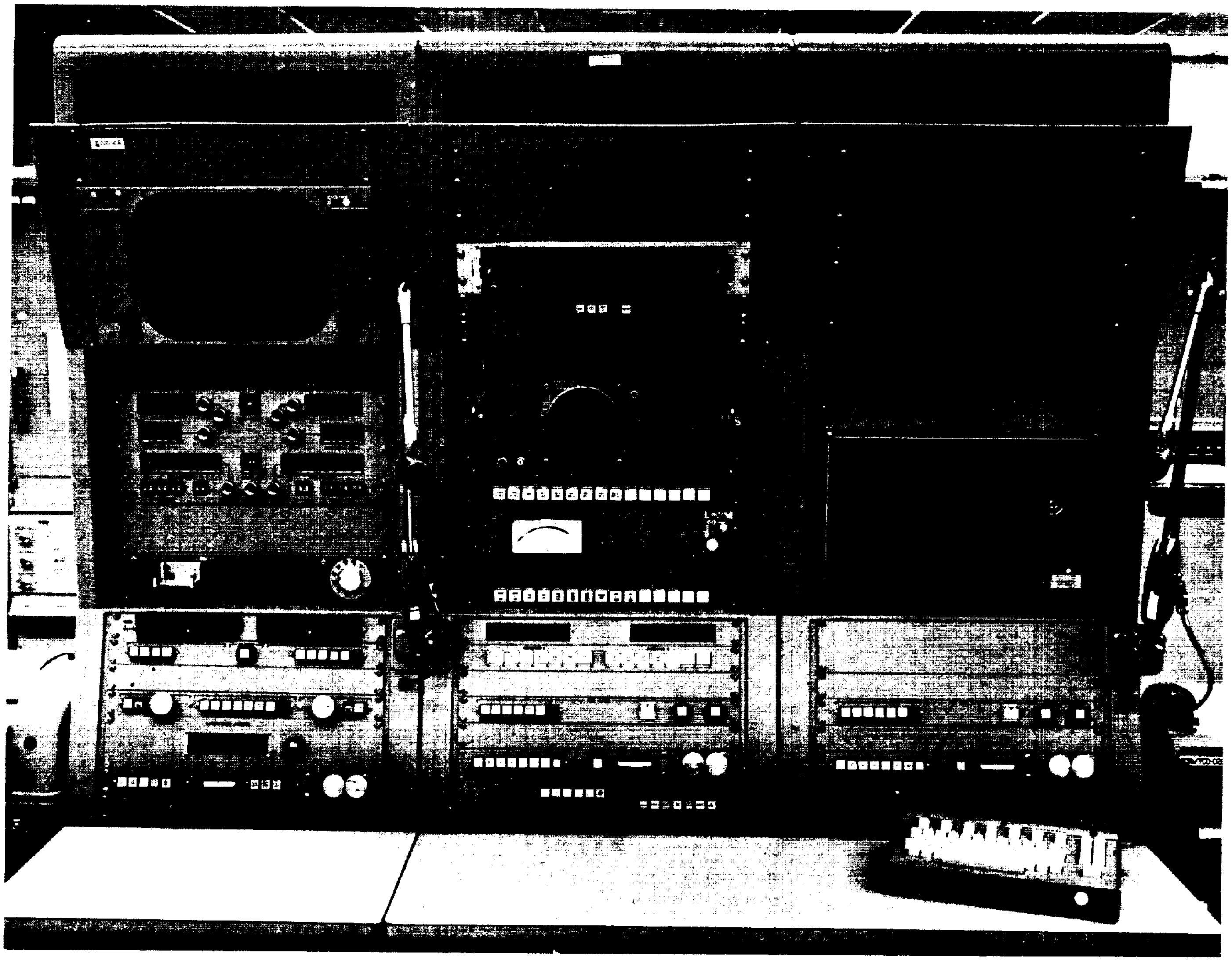

Fig. 1. Simulated DSS control console

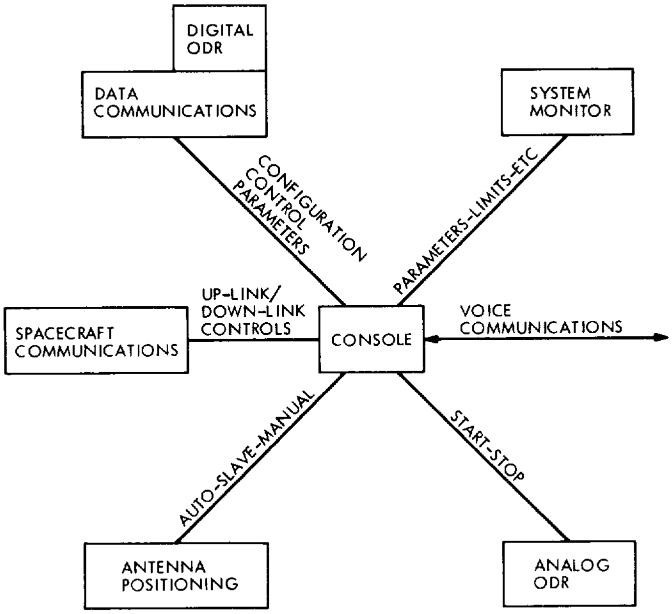

Fig. 2. Station monitor and control function

Design of Shipping Containers for Master Equatorials

H. D. McGinness
DSIF Engineering Section

The delicate nature of the Master Equatorials makes them highly susceptible to damage, especially during transit. A special container has been designed and built for the purpose of shipping assembled Master Equatorials to overseas antenna sites in Australia and Spain. The design features of the shipping containers are outlined in this article, and the advantageous use of motor vehicle shock absorbers is described.

I. Introduction

Because of the delicate nature of the assembled Master Equatorials, a special container was designed and built for the purpose of shipping them from JPL to their overseas antenna sites in Australia and Spain. (Shipment of the units in the disassembled state was considered and rejected because of the expense of constructing adequate reassembly areas near the antennas.) The special ball bearings on both the declination and polar axles are most delicate from a damage point of view; however, the worm gear teeth and the main mirror are also items of concern.

A consideration of possible damage to the ball bearing races caused by acceleration led to the establishment of a 5-g maximum vertical acceleration. Discussions with transportation experts led to the criterion of the ability to sustain a 0.30-m (12-in.) vertical drop of the container without allowing the Master Equatorial to exceed 5-g acceleration. Horizontal accelerations were limited to a value of 1 g.

Prevention of fretting corrosion of the bearing races and balls was also studied. It is recognized that during transit in both airplanes and ground vehicles a steady-state high-frequency excitation may exist for long periods of time. An examination of statistical studies (Ref. 1) suggested that sufficient isolation from such vibration could be obtained by making the natural undamped frequency of the packaged Master Equatorial not more than 3.5 Hz. During shipment both axles of the Master Equatorial are clamped tightly to prevent any oscillation. Both worms are backed away from mesh with their worm gears so as to prevent any possible damage.

II. Description of the Package

The main elements of the package are shown schematically in Fig. 1. The mass of the Master Equatorial is approximately 1820 kg and the suspended base mass is 360 kg. The center of gravity of the total suspended mass of 2180 kg is approximately 0.83 m above the Master Equatorial base and is equidistant from the four springs. The suspended base is a weldment made of rectangular steel tubing $0.103 \times 0.254 \times 0.0048$-m wall thickness. Each spring is actually a cluster of six die springs in parallel. A hydraulic shock absorber is mounted within each spring cluster. Four radius rods connect the suspended weldment to the main base, which is of laminated wood construction with a steel angle border. The Master Equatorial is wrapped in a vapor barrier, and its base is bolted to the suspended base. The springs and shock absorbers are mounted so that they can resist either upward or downward acceleration forces.

The cover is made of aluminum alloy sheet and is bolted to the main base. The overall dimensions of the package are 1.53 × 2.08 × 2.26 m high; its mass, including the Master Equatorial, is approximately 2600 kg. The lower part of the cover can be disassembled and stored within the upper part which when attached to the main base gives an overall height of 1.02 m. Since only one container was built for shipping two Master Equatorials, the reduced height facilitates the return shipment of the container.

The detail design is shown on JPL Drawing 9350283. Figures 2 and 3 show various design details. The container was built by the Boller and Chivens Division of the Perkin Elmer Corporation.

III. Dynamic Analysis

Since the mass of the suspended parts is approximately 85% of the total mass of the package, and because the unsprung base is largely wood, it is believed that a simple one-degree-of-freedom model will approximate the behavior of this system. The elements of this system are shown in Fig. 4.

The differential equation of motion of this system is

$$m\ddot{x} = -kx - b\dot{x} + mg \tag{1}$$

subject to the initial conditions,

$$x_0 = 0, \qquad \dot{x}_0 = \sqrt{2gh} \tag{1a}$$

where

m = mass

k = total spring constant in force per length

b = damper coefficient in force per unit velocity

g = acceleration of gravity

x_0 = initial displacement

$\dot{x}_0$ = initial velocity

$\dot{x}$ = velocity

$\ddot{x}$ = acceleration

and let

$\omega^2 = \dfrac{k}{m}$ be the undamped natural frequency

$\zeta = \dfrac{b}{2m\omega}$ be the damping ratio

$q = \omega\sqrt{1-\zeta^2}$

The solution of Eqs. (1) and (1a) is

$$x = e^{-\zeta\omega t}\left[-\frac{g}{\omega^2}\cos qt + \left(\frac{\sqrt{\frac{2gh}{\omega^2}} - \frac{\zeta g}{\omega^2}}{\sqrt{1-\zeta^2}}\right)\sin qt\right] + \frac{g}{\omega^2} \tag{2}$$

The first three time derivatives of Eq. (2) are, respectively,

$$\dot{x} = e^{-\zeta\omega t}\left[\sqrt{2gh}\cos qt + \left(\frac{\frac{g}{\omega} - \sqrt{2gh}\,\zeta}{\sqrt{1-\zeta^2}}\right)\sin qt\right] \tag{3}$$

$$\ddot{x} = e^{-\zeta\omega t}\Bigg[(g - 2\zeta\omega\sqrt{2gh})\cos qt + \left(\frac{\sqrt{2gh}\,\omega(2\zeta^2-1) - \zeta g}{\sqrt{1-\zeta^2}}\right)\sin qt\Bigg] \tag{4}$$

$$\frac{d\ddot{x}}{dt} = e^{-\zeta\omega t}\Bigg\{[-2\omega\zeta g + \omega^2\sqrt{2gh}(4\zeta^2-1)]\cos qt + \left[\frac{\zeta\omega^2\sqrt{2gh}(3-4\zeta^2) + \omega g(2\zeta^2-1)}{\sqrt{1-\zeta^2}}\right]\sin qt\Bigg\} \tag{5}$$

For the problem at hand, the important quantities are the maximum absolute values of $\ddot{x}$ and x, because they determine, respectively, the maximum force on the suspended mass, and the necessary clearance between the suspended mass and the container. The maximum displacement $x_{\max}$ can be found by setting the bracketed term of Eq. (3) equal to zero, determining qt, and substituting its value into Eq. (2). The maximum value of $\ddot{x}$ occurs at $t = 0$ if Eq. (5) is not negative for $t = 0$. Otherwise the maximum value of $\ddot{x}$ is found by setting the braced term of Eq. (5) equal to zero, determining qt, and substituting its value into Eq. (4). These results are

$$x_{\max} = e^{-\zeta\omega t}\left[\frac{1}{\omega^2}\sqrt{g\,(2h\omega^2 + g - 2\sqrt{2gh}\,\omega\zeta}\,\right] + \frac{g}{\omega^2} \qquad (6)$$

where

$$\zeta\omega t = \frac{\zeta}{\sqrt{1-\zeta^2}}\left[\arctan\frac{\sqrt{1-\zeta^2}\sqrt{2gh}}{\sqrt{2gh}\,\zeta - \frac{g}{\omega}}\right] \qquad (6a)$$

and

$$\ddot{x}_{\max} = g - 2\zeta\omega\sqrt{2gh} \qquad (7)$$

when

$$[-2\omega\zeta g + \omega^2\sqrt{2gh}\,(4\zeta^2 - 1)] \geqq 0$$

$$\ddot{x}_{\max} = -e^{-\zeta\omega t}\sqrt{2\omega^2 gh + g^2 - 2\omega g\zeta\sqrt{2gh}} \qquad (7a)$$

where

$$\zeta\omega t =$$

$$\frac{\zeta}{\sqrt{1-\zeta^2}}\left\{\arctan\frac{\sqrt{1-\zeta^2}\,[\omega^2\sqrt{2gh}\,(1-4\zeta^2)+2\omega g\zeta]}{-\omega g\,(1-2\zeta^2)+\omega^2\sqrt{2gh}\,(3\zeta-4\zeta^3)}\right\} \qquad (7b)$$

when

$$[-2\omega\zeta g + \omega^2\sqrt{2gh}\,(4\zeta^2 - 1)] < 0$$

Thus, the important quantities $x_{\max}$ and $\ddot{x}_{max}$ are given in terms of the parameters stipulated in the design specification and the damping ratio.

Displacements and accelerations were computed using the following parametric values:

$\omega = 19.4$ radians per second

$h = 0.305$ meter

$g = 9.8$ meters per second squared

Figure 5 gives the displacement ratio x/x_{ST}, where x_{ST} is the static displacement, and the acceleration in g as a function of time for three different damping ratios. Figure 6 shows the maximum displacement ratio and the maximum acceleration as a function of the damping ratio. Although the original specification of 5 g was met with zero damping, the corresponding displacement was difficult to accomplish in the design. As Fig. 6 demonstrates, a damping ratio of 0.40 reduces the maximum displacement ratio from 6 to 3.5, and reduces the acceleration from 5 to 3.6 g.

IV. Selection of the Shock Absorbers

The preceding equations are based upon a viscous damper; that is, one whose resisting force is proportional to the velocity. Commercial hydraulic shock absorbers are likely to vary considerably from this characteristic, which is probably why manufacturers are reluctant to specify a force per unit velocity. Reference 2 states that dampers involving orifice flow have forces more nearly proportional to the square of the velocity.

Two different motor vehicle shock absorbers were tested. The more expensive one had entirely different characteristics in compression and extension, whereas the other one, which cost \$6.00, appeared to be the same in the two modes. The shock absorber was clamped in a vise and moved by exerting a constant force through a spring balance scale. The time intervals to move various distances under a constant force were recorded. The damper coefficient b was computed as the product of force and time divided by distance. Different values of force were used without affecting the computed value of b. However, all forces were small in comparison to what would occur at the end of the specified drop for the container, this latter force being 100 to 200 times the test forces. As first tested, the shock absorber had b values of 1750 to 2600 newtons per meter per second. The hydraulic fluid was drained and replaced with SAE No. 30 engine oil, with the result that the b value increased to 8400 and 10,500 newtons per meter per second, respectively, for compression and extension. Considering that there are four absorbers in parallel, the damper ratio was computed to be 0.40 in compression. These are the units which are presently installed in the shipping container.

The addition of four very inexpensive commercial parts has reduced considerably both the maximum acceleration and displacement as calculated by the foregoing analysis. Drop tests were not made on the shipping container, but it has been used successfully in transporting the Master Equatorials to their overseas sites, since tests on the installed instruments have verified that there has been no damage incurred.

References

1. *Shock and Vibration Handbook,* Vol. 3, Chap. 47, Edited by C. M. Harris and C. E. Crede, McGraw-Hill Book Co., Inc., New York, 1961.
2. *Shock and Vibration Handbook,* Vol. 2, p. 31-12, edited by C. M. Harris and C. E. Crede, McGraw-Hill Book Co., Inc., New York, 1961.

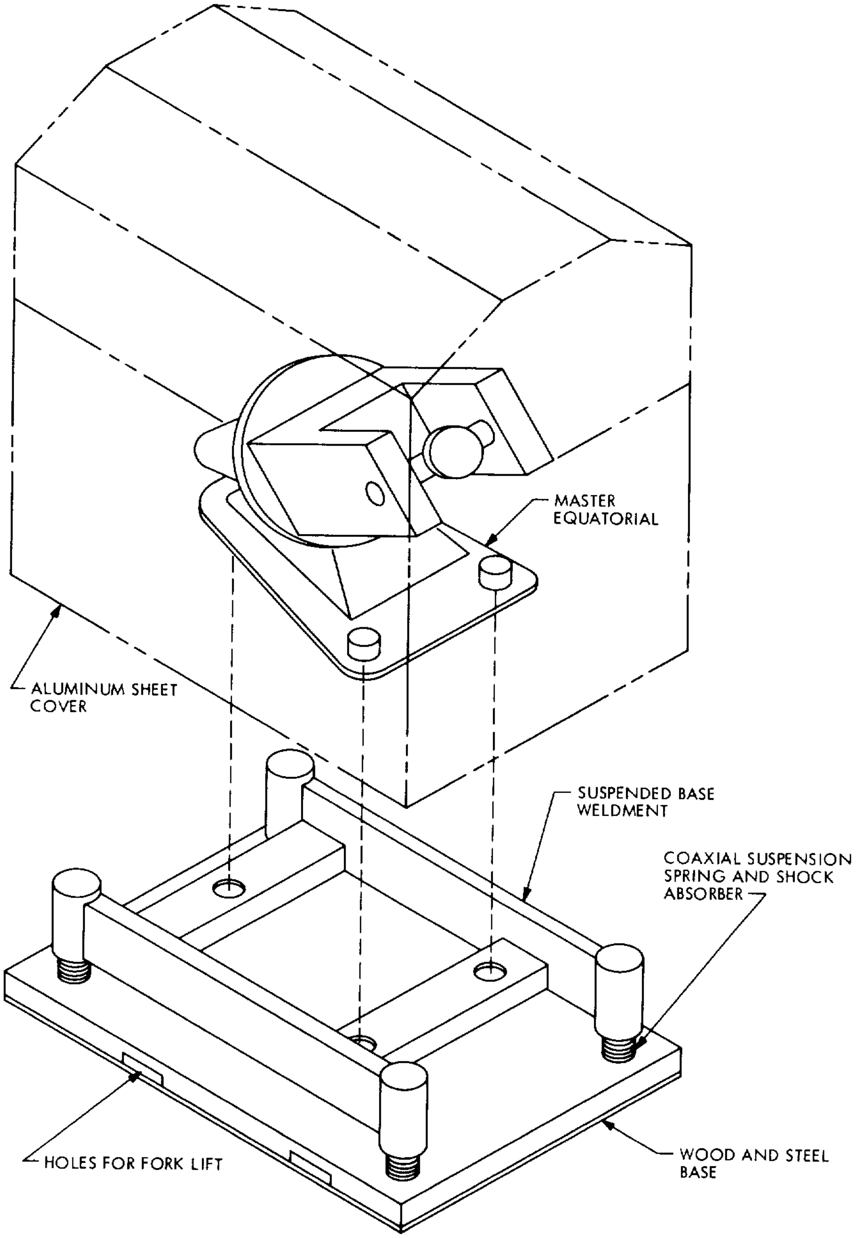

Fig. 1. Exploded view of packaged Master Equatorial

Fig. 2. Master Equatorial being placed on container base

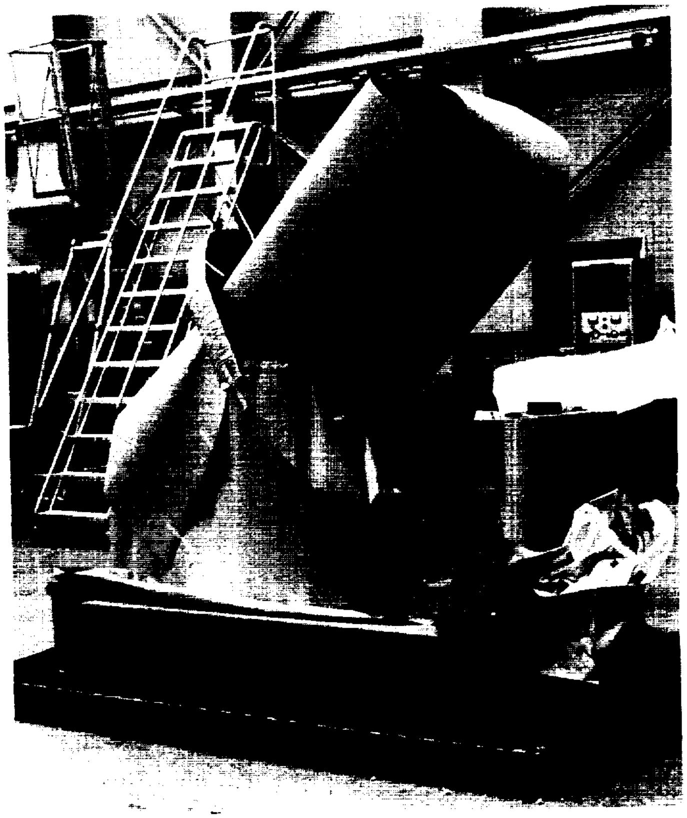

Fig. 3. Preparation of Master Equatorial

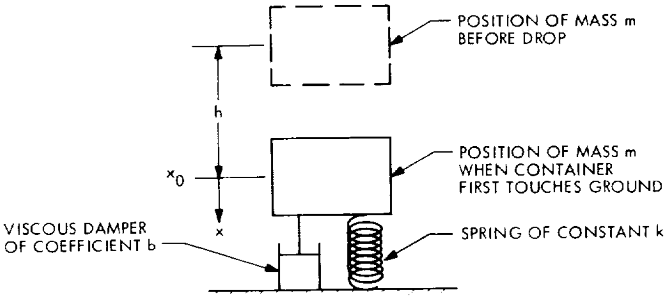

Fig. 4. Dynamic model

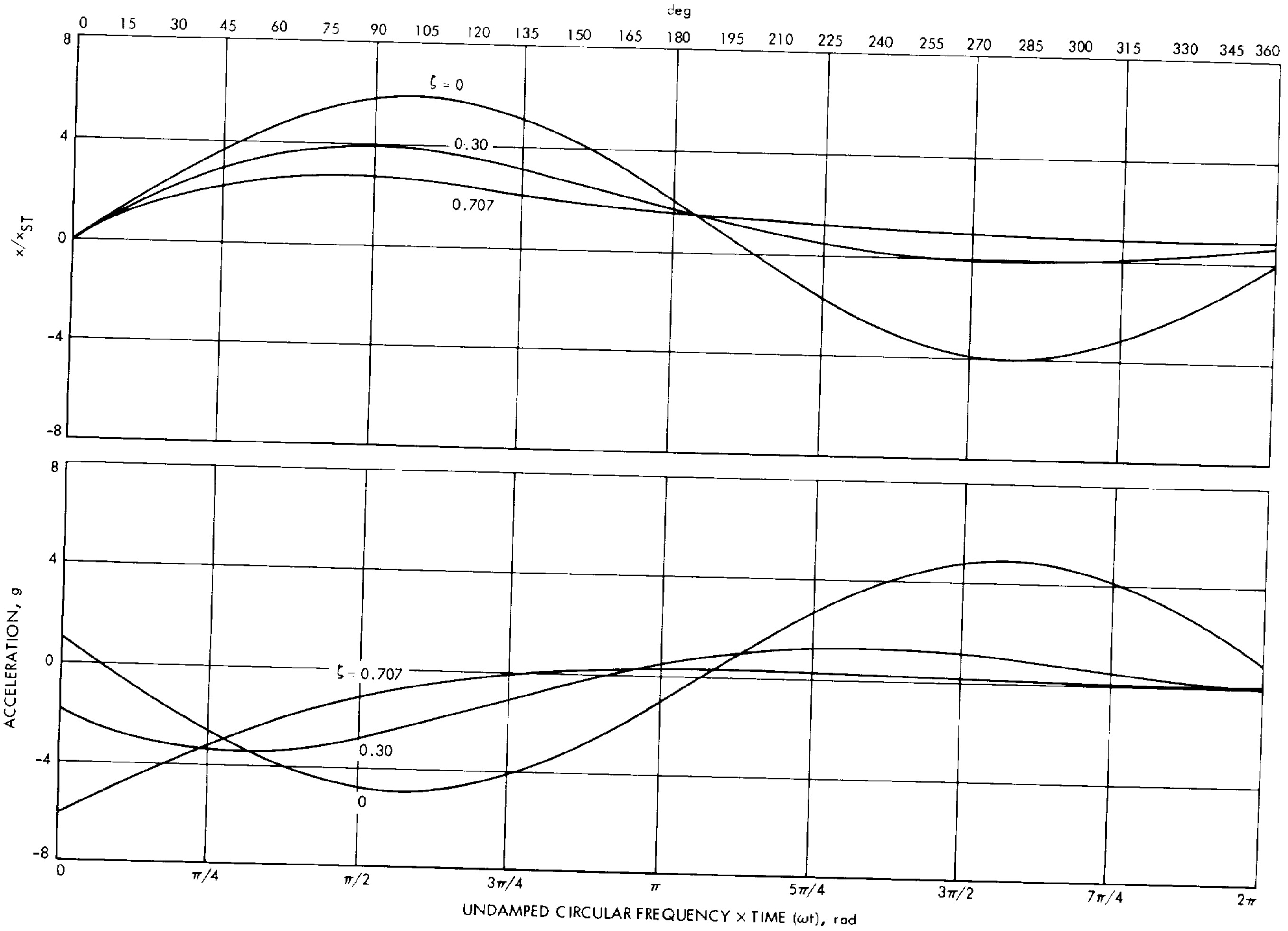

Fig. 5. Displacement and acceleration versus angular displacement

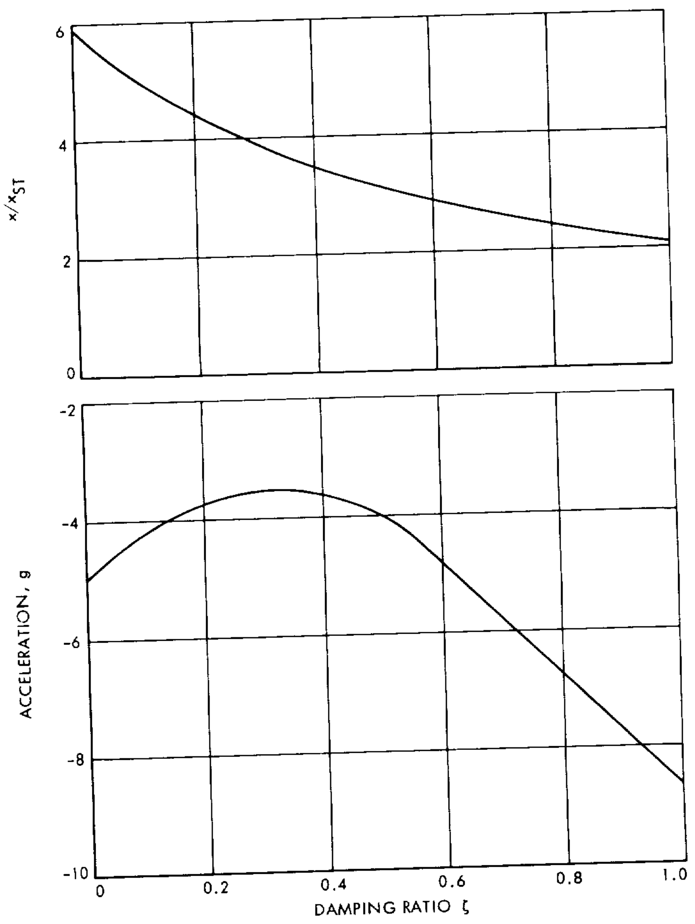

Fig. 6. Maximum acceleration and displacement versus damping ratio

Bibliography

Anderson, J. D., *Determination of the Masses of the Moon and Venus and the Astronomical Unit from Radio Tracking Data of the Mariner II Spacecraft.* Technical Report 32-816. Jet Propulsion Laboratory, Pasadena, Calif., July 1, 1967.

Anderson, J. D., et al., "The Radius of Venus as Determined by Planetary Radar and Mariner V Radio Tracking Data," *J. Atmos. Sci.*, pp. 1171–1174, Sept. 25, 1968.

Berman, A. L., *Tracking System Data Analysis Report, Ranger VII Final Report*, Technical Report 32-719, Jet Propulsion Laboratory, Pasadena, Calif., June 1, 1965.

Berman, A. L., *ABTRAJ–On-Site Tracking Prediction Program for Planetary Spacecraft*, Technical Memorandum 33-391. Jet Propulsion Laboratory, Pasadena, Calif., Aug. 15, 1968.

Cain, D. L., and Hamilton, T. W., *Determination of Tracking Station Locations by Doppler and Range Measurements to an Earth Satellite*, Technical Report 32-534. Jet Propulsion Laboratory, Pasadena, Calif., Feb. 1, 1964.

Carey, C. N., and Sjogren, W. L., "Gravitational Inconsistency, in the Lunar Theory: Confirmation by Radio Tracking," *Science*, Vol. 160, pp. 875, 876, Apr.–June 1968.

Curkendall, D. W., and Stephenson, R. R., "Earthbased Tracking and Orbit Determination–Backbone of the Planetary Navigation System," *Astronaut. Aeronaut.*, Vol. 7, May 1970.

Curkendall, D. W., "Planetary Navigation: The New Challenges," *Astronaut. Aeronaut.*, Vol. 7, May 1970.

Efron, L., and Solloway, C. B., *Proceedings of the Conference on Scientific Applications of Radio and Radar Tracking in the Space Program*, Technical Report 32-1475. Jet Propulsion Laboratory, Pasadena, Calif., July 1970.

Flanagan, F. M., et al., *Deep Space Network Support of the Manned Space Flight Network for Apollo: 1962–1968*, Technical Memorandum 33-452, Vol. I. Jet Propulsion Laboratory, Pasadena, Calif., July 1970.

Flanagan, F. M., et al., *Deep Space Network Support of the Manned Space Flight Network for Apollo: 1969–1970*, Technical Memorandum 33-452, Vol. II. Jet Propulsion Laboratory, Pasadena, Calif., May 1, 1971.

Fjeldbo, G., and Eshleman, V. R., "Radio Occultation Measurements and Interpretations," in *The Atmospheres of Venus and Mars*, p. 225. Gordon and Breach, Science Publishers, Inc., New York, N.Y.

Georgevick, R. M., "Mathematical Model of the Solar Radiation Force and Torques Acting on the Components of a Spacecraft," Technical Memorandum 33-494. Jet Propulsion Laboratory, Pasadena, Calif., Oct. 1, 1971.

Goldstein, R. M., "Radar Time-of-Flight Measurements to Venus," *Astron. J.*, Vol. 73, No. 9, Aug. 1968.

Goldstein, R. M., and Rumsey, H., Jr., "A Radar Snapshot of Venus," *Science*, Vol. 169, Sept. 1970.

Bibliography (contd)

Gordon, H. J., et al., *The Mariner 6 and 7 Flight Paths and Their Determination From Tracking Data,* Technical Memorandum 33-469. Jet Propulsion Laboratory, Pasadena, Calif., Dec. 1, 1970.

Hamilton, T. W., et al., *The Ranger IV Flight Path and Its Determination From Tracking Data,* Technical Report 32-345. Jet Propulsion Laboratory, Pasadena, Calif., Sept. 15, 1962.

Kellermann, K. I., et al., "High Resolution Observations of Compact Radio Sources at 13 Centimeters," *Astrophys. J.*, Vol. 161, pp. 803–809, Sept. 1970.

Kliore, A., "Radio Occultation Measurements of the Atmospheres of Mars and Venus," in *The Atmospheres of Venus and Mars*, p. 205. Gordon and Breach Science Publishers, Inc., New York, N. Y.

Labrum, R. G., Wong, S. K., and Reynolds, G. W., *The Surveyor V, VI, and VII Flight Paths and Their Determination from Tracking Data,* Technical Report 32-1302. Jet Propulsion Laboratory, Pasadena, Calif., Dec. 1, 1968.

Lieske, J. H., and Null, G. W., "Icarus and the Determination of Astronomical Constants," *Astron. J.*, Vol. 74, No. 2, Mar. 1969.

Lorell, J., and Sjogren, W. L., *Lunar Orbiter Data Analysis,* Technical Report 32-1220. Jet Propulsion Laboratory, Pasadena, Calif., Nov. 15, 1967.

Lorell, J., *Lunar Orbiter Gravity Analysis,* Technical Report 32-1387. Jet Propulsion Laboratory, Pasadena, Calif., June 15, 1969.

Lorell, J., et al., "Celestial Mechanics Experiment for *Mariner,*" Icarus, Vol. 12, Jan. 1970.

McNeal, C. E., *Ranger V Tracking Systems Data Analysis Final Report,* Technical Report 32-702. Jet Propulsion Laboratory, Pasadena, Calif., Apr. 15, 1965.

Melbourne, W. G., et al., *Constants and Related Information for Astrodynamical Calculations,* Technical Report 32-1306. Jet Propulsion Laboratory, Pasadena, Calif., July 15, 1968.

Melbourne, W. G., "Planetary Ephemerides," *Astronaut. Aeronaut.*, Vol. 7, May 1970.

Miller, L., et al., *The Atlas–Centaur VI Flight Path and Its Determination from Tracking Data,* Technical Report 32-911. Jet Propulsion Laboratory, Pasadena, Calif., Apr. 15, 1966.

Moyer, T. D., "Mathematical Formulation of the Double-Precision Orbit Determination Program (DPODP)," Technical Report 32-1527, Jet Propulsion Laboratory, Pasadena, Calif., May 17, 1971.

Mulhall, B. D., et al., *Tracking System Analytic Calibration Activities for the Mariner Mars 1969 Mission,* Technical Report 32-1499. Jet Propulsion Laboratory, Pasadena, Calif., Nov. 15, 1970.

Mulholland, J. D., and Sjogren, W. L., *Lunar Orbiter Ranging Data,* Technical Report 32-1087. Jet Propulsion Laboratory, Pasadena, Calif., Jan. 6, 1967.

Bibliography (contd)

Mulholland, J. D., *Proceedings of the Symposium on Observation, Analysis, and Space Research Applications of the Lunar Motion,* Technical Report 32-1386. Jet Propulsion Laboratory, Pasadena, Calif., Apr. 1969.

Muller, P. M., and Sjogren, W. L., *Consistency of Lunar Orbiter Residuals With Trajectory and Local Gravity Effects,* Technical Report 32-1307. Jet Propulsion Laboratory, Pasadena, Calif., Sept. 1, 1968.

Muller, P. M., and Sjogren, W. L., *Lunar Mass Concentrations,* Technical Report 32-1339. Jet Propulsion Laboratory, Pasadena, Calif., Aug. 16, 1968.

Null, G. W., Gordon, H. J., and Tito, D. A., *Mariner IV Flight Path and Its Determination From Tracking Data,* Technical Report 32-1108. Jet Propulsion Laboratory, Pasadena, Calif., Aug. 1, 1967.

O'Neil, W. J., et al., *The Surveyor III and Surveyor IV Flight Paths and Their Determination From Tracking Data,* Technical Report 32-1292. Jet Propulsion Laboratory, Pasadena, Calif., Aug. 15, 1968.

Pease, G. E., et al., *The Mariner V Flight Path and Its Determination From Tracking Data,* Technical Report 32-1363. Jet Propulsion Laboratory, Pasadena, Calif., July 1, 1969.

Renzetti, N. A., *Tracking and Data Acquisition for Ranger Missions I–V,* Technical Memorandum 33-174. Jet Propulsion Laboratory, Pasadena, Calif., July 1, 1964.

Renzetti, N. A., *Tracking and Data Acquisition for Ranger Missions VI–IX,* Technical Memorandum 33-275. Jet Propulsion Laboratory, Pasadena, Calif., Sept. 15, 1966.

Renzetti, N. A., *Tracking and Data Acquisition Support for the Mariner Venus 1962 Mission,* Technical Memorandum 33-212. Jet Propulsion Laboratory, Pasadena, Calif., July 1, 1965.

Renzetti, N. A., *Tracking and Data Acquisition Report, Mariner Mars 1964 Mission: Near-Earth Trajectory Phase,* Technical Memorandum 33-239, Vol. I. Jet Propulsion Laboratory, Pasadena, Calif., Jan. 1, 1965.

Renzetti, N. A., *Tracking and Data Acquisition Report, Mariner Mars 1964 Mission: Cruise to Post-Encounter Phase,* Technical Memorandum 33-239, Vol. II. Jet Propulsion Laboratory, Pasadena, Calif., Oct. 1, 1967.

Renzetti, N. A., *Tracking and Data Acquisition Report, Mariner Mars 1964 Mission: Extended Mission,* Technical Memorandum 33-239, Vol. III. Jet Propulsion Laboratory, Pasadena, Calif., Dec. 1, 1968.

Renzetti, N. A., *Tracking and Data System Support for Surveyor: Missions I and II,* Technical Memorandum 33-301, Vol. I. Jet Propulsion Laboratory, Pasadena, Calif., July 15, 1969.

Renzetti, N. A., *Tracking and Data System Support for Surveyor: Missions III and IV,* Technical Memorandum 33-301, Vol. II. Jet Propulsion Laboratory, Pasadena, Calif., Sept. 1, 1969.

Renzetti, N. A., *Tracking and Data System Support for Surveyor: Mission V,* Technical Memorandum 33-301, Vol. III. Jet Propulsion Laboratory, Pasadena, Calif., Dec. 1, 1969.

Bibliography (contd)

Renzetti, N. A., *Tracking and Data System Support for Surveyor: Mission VI*, Technical Memorandum 33-301, Vol. IV. Jet Propulsion Laboratory, Pasadena, Calif., Dec. 1, 1969.

Renzetti, N. A., *Tracking and Data System Support for Surveyor: Mission VII*, Technical Memorandum 33-301, Vol. V. Jet Propulsion Laboratory, Pasadena, Calif., Dec. 1, 1969.

Renzetti, N. A., *Tracking and Data System Support for the Mariner Venus 67 Mission: Planning Phase Through Midcourse Maneuver*, Technical Memorandum 33-385, Vol. I. Jet Propulsion Laboratory, Pasadena, Calif., Sept. 1, 1969.

Renzetti, N. A., *Tracking and Data System Support for the Mariner Venus 67 Mission: Midcourse Maneuver Through End of Mission*, Technical Memorandum 33-385, Vol. II. Jet Propulsion Laboratory, Pasadena, Calif., Sept. 1, 1969.

Renzetti, N. A., *Tracking and Data System Support for the Pioneer Project. Pioneer VI. Prelaunch to End of Nominal Mission*, Technical Memorandum 33-426, Vol. I. Jet Propulsion Laboratory, Pasadena, Calif., Feb. 1, 1970.

Renzetti, N. A., *Tracking and Data System Support for the Pioneer Project. Pioneer VII. Prelaunch to End of Nominal Mission*, Technical Memorandum 33-426, Vol. II. Jet Propulsion Laboratory, Pasadena, Calif., Apr. 15, 1970.

Renzetti, N. A., *Tracking and Data System Support for the Pioneer Project. Pioneer VIII. Prelaunch Through May 1968*, Technical Memorandum 33-426, Vol. III. Jet Propulsion Laboratory, Pasadena, Calif., July 15, 1970.

Renzetti, N. A., *Tracking and Data System Support for the Pioneer Project. Pioneer IX. Prelaunch Through June 1969*, Technical Memorandum 33-426, Vol. IV. Jet Propulsion Laboratory, Pasadena, Calif., Nov. 15, 1970.

Renzetti, N. A., *Tracking and Data System Support for the Pioneer Project. Pioneer VI. Extended Mission: July 1, 1966–July 1, 1969*, Technical Memorandum 33-426, Vol. V. Jet Propulsion Laboratory, Pasadena, Calif., Feb. 1, 1971.

Renzetti, N. A., *Tracking and Data System Support for the Pioneer Project. Pioneer VII. Extended Mission: February 24, 1967–July 1, 1968*, Technical Memorandum 33-426, Vol. VI. Jet Propulsion Laboratory, Pasadena, Calif., Apr. 15, 1971.

Renzetti, N. A., *Tracking and Data System Support for the Pioneer Project. Pioneer VII. Extended Mission: July 1, 1968–July 1, 1969*, Technical Memorandum 33-426, Vol. VII. Jet Propulsion Laboratory, Pasadena, Calif., Apr. 15, 1971.

Renzetti, N. A., *Tracking and Data System Support for the Pioneer Project. Pioneer VIII. Extended Mission: June 1, 1968–July 1, 1969*, Technical Memorandum 33-426, Vol. VIII. Jet Propulsion Laboratory, Pasadena, Calif., May 1, 1971.

Renzetti, N. A., *Tracking and Data System Support for the Pioneer Project. Pioneers VI–IX. Extended Missions: July 1, 1969–July 1, 1970*. Technical Memorandum 33-426, Vol. IX. Jet Propulsion Laboratory, Pasadena, Calif., Aug. 15, 1971.

Sjogren, W. L., *The Ranger III Flight Path and Its Determination From Tracking Data*, Technical Report 32-563. Jet Propulsion Laboratory, Pasadena, Calif., Sept. 15, 1965.

Bibliography (contd)

Sjogren, W. L., et al., *The Ranger V Flight Path and Its Determination From Tracking Data,* Technical Report 32-562. Jet Propulsion Laboratory, Pasadena, Calif., Dec. 6, 1963.

Sjogren, W. L., et al., *The Ranger VI Flight Path and Its Determination From Tracking Data,* Technical Report 32-605. Jet Propulsion Laboratory, Pasadena, Calif., Dec. 15, 1964.

Sjogren, W. L., et al., *Physical Constants as Determined From Radio Tracking of the Ranger Lunar Probes,* Technical Report 32-1057. Jet Propulsion Laboratory, Pasadena, Calif., Dec. 30, 1966.

Sjogren, W. L., *Proceedings of the JPL Seminar on Uncertainties in the Lunar Ephemeris,* Technical Report 32-1247. Jet Propulsion Laboratory, Pasadena, Calif., May 1, 1968.

Sjogren, W. L., "Lunar Gravity Estimate: Independent Confirmation," *J. Geophys. Res.*, Vol. 76, No. 29, Oct. 10, 1971.

Spier, G. W., "Design and Implementation of Models for the Double Precision Trajectory Program (DPTRAJ)," Technical Memorandum 33-451, Jet Propulsion Laboratory, Pasadena, Calif., Apr. 15, 1971.

Stelzried, C. T., *A Faraday Rotation Measurement of a 13-cm Signal in the Solar Corona,* Technical Report 32-1401. Jet Propulsion Laboratory, Pasadena, Calif., July 15, 1970.

Stelzried, C. T., et al., "The Quasi-Stationary Coronal Magnetic Field and Electron Density as Determined From a Faraday Rotation Experiment," *Sol. Phys.*, Vol. 14, No. 2, pp. 440–456, Oct. 1970.

Thornton, J. H., Jr., *The Surveyor I and Surveyor II Flight Paths and Their Determination From Tracking Data,* Technical Report 32-1285. Jet Propulsion Laboratory, Pasadena, Calif., Aug. 1, 1968.

Vegos, C. J., et al., *The Ranger IX Flight Path and Its Determination From Tracking Data,* Technical Report 32-767. Jet Propulsion Laboratory, Pasadena, Calif., Nov. 1, 1968.

Winn, F. B., *Selenographic Location of Surveyor VI, Surveyor VI Mission Report: Part II. Science Results,* Technical Report 32-1262. Jet Propulsion Laboratory, Pasadena, Calif., Jan. 10, 1968.

Winn, F. B., "Post Landing Tracking Data Analysis," in *Surveyor VII Mission Report: Part II. Science Results,* Technical Report 32-1264. Jet Propulsion Laboratory, Pasadena, Calif., Mar. 15, 1968.

Winn, F. B., "Post Lunar Touchdown Tracking Data Analysis," in *Surveyor Project Final Report: Part II. Science Results,* Technical Report 32-1265. Jet Propulsion Laboratory, Pasadena, Calif., June 15, 1968.

Winn, F. B., *Surveyor Posttouchdown Analyses of Tracking Data,* NASA SP-184. National Aeronautics and Space Administration, Washington, D.C., p. 369.

Wollenhaupt, W. R., et al., *The Ranger VII Flight Path and Its Determination From Tracking Data,* Technical Report 32-694. Jet Propulsion Laboratory, Pasadena, Calif., Dec. 15, 1964.

NASA — JPL — Coml., L.A., Calif.